Deutsche
Forschungsgemeinschaft

# Geochemical Processes

Conceptual Models for
Reactive Transport
in Soil and Groundwater

*Geochemical Processes: Conceptual Models for Reactive Transport in Soil and Groundwater.*
*Research Report.* Deutsche Forschungsgemeinschaft (DFG).
 ISBN: 978-3-527-27764-3

Deutsche
Forschungsgemeinschaft

# Geochemical Processes

## Conceptual Models for Reactive Transport in Soil and Groundwater

Edited by
Horst D. Schulz and Georg Teutsch

Research Report

WILEY-VCH

DFG

Deutsche Forschungsgemeinschaft
Kennedyallee 40, D-53175 Bonn, Federal Republic of Germany
Postal address: D-53170 Bonn
Phone: ++49/228/885-1
Telefax: ++49/228/885-2777
E-Mail: postmaster@dfg.de
Internet: http://www.dfg.de



Library of Congress Card No.: applied for

A catalogue record for this book is available from the British Library.

Bibliographic information published by Die Deutsche Bibliothek
Die Deutsche Bibliothek lists this publication in the Deutsche Nationalbibliografie;
detailed bibliographic data is available in the Internet at http://dnb.ddb.de.

ISBN 3-527-27764-1



Cover Design and Typography: Dieter Hüsken.
Composition: Hagedorn Kommunikation, Viernheim.
Printing: betz-druck gmbh, Darmstadt.
Bookbinding: J. Schäffer GmbH & Co. KG, Grünstadt.

Printed in the Federal Republic of Germany.

# Contents


**1 Modelling Contaminant Transport in Anthropogenic Soil: Reconstruction of Spatial Heterogeneity by Analysing the Relations of Adjacent Pedofacies**
*Kai Uwe Totsche, Ingrid Kögel-Knabner and Harald Weigand* . . . . . 1

1.1 Introduction . . . . . 2

1.2 Characterising Spatial Heterogeneity of Soils at Anthropogenic Sites: the Testfeld Süd . . . . . 4

1.3 Reconstruction of Spatially Variable Pedofacies with a Structure-imitating Stochastic Approach Based on Markov Processes . . . . . 9
1.3.1 Markov Chain Theory . . . . . 10
1.3.2 Continuous-lag Markov Chains . . . . . 10

1.4 Assessing the Risk for PAH Deep Seepage at Industrial Contaminated Sites . . . . . 14

1.5 Summary and Conclusion . . . . . 17

1.6 References . . . . . 18

**2 Concepts for Modelling of Heterogeneous Flow Processes in Soil Columns on the Basis of Tomographic Radiotracer Experiments**
*Michael Richter* . . . . . 20

2.1 Introduction . . . . . 21

2.2 Technology and Applicability of the Positron Emission Tomography (PET) for Transport Studies in Soil Columns . . . . . 21

2.3 Typical Results of PET-Studies of the Hydrodynamics in Soil Columns . . . . . 24
2.3.1 Experimental . . . . . 24
2.3.2 PET-Measurements of Tracer Distribution in the Model Soil Column . 25

2.4 Calculation of Velocity Distributions . . . . . 28

2.5 Concepts of Modelling of Flow Processes in Soil Columns . . . . . 30
2.5.1 Estimation of Parameters by Inverse Modelling . . . . . 30
2.5.2 Partition of the Column in Regions with Different Flow Characteristics . . . . . 31
2.5.3 Modelling with Reference to the Dispersion Model . . . . . 33
2.5.4 Support of Conventional Measuring Technique . . . . . 34

2.6 References . . . . . 38

**3 Upscaling of Hydraulic and Hydrogeochemical Aquifer Parameters Using an Approach Based on Sedimentological Facies**
*Thomas Ptak and Rudolf Liedl* . . . . . 39

3.1 Introduction . . . . . 39

3.2 The Three-dimensional Reactive Transport Modelling Approach . . . 41
3.2.1 Facies-based Characterization of Hydraulic and Hydrogeochemical Aquifer Properties . . . . . 42
3.2.2 Generation of Three-dimensional Facies and Fields of Hydraulic and Hydrogeochemical Aquifer Parameters . . . . . 44
3.2.3 Modelling of Flow and Reactive Transport . . . . . 47

3.3 Example of Application . . . . . 49

3.4 Conclusions and Future Work . . . . . 53

3.5 References . . . . . 53

**4 DiffMod7 – Modelling Oxygen Diffusion and Pyrite Decomposition in the Unsaturated Zone Based on Ground Air Oxygen Distribution**
*Henrik Hecht, Martin Kölling and Norbert Geisler* . . . . . 55

4.1 Introduction . . . . . 55

4.2 Data Basis for Model Development . . . . . 57

4.3 The Model (DiffMod7) . . . . . 58
4.3.1 Model Concept . . . . . 58
4.3.1.1 Diffusive Transport . . . . . 58
4.3.1.2 Pyrite Weathering . . . . . 60
4.3.1.3 Convective Transport . . . . . 61
4.3.2 Computer Implementation of Model and User Interface . . . . . 61
4.3.3 Example . . . . . 62
4.3.4 Modelling Column Experiments . . . . . 64
4.3.5 Running Scenarios . . . . . 67
4.3.6 Field Test . . . . . 72

4.4 Discussion . . . . . 74

4.5 Summary . . . . . 76

4.6 References . . . . . 77

**5 Speciation and Sorption for Risk Assessment: Modelling and Database Applications**
*Vinzenz Brendler, Thuro Arnold, Sture Nordlinder, Harald Zänker and Gert Bernhard* . . . . . 79

5.1 Introduction . . . . . 79

5.2 Geochemical Speciation and Sorption . . . . . 80
5.2.1 The Concept of "Smart $K_d$" . . . . . 81
5.2.1.1 Application Case: Sorption onto Rocks . . . . . 83
5.2.1.2 Application Case: Colloids in Mines . . . . . 85
5.2.1.3 Application Case: Uranium Migration . . . . . 87
5.2.2 Mineral-Specific Sorption Database . . . . . 91

5.3 References . . . . . 93

**6 New Geochemical Simulator Rockflow-RTM: Development and Benchmarking**
*Abderrahamne Habbar, Olaf Kolditz and Werner Zielke* . . . . . 95

6.1 Introduction . . . . . 96

6.2 Governing Equations . . . . . 96
6.2.1 Nonequilibrium Equations . . . . . 96
6.2.2 Equilibrium Equations . . . . . 98

6.3 Numerical Method . . . . . 99

6.4 Software Concept . . . . . 100

6.5 Examples . . . . . 101
6.5.1 Nitrification Process in a Porous Column . . . . . 102
6.5.2 Geochemical Nonequilibrium Effects . . . . . 104
6.5.3 TCE Transformation . . . . . 105
6.5.4 Matrix Diffusion . . . . . 107
6.5.5 Two-Member Decay Chain in Fracture-Matrix System . . . . . 110
6.5.6 Two-Member Decay Chain in Fracture-Matrix System . . . . . 111

6.6 Conclusions . . . . . 113

6.7 References . . . . . 114

**7 Modelling Reactive Transport of Organic Solutes in Groundwater with a Lagrangian Streamtube Approach**
*Michael Finkel, Rudolf Liedl and Georg Teutsch* . . . . . 115

7.1 Introduction . . . . . 115

7.2 Reactive Transport Model SMART . . . . . 117
7.2.1 Streamtube Approach . . . . . 117
7.2.2 Accounting for Reactive Processes . . . . . 119
7.2.3 Numerical Evaluation of Breakthrough Curves . . . . . 120

7.3 Reactive Transport of Phenanthrene and Terrasurf G50 . . . . . 123
7.3.1 Conceptual Model of Relevant Processes . . . . . 123
7.3.2 Remediation Scenario . . . . . 125
7.3.3 Process Parameters . . . . . 126
7.3.4 Conservative Transport Description . . . . . 127
7.3.5 Reactive Transport Simulations . . . . . 127
7.3.5.1 Influence of Aquifer Properties on Transport of PHE . . . . . 127
7.3.5.2 Impact of Non-Ionic Surfactant TG50 on Transport of PHE . . . . . 130

7.4 Summary and Conclusions . . . . . 131

7.5 References . . . . . 132

**8 Conception of a GIS-Based Data Model for Combined Hydrochemical and Hydraulic Balance Calculations in Pleistocene Landscapes – an Approach of Regionalization**
*Christoph Merz, Peter Schuhmacher, Jörg Steidl and Andreas Winkler* . . . . . 135

8.1 Introduction . . . . . 136

8.2 Material and Methods . . . . . 136

8.3 Results . . . . . 139
8.3.1 Stoebber Watershed . . . . . 139
8.3.2 Oderbruch . . . . . 140
8.3.2.1 Introduction . . . . . 140
8.3.2.2 Material and Methods . . . . . 142
8.3.2.3 Results . . . . . 142
8.3.3 Ucker Watershed . . . . . 148

8.4 Discussion . . . . . 150

8.5 References . . . . . 152

**9 The "Virtual Aquifers" – Concept as a Tool for Evaluation of Exploration, Remediation and Monitoring Strategies**
*Dirk Schäfer, Andreas Dahmke, Olaf Kolditz and Georg Teutsch* . . . . 154

9.1 Introduction . . . . . 154

9.2 Examples for the Use of the Virtual Aquifer Concept . . . . . 156
9.2.1 Effect of Screening and Pumping Rate on Measured Concentrations in a Heterogeneous Aquifer . . . . . 156
9.2.2 The Effect of Mixing in an Observation Well on Evaluation of Natural Attenuation Processes in a Heterogeneous Aquifer . . . . . 160
9.2.3 Monitoring of Natural Attenuation in a Heterogeneous Aquifer . . . . 166

9.3 Problems and Requirement for Additional Scientific Research . . . . . 168

9.4 The "Virtual Aquifer" Project . . . . . 170

9.5 References . . . . . 171

**10 Two-Dimensional Two-Step Modelling of 250 Years of Transport and Reactions in a Virtual Anoxic Aquifer (Oderbruch, Eastern Germany)**
*Gudrun Massmann and Horst D. Schulz* . . . . . 173

10.1 Introduction . . . . . 174
10.1.1 Why 2D-Modelling of Transport and Reactions? . . . . . 174
10.1.2 Why the Study Site Oderbruch? . . . . . 175

10.2 The Study Site: Hydraulic Conductivity and Iron(III) Concentration of the Aquifer . . . . . 176

10.3 Principle Structure of the Two-Step Model . . . . . 181
10.3.1 Physical Transport Using the Technique of Explicit Differences . . . . 181
10.3.2 Geochemical Reactions . . . . . 182

10.4 Calibration of the Model with Measured Values of DOC . . . . . 182

10.5 Validation of the Model with Measured Values for Dissolved Iron . . . . . 185

10.6 Discussion . . . . . 187

10.7 References . . . . . 189

**11 Redox-Transport Modelling for the Oderbruch Aquifer**
*Ekkehard Holzbecher, Christoph Horner, Gudrun Massmann, Asaf Pekdeger and Christoph Merz* . . . . . 191

11.1 Introduction . . . . . 192

11.2 Site and Measurement Description . . . . . 193
11.2.1 Hydrogeology . . . . . 194
11.2.2 Water Chemistry . . . . . 195

11.3 Modelling Concept . . . . . 197
11.3.1 Reaction Model . . . . . 198
11.3.2 Reactive Transport Simulation . . . . . 202

11.4 Model Implementation . . . . . 203
11.4.1 Model Application . . . . . 204
11.4.1.1 Generic Precipitation/Dissolution . . . . . 204
11.4.1.2 Precipitation/Dissolution, Carbonate and Acid-Based Chemistry . . . . . 205

11.4.2 Parameterisation . . . . . 206
11.4.2.1 Generic Precipitation/Dissolution . . . . . 206
11.4.2.2 Precipitation/Dissolution, Carbonate and Acid-Based Chemistry . . . . . 208

11.5 Results from Measurements and Modelling . . . . . 210

11.6 Conclusions . . . . . 212

11.7 References . . . . . 213

**12 Oxoanion Transport in Aquifers Containing Iron Hydroxide – Modelling of Column Experiments with PHREEQC2**
*Max Kofod, Verena Haury, Nandimandalam Janardhana Raju and Margot Isenbeck-Schröter* . . . . . 215

12.1 Introduction . . . . . 216

12.2 Experimental Set-Up and Analytical Methods . . . . . 216

12.3 Modelling of the Oxoanion Breakthrough . . . . . 218
12.3.1 Data Used . . . . . 218
12.3.2 Parameters Describing the Available Surface . . . . . 219
12.3.3 pH Buffering . . . . . 220
12.3.4 Cell Number and Diffuse Layer Options . . . . . 220

12.4 Results . . . . . 224
12.4.1 Model Runs Using the Site Density of Amorphous Iron Hydroxide and Goethite . . . . . 224
12.4.2 Fitting the Site Densities . . . . . 225
12.4.3 pH Modelling . . . . . 225

12.5 Summary and Conclusions . . . . . 227

12.6 References . . . . . 228

**13 Problems of Upscaling the Time in $Fe^0$ Reactive Barriers**
*Markus Ebert, Andreas Dahmke, Ralf Köber and Dirk Schäfer* . . . . . 229

13.1 Introduction . . . . . 230

13.2 Microbially Mediated Processes . . . . . 231

13.3 Degradation Rates and Flow Velocity . . . . . 232

13.4 Mineral Reactions, Passivation and Degradation Rates . . . . . 234

13.5 Conclusions . . . . . 239

13.6 References . . . . . 240

**14 Comparing Two Approaches for Modelling Natural Attenuation of Organic Compounds in Heterogeneous Porous Media**
*Anita Peter, Rudolf Liedl, Thomas Ptak and Georg Teutsch* . . . . . 242

14.1 Introduction . . . . . 243

14.2 Model Approaches . . . . . 243
14.2.1 The Lagrangian Model . . . . . 243
14.2.2 The Eulerian Model . . . . . 244

14.3 Reactive Transport Modelling of the 'Testfeld Süd' Site . . . . . 244

14.4 Results and Discussion . . . . . 245

14.5 References . . . . . 248

**15 A Steady-State Approach to Model Redox Potentials in Groundwaters Contaminated with Chlorinated Ethenes**
*Stefan Peiffer and Christine Nohlen* . . . . . 250

15.1 Introduction . . . . . 251

15.2 Anaerobic Degradation of Chlorinated Ethenes . . . . . 252

15.3 Evaluation of Literature Data . . . . . 253

15.4 Application of Redox Chemical Information to Predict Degradation Rates . . . . . 255

15.5 A Steady-State Approach to Predict Degradation Rates . . . . . 257

15.6 Conclusion . . . . . 260

15.7 References . . . . . 261

**16 Simulation of Two-Column Experiments on Anaerobic Degradation of Toluene and Xylene**
*Wolfgang Schäfer and Rainer U. Meckenstock* . . . . . 263

16.1 Introduction . . . . . 264

16.2 Set-Up of the Soil Columns . . . . . 265
16.2.1 Experiment 1 . . . . . 265
16.2.2 Experiment 2 . . . . . 265

16.3 Set-Up of the Numerical Model . . . . . 266
16.3.1 Flow and Transport Model . . . . . 266
16.3.2 Degradation Model . . . . . 266

16.4 Model Calibration . . . . . 268

16.5 Testing of Hypotheses on the Interaction between Toluene and Xylene Degradation . . . . . 271
16.5.1 Inhibition of Xylene Degradation by a Substance other than Toluene . . . . . 271
16.5.2 Competition for Sulfate . . . . . 272
16.5.3 Degradation of Toluene and Xylene by a Single Microbial Group . . . 273

16.6 Simulation of Experiment 2 . . . . . 274

16.7 Conclusions and Outlook . . . . . 276

16.8 References . . . . . 278

# Foreword

In the field of groundwater numerical flow modelling has become a standard tool for scientific and also for most of the practical problems. The modelling software has matured during the past 10 years from being user-unfriendly with complex interfaces to a powerful, easy-to-use, windows-based system. For porous media flow in the saturated zone, the basic principle pertinent to all common programmes like MODLFOW, FEFLOW etc. is the solution of the linear DARCY- and continuity-equations. The numerical problems associated with the limitations in discretisation known in earlier days are not a serious burden any more because of the high-speed PCs with hundreds of Mbytes memory available nowadays. Therefore, groundwater flow modelling is not any more a technical challenge but – and this has not changed throughout the years – it remains a conceptual challenge. Furthermore the subsurface heterogeneity still represents a major challenge for the simulation of real world systems. Flow directions, flow velocities and consequently concentration values will depend on the adequate description of the subsurface heterogeneity.

Compared to flow models, geochemical reaction models can be more complex in terms of the processes and parameters involved. These models allow to describe quantitatively numerous reaction paths which occur in natural aquatic systems. The user may deal with a variety of dissolved substances in seepage and groundwater as well as numerous solid substances forming the aquifer material – and all these substances may react in various ways based on characteristic reaction kinetics or reaction rates. In short, one may have to deal with a complex system of interacting processes and a large number of parameters at the same time. The real challenge of geochemical modelling is therefore: how can one reduce the complexity of real world aquatic systems in such a way that it can be adequately described with the models available taking also into account our limited understanding of the system. The modelling software available today, e.g. the programme PHREEQC, is user-friendly and offers a large variety of reaction types as well as large data bases for the reaction constants. Consequently, the (experimental) data requirements needed for the understanding of a real system and also for the prediction of future system states are usually quite high – not to mention the fact that a considerable number of the geochemical processes are not yet fully understood.

An even higher level of complexity is represented by coupled flow and reactive tranport models. One may distinguish between tightly and loosely coupled systems. In

general, the tightly coupled systems use only geochemical models with limited complexity in order to cope with the higher computational burden. On the other hand, the loosely coupled systems sometimes lack the ability of accurately describing the interaction between the flow-, transport- and reaction-components within the model. Today, coupled flow and reactive transport models are commonly used within the research community – mostly for simulating lab experiments but also for the few field experiments where detailed geochemical data is being gathered. Increasingly, these models are also used in practice to analyse simplified scenarios of real world conditions at contaminated sites – e.g. for the simulation of natural attenuation processes. The major challenge is to gather data in order to adequately describe the geochemical reactions. In specific, there is no general solution yet available on how to scale e.g. laboratory measurements to field scale, i.e. over 2 to 3 order of magnitude.

From 1995 until 2001 a considerable number of scientific projects have been funded within the priority programme 546 of the Deutsche Forschungsgemeinschaft (DFG) "Geochemical processes with long-term effects in anthropogenically affected seepage and groundwater". Transport/reaction modelling was a focus of many of the research activities. In the final phase of the priority programme 546 a special workshop was organized (December 2000 in Tübingen) for the modelling groups. The various approaches, know-how, ideas and results gathered during the priority programme were presented and discussed. As a result of the workshop this special volume was put together, describing the concepts and results from the various modelling activities. We are fully aware of the fact that this volume is far from being a complete description of the state-of-the-art in the field of coupled reactive transport modelling. However, it provides an overview – certainly not a complete one – on the research in this field in Germany.

November 2001

Horst D. Schulz, Bremen Georg Teutsch, Tübingen

# Acknowledgements

This book would not exist without the help of all the colleagues listed below. Along with the authors we are grateful to these reviewers for their constructive and helpful comments.

| Reviewer | Institution |
|---|---|
| Andreas Dahmke | Institute for Geoscience, University of Kiel, Germany |
| Markus Ebert | Institute for Geoscience, University of Kiel, Germany |
| Peter Grathwohl | Center for Applied Geoscience, University of Tübingen, Germany |
| Margot Isenbeck-Schröter | Institute of Environmental Geochemistry, University of Heidelberg, Germany |
| Martin Kölling | Department of Geosciences, University of Bremen, Germany |
| Olaf Kolditz | Center for Applied Geoscience, University of Tübingen, Germany |
| Rudolf Liedl | Center for Applied Geoscience, University of Tübingen, Germany |
| Georg Mattheß | Prof. em. Institute for Geoscience, University of Kiel, Germany |
| Stefan Peiffer | Department of Hydrogeology, RWTH Aachen, Germany |
| Asaf Pekdeger | Department of Economic and Environmental Geology, Free University Berlin, Germany |
| Kurt Roth | Institute of Environmental Physics, University of Heidelberg, Germany |
| Dirk Schäfer | Institute for Geoscience, University of Kiel, Germany |
| Wolfgang Schäfer | Interdisciplinary Center for Scientific Computing, University of Heidelberg, Germany |
| Kai Uwe Totsche | Department of Soil Science, Technical University of Munich, Germany |

Furthermore we would like to express our gratitude to Dr. Astrid Hadeler for editorial assistance.

We are also indebted to Dr. Ute Weber of the Deutsche Forschungsgemeinschaft (DFG) for financial support for the workshop on this topic within the framework of the priority programme 546.

# 1 Modelling Contaminant Transport in Anthropogenic Soil: Reconstruction of Spatial Heterogeneity by Analysing the Relations of Adjacent Pedofacies

Kai Uwe Totsche*, Ingrid Kögel-Knabner and Harald Weigand

## Abstract

Flow and transport of water and solutes in soil is controlled by both the structural heterogeneity of the physicochemical soil parameters and the temporal variability of boundary conditions and driving gradients. We will present an approach for the modelling of contaminant transport at highly contaminated industrial sites. Special consideration is put on the reconstruction and mapping of the spatial heterogeneity of adjacent pedofacies with highly contrasting properties. Employing a thorough field survey, we will provide evidence that urban and industrial sites are characterized by a spatial heterogeneity of contaminant sources and sinks which is neither solely random nor regular in nature. To reconstruct the spatial heterogeneity of such sites we applied a conditional stochastic simulation based on the Markov process theory. Markov processes facilitate the reconstruction of spatial random numbers by which the local state solely depends on the direct neighbour and not on more distant occurrences. By doing so we adequately reconstructed both the pedofacies and the contamination levels observed. With a finite and relatively small number of combinations of pedofacies and contamination levels we were able to cover more than 60 % of the spatial heterogeneity of the site. The typical soil profiles were then used with a process-based reactive transport model in order to assess the risk of groundwater contamination. The proposed procedure is a compact, yet mathematically simple and comprehensive approach to a risk-based assessment of soil and groundwater pollution by hazardous substances found at anthropogenic sites of urban and industrial environments.

* Lehrstuhl für Bodenkunde, Department für Ökologie, Wissenschaftszentrum Weihenstephan, Technische Universität München, 85350 Freising Weihenstephan; e-Mail: totsche@pollux.edv.agrar.tu-muenchen.de



*Geochemical Processes: Conceptual Models for Reactive Transport in Soil and Groundwater.*
*Research Report.* Deutsche Forschungsgemeinschaft (DFG).
 ISBN: 978-3-527-27764-3

## 1.1 Introduction

Field scale flow and transport in soil is controlled by both the structural heterogeneity of the physicochemical soil parameters and the temporal variability of boundary conditions and driving gradients. The variability of natural porous media properties is the consequence of different biogeochemical and physical processes. In hydrogeologic systems the most prominent ones are structural deformation, deposition and diagenesis, whereas in soil environments additional processes contribute to the spatial heterogeneity and temporal variability of soil properties: These are structural rearrangement, aggregation, mineral formation, mineralisation and humification of the organic matter as well as the effects of soil organisms and plants. Pedogenic processes lead to structural and physicochemical transformations which result in morphologic differentiation of soils in horizons. Often, the continuation of soil formation over long time periods even modifies the inherited properties of the former parent material, thus providing a complete structural rearrangement for flow and transport processes. Flow and transport pathways in natural porous media are therefore characterised by pronounced spatially variable patterns such as preferential flow and transport phenomena (Beven and Germann, 1982; Seyfried and Rao, 1987; Jardine et al., 1990; Roth et al., 1991; Flury et al., 1995).

The principle orientation of the horizons is perpendicular to the main flow direction which is oriented along the gravitational gradient. Thus, interfaces between individual horizons are oriented in the same way, although they might not be clearly separated, but characterised by diffuse boundaries and interfingering. They may even be disrupted by channels and other features due to, for example, rooting and bioturbation. This situation is even more pronounced for anthropogenic soils, such as in urban or industrial areas. In these soils, the construction, excavation, burying, refilling, and levelling resulted in layered profiles of low lateral continuity (Blume, 1989; Burghardt, 1994; Wiesmann, 1994; Weigand et al., 1998). The different layers are characterised by mostly sharp interfaces in between adjacent materials exhibiting a high contrast in structure and functional properties. The most prominent are the extreme contrasts in physical, chemical, and biological properties of adjacent layers and horizons.

The understanding of the effect of these features on flow and transport is still scarce. Most of the past and present research has concentrated on the spatial variability of properties like the hydraulic conductivity and (effective) porosity of natural porous media (Dagan, 1986; Gelhar, 1986; Jury et al., 1987; Jury and Roth, 1990; Gerke and van Genuchten, 1993). The hydraulic conductivity, for example, which was shown to differ spatially by 13 orders of magnitude (Bear, 1979; Freeze and Cherry, 1979), controls both magnitude of flow and direction of the flowpaths for water and thus also the transport of solutes. In hydrogeologic systems, the large scale structure of the hydraulic conductivity controls groundwater flow, while large and small scale variations control solute spreading and dispersion (Koltermann and Gorelick, 1996). This also holds for soil environments, where small scale variability of the (un)saturated hydraulic conductivity significantly contributes to solute spreading and dispersion. On the meter scale, however, the contrast in the properties of proximate layers or horizons

affects rates and amounts of both liquid and solute release, movement and immobilisation from, through and in soil. The qualitative and quantitative description of the heterogeneity of layered porous media is therefore a mandatory prerequisite for the understanding and prediction of water and solute flux in such environments. Geostatistical methods seem to be inappropriate at such sites, because of (i) the stationarity assumption required to apply these methods (Journel, 1986), (ii) the impossibility to reproduce variable anisotropy directions (Neton et al., 1994), and (iii) a very high and therefore unacceptable nugget effect, that is a high variability at small distances within the variogram as a consequence of the sharp boundaries and contrasting properties.

An alternative and promising approach to evaluate the spatial heterogeneity is based on the reconstruction of series of proximate pedofacies. In this context, a pedofacies is defined as a morphologically and functionally uniform layer. A pedofacies may be a pedogenic soil horizon, a layer of buried homogeneous anthropogenic material, or even a geologic facies. In general, it resembles a layer which is characterised by homogeneous physical, chemical, and biological properties. By analysing the physical and chemical properties relevant to flow and transport, for example hydraulic conductivity, porosity, release rates etc. for each individual pedofacies, the flow and transport of contaminants can then be calculated individually or even for series of successive pedofacies.

In the following, we will introduce a conceptually simple and mathematically comprehensive method to reconstruct spatially heterogeneous soil profiles which resemble series of superimposed pedofacies of contrasting properties. The final goal will be the evaluation of contaminant transport and deep seepage at sites characterised by such soils. At first, we will present evidence for the existence of pedofacies at urban industrial sites employing field data obtained by a spatially resolved field survey. Then we will demonstrate that soil profiles at such sites can be considered as series of pedofacies characterised by sharp boundaries and contrasting properties. The analysis and calculation of the transition frequencies from one pedofacies to another is thereby a measure for the spatial variability at such sites and will be used to condition a stochastic simulation based on the Markov theory. The conditional stochastic simulation is used to reconstruct series of pedofacies (= soil profiles), which are likely for the particular site. The generated soil profiles are then used to evaluate transport and seepage of contaminants. We therefore apply a physically based reactive transport model (PBRTM) which utilises the structural and functional properties analysed for each pedofacies. The PBRTM is then run for all possible series of pedofacies likely to occur at the respective site. Thus, we explicitly consider the relations of adjacent pedofacies with contrasting properties and are able to reconstruct spatially heterogeneous structures such as natural and anthropogenic soils.

## 1.2 Characterising Spatial Heterogeneity of Soils at Anthropogenic Sites: the Testfeld Süd

In this chapter we provide evidence for the existence of soil profiles composed of pedofacies with highly contrasting properties. The results presented here were obtained during a thorough field survey conducted at an urban industrial site, the Testfeld Süd. It is a former manufactured gas work site in a capital city in southwestern Germany, presently used as a gas storage and distribution facility. One of the major pollutants at such sites are, among others, polycyclic aromatic hydrocarbons (PAH). PAH deep seepage from the unsaturated soil zone significantly contributes to the contamination of groundwater (Eiceman et al., 1986). Travel time and travel distance of PAH are controlled by release from the source materials, transport pathways and retardation within the soil profile (Kögel-Knabner and Totsche, 1998). Important processes of PAH release are rate-limited desorption from the immobile soil phase and dissolution from nonaqueous phase liquids like oil, tar, creosote and others. Retardation on the other hand is controlled by sorption to the immobile solid phase, predominantly to organic sorbents (Murphy et al., 1992; Kögel-Knabner and Totsche, 1998). Knowledge on the spatial arrangement of both sources and sinks is therefore mandatory to estimate PAH transport and distribution in the unsaturated zone at such sites (Weigand et al., 1998).

To assess the variability of both sources and sinks for the contaminants at the Testfeld Süd, a field survey was conducted encompassing an area of 31250 $m^2$. Soil sampling was done by ram and core drilling. Representative sampling was performed based on a regular grid screen (Totsche, 1995). Equilateral triangles of 25 m edge length were chosen as base for the grid (Fig. 1.1) to allow also for a geostatistical evaluation in three different directions. This procedure resulted in 126 grid cells, 35 of which were selected randomly and chosen for sampling. The geostatistical analysis, however, revealed that it is inappropriate for such sites.

During field survey the soils were described according to the German soil classification system KA 4 (AG Boden, 1994), which allows the classification of natural and anthropogenic soils based on genetic and morphologic features.

At each sampling point, soil cores were taken and sliced into vertical sections of 0.2 m, to allow for a depth-dependent analysis of texture, contents of stones, amounts of aluminium and iron oxides, and organic and inorganic carbon. Figure 1.2 gives the results from chemical analysis of selected soil properties. The parameters have a high variability, typical for anthropogenic sites. Physical characterisation comprised the analysis of bulk density and hydraulic properties like the capillary pressure-water saturation curve and the saturated hydraulic conductivity.

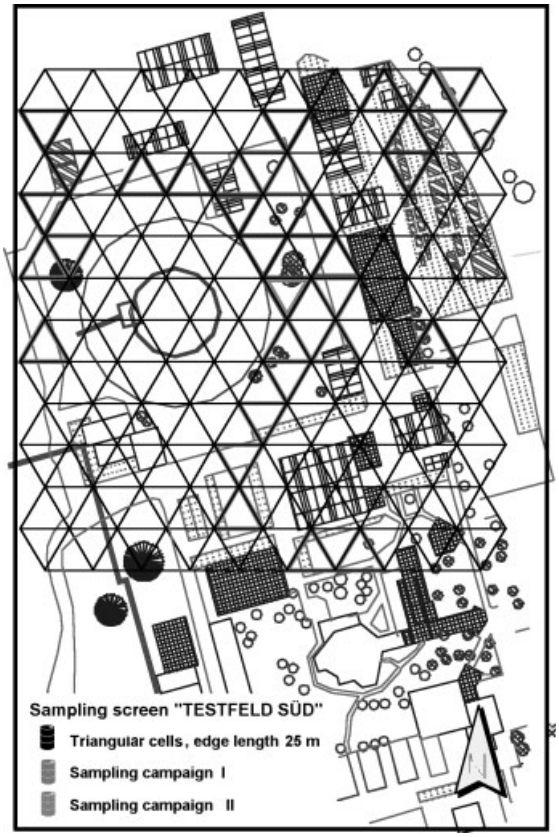


Figure 1.1: Sampling screen used for the heterogeneity assessment of sources and sinks at the Testfeld Süd site.

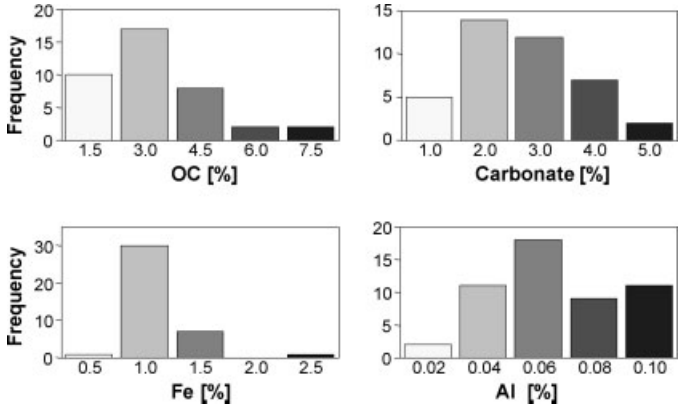


Figure 1.2: Variability of selected solid phase constituents found at the Testfeld Süd. Fe and Al denote total iron and total aluminium. OC = organic carbon

Six different soil forming materials were found and defined as the pedofacies of the Testfeld Süd. These pedofacies are

1. remnants of the gas production, non-aqueous phase liquid (NAPL), like oils, creosote, tar (NL);
2. physically weathered clayey marlstone (CM);
3. pedogenically transformed loamy alluvial deposits, brown, low carbonate content (ptLAD);
4. construction debris (CD);
5. remnants of gas production, soot, slag;
6. pristine loamy alluvial deposits, ochre, high carbonate content (LAD).

Pedofacies 1 and 5 were identified as source layers for the release of the PAH. The transitions between the individual pedofacies were mostly sharp, especially for transitions from 1, 4 and 5, which are clearly imported by human activities, to pedofacies 2, 3 and 6, which are the original autochthonous materials found at this site. However, these pristine pedofacies were not always in their correct geological position, that is clayey marlstone at the base, unaltered loamy alluvial deposit in the middle and the pedogenically transformed alluvial deposit in the top position. The disruption of the proper sedimentological order was due to the intensive construction, digging and levelling activity during the last 150 years which affected the uppermost two meters of the original valley filling. Figure 1.3 gives a schematic presentation of the spatial variability of the soil profiles as revealed by the soil survey. Within the graph, we indicate ran-

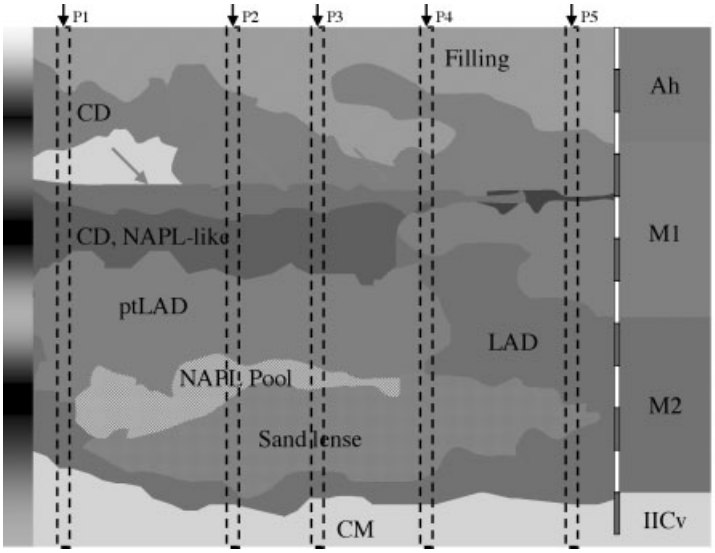


Figure 1.3: Schematic representation of the spatial variability of the soil profiles as revealed by the soil survey. Random locations (P1 through P5) for ram or core sampling are indicated in the figure. The respective soil profiles are given in Table 1.1. The green arrows indicate the location of a former building.

Table 1.1: Soil profiles as a function of the location of the ram/core drilling point.

| Layer | Natural Situation | Anthropogenic situation P1 | P2 | P3 | P4 | P5 |
|---|---|---|---|---|---|---|
| 1 | Humic soil | Filling | Filling | Filling | Filling | Filling |
| 2 | ptLAD | CD | PtLAD | CD | PtLAD | Pt LAD |
| 3 | LAD | CM | LAD | LAD | Filling | LAD |
| 4 | CM | LAD | CD, NL | CD,NL | CD | CM |
| 5 | | CD, NL | Pt LAD | Pt LAD | LAD | |
| 6 | | PtLAD | LAD | LAD | Pt LAD | |
| 7 | | LAD | CM | CM | LAD | |
| 8 | | CM | | PtLAD | | |
| 9 | | | | LAD | | |
| 10 | | | | CM | | |

pt LAD: pedogenically transformed loamy alluvial deposit; LAD: loamy alluvial deposit; CD: construction debris; NL: NAPL-like; CM: Clayey marlstone.

dom locations for ram or core sampling. Based on these locations, we end up with soil profiles different both in the vertical arrangement and in the number of pedofacies (Table 1.1). We also indicate the location of the foundation of a former building (green arrows). This building was torn off, the remnants were excavated, and the remaining cavity refilled with different materials. Such activity can result in almost horizontal interfaces between different pedofacies. In that special case, the building was already constructed on top of allochthonous materials, a typical situation for urban and industrial sites with long utilisation history.

We found that layer thickness in the upper profile regions was around 0.4 m, typical for ditcher excavation and refilling activities (Burghardt, 1994). With increasing depth the amount of construction and destruction debris like gravel, brick and stones decreased. This is simply because the number of excavation cavities decrease with increasing depth.

In order to quantitatively analyse the changeover of pedofacies, we calculated transition frequencies for 0.2 m intervals, that is, we calculated the absolute frequency of the occurrence of one pedofacies on top of itself or on top of another. These numbers were then divided by the absolute number of the occurrence of the respective pedofacies. By this procedure, we were able to calculate relative numbers which represented the relative frequency of all possible transitions (Table 1.2). The diagonal entries of the matrix represent the appearance of one particular pedofacies on top of itself, while the other matrix elements represent the appearance of a pedofacies on top of a different one. The transition frequencies within a matrix row sum up to unity. This resembles the fact that all transitions of the respective pedofacies are taken into account.

By investigating the results of the transition frequency calculation we found that some transitions seem to be more likely than others. For example, we found that pedofacies 4, the construction debris, was exclusively located on top of pedofacies 2, the clayey marlstone ($p_{4,2} = 0.67$). Pedofacies 3, the pedogenically transformed alluvial deposit high in natural organic matter due to OC accumulation during soil formation, is

Table 1.2: Transition frequencies of the 6 different pedofacies identified at the Testfeld Süd. The numbers 1–6 denote the following: 1: Remnants of the gas production, NAPL-like; 2: physically weathered clayey marlstone; 3: pedogenically transformed loamy alluvial deposit, brown, low carbonate content; 4: construction debris; 5: remnants of gas production (soot, slag); 6: loamy alluvial deposits, ochre, high carbonate content. The numbers in the matrix denote the normalised transition frequency. 1 and 5 were identified as the source layers.

| pedofacies / pedofacies | 1 | 2 | 3 | 4 | 5 | 6 |
|---|---|---|---|---|---|---|
| 1 | 0.68 | – | – | – | – | 0.32 |
| 2 | – | 0.90 | – | – | – | 0.10 |
| 3 | – | 0.20 | 0.40 | 0.20 | 0.20 | – |
| 4 | – | 0.67 | – | 0.33 | – | – |
| 5 | – | 0.25 | 0.25 | 0.25 | – | 0.25 |
| 6 | 0.12 | 0.21 | – | – | 0.12 | 0.55 |

found on top of materials 2, 4, and 5. This is, because a layer of pristine, humic rich material was always deposited on top of buried contaminated materials in order to provide a substrate for grass and trees. The detailed investigation of the transition frequencies reveals a certain amount of regularity. Part of the observed transitions could be attributed to soil formation processes, which resemble a generic feature and are therefore regular by definition. Part of the transitions resemble the fact that the spatial arrangement of the pedofacies follow construction, engineering and landscaping principles. Thus, the observed transitions and the spatial arrangement of soil forming materials are not random. We therefore tested the hypothesis of transitions being purely random with a $\chi^2$-test. The test statistic resulted in the rejection of the random hypothesis. Thus, an additional regular component controls the spatial arrangement of the soil forming materials found at this site.

By separating the soil profiles in sections of discrete length, the transition analysis also results in transitions of pedofacies overlying themselves. If some pedofacies are of particular thickness and of larger spatial extent, the transition of these pedofacies on themselves becomes dominant. This can be seen for pedofacies 1, the NAPL-like remnants, with a transition frequency of $p_{1,1} = 0.68$ and pedofacies 2, the clayey marlstone, which has a transition frequency of $p_{2,2} = 0.90$. In contrast, layers of small thickness give low transition frequencies almost or even equal to zero. This is the case for material 5, the soot/slag/tar-like remnants, which has a thickness $< 0.2$ m in general.

Soil at industrial and urban sites is characterised by a pronounced spatial heterogeneity. It was shown that this heterogeneity is not purely random in nature. Such sites can be understood to be composed of series of pedofacies, which represent morphologically and functionally uniform layers with homogeneous physical and chemical properties. The pedofacies are vertically arranged in series to give soil profiles. These

series can be quantitatively analysed by evaluating the transitions between pedofacies. Moreover, we learned that the transitions are not controlled by random but by an additional component of regularity due to the fact that the spatial arrangement of the pedofacies follows construction, engineering and landscaping principles or are the result of soil forming processes. Thus, a mathematical method which is used to quantify or reconstruct the heterogeneity of such sites should be capable to cope with spatial patterns which are characterised neither by pure random nor by pure determination. Such a method will be introduced in the following.

## 1.3 Reconstruction of Spatially Variable Pedofacies with a Structure-imitating Stochastic Approach Based on Markov Processes

The spatial arrangement of the pedofacies at urban industrial sites was found to be highly variable and in between random and regular. However, as a field survey by any means can provide full spatial information on all possible series of pedofacies, some approach must be applied to infer the possible information on soil profiles where no data is available. The goal is to generate series of all possible pedofacies conditioned by the transition frequencies obtained from the field survey. We therefore will apply a method which allows to quantitatively analyse the relations between adjacent pedofacies. Based on this, possible series of pedofacies will be reconstructed reflecting the site heterogeneity which will then be used as a template for the modelling of reactive flow and transport in heterogeneous soils. To do so, we apply a 1-dimensional Markov chain model, assuming that an occurrence of a categorical variable, for example the pedofacies, exclusively depends on the occurrence of an adjoining or the same category. Compared to geostatistical methods Markov chain models provide a more rigorous approach to the stochastic context of adjacent sampling points. Markov chains facilitate the reconstruction of spatially random numbers by which the local state solely depends on the state of the direct neighbour and not on more distant occurrences (Doveton, 1971; Carle and Fogg, 1997).

It is important to note that this approach is guided by the idea not to characterise and map the spatial variability of a specific functional or structural property, for example the hydraulic conductivity or the coefficients for sorption (Rubin and Gomez-Hernandez, 1990; Koltermann and Gorelick, 1996), but rather to characterise the spatial variability of the structures themselves (Carle et al., 1998), that are the pedofacies in this study. Once this is achieved, the spatial distribution of these entities is reconstructed and used as a template for the definition of the spatial distribution of process parameters.

### 1.3.1 Markov Chain Theory

Markov chains describe a sequence $X$ of $n$ observations of a random variable $Z$ (Doveton, 1994; Tuckwell, 1995):

$$X = (Z_1, Z_2.., Z_n) \tag{1}$$

in which $Z$ may adopt $k$ exhaustive and mutually exclusive states $\{z_1,z_2,...z_k\}$. $X$ is called a stationary first order Markov chain, if for every $n > 0$, the probability that $Z_{n+1}$ adopts any of the states $z_1,z_2,...z_k$ is solely dependent on the previous state in $Z_n$.

This is formalised by the one-step transition probability $pr_{ij}$ of adjacent events (Clarke and Disney, 1970):

$$pr_{ij} = Pr\left\{ Z_{n+1} = z_i \,\middle|\, Z_n = z_j \right\} = \frac{Pr\left\{ z_i \cap z_j \right\}}{Pr\left\{ z_j \right\}} \quad i, j = 1..k \tag{2}$$

The one-step transition probabilities can be obtained from the empirical transition frequencies. All possible transitions from one state to another are summarised in the transition probability matrix $P$:

$$P = \begin{bmatrix} pr_{1,1} & pr_{1,2} & \cdots & pr_{1,k} \\ pr_{2,1} & pr_{2,2} & \cdots & pr_{2,k} \\ . & . & \cdots & . \\ pr_{k,1} & pr_{k,2} & \cdots & pr_{k,k} \end{bmatrix} \tag{3}$$

Row 1 denotes the probabilities of a one step transition from state 1 to any other state 1..$k$. The sum of row entries equals unity. The total probability $Pr_{\text{tot}}$ of a specific sequence $X$ is given as the product of the involved one-step transition probabilities:

$$Pr_{\text{tot}} = \prod_{m=1}^{n-1} pr_{i_m, j_{m+1}} \tag{4}$$

with $n$: number of transitions, $i, j = 1..k$.

### 1.3.2 Continuous-lag Markov Chains

Recent applications of the Markov chain theory in geology have introduced continuous-lag modelling of spatial variability (Carle and Fogg, 1997; Fogg et al., 1998). The continuous-lag approach extends the probability of state transitions recorded at fixed intervals (discrete-lag) to any desired interval by considering conditional rates of

change per unit length. Thus, transitions between adjacent events (the pedofacies or the contamination level) are not only dependent on the previous event but also on the vertical extent of the event, which in our case corresponds to the thickness of the pedofacies or the contamination level. Continuous-lag Markov chains avoid overly large bed thickness by reducing the diagonal entries of the transition probability matrix (Rolke, 1991).

Application of continuous-lag Markov chains requires the knowledge of lag-dependent transition probabilities. Through Sylvester's theorem (Agterberg, 1974; Carle and Fogg, 1997) these can be derived from:

$$P(h) = \exp(R \cdot h) = \sum_{l=1}^{k} \exp(\lambda_l \cdot h) \cdot S_l \tag{5}$$

where $P(h)$ denotes the transition probability matrix for any desired lag $h$, $R$ is the transition rate matrix, $\lambda_l$ represent the $1,..,k$ eigenvalues of the transition rate matrix and $S_l$ are the corresponding spectral component matrices. The eigenvalues of $R$ can be obtained from the eigenvalues $(\omega_l(\Delta h))$ of the discrete lag transition probablity matrix $P$ by:

$$\lambda_l = \frac{\ln\ (\omega_l(\Delta h))}{\Delta h} \tag{6}$$

Correspondingly, the spectral component matrices may be obtained from $P$ by:

$$S_l = \frac{\prod_{i \neq l} \left(\omega_i \cdot I - P(\Delta h)\right)}{\prod_{i \neq l} \left(\omega_i(\Delta h) - \omega_l(\Delta h)\right)} \tag{7}$$

where $I$ is the identity matrix.

The continuous-lag transition probabilities were obtained by solving Eqs. (6) and (7) on the basis of the transition probability matrix for the 20 cm interval. Eigenvalues and spectral components were inserted in Eq. (5) to yield transition probabilities for continuous lags.

We will exemplify the result of lag-dependent transition probability by employing data on the variability of the contamination level as found at the Testfeld Süd. Figure 1.4 shows the observed frequencies of the contamination levels. As was seen for the variability of other soil properties (Fig. 1.2), the contamination level was also found to be highly variable in space. Classification of the contamination was based on the

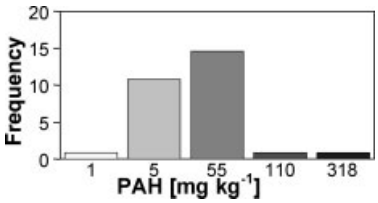


Figure 1.4: Absolute frequency of contamination levels encountered at the Testfeld Süd.

observed PAH concentration classes: PAH concentration less or equal 1 mg $kg^{-1}$ were classified as contamination level CL 1 (very low), PAH concentration between 1 and 55 mg $kg^{-1}$ were classified as CL 2 (low), PAH concentration from 55 to 110 mg $kg^{-1}$ were classified as CL 3 (high), and PAH concentrations higher than 110 mg $kg^{-1}$ were classified as CL 4 (very high).

Figure 1.5 shows the lag-dependence of the transition probabilities of the contamination levels. For the diagonal figures, which are the transitions of one CL on itself, the probability starts at 1 for lag equal to or near zero. The transition probabilities decrease for increasing lag. This resembles the fact that the smaller the lag, the more likely the transition of a CL on itself. With increasing lag, the transition probabilities from one state to itself decrease in favour of transitions to a different state.

For all other transitions, the lag-dependent transition probability starts at zero for vanishing lag. Then, the probabilities increase with increasing lag, but are confined to maximal transition probabilities less than 1. This is because transition probabilities greater than zero for transitions of a CL on a different one presume the trivial fact that at least two contamination levels (categories) are present. Thus, a transition probability of one category to a different one can never approach one.

The assessment of the dynamics of PAH requires the consideration of soil heterogeneity with respect to the soil forming materials and the contamination levels. As was shown elsewhere the PAH burden at the Testfeld Süd was not related to the physicochemical soil characteristics (Weigand et al., 2001). Therefore, we now have to link the

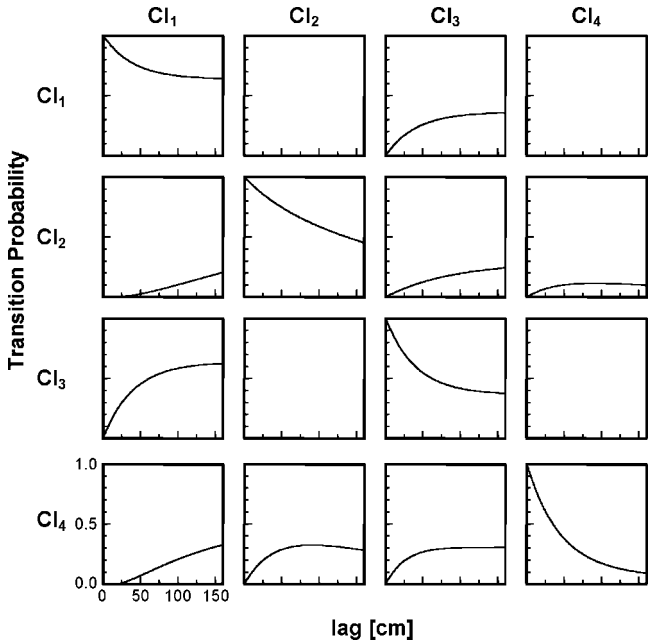


Figure 1.5: Lag-dependence of the transition probability for the contamination levels 1 to 4. The row labelling denotes the subjacent, the column labelling the superjacent contamination level.

series of contamination levels with the soil profiles as given by the series of possible pedofacies.

Let $P$ and $M$ denote categorical variables defined on the sample space of PAH contamination level ($P$) and pedofacies ($M$). Integration of independent $P$ and $M$ into stochastic simulations may be achieved by an a posteriori approach which relies on the intersection of probabilities of individual matrices for $P$ and $M$. By applying Eq. (2) the transition probabilities for $P$ may be expressed as:

$$pr_{ij}^{P} = \frac{Pr\ \{P_{n+1}\ \cap\ P_n\}}{Pr\ \{P_n\}} \tag{8}$$

Analogously the transition probabilities for $M$ are given as:

$$pr_{ij}^{M} = \frac{Pr\ \{M_{n+1}\ \cap\ M_n\}}{Pr\ \{M_n\}} \tag{9}$$

When $P$ and $M$ are independent, the intersection can be calculated by the multiplication rule (Ineichen, 1971), i.e.

$$pr_{ij}^{P\cap M} = pr_{ij}^{P} \cdot\ pr_{ij}^{M} = \frac{Pr\ \{P_{n+1}\ \cap\ P_n\}}{Pr\ \{P_n\}} \cdot \frac{Pr\ \{M_{n+1}\ \cap\ M_n\}}{Pr\ \{M_n\}} \tag{10}$$

Stochastic simulations were performed to generate combined soil profiles that account for both the spatial variability of contamination levels and pedofacies at the Testfeld Süd. Combined soil profiles were generated from bottom to top. In agreement with the average prospection depth, thickness was set to 1.0 m. PAH contamination and matrix properties at the profile base were defined according to the empirical distribution. Stochastic simulations were carried out by stepwise generation of uniformly [0, 1] distributed random numbers in 5000 replicates. This was performed simultaneously for PAH contamination level and pedofacies. The random numbers were assigned to a realisation of pedofacies and PAH contamination level, respectively. At first, the row of the transition probability matrix corresponding to the underlying realisation of PAH contamination and pedofacies was chosen. Then, the cumulative transition probability from the underlying to the subsequent states was calculated from the sum of the row entries in $P$. Third, the random numbers were projected onto the cumulative probability and translated into a realisation of material and contaminant classes. This procedure was repeated until the desired profile thickness had been reached (Weigand et al., 2001). Figure 1.6 gives the result of the first 40 possible combinations of pedofacies and contamination levels revealed by the stochastic reconstruction of both series of pedofacies and contamination levels.

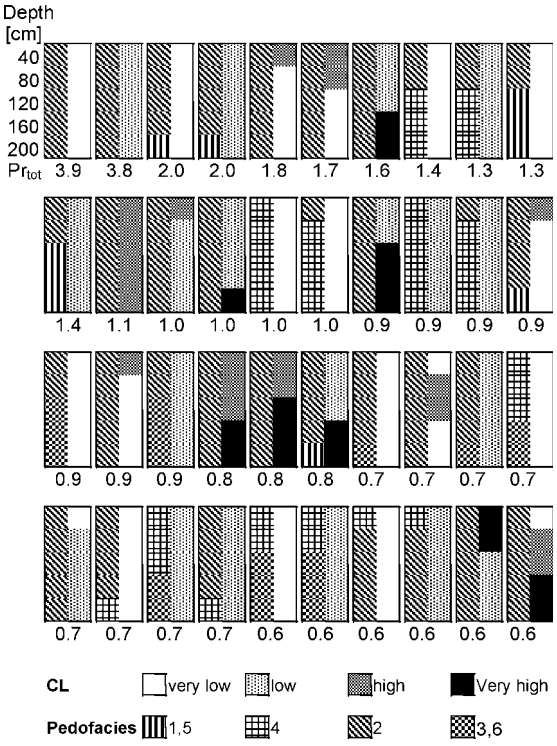


Figure 1.6: Results of the conditional stochastic simulation. The 40 most probable combinations of contamination levels (CL) and pedofacies series are shown, which form the typical soil profiles found at the Testfeld Süd. $Pr_{\mathrm{tot}}$ denotes the total probability.

## 1.4 Assessing the Risk for PAH Deep Seepage at Industrial Contaminated Sites

The final goal of the presented procedure is to estimate PAH deep seepage at urban and industrial sites. The evaluation should be plausible and therefore rely on a process-based model for the transport of reactive solutes through unsaturated porous media. After we succesfully managed to reconstruct possible soil profiles by means of a conditional stochastic simulation based on Markov theory, we now have to run the process-based reactive transport model (PBRTM) for all combinations obtained by the stochastic simulation. As PBRTM we used the model CARRY (Totsche et al., 1996; Knabner et al., 1996), in its current Version 5.5, which allows to model reactive transport of hydrophobic organic contaminants, for example PAH, in layered soils under unsaturated flow conditions. CARRY considers linear and non-linear, equilibrium and non-equi-

librium sorption of PAHs to different solid phase constituents, including organic carbon, and to mobile sorbents, like dissolved and colloidal organic carbon. As numerical solution scheme, finite elements are used to solve the advection-dispersion equation. At the moment, sorption isotherms can be parametrized as linear, Freundlich, Langmuir, BET and the modified Freundlich equation.

In order to run the model, the sorption isotherms and kinetic parameters have to be measured experimentally. Moreover, the release of PAH from the pedofacies representing the source materials for the PAH have to be provided as well. These data were measured by batch and flow reactor techniques (Weigand et al., 2001; Raber and Kögel-Knabner, 1997; Kögel-Knabner et al., 2000). Structural properties of the pedofacies relevant to transport, like porosity, bulk density, mineral composition and organic carbon content were also measured and considered within the model individually for each pedofacies. This information was provided for each individual simulation run. The model domain for each run was taken from the reconstructed soil profiles, of 1 m depth in general. The fragmentation of the soil profiles in different pedofacies was considered explicitly within the model domain, that is, the model domain of an individual simulation run was composed of the same pedofacies as revealed by the reconstruction. Release from the pedofacies which act as source layers was parametrized as a kinetically controlled linear desorption process, while retardation within the padofacies which act like sinks was parametrized as a kinetically controlled Freundlich sorption isotherm. Simulations were run for those combinations of soil profiles and contamination levels, which had a probability of occurrence higher or equal to 0.3 %. This was met by the first 80 combinations of contamination levels and soil profiles, of which the first 40 are given in Fig. 1.6.

Total cumulative probability reached a value of 61 %. Thus, the threshold value selected resulted in a coverage of 61 % of the total variability of the site covered by the 80 combinations of soil profiles and contamination levels.

Simulation with the model CARRY were run for these 80 most likely combinations. As boundary conditions, the mean annual groundwater recharge at Testfeld Süd was used. Total simulation encompassed a period of 50 years. This seems to be a plausible duration for the evaluation of PAH transport at a contaminated site, partly because the major spills occurred during World War II, partly because the PAH represent substances of very low water solubility and thus of very low mobility. Figure 1.7 gives the results of the simulations for 4 selected PAH, Phenanthrene (3 ring), Pyrene (4 ring), Benzo(k)fluoranthen (5 ring) and Benzo(a)pyrene (5 ring). The selection was chosen such that a wide range of water solubility, octanol-water partition coefficients and dissolved organic carbon-water partition coefficients was encompassed (Table 1.3).

Total export of individual PAH compounds was calculated by the weighted export of the individual PAH compounds. As weighting factor, the probability of a specific combination of soil profiles and contamination level was chosen. The weighting factor is thus given by the probability of occurrence as obtained by the stochastic reconstruction of the soil profiles. For all selected PAH the observed export varied by more than 4 orders of magnitude (Fig. 1.7). Export decreases in the order of Phenanthrene > Benzo(k)fluoranthene > Pyrene > Benzo(a)pyrene. Due to the linear relations of the partition coefficients, the export of the individual PAH is proportional to both the

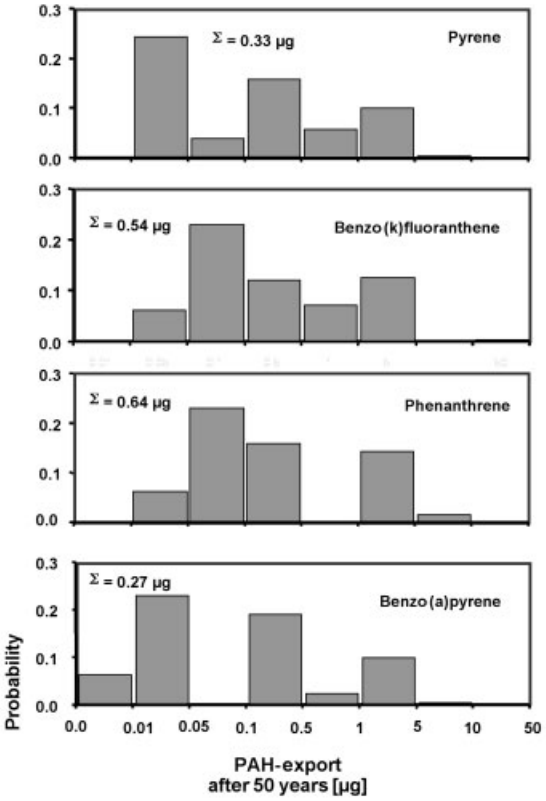


Figure 1.7: Export of selected PAH as simulated with the physically based reactive transport model.

Table 1.3: Physicochemical properties of the PAH used for the simulation.

| PAH | S [g $m^{-3}$] | Log $K_{OW}$ | Log $K_{OC}$ | Log $K_{DOC}$ |
|---|---|---|---|---|
| Phenanthrene | 48 | 4.57 | 4.36 | 4.6 |
| Pyrene | 150 | 5.18 | 4.92 | 5.0 |
| Benzo(k)fluoranthene | 0.76 | 6.5 | 6.5 | 3.6–4.7 |
| Benzo(a)pyrene | 6.31 | 6.5 | 6.6 | 3.9–4.5 |

S: solubility in water; $K_{OW}$: Octanol water partition coefficient; $K_{OC}$: Organic matter water partition coefficient; $K_{DOC}$: Dissolved organic matter – water partition coefficient. Data from Raber and Kögel-Knabner, 1997.

$K_{OC}$ and the amount found in the source material. Thus, the highest export was observed for Phenanthrene and Benzo(k)fluoranthene, although the $K_{OC}$ of Pyrene is much lower than the $K_{OC}$ of Benzo(k)fluoranthene.

With the conducted simulations we are thus able to estimate both: (i) the effect of the individual combination of soil profiles and contamination levels on the export of individual and total PAH and (ii) the overall export of PAH referring to the complete site. While the first is of more scientific interest, the second measure is directly related to a risk-based approach in the evaluation of the hazard for groundwater contamination by PAH seepage from the unsaturated soil zone. The variability of sources and sinks of urban and industrial sites as reflected by the manifold of different combinations of pedofacies and contamination levels is therefore decisive for the overall export of PAH from soils.

## 1.5 Summary and Conclusion

An approach for the modelling of contaminant transport at highly contaminated industrial sites was presented. The focus was on the reconstruction and mapping of the spatial heterogeneity of adjacent pedofacies with highly contrasting properties. Employing a thorough field survey, we provided evidence that urban and industrial sites are characterised by a spatial heterogeneity of contaminant sources and sinks which is neither solely random nor regular in nature. The spatial arrangement of soil pedofacies found at the site is controlled by construction, engineering or landscaping activities, which are intrinsically regular and are characterised by a strong relation between proximate pedofacies. We applied a conditional stochastic simulation based on the Markov process theory in order to map and reconstruct the spatial heterogeneity of such sites. It is important to note that this approach is guided by the idea not to characterise and map the spatial variability of a specific functional or structural property, for example the hydraulic conductivity or the coefficients for sorption, but rather to characterise the spatial variability of the structures itself, that is the spatial arrangement of pedofacies. Once this is achieved, the spatial distribution of these entities is reconstructed and used as a template for the definition of the spatial distribution of parameters relevant to transport.

Markov processes facilitate the reconstruction of spatial random numbers by which the local state solely depends on the direct neighbour and not on more distant occurrences. By applying this theory to field data, we were able to adequately reconstruct both the pedofacies and the contamination levels observed. With a finite and relatively small number of combinations of pedofacies and contamination levels – together they represent typical contaminated soil profiles of the site – we were able to cover more than 60 % of the spatial heterogeneity of the site. The typical soil profiles were then used with a process-based reactive transport model in order to evaluate the export of contaminants from the site as a function of the heterogeneity. By doing so, we were

able to assess the risk of contaminant deep seepage and thus the risk for groundwater pollution.

The proposed procedure is a compact, yet mathematically simple and comprehensive approach to a risk-based assessment of soil and groundwater pollution by hazardous substances found at anthropogenic sites of urban and industrial environments. It is important to note that this procedure requires a thorough and spatially highly resolved field site characterisation to exhaustively describe the pedofacies representative for a particular site.

## 1.6 References


AG Boden (1994): Bodenkundliche Kartieranleitung, 4. ed., p. 392, Hannover.

Agterberg, F. P. (1974): Geomathematics, Elsevier, Amsterdam, pp. 596.

Bear, J. (1979): Hydraulics of Groundwater, MacGraw-Hill, New York, pp. 569.

Beven, K.; Germann, P. (1982): Macropores and water flow through soils. *Water Resour. Res.* **18**(5), 1311–1325.

Blume, H. P. (1989): Classification of soils in urban agglomerations. *Catena* **16**, 269–275.

Burghardt, W. (1994): Soils in urban and industrial environments. *Z. Pflanzenernähr. Bodenk.* **157**, 205–214.

Carle, S. F.; Fogg, G. E. (1997): Modelling spatial variability with one and multidimensional continuous-lag Markov chains. *Math. Geol.* **29**, 891–916.

Carle, S. F.; Labolle, E. M; Weissmann, G. S.; van Brocklin, D.; Fogg, G. E. (1998): Conditional simulation of hydrofacies architecture: A transition probability/Markov approach. In: Fraser, G. S.; Davis, J. M. (Eds.): Hydrogeologic models of sedimentary aquifers, Concepts in hydrogeology and environmental geology 1. SEPM special publication, 147–170.

Clarke, A. B.; Disney, R. L. (1970): Probability and random processes for engineers and scientists, John Wiley & Sons, New York, pp. 346.

Dagan, G. (1986): Statistical theory of groundwater flow and transport: Pore to laboratory, laboratory to formation, and formation to regional scale. *Water Resour. Res.* **22**(9), 120–134.

Doveton, J. H. (1971): An application of Markov chain analysis to the Ayrshire Cole Measures succession. *Scottish J. Geology* **7**, 11–27.

Doveton, J. H. (1994): Theory and applications of vertical variability measures from Markov Chain analysis. In: Yarus, J.; Chambers, R. (Eds.): Stochastic modelling and geostatistics., *AAPG Comput. Appl. Geol.* **3**, 55–63.

Eiceman, G. A.; Davani, B.; Ingram, J. (1986): Depth profiles for hydrocarbons and polycyclic aromatic hydrocarbons in soil beneath waste disposal pits from natural gas production. *Environ. Sci. Technol.* **20**, 508–514.

Flury, M.; Leuenberger, J.; Studer, B.; Flühler, H. (1995): Transport of anions and herbicides in a loamy and sandy field soil. *Water Resour. Res.* **31**(4), 823–835.

Fogg, G. E., Noyes, C. D.; Carle, S. F. (1998): Geology based model of heterogeneous hydraulic conductivity in an alluvial setting. *Hydrogeology J.* **6**, 131–143.

Freeze, R. A.; Cherry, J. A. (1979): Groundwater, Prentice–Hall, Englewood Cliffs, N. J. , pp. 604.

Gelhar, L. W. (1986): Stochastic subsurface hydrology from theory to applications. *Water Resour. Res.* **22**(9), 135–145.

Gerke H. H.; van Genuchten, M. T. (1993): A dual porosity model for simulating the preferential movement of water and solutes in structured porous media. *Water Resour. Res.* **29**, 305–319.

Ineichen, R. (1971): Einführung in die elementare Statistik und Wahrscheinlichkeitsrechnung, Raeber, Luzern, pp. 114.

Jardine, P. M.; Wilson, G. V.; Luxmoore, R. J. (1990): Unsaturated solute transport through a forest soil during rain storm events. *Geoderma* **46**, 103–118.

Journel, A. (1986): Geostatisics: Models and tools for the earth sciences. *Math. Geol.* **18**(1), 119–140.

Jury, W. A.; Roth, K. (1990): Transfer functions and solute movement through soil: Theory and application, Birkhäuser Verlag, Basel, Switzerland.

Jury, W. A.; Russo, D.; Sposito, G. (1987): The spatial variability of water and solute transport properties in unsaturated soil: II. Scaling models of water transport. *Hilgardia* **55**, 33–56.

Knabner, P.; Totsche, K. U.; Kögel-Knabner, I. (1996): The modelling of reactive solute transport with sorption to mobile and immobile sorbents – Part I: Experimental evidence and model development. *Water Resour. Res.* **32**, 1611–1622.

Kögel-Knabner, I.; Totsche, K. U. (1998): Influence of dissolved and colloidal phase humic substances on the transport of hydrophobic organic contaminants in soils. *Phys. Chem. Earth* **23**(2), 179–185.

Kögel-Knabner I.; Totsche, K. U.; Raber, B. (2000): Desorption of PAH from soil in the presence of dissolved organic matter: Effect of solution composition and aging. *J. Environ. Qual.* **29**, 906–916.

Koltermann, C. E.; Gorelick, S. M. (1996): Heterogeneity in sedimentary deposits: A review of structure-imitating, process-imitating and descriptive approaches. *Water. Resour. Res.* **32**(9), 2617–2658.

Murphy, E.M.; Zachara, J. M.; Smith, S. C.; Philips, J. L. (1992): The sorption of humic acids and their role in contaminant binding. *Sci. Total Environm.* **118**, 413–432.

Neton, M. J.; Dorsch, J.; Olson, C. D.; Young, S. C. (1994): Architecture and directional scales of heterogeneity in alluvial fan aquifers. *J. Sedimentary Res.* **64**, 245–247.

Raber B.; Kögel-Knabner, I. (1997): Influence of origin and properties of dissolved organic matter on the partition of PAH. *Eur. J. Soil Sci.* **48**, 443–455.

Rolke, W. A. (1991): Continous-time Markov processes as a stochastic model for sedimentation. *Math. Geol.* **23**, 297–304.

Roth, K.; Jury, W. A.; Flühler, H.; Attinger, W. (1991): Transport of chloride through an unsaturated field soil. *Water Resour. Res.* **27**(10), 2533–2541.

Rubin, Y. G.; Gomez-Hernandez, J. J. (1990): A stochastic approach to upscaling of transmissivity in disordered media: 1. Theory and unconditional simulations. *Water Resour. Res.* **24**(4), 691–701.

Seyfried, M. S.; Rao, P. S. C. (1987): Solute transport in undisturbed columns of an aggregated tropical soil: Preferential flow effects. *Soil Sci. Soc. Am. J.* **51**, 1434–1444.

Totsche, K. U. (1995): Quality Control and Quality Assurance in Applied Soil Microbiology and Biochemistry. In: Alef, K.; Nannipieri, P. (Eds.): Applied Soil Microbiology and Biochemistry, Academic Press, 5–23.

Totsche, K. U.; Knabner, P.; Kögel-Knabner, I. (1996): The modelling of reactive solute transport with sorption to mobile and immobile sorbents. Part II: Modell discussion and numerical simulation. *Water Resour. Res.* **32**, 1623–1636.

Tuckwell, H. C. (1995): Elementary applications of probability theory, Chapman & Hall, London, pp. 292.

Weigand, H.; Totsche, K. U.; Huwe, B.; Kögel-Knabner, I. (2001): PAH mobility in contaminated industrial soils: A Markov chain approach to the spatial variability of soil properties and PAH levels. *Geoderma* **102**, 371–389.

Weigand, H.; Totsche, K. U.; Kögel-Knabner, I.; Huwe, B. (1998): Heterogenität der Bodeneigenschaften und der Schadstoffbelastung eines ehemaligen Gaswerkstandorts. *Grundwasser* **4**(3), 175–182.

Wiesmann, U. (1994): Der Steinkohleteer und seine Destillationsprodukte – Ein Beitrag zur Geschichte der Technik und der Bodenverschmutzung. In: Biologischer Abbau von Polycyclischen Aromatischen Kohlenwasserstoffen. *Schriftenreihe Biol. Abwasserrein.*, **4**, 3–18.

# 2 Concepts for Modelling of Heterogeneous Flow Processes in Soil Columns on the Basis of Tomographic Radiotracer Experiments

Michael Richter*

## Abstract

The heterogeneous structure of a soil or ground water layer influences essentially the reactive transport and has to be taken into consideration in the modelling of these processes. Several methods exist for the investigation of the layer structure, but only tomographic radiotracer methods (**P**ositron-**E**mission-**T**omography (PET)) and in special cases nuclear magnetic resonance methods enable spatially resolved observations of the heterogeneity of mass flows in these layers with a sufficient high resolution.

The fundamental aspects of PET and informations about the experimental technology are presented.

Some examples of PET images of the hydrodynamic flow in a soil column (length 1 m, diameter 10 cm) are given which demonstrate the possibilities of tomographic radiotracer measurements for studies of the heterogeneous mass flow. The local flow velocity distribution in different parts of the soil column varies strongly and has to be considered in the geochemical transport models.

A scheme of the estimation of the spatial velocity distribution from the measured tracer distribution is given and the several concepts are presented for the utilization of these dates for the modelling of hydrodynamic flow processes in soil columns:

- estimation of parameters by inverse modelling,
- partition of the column in regions with different flow characteristics,
- modelling with reference to the dispersion model,
- support of the conventional measuring technique.

* Institut für Interdisziplinäre Isotopenforschung an der Universität Leipzig, Permoserstraße 15, 04318 Leipzig, e-Mail: richterm@rz.uni-leipzig.de



*Geochemical Processes: Conceptual Models for Reactive Transport in Soil and Groundwater. Research Report.* Deutsche Forschungsgemeinschaft (DFG).
 ISBN: 978-3-527-27764-3

## 2.1 Introduction

Soil column experiments with conservative and reactive tracers are used for the development of reactive transport models in soil and groundwater and for the determination of model parameters. The influence of the real structure of the solid layers on the transport and reaction processes is very important and has to be taken into consideration for the development of mathematical transport models (Chin and Wang, 1992). Several methods exist for the investigation of layer structures (ultrasound and electrical tomography, computer tomography with X-rays) (Just et al., 1994; Meyer et al. 1994), but generally these methods give no information about the dynamic processes.

Besides the nuclear magnetic resonance tomography (NMRT) (Baumann et al., 2000) tomographic radiotracer methods enable the spatial resolved investigation of mass transfer processes in heterogeneous structures. In particular the radiotracer tomography is suitable for the determination of the local flow or mass transport velocity distribution under nearly natural conditions because very low tracer concentrations can be used, wich do not change the geochemical situation during the experiment.

In the recent years we have developed a special device for geoscientific tomographic radiotracer studies on basis of the principle of **P**ositron **E**mission **T**omography (PET) which is wellknown in the nuclear medicine (Richter et al. 2000A; Richter et al. 2000B). Much more informations are obtained with PET experiments in comparison with the conventional soil column experiments which are the basis for a better knowledge and modelling of the transfer processes. In the following some concepts are discussed for using these informations for a better modelling of the hydrodynamics in soil columns.

## 2.2 Technology and Applicability of the Positron Emission Tomography (PET) for Transport Studies in Soil Columns

The technique of positron emission tomography (PET), developed for medical applications, offers also the capability to map flow distributions in geological layers. Conservative tracers, marked with a positron emitting radionuclid, can be used for hydrodynamic studies in soil columns. Suitable tracers for such studies are for example kaliumfluoride- or cobalthexacyanocomplex, marked with the positron emitting isotops F-18 and Co-58 respectivly.

The emitted positrons react within a short range with electrons of the surrounding matter and produces two γ-quants, leaving the object in opposite direction with an angle of nearly 180° (annihilation radiation).

A pair of opposite radiation detectors outside the object defines a **L**ine **O**f **R**esponse (LOR). When in both detectors the γ-quants are detected simultaneously

(coincidence measuring), one knows that the tracer isotope was somewhere on the line between the detector pair. The LOR is the projection of the tracer concentration distribution in the solid angle, given by the position of the coinciding detector pair. The tracer concentration distribution is sampled by a large number of LOR´s, from which the tomographic image is reconstructed.

The current generation of commercial available PET-cameras, developed for applications in the nuclear medicine, consists of 20–30 detector rings with 600–800 detectors per ring. The ring diameter is 80–90 cm and the field of view (range for image reconstruction) is 55 cm in radial and 15 cm in transaxial (= horizontal) direction.

The spatial resolution is in the range of 5–8 mm and the measuring time for one object position amounts to approximately 10 min.

These PET-cameras can also be used for transport studies in soil columns. But they were developed for the special demands of nuclear medical diagnostics. The algorithm for the image reconstruction and the error corrections are specialized for these applications.

Dimension and arrangement of the detectors are not optimal for investigations of soil columns. Therefore, a special PET-camera for geoscientific studies is in development (Richter et al., 2000A).

This device consist of two opposite detector heads. Each head contains 16 detectors. $16 \times 16 = 256$ different LOR´s are measured at each object position. The object is moved step by step between the detector heads in horizontal and vertical direction and also rotated step by step. On this way the large number of LORs, necessary for the image reconstruction, can be measured.

Soil columns with diameters up to 12 cm and a length up to 100 cm can be measured with this device in vertical position. The specific properties of the sample can be taken into consideration in the image reconstruction and error correction.

A spatial resolution of 3 mm can be realized when the measurement is done with a sufficient small step width. The measuring time is significant longer compared to the comercial PET-cameras (several hours). The flow rate for soil column experiments is often low in relation to the natural condition, so that measuring times of several hours are acceptable.

At the moment small PET-cameras (microPET) will be developed at several research centers. They use small detector crystals which are arranged in rings with diameters of 20–25 cm (Chatziioannou et al., 1999 ). In future such devices could also be used for transport studies in geological layers.

Besides the tomographic radiotracer methods some other methods exist for non-destructive measurements of spatial flow distributions in soil columns (Table 2.1).

Table 2.1: Methods for non-destructive measurments of spatial flow distributions in soil columns.

| Method | Spatial Resolution | Advantages | Disadvantages |
|---|---|---|---|
| Transmission Computer Tomography | 10 µm | high resolution for matrix structure | no contrast for flow measurments |
| Acoustic Tomography | 5 cm | no tracer necessary | acoustic reflections on grain surfaces, no possibility for velocity measurements by steady state flow |
| Electrical Tomography | 3–5 cm | no tracer necessary | electrodes inside the column, no possibility for velocity measurements by steady state flow |
| Nuclear Magnetic Resonance Tomography | 0.5 mm | in general no tracer necessary | special low field devices necessary, high spatial resolution only by large pore volumes, measuring of velocity by steady flow demand high tracer concentrations, no detection of flow in single small pores ($\varnothing < 0.5$ mm) (detection limit $10^{18}$ spins) |
| Positron Emisssion Tomography | 3–8 mm | low tracer concentration, which not influences the geochemical regime; measurement of spatial velocity by steady state flow possible; flow detection also in single small pores ($\varnothing < 0.5$ mm) | special radioactive tracer necessary, commercial PET-cameras only for medical applications available |

## 2.3 Typical Results of PET-Studies of the Hydrodynamics in Soil Columns

### 2.3.1 Experimental

The flow distribution in a model soil column (length 1 m, diameter 10 cm) with defined disturbing inserts (Fig. 2.1) was studied to demonstrate the feasibility of PET-studies. The measurements were carried out with a commercial PET-camera (Siemens: ECAT EXACT HR (3D)). Kaliumfluoride, marked with the positron emitting isotope F-18 (half life time 110 min), was applied as hydrodynamic tracer. Fluorides of two-valent cations are only slightly soluble. The radio tracer would be absorbed in the col-

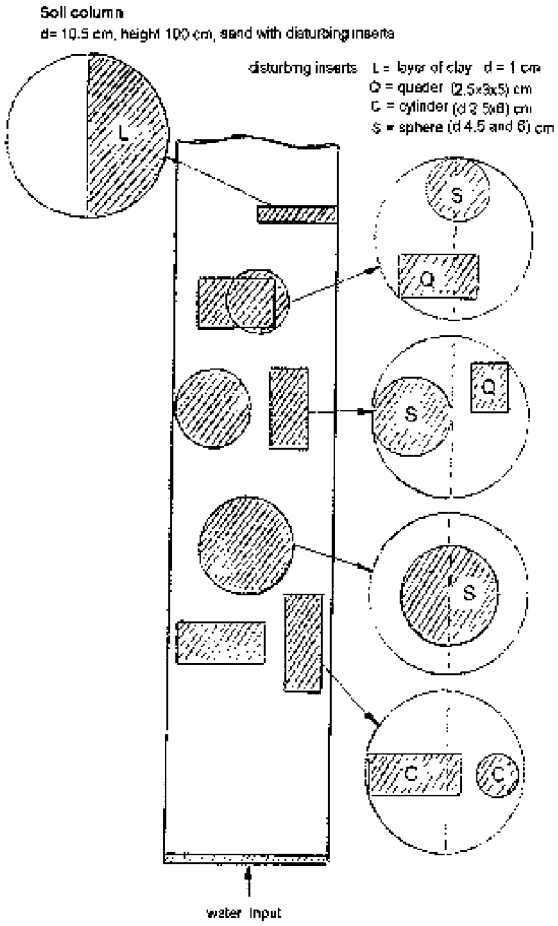


Figure 2.1: Soil column with disturbing inserts.

Table 2.2: Experimental conditions for hydrodynamic PET studies in soil columns.

| Test series | Specific flow rate | Tracer solution | Specific activity | Injection form | Volume of tracer solution |
|---|---|---|---|---|---|
| 1 | 0.002 cm/s | 0.1 M KF / F-18 | 80 MBq/cm$^3$ | pulse | 2 cm$^3$ |
| 2 | 0.004 cm/s | 0.1 M KF / F-18 | 174 kBq/cm$^3$ | step | 2000 cm$^3$ |

umn when it reacts with these cations. Therefore a 0.1 M KF-solution was feeded into the column before the tracer experiment to desorb the two-valent cations from the soil surface. After this the sorption of the F-18 could be reduced to such an extent, that a perfect conservative behaviour was observed. This could be verified by measurements of the residence time distributions with the KF-tracer in comparison with residence time distributions, measured with a KBr-tracer, which is used commonly for hydrodynamic studies in soil columns.

The characteristic of the measurement conditions is summarized in Table 2.2. The tracer concentration distribution was measured in different cross sections at different times after the tracer injection.

### 2.3.2 PET-Measurements of Tracer Distribution in the Model Soil Column

Some examples are given which demonstrate the information content of tomographic tracer studies in soil columns. Figure 2.2 shows a typical distribution of the tracer concentration in a cross section of a sand layer without additional heterogeneous inclusions. The channel with high flow velocity (red) and the region with very low velocity (blue and black) are conspicuous and the quantity of each flow regime can be determined.

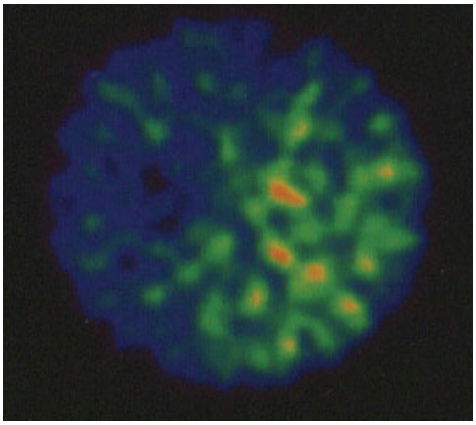

Figure 2.2: Tracer concentration distribution in the cross section of a sand layer.

The tracer distribution in two column cross sections measured 30 min after the impuls input is represented in Fig. 2.3. The largest mean concentration was measured at this time in the cross section 10.25 cm. The same concentration was measured in a small region in the cross section 21.5 cm. On basis of these dates the flow velocities could be estimated. The mean velocity was 0.0055 cm/s, but in a limited part of the cross section the flow velocity was 0.01 cm/s.

Measurements of the same cross section at different times also give informations for the velocity distribution (Fig. 2.4). A flow velocity of 0.01 cm/s can be estimated

(a) 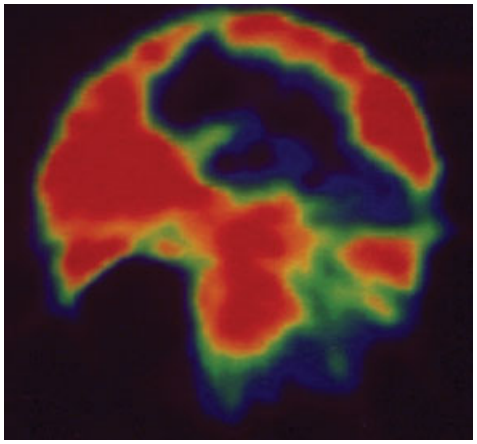 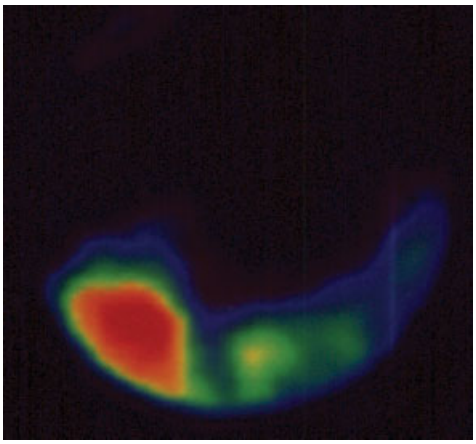 (b)

Figure 2.3: Tracer distribution in two different cross sections 30 min after tracer input: (a) cross section 10.25 cm above the column bottom; (b) cross section 21.5 cm above the column bottom. Tracer concentration: high – red, middle – green, small – blue, black – zero.

(a) 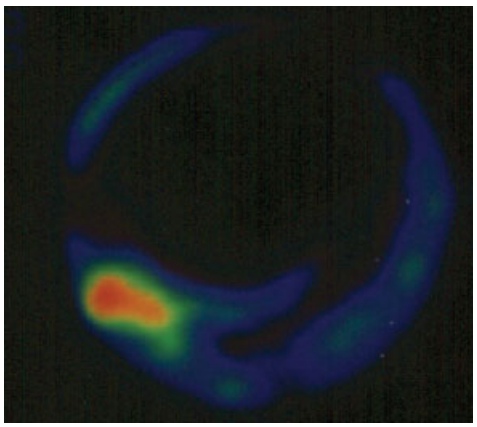 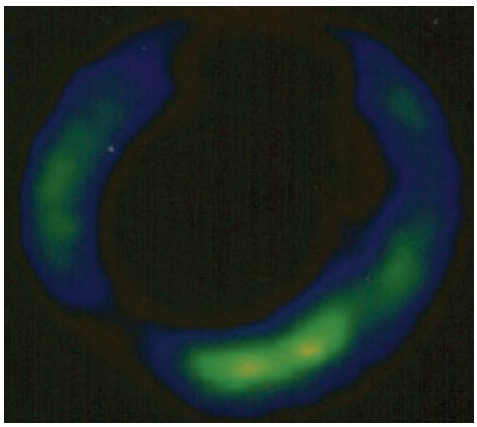 (b)

Figure 2.4: Tracer distribution in a cross section at different times: (a) tracer concentration distribution 30 min after tracer input; (b) Tracer concentration distribution 45 min after tracer input. Tracer concentration: high – red, middle – green, small – blue, black – zero.

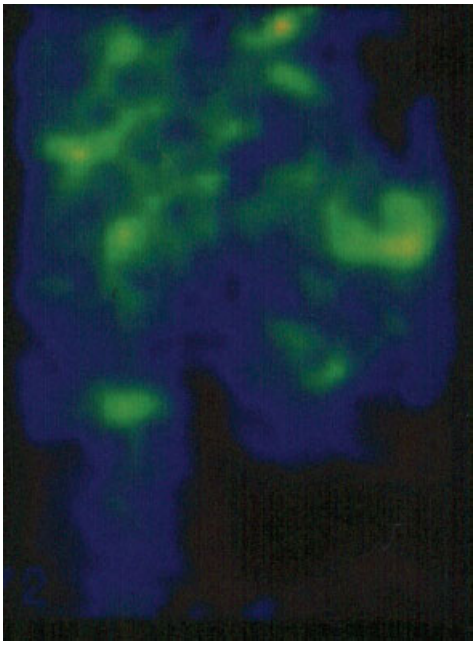

Figure 2.5: Axial tracer distribution in the sand layer in the surrounding of a clay lense. Tracer concentration: high – red, middle – green, small – blue, black – zero.

for the red region in the left image from the temporal concentration variation in this region (Section 2.4). In the red region of the right image the high tracer concentration appears 15 min later, which corresponds to a velocity of 0.006 cm/s.

The axial tracer distribution can be reconstructed from tomographic images of neighbouring cross sections. Figure 2.5 shows the axial tracer distribution in a sand layer in the vicinity of a clay lense. The lense had a thickness of 1 cm and covered the half cross section. Stagnant regions exist above and under the lense, which have an axial extension of 4.5 cm.

Hydrodynamic problems of the entrance zone of soil columns are shown in Fig. 2.6. The tracer concentration shows a strong influence of wall flow in the entrance zone. The parabolic concentration profil, which is an essential condition for the validity of the dispersion model, developes only after a longer distance from the column bottom.

(a) 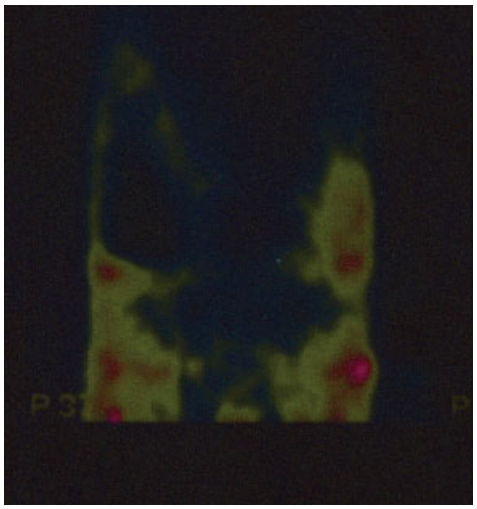 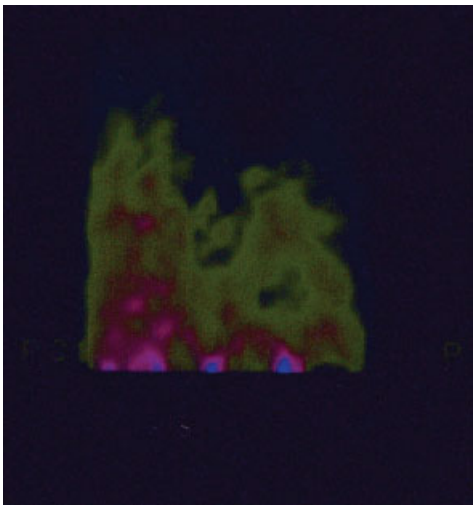 (b)

Figure 2.6: Axial tracer front in the entrance section and a inside section of the column: (a) section 3 –18 cm; (b) section 23–38 cm. Tracer concentration: high – red, middle – green, small – blue, black – zero.

## 2.4 Calculation of Velocity Distributions

The primary results of PET-measurements are spatially resolved tracer concentration distributions. For the modelling of transfer processes we need the velocity distribution. It is necessary for the calculation of the velocity distribution to determine the tracer concentration in two neighbouring cross sections ($Q_1$ and $Q_2$) (distance $\Delta l$) at two times ($t$ and $t + \Delta t$) while the tracer pulse is passing the cross sections.

Area ranges ($F_q$) of equal tracer concentration are selected from the tomographic images of the cross sections and the specific activities $A_1(t)$ and $A_2(t)$ (Bq/cm$^2$) are determined in these area ranges. The same is done with the images, measured at time $t + \Delta t$ (specific activities $A_1(t + \Delta t)$, $A_2(t + \Delta t)$).

The velocity distribution in $F_q$ can be approximated by a parabolic function. Figure 2.7 shows the parabolic flow profiles at times $t$ and $t + \Delta t$ in a transaxial section of $F_q$ while the tracer pulse front is passing the cross sections $Q_1$ and $Q_2$.

The following relations can be derived from the geometrical values (lenght $l_i$, radius $R_{ij}$) defined in Fig. 2.7.

The mean flow velocity is in $F_q$:

$$v_q = \Delta l / \Delta t;\ \Delta l = l_2 - l_1 \tag{1}$$

$$l_1 \approx (R_{11} / R_{12}) \cdot l_2\ ;\ l_2 \approx [R_{12} / (R_{12} - R_{22})] \cdot \Delta l_q \tag{2}$$

$$\Delta l \approx [(1 - R_{11} / R_{12}) / (1 - R_{22} / R_{12})] \cdot \Delta l_q \tag{3}$$

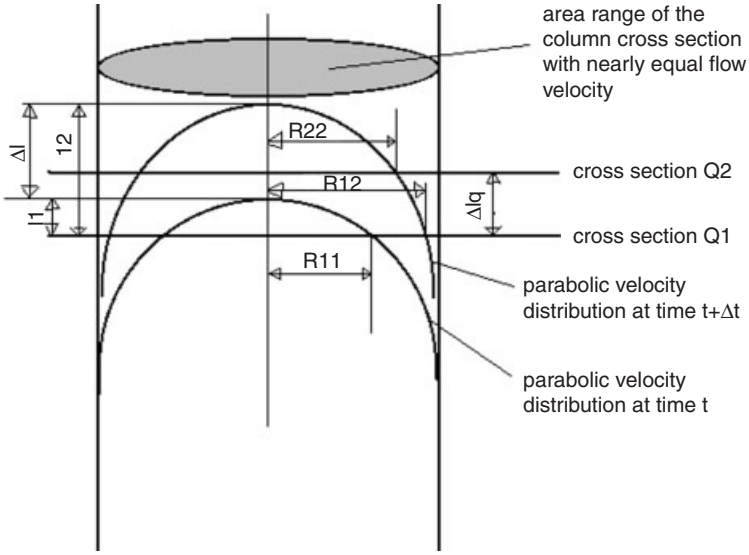


Figure 2.7: Scheme for the determination of flow velocity distributions from tomographic tracer concentration measurements.

The specific activity is proportional to the part of $F_q$ which the parabolic profile covered at the measuring time in the particular cross section. Therefore, the following relations for the activity ratios can be derived:

$$a_t = A_1(t) / A_1(t + \Delta t) = (R_{11} / R_{12})^2 \tag{4}$$

$$a_q = A_2(t + \Delta t) / A_1(t + \Delta t) = (R_{22} / R_{12})^2 \tag{5}$$

With Eqs. (1), (3), (4) and (5) the velocity in the area range $F_q$ can be calculated:

$$v_q = [(1 - \sqrt{a_t}) / (1 - \sqrt{a_q})] \cdot [\Delta l_q / \Delta t] \tag{6}$$

The flow velocity can be calculated from the activity ratios in the area range $F_q$. It is not necessary to determine absolute values of the specific activity.

## 2.5 Concepts of Modelling of Flow Processes in Soil Columns

### 2.5.1 Estimation of Parameters by Inverse Modelling

The column is divided in elementary cells with constant porosity and constant hydraulic conductivity. The modelling can be done two- or three-dimensional. A two-dimensional model demands the values of porosity ($P(x,y)$) and hydraulic resistance ($R(x,y)$), which corresponds with the inverse of the hydraulic conductivity, for each elementary cell ($x,y$).

The parameter sets $P(x,y)$ and $R(x,y)$ can be determined from the local tracer concentration and velocity distributions measured in each cross section of the column.

The following equations are used to determine the parameters for a two-dimensional model

Darcy equation: $$P \cdot R \cdot u = \frac{\partial \Gamma}{\partial x}; P \cdot R \cdot v = \frac{\partial \Gamma}{\partial y} \tag{7}$$

Mass balance: $$\frac{\partial}{\partial x}\left(\frac{1}{R}\frac{\partial \Gamma}{\partial x}\right) + \frac{\partial}{\partial y}\left(\frac{1}{R}\frac{\partial \Gamma}{\partial y}\right) = 0 \tag{8}$$

$\Gamma(x,y) = A \cdot x$ is the hydraulic potential ($A$ = mean potential increase); $u(x,y)$, $v(x,y)$ are the velocity components.
Elimination of $\Gamma(x,y)$ yields the equations:

$$\frac{\partial (P \cdot R \cdot u)}{\partial y} - \frac{\partial (P \cdot R \cdot v)}{\partial x} = 0 \tag{9}$$

$$\frac{\partial (P \cdot u)}{\partial x} + \frac{\partial (P \cdot v)}{\partial y} = 0 \tag{10}$$

with the boundary condition:

$$v(-X, y) = v(X, y) = v(x, -Y) = v(x, Y) = 0 \tag{11}$$

and the additional condition:

$$\int_{-X}^{X} P(x,y) \cdot R(x,y) \cdot u(x,y) dx = 2Ax \tag{12}$$

If the parameter sets $R(x,y)$ and $P(x,y)$ are determined, a modelling of the hydrodynamics with wellknown numerical algorithm is possible.

The dimension of the elementary cells should be chosen in relation to the general aim of the soil column experiment. The minimal size of the cell is determined by the spatial resolution of the tomographic method ($3 \times 3 \times 3$ mm$^3$). Generally it will be nec-

essary to reduce the experimental and theoretical expense by using a smaller number of larger elementary cells, because it is extremly time consuming and costly to measure the flow distribution in the cross sections of the whole column with a step width of 3 mm.

The dimension of elementary cells should be chosen in correspondence with the extend of the second order structure heterogeneities (macroscopic ranges with different porosity). Mean values of porosity and hydraulic resistance can be determined for each cell. The microscopic structure (pore system) can not be resolved by PET.

### 2.5.2 Partition of the Column in Regions with Different Flow Characteristics

The velocity distribution in the cross section can be simplified by introduction of a limited number of velocity ranges. Each range is characterized by the flow condition and its part of area in the cross section (Fig. 2.8). A separate flow model with a special transfer function $\Phi(s)$ can be applied for each flow range and combined in a simple way if linear models and the Laplace- or Fourier-transformation are used.

In Table 2.3 some examples of transfer functions and the combination for the hydrodynamic modelling are given.

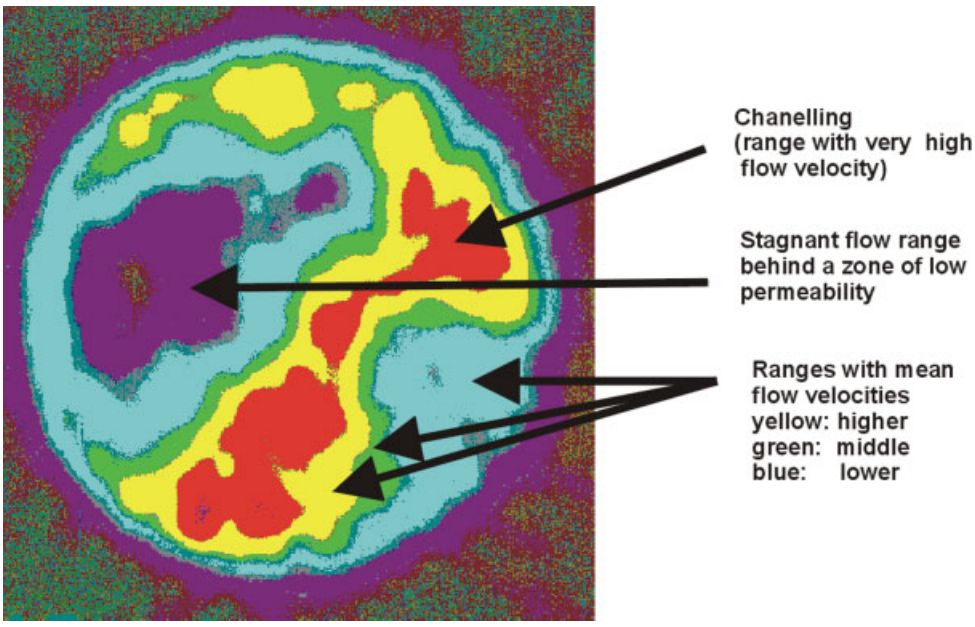


Figure 2.8: Partition of the column in discrete ranges with different flow regimes.

Table 2.3: Transfer functions of one-dimensional hydrodynamic models and model combinations.

| Hydrodynamic model | Transfer function (Laplace transform $\Phi(s)$) | Model parameters |
|---|---|---|
| Plug flow | $\Phi(s) = \exp(-s\tau)$ | $\tau$ = Mean residence time |
| Dispersion flow | $\Phi(s) = \exp\left(\frac{Pe}{2}\left(1-\sqrt{1+\frac{4s\tau}{Pe}}\right)\right)$ | $Pe = (du/D)$ = Peclet number<br>$d$ = Column diameter<br>$D$ = Dispersion coefficient<br>$u$ = Mean flow velocity |
| Cell model | $\Phi(s) = \frac{1}{(1+(s\tau/N))^N}$ | $N$ = Number of cells |
| Cell model with backflow | $\Phi(s) = \left(\frac{2(1+r)}{1+(s\tau/N)+2r\sqrt{(1+(s\tau/N))^2+4r(s\tau/N)}}\right)^N$ | $r$ = Part of back flow |
| Flow with stagnant ranges | $\Phi(s,\tau) \Rightarrow \Phi(s,\tau^*)$<br>$\tau^* = \tau\left(1+\frac{k}{s+(1-f)(k/f)}\right)$ | $f$ = Part of stagnant volume<br>$k$ = Mass transfer coefficient between stagnant and dynamic ranges |
| Parallel flow regimes | $\Phi(s) = \sum_{i=1}^{n} \alpha_i \Phi_i(s)$ | $\alpha_i$ = Part of flow regime $\Phi_i$ |
| Different flow regimes in axial sections | $\Phi(s) = \prod_{i=1}^{n} \Phi_i(s)$ | $\Phi_i(s)$ = Flow regime in section i |
| Recirculation | $\Phi(s) = \frac{\Phi_1(s)}{1+\beta\Phi_1(s)\Phi_2(s)}$ | $\beta$ = Part of recirculation flow<br>$\Phi_1(s)$ = Main flow<br>$\Phi_2(s)$ = Back flow |

The parameters of each individual transfer function $\Phi_i(s)$ can be estimated separately from the tomographic measurements and the complete transfer function for the column is calculated with the relations for parallel flow regimes and the combination of axial sections given in Table 2.3.

The flow distribution in Fig. 2.8 can be described by parallel plug flow (channeling red area) $\Phi_1(s)$ and dispersion flow (yellow, green, blue area) with stagnant regions (violet area) $\Phi_2(s)$.

channeling (red region): $\Phi_1(s) = \exp(-s\tau_1)$ (13)

dispersion flow with stagnant regions: $\Phi_2(s) = \exp\left(\frac{Pe}{2}\left(1-\sqrt{1+\frac{4s\tau_2^*}{Pe}}\right)\right); \tau_2^* = \left(1+\frac{k}{s+(1-f)(k/f)}\right)$ (14)

complete transfer function: $\Phi(s) = \alpha_1\Phi_1(s) + \alpha_2\Phi_2(s); \alpha_1 + \alpha_2 = 1$ (15)

$\alpha_1$ is the part of channel flow (ratio of the red area to the cross section).

$\alpha_2 = 1 - \alpha_1$ is the part of dispersion flow with stagnant regions.

*f is* the part of stagnant volume in relation to the region of dispersion flow (ratio of the violet area to the sum of the yellow, green and blue areas in Fig. 2.8).

The residence times for the channeling flow and dispersion flow respectively ($\tau_1$ and $\tau_2$) can be estimated from the velocity distribution (Section 2.4).

$Pe = (l \cdot d)/D_{ax} \cdot \tau_2)$ is the Peclet-number ($l$ = column length, $d$ = column diamter, $D_{ax}$ = dispersion coefficient). The value can be estimated from concentration gradient in the dispersion flow range (yellow > green > blue).

$k$ = mass transfer coefficient between the stagnant region and the dispersion flow can be estimated from the temporal increase of the tracer concentration in the stagnant region.

### 2.5.3 Modelling with Reference to the Dispersion Model

The one dimensional dispersion model is used frequently for the evaluation of soil column experiments. Thereby it is supposed implicitly that the tracer concentration distribution measured on the column exit represents the mean value of the cross section (column radius $R$):

$$C^*(z,t) = \frac{2}{R^2}\int_0^R C(z,r,t)rdr \tag{16}$$

The effective dispersion coefficient ($D_{eff}$) calculated with the function $C^*(z,t)$ at $z = l$ ($l$ = column length) is influenced both by axial dispersion ($D_{ax}$) and radial dispersion ($D_{rad}$):

$$D_{eff} = D_{ax} + \frac{f(v(r,z))}{D_{rad}} \tag{17}$$

$f(v(r,z))$ is an integral function of the flow velocity distribution $v(r,z)$ in the column cross sections.

If the velocity distribution is different in different cross sections the effective dispersion coefficient is not constant but a function of column length *z:*

$$D_{eff} = D_{eff}(z) \tag{18}$$

The velocity distribution and the function $D_{eff}(z)$ can be calculated from the results of tomographic tracer experiments. On this way a more accurate hydrodynamic modelling and therefore a more exact determination of geochemical parameters is possible.

### 2.5.4 Support of Conventional Measuring Technique

Generally tomographic measurements can be carried out only for a few column experiments, because they are time consuming and costly. In this case the results should be used for a better interpretation of the residence time distribution measured with the conventional measuring technique and to make a statement about the exactness of the used hydrodynamic model.

One or two special phenomena (for example channeling or stagnant regions) which influence strongly the geochemical modelling can be added to the dispersion model, if the tomographic measurements demonstrate that these phenomena are essential for the modelling of hydrodynamics.

For these reasons the conventional measurements of the residence time distribution should be realized very exactly. An important influence on the information content of the tracer output function has the shape of the input function. Between the transmission function of the object $\Phi(\omega)$ (Fourier transform of the hydrodynamic model) and the power spectrum of the tracer input function $C_{in}(\omega)$ and the power spectrum of the tracer output concentration distribution $C_{out}(\omega)$ the following relation exists for linear models:

$$C_{out}(\omega) = \Phi(\omega) \cdot C_{in}(\omega) \tag{19}$$

Power spectra are the Fourier transform of the tracer concentration function $C(t)$

$$C_{in/out}(\omega) = \int_0^\infty C_{in/out}(t) \cdot e^{-i\omega t} dt \tag{20}$$

If the limit of frequency in the input function ($\omega_l$) is low, than the output function $C_{out}(\omega)$ contains no information about $\Phi(\omega)$ in the range $\omega > \omega_l$.

Table 2.4 shows the power spectra of some input functions. Impulse and stochastic functions have high limit frequencies. Therefore impulse or stochastic methods should be prefered for tracer experiments in soil columns.

The stochastic input ($c_x(t)$) and output functions ($c_y(t)$) of the tracer concentration are evaluated with the correlation theorie (Lee, 1964; Solodnikov, 1971).

Table 2.4: Power spectra and limit frequencies of several tracer input functions.

| Input function | Signal shape | Power spectrum | Limit frequency ($\omega_l$) $C(\omega_l)/C(0) = 0.01$ |
|---|---|---|---|
| $\delta$-impulse |   | $C(\omega)$ = const | $\omega_l = \infty$ |
| Step function | 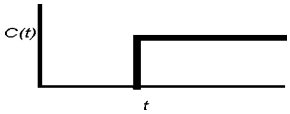  | $C(\omega) = 1/\omega$ | $\omega_l = 100$ |
| Harmonic input (frequency $\omega_0$) | 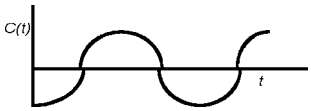  | $C(\omega) = \delta(\omega - \omega_0)$ | only information for $\Phi(\omega_0)$ |
| White noise | 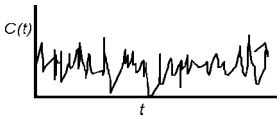  | $C(\omega)$ = const | $\omega_l = \infty$ |
| Real impulse $C(t) = \exp(-\lambda t)$ | 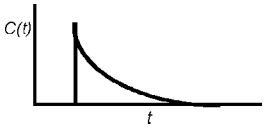  | $C(\omega) = 2\lambda/(\lambda^2 + \omega^2)$ | $\omega_l \approx 100\ \lambda$ |
| PRBS sequence N = 15 Pulse interval $\Delta t$ | 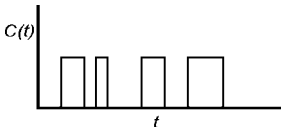  | $C(\omega) = (4/(\Delta t\ \omega^2)) \cdot \sin^2(\Delta t\ (\omega/2))$ | $\omega_l \approx 10\ \pi / \Delta t$ |

The auto correlation function of the input concentration is defined as

$$\varphi_{xx}(\tau) = \lim_{T\to\infty} \frac{1}{2T} \int_{-T}^{T} c_x(t) \cdot c_x(t+\tau)\, dt \tag{21}$$

and the cross correlation function is defined as

$$\varphi_{xy}(\tau) = \lim_{T\to\infty} \frac{1}{2T} \int_{-T}^{T} c_x(t) \cdot c_y(t+\tau)\, dt \tag{22}$$

$\varphi_{xy}(\tau)$ has the following properties:

$$\varphi_{xy}(\infty) = 0; \varphi_{xy}(\tau) = \varphi_{xy}(-\tau) \tag{23}$$

The general relation between the input and output signal for a linear model is given by the convolution integral:

$$c_y(t) = \int_{-\infty}^{+\infty} c_x(t-\theta) \cdot g(\theta) d\theta \tag{24}$$

$g(\theta)$ is the weighting function. The Laplace transform of $g(\theta)$ is the transfer function.

Examples for hydrodynamic models are compiled in Table 2.3.

Multiplication of Eq. (24) with $c_x(t)$ and integration results in

$$\varphi_{xy}(\tau) = \int_{-\infty}^{+\infty} \varphi_{xx}(\tau-\theta) \cdot g(\theta) d\theta \tag{25}$$

The same relations exist for the correlation functions as for the concentration functions of the input and output flows.

When the output signal is interfered by stochastic disturbances, the estimation of the weighting function will be incorrect with Eq. (24). Equation (25) gives exact results since the stochastic disturbances do not correlate with the input signals. Therefore they do not contribute to the correlation functions. On this way the stochastic errors of the measuring values are eliminated.

A further advantage of the correlation functions is the optimal adaption of nonlinear processes to linear models (Wiener, 1950).

But experiments with stochastic input signal demand a long measuring period to determine the cross correlation functions with sufficient accuracy.

For tracer experiments periodic sequences of **p**seudo **r**andom **b**inary **s**ignals (PRBS) can be used, which show good results after a shorter measuring period (Havlicek and Cermak, 1977; Unbehauen and Funk, 1974). A PRBS sequence consists of a stochastic series of rectangular tracer pulses (concentration $c$, time interval $\Delta t$). The sequences recur with a period $T$. Each period is divided into $N$ time intervalls ($T = N \cdot \Delta t$).

The following correlation functions can be defined for a PRBS input tracer distribution $P_{in}(t)$ and the output tracer distribution $P_{out}(t)$:

$$\varphi^*_{xx}(\tau) = \frac{1}{T} \int_0^T P_{in}(t) \cdot P_{in}(t+\tau) dt \tag{26}$$

$$\varphi^*_{xy}(\tau) = \frac{1}{T} \int_0^T P_{in}(t) \cdot P_{out}(t+\tau) dt \tag{27}$$

In connection with Eq. (25) this results in:

$$\varphi_{xy}(\tau) = \int_0^T \varphi^*_{xx}(\tau - \theta) \cdot g(\theta) d\theta + \int_T^{2T} \varphi^*_{xx}(\tau - \theta) \cdot g(\theta) d\theta + \ldots \tag{28}$$

The period T can be chosen so that $g(\theta) \approx 0$ for $\theta > T$. This condition is satisfied in the most cases, when $T$ is double the residence time of the system. Then the following relation is valid:

$$\varphi^*_{xy}(\tau) \approx \int_0^T \varphi^*_{xx}(\tau - \theta) \cdot g(\theta) d\theta \tag{29}$$

If the PRBS-Period consists of $N = 2^n\text{-}1$ ($n > 4$) time intervalls ($\Delta t$) with stochastic distributed tracer pulses (concentration $c$), than the auto correlation function is

$$\varphi^*_{xx}(\tau) = \begin{cases} c^2\left(1 - \dfrac{N+1}{N}\dfrac{\tau}{\Delta t}\right); 0 \le \tau \le \Delta t \\ c^2\left(-\dfrac{1}{N}\right); 0 \le \tau \le (N-1)\Delta t \\ c^2\left(\dfrac{N+1}{N}\dfrac{\tau}{\Delta t} - N\right); (N-1)\Delta t \le \tau \le N\Delta t \end{cases} \tag{30}$$

The cross correlation function $\varphi_{xy}(\tau)$ can be calculated with Eq. (29) and (30)

$$\varphi^*_{xy}(\tau) = c^2 \frac{N+1}{2} \Delta t \cdot g(\tau) - \frac{c^2}{N} \int_0^{\tau} g(\vartheta) d\vartheta \tag{31}$$

The weighting function of the system $g(\theta)$ can be estimated with Eq. (31) from the cross correlation function of the PRBS tracer experiment. The weighting function can be used for the validation of the model and the determination of the model parameters. Generally it is sufficient to measure for two PRBS periods. Stationary conditions are adjusted during the first period. The measured tracer output concentrations of the second period are used for the calculation of the cross correlation function.

## 2.6 References

Baumann, T. et al. (2000): *Environ. Sci. Technol.* **34**, 8–31.
Chatziioannou, A. F. et al. (1999): *J. Nuclear Med.* **40,** 1164–1175.
Chin, D. A.; Wang, T. (1992): *Water Resources Res.* **28**, 1531–1542.
Havlicek, A.; Cermak, I. (1977): *Coll. Czech. Chem. Soc.* **42**, 2094.
Just, A. et al. (1994): *Zeitschr. Geolog. Wiss.* **22**, 617–621.
Lee, Y. W. (1964): Statistical theory of communication, Wiley & Sons, New York.
Meyer, P. et al. (1994): *Zeitschr. geolog. Wiss*. **22**, 485–487.
Richter, M. et al. (2000A): *Zeitschr. angew. Geologie* **46**, 101–109.
Richter, M.et al. (2000B): Positron Emission Tomography for studies of water flow in soil columns. In: Appl. Mineralogy, Vol. 2, Rammlmair et al. (Eds.): Balkema, Rotterdam.
Solodnikow, W. W. (1971): Grundlagen automatischer Regelsysteme*,* Bd. 2, Verlag Technik, Berlin.
Unbehauen, H.; Funk, W. (1974): *Regelungstechnik* **9**, 269.
Wiener, N. (1950): Extrapolation, interpolation and smoothing of stationary time series, Wiley & Sons, New York.

# 3 Upscaling of Hydraulic and Hydrogeochemical Aquifer Parameters Using an Approach Based on Sedimentological Facies

Thomas Ptak* and Rudolf Liedl

## Abstract

It is well known that hydraulic and hydrogeochemical aquifer heterogeneities have a dominating impact on the transport and spreading of reactive compounds dissolved in groundwater. To be able to consider both types of heterogeneity, a three-dimensional finite-difference reactive solute transport modelling approach was developed, being an essential component of a methodology allowing for the upscaling of small-scale laboratory measurements. Sorption and desorption in the heterogeneous aquifer material can be introduced using a diffusion-based formulation at grain scale. The intra-particle diffusion process is simulated for each lithological component and each grain size fraction of the aquifer material. For a practical application of the code, the data needed are introduced into each model cell individually following a facies-based approach. The first modelling results emphasize a strong impact of the lithological aquifer material composition and confirm the need for a complex process-based reactive transport modelling approach with spatially variable hydraulic and hydrogeochemical aquifer parameter fields.

## 3.1 Introduction

Many organic contaminants in groundwater not only undergo advection, dispersion and degradation, but are also subject to sorption and desorption resulting in contaminant spreading which is retarded as compared to the transport of non-reactive compounds. It has been found that sorption and desorption processes in general cannot be adequately described by invoking the local equilibrium assumption (Sardin et al., 1991). Rather, sorption and desorption of organic compounds may exhibit a strong kinetic behavior, associated with an effective retardation factor increasing with time (e.g. Ball and

*Institut und Museum für Geologie und Paläontologie, Universität Tübingen, Sigwartstr. 10, 72076 Tübingen; e-Mail: thomas.ptak@uni-tuebingen.de



*Geochemical Processes: Conceptual Models for Reactive Transport in Soil and Groundwater. Research Report.* Deutsche Forschungsgemeinschaft (DFG).
 ISBN: 978-3-527-27764-3

Roberts, 1991A and B; Grathwohl, 1992; Grathwohl and Reinhard, 1993). Diffusive processes are mainly responsible for the sorption kinetics (e.g. Pignatello and Xing, 1996; Grathwohl, 1997). The solute is subject to diffusive transport within the fluid phase of the intra-particle pores, and equilibrium sorption/desorption onto the intra-particle pore walls governed by a non-linear isotherm. Equilibrium sorption onto outer grain surfaces does not significantly contribute to the retarded transport of the organic species.

Dealing with reactive transport modelling at field scale, both the hydraulic and the physico-chemical (hydrogeochemical) aquifer heterogeneities have to be considered. It is well known that aquifer structural properties, i.e. size, position and amount of clay lenses, sand and gravel layers, and the resulting heterogeneous distribution of hydraulic conductivity and porosity, significantly control groundwater flow and spreading of solutes (e.g. Dagan, 1989; Gelhar, 1993). At this macroscopic scale, the solute plume may be distorted by these hydraulic heterogeneities. In addition to this, hydrogeochemical aquifer heterogeneity, i.e. different intra-particle sorption and diffusion properties for different source rocks of the aquifer material (lithocomponents) grouped in different grain size fractions, influence the interaction of reactive solutes with the aquifer material (e.g. Grathwohl and Kleineidam, 1995; Karapanagioti et al., 1999; Kleineidam et al., 1999; Rügner et al., 1999), and may tend to enhance tailing of reactive solutes, compared to non-reactive ones (e.g. Burr et al., 1994).

Large-scale transport models accounting for non-equilibrium solute retardation have been presented, for instance, by Gerke and van Genuchten (1993) and Vogel et al. (2000). In the dual-porosity models discussed by these authors it is assumed that the rate of solute transfer between a mobile and an immobile fluid phase is proportional to the concentration difference between the two phases. The linearity of the rate law is not shown to be related to a specific hydrogeochemical process in the subsurface. In contrast to this, a process-based modelling approach describing mass transfer by intra-particle diffusion is used by Harvey and Gorelick (1995) and Haggerty and Gorelick (1995) who simulate sorption/desorption kinetics for aquifer material with different grain size fractions. However, these models do not account for the non-uniform lithological composition of the aquifer material and the non-linearity of the intra-particle sorption/desorption isotherm.

To be able to consider both, the physical (hydraulic conductivity, porosity) and the hydrogeochemical aquifer heterogeneities (different intra-particle sorption and diffusion parameters for different lithological components of the aquifer material and the different grain size fractions) in a process-based manner, a three-dimensional finite-difference solute transport modelling approach was developed, being integrated in an approach for upscaling hydraulic and hydrogeochemical parameters measured at laboratory-scale to field-scale scenarios.

In this contribution, the basic steps and mathematics of the new upscaling approach based on sedimentological facies are described. It is shown how three-dimensional hydraulic and hydrogeochemical aquifer parameter distributions can be obtained using a facies-based categorical variable approach, allowing an application to real case situations. Finally, some examples of application are given, which emphasize the strong impact of the lithological aquifer material composition and of the associated hydrogeochemical aquifer heterogeneity on model results predicting kinetic sorption/desorption of organic contaminants.

## 3.2 The Three-dimensional Reactive Transport Modelling Approach

The concept and the basic steps of the reactive transport simulation approach are summarized in Fig. 3.1. At first, lithofacies types, i.e. aquifer material categories are assigned to aquifer material samples obtained from drill cores. Each facies type is characterized with respect to representative hydraulic and hydrogeochemical properties. Then, generally based on a geostatistical analysis, a spatial distribution of lithofacies types is generated. Since each lithofacies type has characteristic hydraulic and

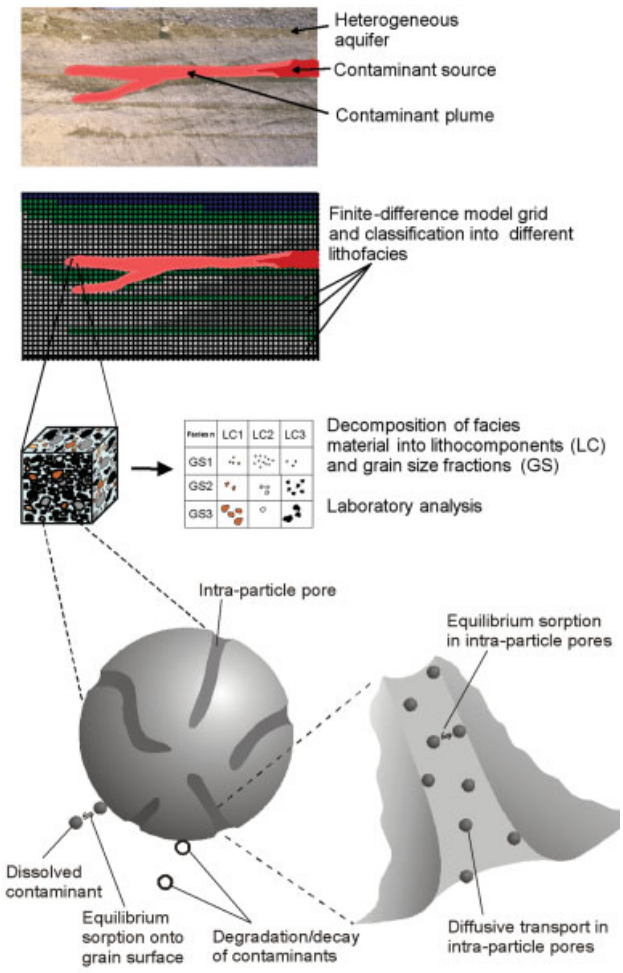


Figure 3.1: Concept and basic steps of the three-dimensional reactive transport modelling approach.

hydrogeochemical properties, this simulation step results in three-dimensional hydraulic and hydrogeochemical aquifer parameter fields. Finally, flow and transport simulations are performed for the reactive solutes within the generated hydraulic and hydrogeochemical parameter fields, with an aquifer geometry as well as initial and boundary conditions according to the field-scale scenario. In addition, an ensemble of equiprobable realizations of the aquifer parameter fields may yield an assessment of parameter uncertainty in a Monte-Carlo-type stochastic framework.

In the following, the individual steps of the facies-based reactive transport modelling approach are described more detailed.

### 3.2.1 Facies-based Characterization of Hydraulic and Hydrogeochemical Aquifer Properties

For an application of the modelling approach, the aquifer is represented by a three-dimensional finite-difference model grid. Due to the hydraulic and hydrogeochemical aquifer heterogeneity, the lithological composition and the grain size distribution may differ from one model cell to another. The data needed are introduced into each model cell following a facies-based categorical variable approach (Fig. 3.1). Since it is known that aquifer hydraulic properties are closely linked to the sedimentary lithofacies (for example well sorted sand, gravel with fine grain matrix etc., e.g. Kleineidam et al., 1999), the aquifer body is at first classified at the model cell scale (order of tens of cm) into typical lithofacies types (Ptak, 1997), which may be interpreted as aquifer material categories. Herfort (2000) has shown that grain size distribution curves of aquifer materials samples (usually sections of about 10 to 20 cm length of drill cores with 10 cm diameter) may be used for this classification, employing for example the K-means multivariate clustering algorithm (McQueen, 1967). In addition, categories or lithofacies types may also be attributed as soft information by an expert geologist (sedimentologist) through a visual inspection of drill core material. In this way, a large number (order of several hundreds to a few thousand) of aquifer material categories, together with their position within the aquifer, can be obtained at affordable costs.

The classification into M categories (clusters) respective lithofacies types based on N grain size distribution curves is shown in Fig. 3.2. The K-means algorithm requires a discretization of each grain size distribution curve (cdf of grain size (GS)) into P classes, which describe the mass fractional contributions of individual grain size fractions to the total sample mass (Fig. 3.2). The number of categories M and of classes P depends on the site specific sedimentological composition of the aquifer, and experience is needed for the definition of these numbers.

After clustering, the values of M binary categorical variables ($clu_1 - clu_M$) are defined for each observation at a location $\underline{x}_j$ in space using the indicator transformation (Fig. 3.2). Herewith, each observation point is assigned a categorical variable $clu_i$ (“cluster number”) by setting:

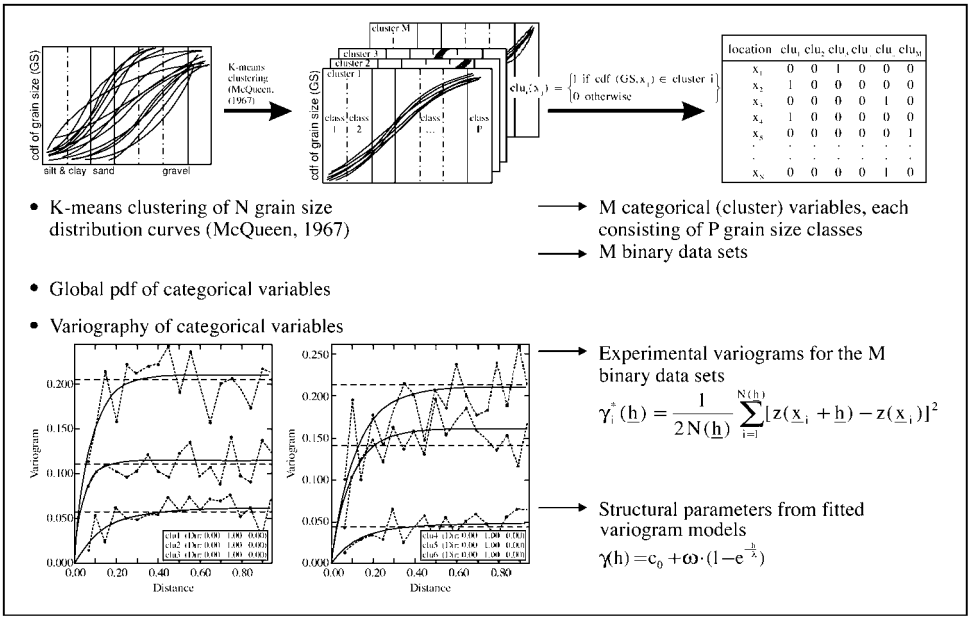


Figure 3.2: Geostatistical analysis of aquifer material grain size distribution curves.

$$clu_i(\underline{x}_j) = \begin{cases} 1 & if \quad cdf\,(GS, \underline{x}_j) \in cluster\ i \\ 0 & otherwise \end{cases} \tag{1}$$

where $i = 1, \ldots, M$ and $j = 1, \ldots, N$. Since the categorical variables $clu_i$ are exclusive, one of these M variables is assigned the value 1 and the remaining M – 1 are assigned the value 0 for each location $\underline{x}_j$, thus yielding M binary data sets, one for each cluster (Fig. 3.2). Then, the spatial correlation of the M categorical variables is investigated by computing experimental variograms and fitting for example exponential variogram models in vertical and two principal horizontal directions for each cluster variable $clu_i$ (Fig. 3.2). The experimental variogram is defined by:

$$\gamma^*_i(\underline{h}) = \frac{1}{2\,N(\underline{h})} \sum_{i=1}^{N(\underline{h})} \left[\, z(\underline{x}_i + \underline{h}) - z(\underline{x}_i) \,\right]^2 \tag{2}$$

$N(\underline{h})$ is the number of cluster variable values $z(\underline{x}_i + \underline{h})$, $z(\underline{x}_i)$ separated by the distance vector $\underline{h}$. The exponential variogram model is given by:

$$\gamma(h) = c_o + \omega \cdot \left(1 - e^{-\frac{h}{\lambda}}\right) \tag{3}$$

where $c_o$ is the nugget, $\omega$ the sill, $h = |\underline{h}|$, and $\lambda$ is the correlation length. Figure 3.3 shows examples of variograms for the categorical variables.

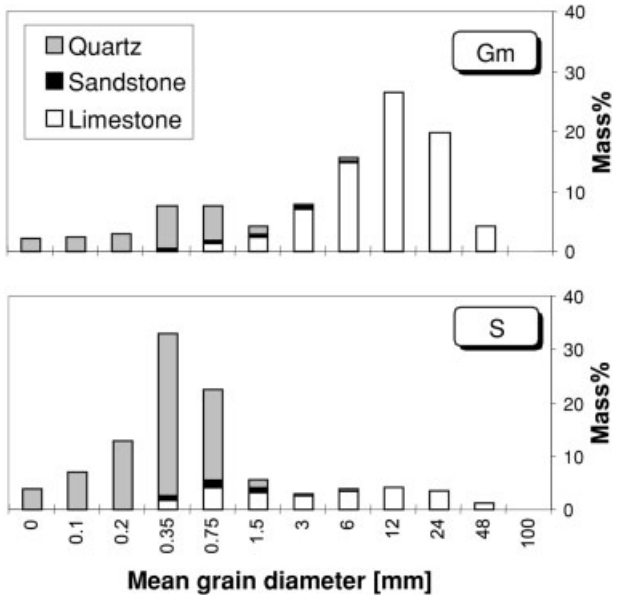


Figure 3.3: Examples of the lithological composition of two lithofacies (Gm = gravel with fine grain matrix, S = well sorted sand) from the Neckar Valley, Germany (Herfort, 2000).

Then, for each lithofacies (aquifer material category, cluster of grain size distribution curves), characteristic sediment samples are collected, and a sediment material decomposition and analysis/batch experiment procedure is applied (Fig. 3.1) to obtain the lithofacies-specific hydraulic parameters, mass fraction of ($j$,$k$)-grains (here $j$ = index denoting a lithological component and $k$ = index denoting a grain size class) and the lithocomponent-specific hydrogeochemical parameters, which are described below in Section 3.2.3. Herfort (2000) has shown that each facies exhibits different hydraulic and hydrogeochemical parameters. Of course, depending on the aquifer genesis, the facies properties may be site specific. Figure 3.3 shows an example of the lithological composition of two facies.

### 3.2.2 Generation of Three-dimensional Facies and Fields of Hydraulic and Hydrogeochemical Aquifer Parameters

In the next step, a facies type has to be assigned to each finite-difference model cell within the simulation domain. For this task, the experimental histogram of the clusters (cluster1 – clusterM) and the cluster variogram models are used to generate conditioned equiprobable three-dimensional realizations of the facies fields described by categorical variables. For the facies-based approach used here, the three-dimensional conditional sequential indicator simulation method (SIS) for categorical variables

(Deutsch and Journel, 1992) is applied. This method is based on an indicator kriging approach. It is able to honour extreme values and allows for consideration of soft information and of more than one spatial structure of the investigated data. Geological expert knowledge about facies distribution and composition, as well as information on aquifer specific sedimentation processes is helpful in this step (Vert et al., 1999).

It is well known that many aquifer materials were deposited in a braided river depositional environment. Braided river environments are characterized by continuous and partly eroded sinuous channels, i.e. sedimentary structures with periodically changing horizontal directions, consisting of sand and gravel, and by minor silty and clayey sediment zones within abandoned channels. The channel structure may significantly control spreading of solutes, especially if the characteristic structural element length is in the order of the investigation scale. To allow the generation of aquifer realizations with sinuous and partly eroded structural elements, the indicator-based geostatistical simulation technique was improved by imposing directional trends on indicator variogram models and merging of different stochastic facies images (Vert et al., 1999).

The stochastic braided river aquifer realizations are generated in three steps. First, a three-dimensional facies model is developed, using all available geological information (lithological description of cores, sieve analyses and interpretation as explained above, expert knowledge of meandering and braided river sedimentary systems). This facies model describes the sedimentological structures of the heterogeneous aquifer. Then, in a second step, stochastic realizations of the facies distribution are generated using SIS. Here, in addition to the conventional SIS approach as used before, simulated direction trends are imposed on the anisotropy axes of the indicator variogram models within each kriging neighbourhood. The principal horizontal directions of the variogram models represent the directions of the axis of the channels. By imposing different direction trends on the variogram models, families of channels are generated and merged together in order to obtain a facies image of the braided river environment. At last, in the third step, based on the facies distribution and using multi-Gaussian simulation to assign (spatially variable) hydraulic conductivities to each individual facies, heterogeneous three-dimensional hydraulic conductivity fields are obtained. This improved stochastic simulation approach is summarized in Fig. 3.4, where the sinuous structural elements can be recognized. The advantage of the improved stochastic simulation approach to generate highly complex heterogeneous aquifer realizations is the possibility to integrate both measured data sets and (categorical) geological information as well as expert knowledge concerning the depositional environment (facies relationships, sequences, associations, frequency and geometry of structural elements, e.g. channel deposits etc.). A much more realistic image of the subsurface is obtained as compared to conventional geostatistical approaches. Especially large scale aquifer structures, for example elements of a braided river system, can be incorporated, and the aquifer realizations can still be conditioned based on hard and soft information.

Since, as an outcome of the geostatistical generation step, a facies type is assigned to each model cell, and since each facies exhibits characteristic hydraulic and hydrogeochemical parameters as shown by Herfort (2000), three-dimensional hydraulic and hydrogeochemical aquifer parameter distributions are obtained simulta-

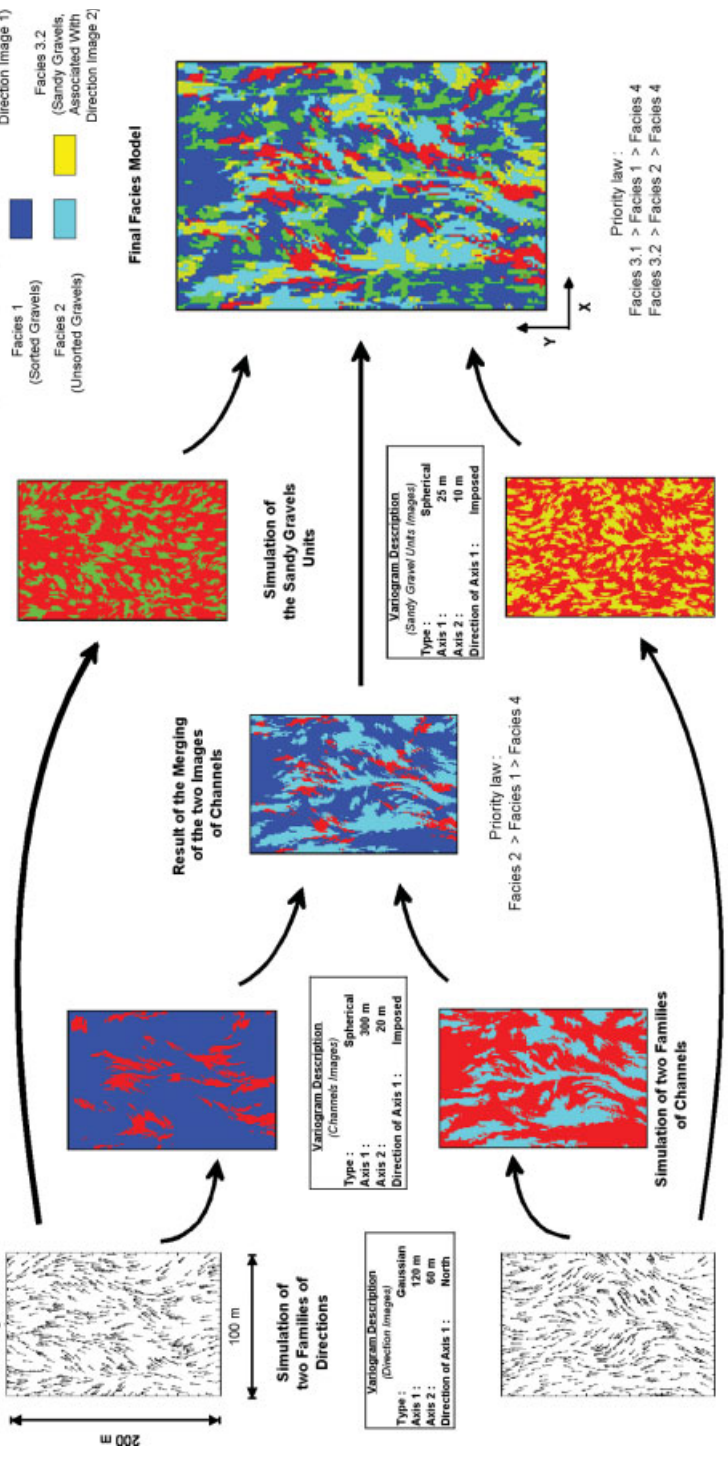


Figure 3.4: Principle of stochastic simulation of facies distributions of a braided river sedimentary environment (Vert et al. 1999).

neously. These parameter distributions are then used in a next step for reactive transport simulations at field scale, employing the numerical code described below. In this way, an upscaling of laboratory measurements for a numerical simulation of field-scale scenarios is achieved implicitly, without the need to define field-scale effective parameter values.

### 3.2.3 Modelling of Flow and Reactive Transport

As stated above, both the lithological composition and the grain size distribution may affect the interaction of contaminants with the aquifer material, i.e. the contaminant mass uptake and release due to intra-particle sorption and diffusion at grain scale. In order to investigate this interaction, aquifer material samples can be separated into individual lithological components $j$ and grain size fractions $k$, and laboratory analyses and batch experiments can be performed as stated in Section 3.2.1 and as shown schematically in Fig. 3.1. As a result, (a) the lithological composition of each characteristic grain size fraction of the aquifer material, i.e. the percentage of, for instance, sandstone, limestone, quartz etc., is obtained as well as (b) the hydrogeochemical parameters characterizing the processes of intra-particle sorption and diffusion for each individual lithocomponent. In the following it is shown in detail how this information is introduced into a numerical reactive transport modelling code.

Sorption and desorption of reactive solutes is introduced using a diffusion-based formulation at grain scale, instead of employing simple transfer rate models involving empirical parameters. In each model cell, the retarded intra-particle diffusion process in the heterogeneous aquifer material is simulated for each lithological component and each grain size fraction. As the grains are assumed to be spherically symmetrical this equation can be written as:

$$\frac{\partial}{\partial t}\left[\varepsilon_j\, c_{jk} + \left(1-\varepsilon_j\right)\rho_j \sigma_{jk}\right] = \frac{D_{aq}}{\tau_j}\frac{1}{r^2}\frac{\partial}{\partial r}\left[r^2 \frac{\partial}{\partial r}\left(\varepsilon_j\, c_{jk}\right)\right] \tag{4}$$

with $t$ = time [T], $r$ = radial coordinate [L], $D_{aq}$ = aqueous diffusion coefficient of the reactive solute [$L^2T^{-1}$], $\tau_j$ = tortuosity of intra-particle pores of a lithological component $j$ [–], $\varepsilon_j$ = intra-particle porosity of lithological component $j$ [–], $\rho_j$ = dry solid density of lithological component $j$ [$ML^{-3}$], $c_{jk}$ = concentration of chemical dissolved in the fluid phase within intra-particle pores of the ($j$,$k$)-grains [$ML^{-3}$], $\sigma_{jk}$ = mass of chemical sorbed onto surfaces of intra-particle pores of the ($j$,$k$)-grains per unit mass of the ($j$,$k$)-grains [–]. Equation (4) needs data obtained from the aquifer material decomposition, analysis and batch experiments shown in Fig. 3.1. The tortuosity $\tau_j > 1$ has been introduced in order to account for the reduction of diffusion due to the crooked flow paths along the intra-particle pores. Furthermore, diffusion is retarded due to equilibrium sorption onto the surfaces of the intra-particle pores. This process can be quantified by:

$$\sigma_{jk} = G_{jk}\left(c_{jk}\right) \tag{5}$$

where $G_{jk}$ stands for the type of sorption/desorption isotherm to be employed. The specific isotherms are again obtained from an aquifer material analysis (Fig. 3.1) and accompanying batch experiments.

From the intra-particle diffusion equation (4) the mass of a chemical within the ($j$,$k$)-grains can be given per unit volume by:

$$m_{jk} = \frac{\rho\, f_{jk}}{\frac{4\pi}{3} R_k^3 \left(1-\varepsilon_j\right)\rho_j} \cdot \int_0^{R_k} 4\pi r^2 \left[\varepsilon_j c_{jk} + \left(1-\varepsilon_j\right)\rho_j \sigma_{jk}\right] dr \tag{6}$$

where $R_k$ = grain radius of grain size class $k$ [L] and $f_{jk}$ = mass fraction of ($j$,$k$)-grains [–] according to the aquifer material lithological and grain size decomposition shown in Fig. 3.1. In equation (6) the integral represents the mass of the chemical within each individual ($j$,$k$)-grain and the ratio in front of the integral equals the number of the ($j$,$k$)-grains per unit volume. This mass is required for solving the reactive transport equation:

$$\frac{\partial}{\partial t}\left[nc + \sum_{j,k}\left(f_{jk}\rho s_{jk} + m_{jk}\right)\right] + \operatorname{div}\left(v_f c - nD \operatorname{grad} c\right) = Nc' - \lambda_d nc - \rho \sum_{j,k} f_{jk} \lambda_{d,\,jk}\, s_{jk} \tag{7}$$

with $n$ = effective inter-particle porosity [–], $\rho$ = bulk density [ML$^{-3}$], $c$ = solute concentration [ML$^{-3}$], i.e. mass of a dissolved chemical compound per unit volume of effective inter-particle pore space, $D$ = local dispersion tensor [L$^2$T$^{-1}$], $\lambda_d$ = degradation rate for the chemical dissolved in inter-particle pore space [T$^{-1}$], $s_{jk}$ = mass of the chemical compound sorbed onto surfaces of the ($j$,$k$)-grains per unit mass of the ($j$,$k$)-grains [–], $\lambda_{d,jk}$ = degradation rate for the chemical sorbed onto surfaces of ($j$,$k$)-grains [T$^{-1}$], $m_{jk}$ = mass of the chemical in intra-particle pores of the ($j$,$k$)-grains per unit volume [ML$^{-3}$], and $c'$ = concentration of injected or withdrawn solute [ML$^{-3}$] (for withdrawal $c' = c$). Sorption of chemicals onto the outer grain surfaces is assumed to occur under equilibrium conditions so that sorption isotherms:

$$s_{jk} = F_{jk}(c) \tag{8}$$

can be employed for each lithological component $j$ and each grain size class $k$. $F_{jk}$ may denote any type of isotherm such as linear, Freundlich, or others, obtained from laboratory batch experiments (Fig. 3.1).

To solve the above system of model equations appropriate initial and boundary conditions have to be provided. In particular, solute concentrations in inter- and intra-particle pore space are related by:

$$c_{jk}\left(\underline{x}, r = R_k, t\right) = c(\underline{x}, t) \tag{9}$$

for any point $\underline{x}$ in a one-, two- or three-dimensional model domain, i.e. solute concentration is assumed to vary continuously at the "interface" between inter- and intra-particle pore space ($r = R_k$).

Additional initial and boundary conditions have to be specified for inter-particle transport according to the scenario to be modelled.

The mathematical model presented in this section has to be solved numerically due to the complex interaction of large (field-) scale transport and local (grain-) scale diffusion as well as linear or non-linear equilibrium sorption/desorption processes. For this purpose, a solution technique has been developed combining the well known three-dimensional groundwater transport simulation code MT3D (Zheng, 1990) and a new finite-difference code IPD (Jaeger and Liedl, 2000) for the intra-particle diffusion. The added IPD module simulates within each model cell the retarded intra-particle diffusion process in heterogeneous aquifer material by solving Eq. (4) for each lithological component $j$ and each grain size class $k$. The extended version of MT3D is called MT3D-IPD. The numerical solution of the transport model equations (4)–(9) is performed by this software under the assumption that solute concentration in the *inter*-particle pore space is uniform within each MT3D model cell. This assumption, of course, is inherent to any numerical modelling approach, although some information about the concentration distribution within the large-scale model cells may be desired. This information, however, can only be obtained by refining the model cells. To investigate the impact of the cell size of a large-scale numerical transport model on predicting intra-particle sorption and desorption would certainly be an instructive task but it is clearly beyond the scope of this paper which is intended to introduce the basic model concept.

## 3.3 Example of Application

In order to demonstrate the applicability of the modelling approach, and to emphasize the importance of a correct representation of aquifer material lithology in reactive transport simulations, a simple one-dimensional example scenario has been selected, representing flow and transport during a column experiment. The flow in the column is steady-state without sources or sinks ($N = 0$). Hydraulic conductivity and effective inter-particle porosity are set equal to $K = 10^{-4}$ m/s and $n = 0.4$, respectively. The length of the column is $L = 0.2$ m, and a constant head difference is maintained such that linear velocity $v_f/n$ equals 1 m/d = $1.16 \cdot 10^{-5}$ m/s. Longitudinal dispersivity is assumed to be $\alpha_L = 4 \cdot 10^{-4}$ m. All modelling exercises refer to a continuous injection of Phenanthrene with an input concentration $c_{in} = c(x{=}0,t) = 40$ $\mu$g/L into an initially uncontaminated column. Phenanthrene, which belongs to the group of polycyclic aromatic hydrocarbons (PAHs), was chosen here as a representative pollutant compound, since it belongs to the US-EPA priority pollutant list. The aqueous diffusion coefficient of Phenanthrene equals to $5.72 \cdot 10^{-6}$ cm$^2$/s. As the modelling studies are focused on the

investigation of intra-particle diffusion, decay and sorption onto outer grain surfaces are neglected, i.e. $\lambda_d = \lambda_{d,jk} = 0$ and $s_{jk} = 0$, respectively. Sorption onto the walls of the intra-particle pores is modelled by Freundlich isotherms, so that Eq. (5) now reads:

$$\sigma_{jk} = G_{jk}(c_{jk}) = K_{Fr,jk}\, c_{jk}^{n_{Fr,jk}} \tag{10}$$

with $K_{Fr,jk}$ = Freundlich coefficient $[(M^{-1}L^3)^{nFr,jk}]$ and $n_{Fr,jk}$ = Freundlich exponent [–] of the $(j,k)$-grains.

The intra-particle diffusion of Phenanthrene is studied for three lithological components with different sorption/desorption properties: sandstone, light-colored limestone and dark-colored limestone. Parameters of these lithological components resemble data published by Kleineidam et al. (1999) and are summarized in Table 3.1.

In order to maintain a constant surface-to-volume ratio all grains are assumed to have the same radius $R_k = 0.015$ cm. As an example of the results, Fig. 3.5 shows breakthrough curves (BTCs) at the column outlet obtained from four model test runs (runs 1–4) simulating sorption. The runs can be distinguished by the varying mass fractions $f_j$ for each lithological component (Tab. 3.2).

It can be seen that the first breakthrough for the sandstone column (run 2) occurs at later times than for the limestone columns. This is due to the higher apparent intra-particle diffusion coefficient $D_{app,j}$ of the sandstone grains where $D_{app,j}$ is defined by:

$$D_{app,j} = \frac{\varepsilon_j\, D_{aq}}{\left(\varepsilon_j + (1-\varepsilon_j)\,\rho_j\, n_{Fr,j} K_{Fr,j}\, c_j^{n_{Fr,j}-1}\right)\tau_j} \tag{11}$$

Table 3.1: Hydrogeochemical parameters of lithocomponents (model input data).

| | Sandstone | Light-colored limestone | Dark-colored limestone |
|---|---|---|---|
| Intra-particle porosity $\varepsilon_j$ [–] | 0.0195 | 0.0054 | 0.0035 |
| Tortuosity $\tau_j$ [–] | 12 | 20 | 590 |
| Dry solid density $\rho_j$ [g/cm$^3$] | 2.69 | 2.73 | 2.74 |
| Freundlich coefficient $K_{Fr,j}$ $[(mL/\mu g)^{nFr,j}]$ | $2.9 \times 10^{-6}$ | $5.5 \times 10^{-6}$ | $3.6 \times 10^{-5}$ |
| Freundlich exponent $_{nFr,j}$ [–] | 0.66 | 0.67 | 0.33 |

Table 3.2: Mass fractions [%] of lithocomponents for the different model runs.

| | Sandstone | Light-colored limestone | Dark-colored limestone |
|---|---|---|---|
| Runs 1, 5 | 33.33 | 33.33 | 33.33 |
| Runs 2, 6 | 100 | 0 | 0 |
| Runs 3, 7 | 0 | 100 | 0 |
| Runs 4, 8 | 0 | 0 | 100 |

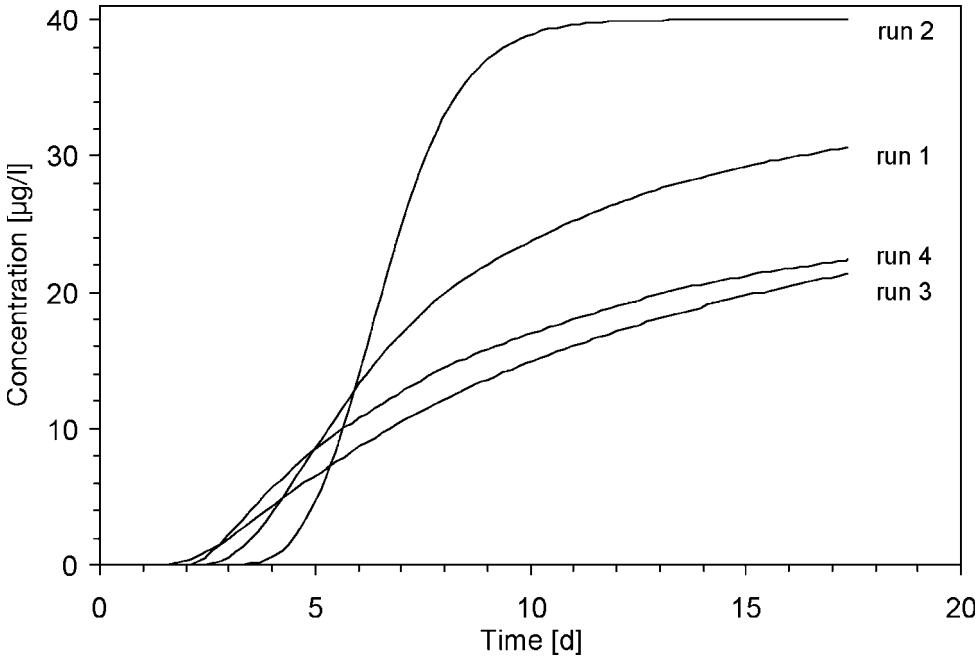


Figure 3.5: Breakthrough curves for sorption model runs.

The long-term behaviour is explained by the sorption capacity factors:

$$\varepsilon_j + \left(1-\varepsilon_j\right)\rho_j \, n_{Fr,j} \, K_{Fr,j} \, c_j^{n_{Fr,j}-1} \tag{12}$$

These factors provide a qualitative measure for the amount of contaminant which can be stored per solid mass in the intra-particle pores of each lithological component for a certain solute concentration in the inter-particle pores. The low capacity factor of the sandstone explains why the BTC belonging to model run 2 approaches the input concentration much more rapidly than the BTCs for the limestone columns. For comparison, Fig. 3.5 also shows the BTC for a column filled with sandstone, light-colored limestone and dark-colored limestone at identical mass fractions (run 1). Of course, this BTC cannot be obtained by simple arithmetic averaging of the BTCs representing the lithologically homogeneous cases. This is mainly due to the temporally changing ratios of contaminant uptake by the three lithological components and the non-linear isotherms.

For the numerical modelling of Phenanthrene desorption, again four runs (run 5–8, see Tab. 3.2) were performed, with hydraulic conditions and lithological compositions according to the preceding sorption runs. It was assumed that initially all lithocomponents are at sorption equilibrium, and that the concentration of dissolved Phenanthrene in the interparticle space equals 40 $\mu$g/L. Desorption was initiated by setting the Phenanthrene concentration at the column inflow to zero.

Figure 3.6 shows the Phenanthrene breakthrough curves for the model runs 5–8, again at the model column outlet.

Comparing the homogeneous lithology runs 6–8, it is seen that the sandstone column initially exhibits the highest Phenanthrene concentration (or mass flux respectively) over a relatively long time period of about three days. Then the concentration decreases very fast to the lowest level, after only about 15 days of desorption. This behaviour can be explained by the high apparent diffusion coefficient and the low capacity factor of the sandstone. According to the ratios of the apparent diffusion coefficients and the capacity factors of the limestones, the light-colored limestone initially releases more mass, i.e. a higher outflow concentration, compared to the dark-colored limestone. However, at late time, the limestone breakthrough curves intersect, and the dark-colored limestone produces the highest outflow concentration, which decreases only very slowly. This result shows that individual lithocomponents may act as a long-term continuous contaminant source, producing significant dissolved contaminant mass fluxes at a very large time scale (possibly hundreds of years). Due to the desorption from the dark-colored limestone, a long tailing can also be expected for the breakthrough curve obtained from model run 5 with a mixed lithology scenario (see Tab. 3.2 and Fig. 3.6). Of course, due to the reasons explained above, this breakthrough curve cannot be obtained by averaging the breakthrough curves from the lithologically homogeneous model runs 6–8. The pronounced tailing explains, why pump-and-treat remediation technologies very often proved to be inefficient, requiring excessive cleanup times (e.g. Wiedemeier et al., 1999). As the dark-colored limestone has the smallest contaminant release rate, this lithocomponent may act as a long-term source for a contaminant plume.

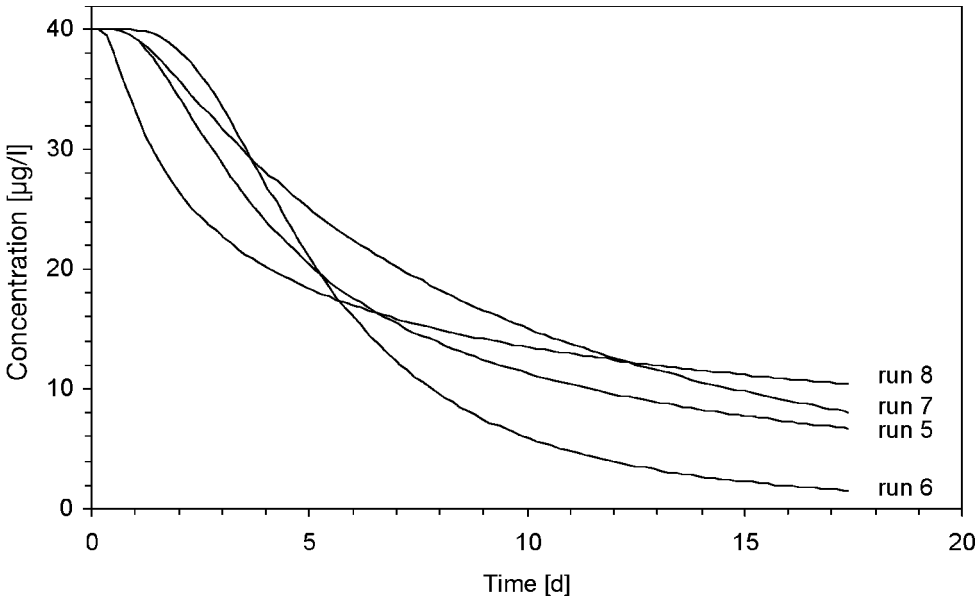


Figure 3.6: Breakthrough curves for desorption model runs.

## 3.4 Conclusions and Future Work

The joint simulation of sorption and desorption at small scale and groundwater flow and transport at large scale, which is regarded as an essential prerequisite for simulating field-scale scenarios of reactive solute spreading, is included in a simulation method based on the characterization of sedimentological facies. A subsequent generation of spatially variable facies distributions offers an effective possibility to consider heterogeneous, i.e. spatially variable, hydraulic and hydrogeochemical aquifer parameter fields. The method allows for an upscaling of laboratory measurements to field-scale scenarios without the need to introduce empirical and/or scale-dependent effective parameter values, or some a priori correlation functions of hydraulic conductivities and distribution coefficients. It offers a broad field of applications, for example for the assessment of plume spreading and groundwater contamination risk at polluted sites, for the evaluation of the natural attenuation potential, or for the planning of active remediation activities. Forthcoming papers will include three-dimensional scenarios with complex initial and boundary conditions, spatially variable distributions of hydraulic and hydrogeochemical aquifer parameters as well as the coupled simulation of biodegradation processes.

## 3.5 References

Ball, W. P.; Roberts, P. V. (1991A): Long-term sorption of halogenated organic chemicals by aquifer material – 1. Equilibrium. *Environ. Sci. Technol.* **25**(7), 1223–1237.

Ball, W. P.; Roberts, P. V. (1991B): Long-term sorption of halogenated organic chemicals by aquifer material – 2. Intraparticle diffusion. *Environ. Sci. Technol.* **25**(7), 1237–1249.

Burr, D. T.; Sudicky, E. A.; Naff, R. L. (1994): Nonreactive and reactive solute transport in three-dimensional heterogeneous porous media: Mean displacement, plume spreading, and uncertainty, *Water Resour. Res.* **30**(3), 791–815.

Dagan, G. (1989): Flow and transport in porous formations, Springer, Berlin.

Deutsch, C. V.; Journel, A. G. (1992): GSLIB Geostatistical software library and user's guide, Oxford University Press, New York, pp. 340.

Gelhar, L. W. (1993): Stochastic subsurface hydrology, Prentice Hall, Englewood Cliffs.

Gerke, H. H.; van Genuchten, M. T. (1993): A dual-porosity model for simulating the preferential movement of water and solutes in structured porous media. *Water Resour. Res.* **29**(4), 305–319.

Grathwohl, P. (1992): Persistence of contaminants in soils and sediments due to diffusion-controlled desorption In: Richter, P. L.; Herndon, R. C. (Eds.): Int. Symp. on Environmental Contamination in Central and Eastern Europe, Budapest, 604–606.

Grathwohl, P. (1997): Diffusion in natural porous media – Contaminant transport, sorption/desorption and dissolution kinetics, Kluwer, Dordrecht.

Grathwohl, P.; Kleineidam, S. (1995): Impact of heterogeneous aquifer materials on sorption capacities and sorption dynamics of organic contaminants. In: Kovar, K.; Krasny, J. (Eds.): Groundwater quality: Remediation and protection. *IAHS Publ.* **225**, 79–86.

Grathwohl P.; Reinhard M. (1993): Desorption of trichloroethylene in aquifer material: Rate limitations at the grain scale. *Environ. Sci. Technol.* **27**(12), 2360–2366.

Haggerty, R.; Gorelick, S. M. (1995): Multiple-rate mass transfer for modelling diffusion and surface reactions in media with pore-scale heterogeneity. *Water Resour. Res.* **31**(10), 2382–2400.

Harvey, C. F.; Gorelick, S. M. (1995): Temporal moment-generating equations: Modelling transport and mass transfer in heterogeneous aquifers. *Water Resour. Res.* **31**(8), 1895–1911.

Herfort, M. (2000): Reactive transport of organic compounds within a heterogeneous porous aquifer. Ph. D. Thesis, C54, University of Tübingen, Center for Applied Geoscience, Tübingen, pp. 59.

Jaeger, R.; Liedl, R. (2000): Prognose der Sorptionskinetik organischer Schadstoffe in heterogenem Aquifermaterial (Predicting sorption kinetics of organic contaminants in heterogeneous aquifer material). *Grundwasser* **5**(2), 57–66.

Karapanagioti, H. K.; Sabatini, D. A.; Kleineidam, S.; Grathwohl, P.; Ligouis, B. (1999): Phenanthrene sorption with heterogeneous organic matter in a landfill aquifer material. *Phys. Chem. Earth (B)* **24**(6), 535–541.

Kleineidam, S.; Rügner, H.; Grathwohl, P. (1999): Impact of grain scale heterogeneity on slow sorption kinetics. *Environ. Toxic. Chem.* **18**(8), 1673–1678.

M$^{c}$Queen, J. (1967): Some methods for classification and analysis of multivariate observations. *5th Berkeley Symposium on Mathematics, Statistics and Probability* **1**, 281–298.

Pignatello, J. J.; Xing, B. (1996): Mechanisms of slow sorption of organic chemicals to natural particles. *Environ. Sci. Technol.* **30**(1), 1–11.

Ptak, T. (1997): Evaluation of reactive transport processes in a heterogeneous porous aquifer within a non-parametric numerical stochastic transport modelling framework based on sequential indicator simulation of categorical variables. In: Soares, A. et al. (Eds.): geoENV I – Geostatistics for Environmental Applications, Kluwer, 153–164.

Rügner, H.; Kleineidam, S.; Grathwohl, P. (1999): Long term sorption kinetics of Phenanthrene in aquifer materials. *Environ. Sci. Technol.* **33**(10), 1645–1651.

Sardin, M.; Schweich, D.; Leij, F. J.; van Genuchten, M. T. (1991): Modelling the non-equilibrium transport of linearly interacting solutes in porous media: A review. *Water Resour. Res.* **27**(9), 2287–2307.

Vert, M.; Ptak, T.; Biver, P.; Vittori, J. (1999): Geostatistical generation of three-dimensional aquifer realizations using the conditional SIS approach with direction trends imposed on variogram models. In: Gomez-Hernandez, J. J. et al. (Eds.): geoENV II – Geostatistics for Environmental Applications, Kluwer, 343–354.

Vogel, T.; Gerke, H. H.; Zhang, R.; van Genuchten, M. T. (2000): Modelling flow and transport in a two-dimensional dual-permeability system with spatially variable hydraulic properties, *J. Hydrol.* **238**(1–2), 78–89.

Wiedemeier, T. H.; Rifai, H. S.; Newell, C. J.; Wilson, J. T. (1999): Natural attenuation of fuels and chlorinated solvents in the subsurface. Wiley, New York, pp. 615.

Zheng, C. (1990): MT3D – A modular three-dimensional transport model for simulation of advection, dispersion and chemical reactions of contaminants in groundwater systems. S. S. Papadopoulos and Associates, Inc.

# 4 DiffMod7 – Modelling Oxygen Diffusion and Pyrite Decomposition in the Unsaturated Zone Based on Ground Air Oxygen Distribution

Henrik Hecht*, Martin Kölling and Norbert Geisler

## Abstract

In the context of a project on pyrite weathering and the associated oxygen transport in the unsaturated zone of lignite open mining dumps a model for pyrite weathering in the unsaturated zone was developed from a simple model idea. It was validated in laboratory column experiments. The model allows the quantification of the processes occurring in the laboratory experiments and thus an identification of the relevant mechanisms, as well as the forecasting of the course of such experiments. A transfer to low complexity natural systems is possible by the simplicity of the model. With the help of the model, the oxygen penetration depth and the associated depyritization depth of a 43 years old dump body could be predicted and validated by in situ measurements of the oxygen distribution and by the determination of pyrite contents.

## 4.1 Introduction

Scientific investigations include the development of plausible model conceptions. In many cases these model conceptions lead to the development of computer models, which are – in the ideal case – not only able to describe the investigations made but can also be used for prognosis purposes. An important point associated with the development of such models is the identification of the relevant process-controlling parameters. The simpler these models are regarding computational effort and parameter scope, the easier they may be scaled up to large-dimensioned natural systems. Modelling of natural systems usually requires processing a large quantity of base data including a more complicated parameterization.

* Fachbereich 5 – Geowissenschaften, Universität Bremen, Postfach 330440, 28334 Bremen; e-Mail: hhecht@uni-bremen.de



*Geochemical Processes: Conceptual Models for Reactive Transport in Soil and Groundwater. Research Report.* Deutsche Forschungsgemeinschaft (DFG).
 ISBN: 978-3-527-27764-3

The degradation of pyrite with oxygen causes the release of very large quantities of iron and sulphuric acid. Successive reactions induced by pyrite weathering result in heavy metal release and both dissolution and formation of minerals. Sorption processes additionally entail strong modifications of the seepage water and groundwater chemistry. The basic mechanisms associated with pyrite weathering are reviewed in Evangelou (1995), Appelo and Postma (1994) and Nordstrom (1982). The initial cause of complex processes is the contact of pyrite with atmospheric oxygen when pyrite-bearing material is being exposed. In the investigations presented here, special attention was put on both the oxygen recharge and the pyrite turnover in the zone of reaction. The relevant processes are convective and diffusive oxygen transport as well as the pyrite reactivity (specific mineral surface, turnover rates).

In column experiments, convective transport processes were important only in the sense of gas volume recharge following oxygen consumption. Diffusive oxygen recharge was identified as the most important transport process. For the implementation in a model, different numerical solutions are available. In each case, the soil-physic characteristics (porosity, water content, tortuosity factor) determining the soil-specific diffusion coefficient have a crucial influence on the oxygen flux. Comprehensive reviews of transport modelling and soil-physic parameters are given e.g. by Boudreau (1997) and Grathwohl (1998). Since the characteristics of the pyrite grains are responsible for the direct interaction between pyrite and oxygen, the grain modification in the course of pyrite decomposition has a direct influence on oxygen fluxes and pyrite turnover. Therefore, the modification of pyrite grains must be considered.

Different approaches for modelling pyrite decomposition in the saturated and/or unsaturated zone of overburden material have been described in the literature. At present, the model developed furthest is probably the programme MINTOX (Wunderly et al., 1996), which couples linear oxygen diffusion, pyrite decomposition by means of a shrinking core model (Davis and Ritchie, 1986), geochemical equilibrium calculations and two-dimensional transport. A similar model concept was used by Gerke et al. (1998) for the calculation of acid mine drainage producing processes in lignite dumps. Prein (1994) developed the linear model SAPY for pyrite decomposition in lignite open mining dumps, which considers the relevant transport processes in the liquid and in the gaseous phase and which allows to calculate the distribution of the reaction products in different dump structures. Puura et al. (1999) developed a model for the atmospheric oxidation of pyrite bearing waste rock. It considers the calculation of the oxygen recharge in waste dumps and shale lumps containing sulfide minerals. Pyrite oxidation and carbonate buffering are calculated within a common reaction term. Xu et al. (2000) modelled pyrite oxidation and discrete event type processes under saturated and unsaturated conditions with the help of two transport reaction models in fractured rocks.

In the development of the model presented here, a focus was put on simple and plausible operability as well as a clear visualization of the processes. The effects of parameter modifications may be observed while the calculations are going on. The model is limited to processes identified as substantial in the systems examined, which drastically reduces calculation time. One aim was to show that even with a simplified model approach the major processes may be described and predicted.

## 4.2 Data Basis for Model Development

In a column experiment on pyrite decomposition in the unsaturated zone of overburden material of an open cast lignite mine both the column effluent and the soil gas oxygen content were monitored. The columns were constructed from perspex pipes with a diameter of 10 cm and a length of 85 cm. The columns were filled with overburden material from the open cast lignite mine Garzweiler, West Germany. The column was irrigated twice a day during total experiment duration of 600 days and sampled once a week. In the effluent solution the reaction products of pyrite decomposition and successive processes (sorption, solution, etc.) were determined. Along the soil profile in the column the progressing pyrite decomposition could be observed within the unsaturated zone by soil gas oxygen measurement with a modified optical measuring system (Microx 1, company Presens (www.presens.de), Holst et al., 1995). The pyrite-bearing overburden material was examined for both its soil-physical parameters (particle size distribution, water content, soil-specific diffusion coefficient) and chemical characteristics (pyrite content (chrome extraction after Volkov and Zhabina (1977)), elemental composition).

In the lower 20 cm of the column, no more open pore space is found due to increased water saturation. The pyrite in this zone is not involved in the alteration of the column in relevant quantities. The results of the parameters important for the model development are represented in Fig. 4.1. It shows the cumulative amount of the iron release over time and the associated development in the oxygen depth distribution during the depyritization. Additionally, the pyrite content in the ideally unsaturated area of the column is plotted. It is the pyrite quantity, which is available for reactions with diffusively transported oxygen.

Approximately a few days after the beginning of the experiment equilibrium between oxygen consumption and oxygen recharge is established. Subsequently, the oxygen penetrates more and more deeply into the column and thus reflects a progres-

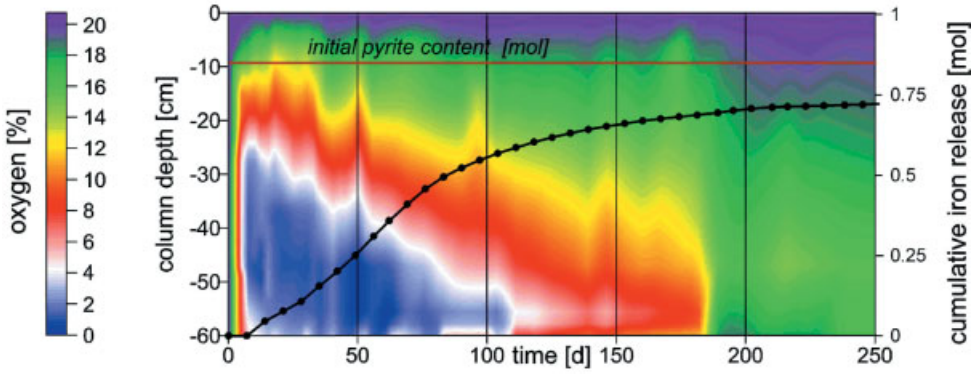


Figure 4.1: Pyrite decomposition in soil column experiment; development of oxygen depth distribution and cumulative amount of iron release over time; initial pyrite content.

sive depyritization of the material. After approximately 180 days, the oxygen concentration sharply increases throughout the column indicating the end of the pyrite decomposition process within the ideally unsaturated area of the column. The discharge of the primary reaction products iron and sulfate also reflects the processes in the column. The initial discharge solution is characterized by washout of pyrite weathering products that have been formed in the material prior to the beginning of the experiment. Within the first hundred days the release of iron and sulfate becomes nearly constant. This is controlled by the approximately constant pyrite degradation on the column. After 100 days the release slightly decreases as the front of the active pyrite decomposition zone reaches the lower end of the column. After approximately 200 days the majority of the reaction products released within the unsaturated area of the column have been washed off the column. The subsequent residual release of pyrite oxidation products is characterized by reduced oxygen availability in the lower nearly water-saturated part of the column.

## 4.3 The Model (DiffMod7)

### 4.3.1 Model Concept

The data obtained in the column experiments form the basis for the development of a model for pyrite decomposition in the unsaturated zone. The model was programmed in Visual Basic 6. Visual programming languages allow a quick and easy way of establishing an intuitive graphical user interface, which provides a graphical control of the model calculations at runtime. The model presented here is an iterative cell model, which calculates the diffusive oxygen recharge and the oxic pyrite decomposition in the unsaturated zone. A simple transport of the reaction products with the seepage water is integrated into the model. No special attention is paid to diffusive/dispersive effects in the liquid phase or on secondary mineral reactions which are not included in the present state of the model.

#### 4.3.1.1 Diffusive Transport

A pyrite decomposition process is an instationary process since the solid phase reactant is being consumed under pyrite-oxidizing conditions causing changes in both reactive surface and mineral mass. Only in a fictitious system, in which the velocity of the depyritization front penetration by chance equals the surface erosion stationary conditions may be found. Diffusion under instationary conditions may be described by numerical solutions of the transport reaction equation considering Ficks second law. Reactions can be integrated quite simply, if transport and reaction are decoupled in a

combined mixing cell/analytical model (Schulz and Reardon, 1983). Equation (1) shows the diffusion/dispersion part of the explicit solution of the transport reaction equation (e.g. Boudreau, 1997) used in our model. In DiffMod7, convective oxygen recharge resulting from the loss in gas volume is not calculated within the transport reaction equation. The reaction term is separated as well. The advantage of the procedure is that for the calculation of the new concentrations only the concentrations in the previous time step must be known.

$$C_t^1 = C_{t-\Delta t}^1 + \Delta t \cdot D_{sed} \cdot \left( \frac{C_{t-\Delta t}^2 - 2 \cdot C_{t-\Delta t}^1 + C_{t-\Delta t}^0}{(\Delta x)^2} \right) \tag{1}$$

$C_t^1$ calculated concentration in the regarded cell [mol m$^{-3}$],

$C_{t-\Delta t}^1$ concentration of the regarded cell in the previous time step [mol m$^{-3}$],

$C_{t-\Delta t}^0$ concentration of the previous cell in the previous time step [mol m$^{-3}$],

$C_{t-\Delta t}^2$ concentration of the next cell in the previous time step [mol m$^{-3}$],

$D_{sed}$ soil-/sediment-specific diffusion coefficient [mol m$^{-2}$s$^{-1}$] (Eq. (3)),

$\Delta t$ time step [s],

$\Delta x$ cell height [m].

Equation (1) is stable only for certain combinations of $\Delta t$ and $\Delta x$ (e.g. Mitchell and Griffiths, 1980). The condition, which has to be met in order to prevent oscillations within the calculation, reads:

$$\Delta t \leq \frac{(\Delta x)^2}{2 \cdot D_{sed}} \cdot \tag{2}$$

The soil-specific diffusion coefficient is the diffusion coefficient corrected for the soil-physic parameter tortuosity ($\theta$) in free air (e.g. Boudreau, 1997).

$$D_{sed} = \frac{D_0}{\theta^2} \tag{3}$$

$D_0$ pressure- and temperature-corrected diffusion coefficient in free air.

The tortuosity describes the ratio of the (average) incremental distance that an ion/molecule must travel to cover the direct distance in the direction of diffusion (Berner, 1980) and is thus the factor, which describes the increase in travel distance in the porous medium. Since the definitions of tortuosity in literature indicate small however substantial differences (an excellent overview of different procedures, equations and definitions is given by Boudreau (1997)), the definition used here is described briefly. The diffusion coefficient is corrected by the squared tortuosity. The square of the tortuosity is called tortuosity factor (Carman, 1937). This factor represents the

entire correction factor for the calculation of the soil-specific diffusion coefficient from the diffusion coefficient in free air (Boudreau, 1997). The tortuosity factor is not a measurable parameter. It may be calculated from empirical equations. Within the model, Eq. (4) is used for the calculation of the tortuosity factor from the diffusion-effective porosity ($\varphi_e$). It results in a good general solution for fine-grained sediments (Boudreau, 1997).

$$\theta^2 \approx 1 - 2 \cdot \ln(\varphi_e) = 1 - \ln(\varphi_e^2) \tag{4}$$

The soil-physical parameters in natural systems vary with depth. A weighting of the parameters of the interacting cells has to be integrated into the calculation of the diffusive flux with the explicit solution (e.g. Landenberger, 1998). Equation (5) shows the equation used for the calculation of the oxygen concentration in DiffMod7. The topmost and the bottommost cell of the model are calculated separately in consideration of upper and lower boundary conditions.

$$C_t^1 = C_{t-\Delta t}^1 + \frac{\Delta t \cdot D_0}{2 \cdot \Delta x^2} \cdot \left[ \left( \frac{1}{\theta_1^2} + \frac{1}{\theta_2^2} \right) \cdot \left( C_{t-\Delta t}^2 - C_{t-\Delta t}^1 \right) - \left( \frac{1}{\theta_0^2} + \frac{1}{\theta_1^2} \right) \cdot \left( C_{t-\Delta t}^1 - C_{t-\Delta t}^0 \right) \right] \tag{5}$$

$\theta_0^2$ tortuosity factor previous cell,

$\theta_1^2$ tortuosity factor current cell,

$\theta_2^2$ tortuosity factor next cell.

#### 4.3.1.2 Pyrite Weathering

In the model DiffMod7 the diffusion of oxygen within the unsaturated zone is calculated considering weighted soil-specific parameters according to the stability criteria. After each time step for which the diffusive flux between the cells was calculated, the oxygen consumption by pyrite oxidation is determined for this time interval. The oxygen consumption is calculated as a function of the pyrite quantity available, the pyrite grain surface and the pyrite oxidation rate. The reaction equation forming the basis for pyrite decomposition within the model reads:

$$FeS_2 + \tfrac{15}{4} O_2 + \tfrac{1}{2} H_2O \leftrightarrow Fe^{3+} + 2SO_4^{2-} + H^+ \tag{6}$$

Due to the oxidation process, the pyrite quantity within a cell decreases with time, while the specific pyrite grain surface increases by the slow decrease in grain size during the decomposition. The increase of the specific surface is implemented as function of the pyrite quantity according to Eq. (7).

$$A_{py}^t = \sqrt[3]{\frac{m_{py}^{t_0}}{m_{py}^t}} \cdot A_{py}^{t_0} \tag{7}$$

$A_{py}^{t}$ current specific surface of the pyrite in cell,

$A_{py}^{t_0}$ initial value of the specific surface of the pyrite,

$m_{py}^{t}$ current pyrite quantity in cell,

$m_{py}^{t_0}$ initial value of the pyrite quantity in cell.

#### 4.3.1.3 Convective Transport

Convective gas phase transport in natural unsaturated soil systems may be induced by variations in temperature, air pressure and groundwater, by wind pressure or by seepage water movement after rain events. All these processes are of minor importance in lab column experiments and have not been implemented in DiffMod7. The only convective movement in the gaseous phase considered in DiffMod7 is the ground air recharge due to gas volume decrease caused by oxygen consumption. The effects of this type of convection have to be taken into consideration as they result in an increase of the initial oxygen penetration depth or the thickness of the pyrite oxidation zone and thus induce an increase of the total pyrite decomposition rate on the column by 10 to 15 %.

The seepage transport of the reaction products in DiffMod7 is only determined by the seepage velocity. Secondary mineral reactions that might affect the transport by transfer of reaction products from liquid phase into solid phase are neglected.

### 4.3.2 Computer Implementation of Model and User Interface

Figure 4.2 shows the user interface of the model. Basic input parameters are the total depth, the model surface area, the density and the overall porosity of the material and its pyrite content, the pyrite grain surface or a pyrite grain size, a pyrite oxidation rate and the infiltration. Since the programme was originally developed for the modelling of column experiments, these input parameters are not variable with depth. The tortuosity factor, the diffusion-effective porosity and the initial oxygen concentrations may vary with depth and may be individually input for each cell. The uppermost cell represents the ambient air. The lower boundary is defined by a zero gradient condition. Checking the “no convection” control button can deactivate the convective transport described above. The input of the model time step duration is automatically validated for meeting the stability criteria. In addition to the total model time the time steps after which intermediate values of oxygen concentration, pyrite content, pyrite surface, pyrite decomposition and seepage water concentration in each cell are stored in a result file. These values allow the plotting of time-depth distributions of these parameters after the model run. During the model calculation the oxygen concentration, the pyrite quantity and the pyrite decomposition over depth are displayed as diagrams on the right side of the user interface. The maximum of the x-axes is scaled automatically to ambient air oxygen, the initial pyrite content and the initial pyrite decomposition. The

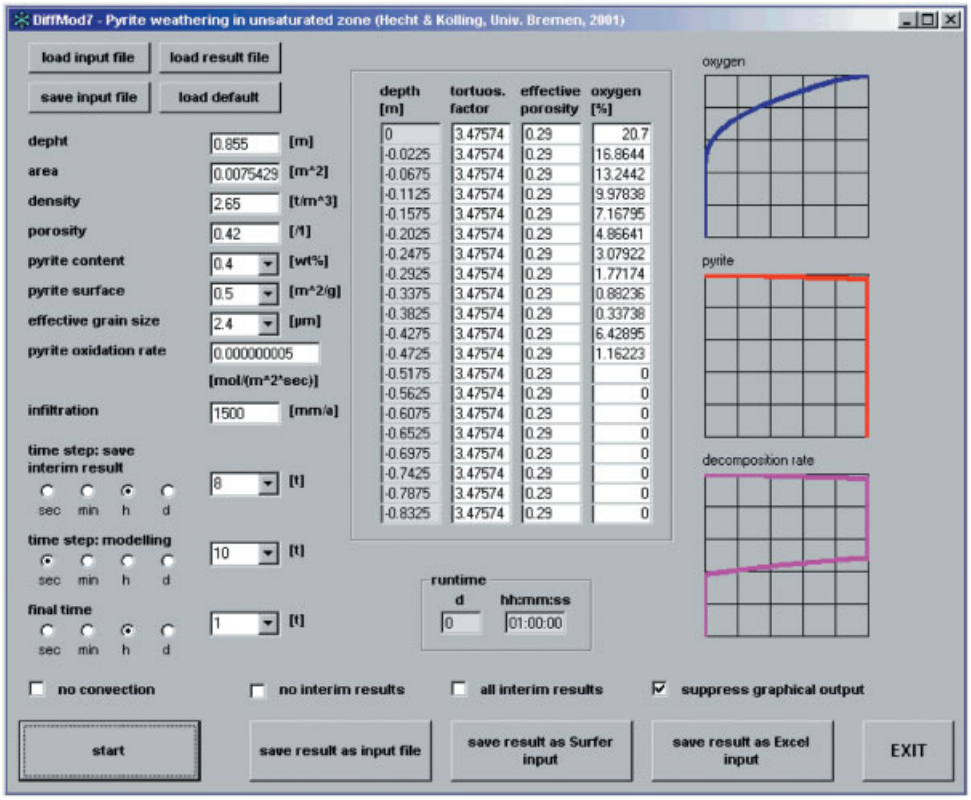


Figure 4.2: DiffMod7 – Graphical user interface.

graphical representation of intermediate results at runtime very well illustrates the processes going on, yet calculations may be strongly accelerated by checking the "suppress graphical output" control if needed. The screen output then reduces to updating the elapsed model time. The start conditions of each model run may be saved in an input file. The results of the model run along with all intermediate results can be stored as data sets compatible with Excel or Surfer.

### 4.3.3 Example

Figure 4.3 shows an example of a model run with appropriate start parameters. Equilibrium between oxygen consumption and oxygen recharge is quickly established on the column indicated by a stable oxygen depth profile. The graphs of pyrite oxidation rates show that initially throughout the oxygen penetration depth equal amounts of oxygen are consumed by the pyrite oxidation due to uniform initial amounts of available pyrite surface.

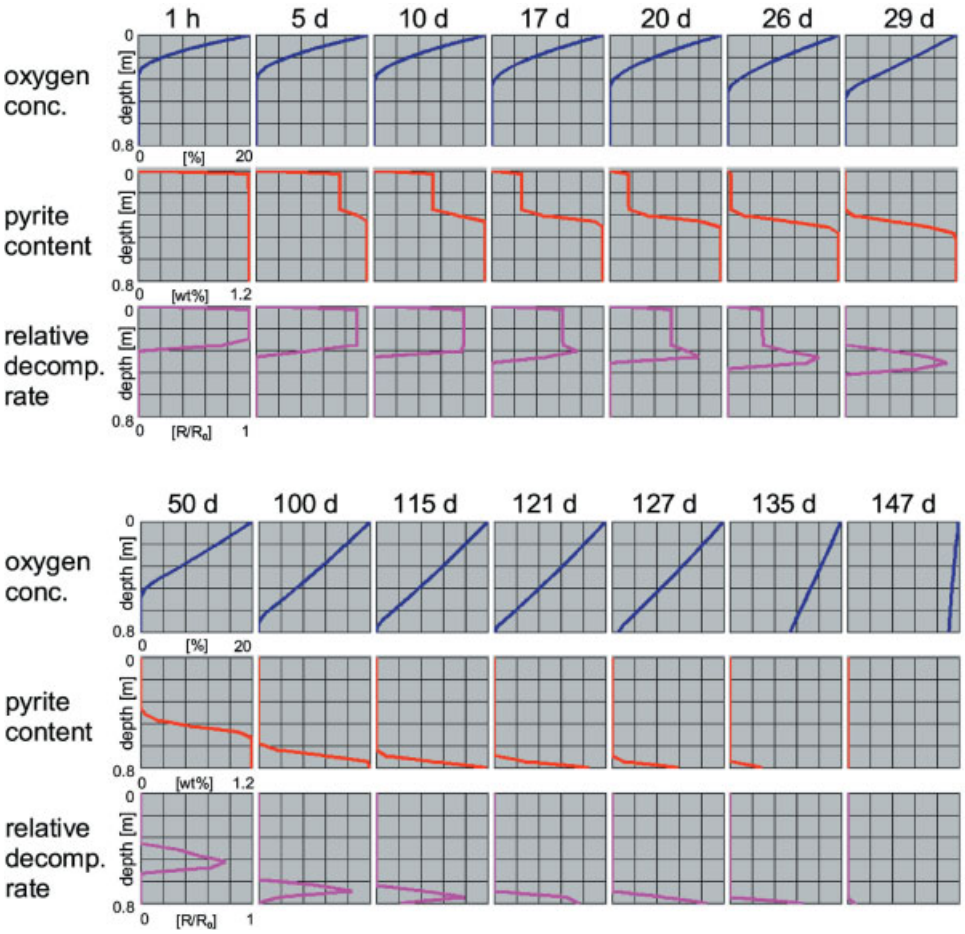


Figure 4.3: Example model run. Graphical output DiffMod7 during calculation. Start parameters: pyrite content: 1.2 wt.%; specific pyrite surface: 1 [$m^2g^{-1}$]; pyrite oxidation rate: $5 \times 10^{-9}$ [mol $m^{-2}s^{-1}$]; effective porosity: 0.29; tortuosity factor: 3.33.

The broad zone of equal decomposition rates remains existing until the entire pyrite is weathered (29 days). During this period the pyrite quantity in this zone slowly decreases and the decomposition rate decreases such that oxygen may gradually penetrate further down into the unweathered material. The change from a mainly surface controlled to a mainly diffusion controlled process is indicated by the evolution of a reaction front which plots as a peak in decomposition rates and which is also indicated in the pyrite depth distribution by a sharp separation of a pyrite-free upper layer and a lower layer with initial pyrite content. After 29 days the uppermost part of the model system is depyritized and the reaction front starts moving further down into the sediment. Due to decreasing fluxes caused by increasing diffusion distances from the surface to the reaction front, both the decomposition rates and the thickness of the reac-

tion front decrease with time. The maximum decomposition rates are not found in the cell with the highest pyrite content, but in the cell above since only there sufficient quantities of oxygen are available. The reaction front slowly moves into the sediment, until the entire pyrite has been consumed. After approximately 150 days the decomposition process is finished, so that in all depths ambient air oxygen concentration is achieved.

One remarkable result of this model calculation is the shape of the oxygen depth profiles. Although at the beginning of the model calculation the reaction rates throughout the entire oxygen penetration depth are constant, the oxygen profiles are only slightly curved. The interpretation of an oxygen profile of this kind as presented e.g. in Schulz (2000) would assume rather low reaction rates in the upper part of the sediment column and the main reaction zone would be expected where the oxygen-depth curve shows an increased curvature. Starting from the 29th day the oxygen almost linearly decreases with depth indicating oxygen flux into a sink located at the depth where the oxygen concentration becomes zero. The reaction front is remarkably wider than the zone of change in the slope of the oxygen depth distribution seems to be. The change in slope is reflected in the decomposition rates, which are in interaction with the change in oxygen concentration differences. In this model run, the oxygen profiles also reflect the effects of convective oxygen transport. After the uppermost layer of the column has been depyritized, the oxygen-depth distribution changes from a concave to a convex shape. This effect is caused by the superposition of diffusive oxygen recharge and the convective recharge caused by the decrease in gas volume (transition of oxygen from the gaseous phase to the liquid species sulfate). The gas volume loss in the reaction zone causes a convective downward shift of ground air. The type of convection considered here thus characteristically modifies the shape of the oxygen profile and the associated oxygen flux. As described above additional modifications of the oxygen depth distribution by convection may occur in natural systems.

### 4.3.4 Modelling Column Experiments

The input parameters necessary for the modelling of the column experiment described in Section 4.2 are well known from analysis of the column material and from the experimental boundary conditions except for the tortuosity factors, which cannot be measured directly. In this case, they are calculated according to Eq. (4). Additionally, the parameters pyrite grain surface and pyrite oxidation rate, which are initially difficult to determine for natural material, are necessary for modelling. An oxidation rate of $7 \times 10^{-9}$ [mol $m^{-2}s^{-1}$] has been assumed. Kölling (1990) found oxidation rates in this order of magnitude for pyrite decomposition processes under ideal conditions catalysed by *Thiobacillus ferrooxidans*. Values for the grain size of early diagenetically formed pyrites within the overburden material are given in Friedrich et al. (1999). A good estimate for the specific surface is 0.5 [$m^2\,g^{-1}$], assuming some grain roughness. Finally, adjusting these two parameters leads to a fit of the modelled oxygen time-depth distribution to the measured data. The results are presented in Fig. 4.4. The

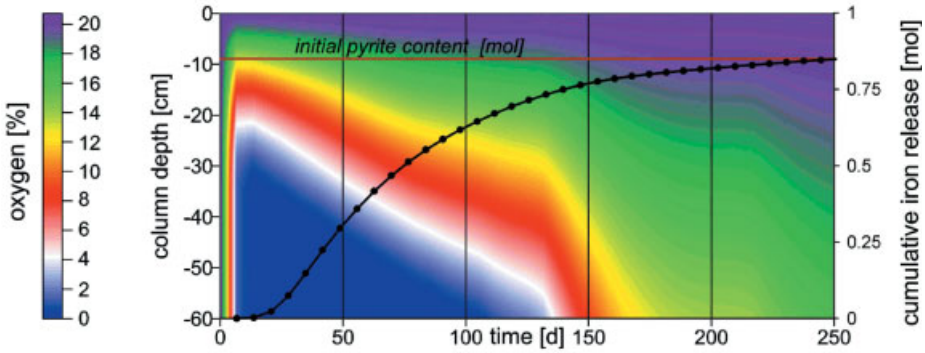


Figure 4.4: Modelled oxygen time-depth distribution and cumulative iron release during pyrite decomposition in column experiment (compare experimental data in Figure 4.1).

measured oxygen time-depth distribution is very well reflected in the model calculation for the uppermost 60 cm of the column (ideally unsaturated area). In the lower area of the column (not ideally unsaturated) pyrite decomposition characterized by low oxidation rates continues for a very long time. The model calculation yields a discharge of reaction products with the seepage water, which corresponds with the measured values of the column experiment (compare Fig. 4.1). The similarity of measured and predicted discharge may serve as an independent validation of the model indicating that the major processes are obviously implemented at a reasonable accuracy level. The differences between observed and modelled iron discharge are affected by the precipitation of secondary iron bearing minerals (Hecht and Kölling, accepted) which have not been considered in this model.

The model calculation additionally yields results on the time depth distribution of pyrite decomposition rates, pyrite contents and the reaction product concentration in the seepage water (Fig. 4.5). The decomposition rate plot clearly shows the formation of the initial pyrite decomposition zone in the uppermost 30 cm of the column. Within this area the decomposition rates are limited mainly by the pyrite grain surface available so that a maximum decomposition is established which is uniform at all depths throughout this zone due to the sufficient oxygen supply. The decomposition rate in this zone decreases with time caused by the decrease of the pyrite quantity. The decrease in decomposition rates is slower than determined only by the decrease in pyrite quantity due to the simultaneous reduction of grain size and increase in specific grain surface. The reduced oxidation rates allow the oxygen to penetrate into deeper areas of the sediment column resulting in the formation of a pyrite oxidation front. The maximum in the decomposition rate depth distribution (green area) decreases with time as the reaction front proceeds into the sediment. At the lower end of the unsaturated part of the column the decomposition rate reduces to 75 % of the maximum rate due to the diffusively controlled oxygen recharge. The fluctuations within the turnover rates result from the spatial resolution of the model and are not the result of oscillations.

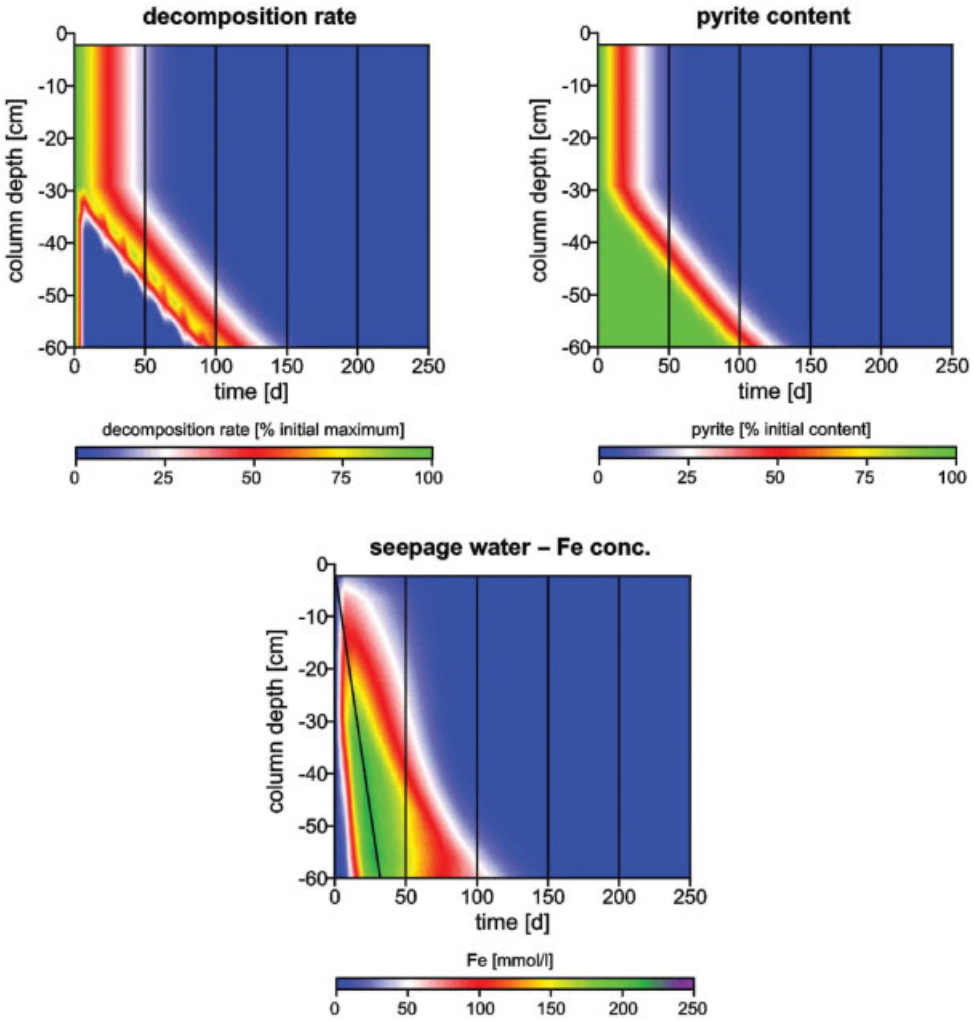


Figure 4.5: Modelled time-depth distribution of pyrite decomposition rates, pyrite contents and reaction product concentrations in the seepage water.

The depth-time distribution of the pyrite content also shows the depyritization. The comparison of the decomposition rates with the pyrite content plots reveals that initially a sufficient amount of pyrite is available in the lower part of the sediment. However, no pyrite oxidation occurs, since oxygen is consumed in the upper layers. The depth-time distribution of the seepage water concentrations results from the seepage water velocity, the pyrite decomposition rate and the velocity with which the reaction front moves downward. The position of a water particle with a constant seepage water velocity plots as a straight line in the time depth diagram. The edge of the high seepage water concentration area in space and time is determined by seepage water

velocity. Since a constant seepage water velocity has been assumed the high concentration seepage waters proceed linearly. Maximum seepage water concentrations are found in the water which has been at the top of the uppermost reaction zone at the start of the experiment since on its way down this water travels through the layers with the highest decomposition rates for the maximum duration. The solid line in Fig. 4.5 (bottom) marks this water. The temporal change in concentration at a given depth is characterized by a sharp increase as the edge of the plume reaches the depth of interest followed by a continuous decrease. In the lower part of the sediment the velocity of depyritization determines the shape of the back flank of the high concentration area in space and time. The fact that during the first 50 days a broader zone of fairly high concentrations evolves in the upper part of the sediment is caused by the uniformly high decomposition rates in the initially broad decomposition zone. In a larger system closer to natural conditions the characteristics of the distribution of pyrite weathering products in depth and time are pronounced more strongly.

### 4.3.5 Running Scenarios

The sensitivity of the model system to variations in the individual parameters can be checked easily using the computer model. One advantage is the possibility of checking different strategies to prevent pyrite oxidation for their efficiency. In the following examples, the final fit parameters for modelling the column experiment were used as base values. At first, the relevance of the soil-physical parameters should be considered. Effective porosity and tortuosity are in direct relation to each other. A change in effective porosity causes a change in tortuosity. Regarding this interaction, the effect on the diffusively controlled pyrite decomposition is more pronounced. Nevertheless, the effects of changes in these two parameters will first be regarded separately.

Halving the diffusion-effective porosity over the entire model depth results in a decrease of initial pyrite decomposition to approximately 60 to 70 % (compare Fig. 4.6). In the uppermost layer the oxygen supply is sufficiently large. The decomposition rate is the same as the result of the original calculation. Initially, the downward oxygen flux decreases to 50 % due to the bisected diffusion-effective cross section. However, the reduced oxygen flux is balanced by a reduced volume to be filled resulting in exactly the same concentration distribution as before. Without oxygen consumption the oxygen flux is bisected when the porosity is bisected. The oxygen consumption results in steeper gradients of oxygen concentration, consequently increasing oxygen flux to over 50 % of the original flux.

The discharge curve shows the characteristics of the different stages of pyrite decomposition inside the model column more clearly. At first, no discharge takes place, because the reaction products formed within the upper layer of the column are transported with the seepage water to the outlet. This first stage is followed by a period of constantly high discharges, which reflects the pyrite decomposition in the uppermost layers close to the surface. The third stage is a decrease of discharge, after the wide superficial oxidation zone has become pyrite-free and the main release occurs in

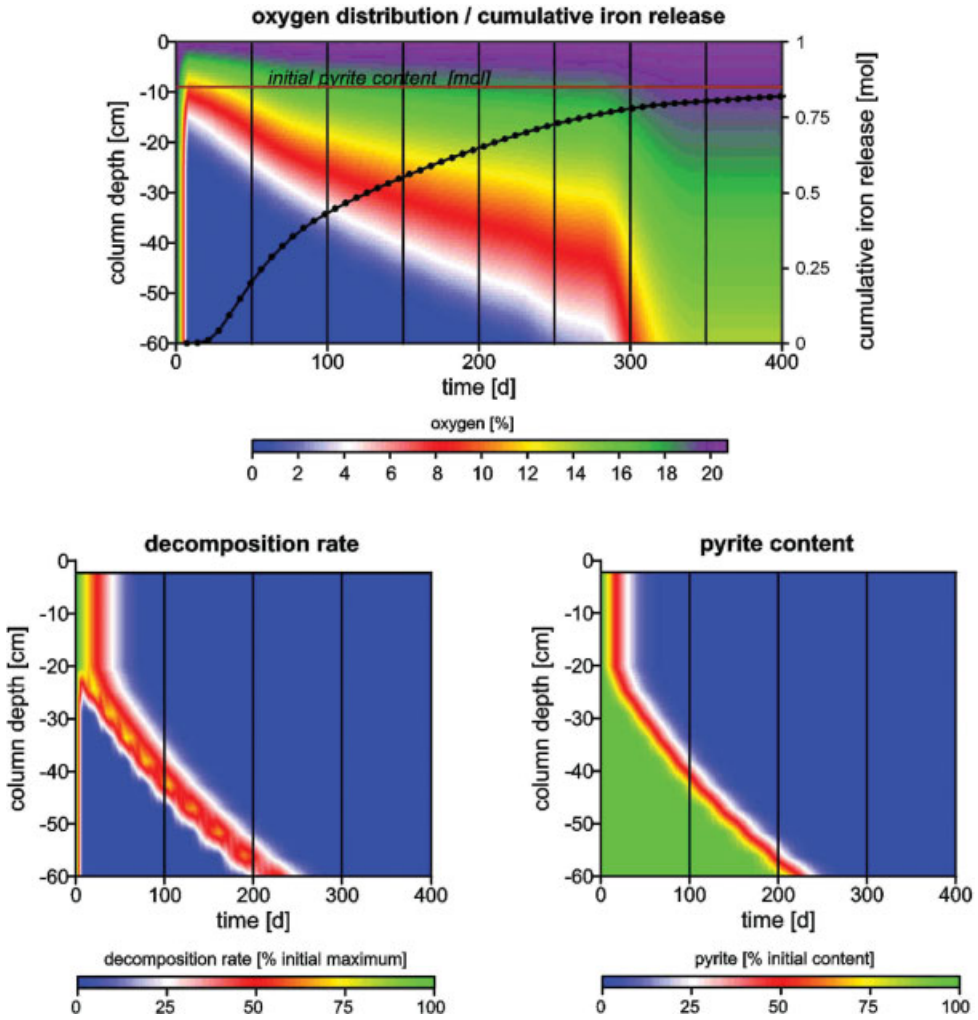


Figure 4.6: Modelled time-depth distribution of oxygen concentrations, pyrite decomposition rates and pyrite contents; cumulative iron release; bisected diffusion-effective porosity with regard to modelled column experiment; (same effect as duplication of tortuosity factor).

a narrow pyrite oxidation front, which is slowly proceeding downwards. With increasing distance of the oxidation front from the surface the oxygen gradient decreases causing a decrease in release rates. Another steep decrease in discharge occurs when the pyrite oxidation front reaches the lower not ideally unsaturated zone of the model system. After this point in time, there is no oxygen limitation in the unsaturated zone (oxygen is found in all depths), but a limitation by the residual pyrite surface. After the upper zone of the column has become completely pyrite-free the discharge is nearly terminated.

On the other hand, doubling the effective porosity leads to exactly inverse effects. The initial pyrite turnover rises to 150 % of the reference turnover.

Doubling the tortuosity factor while maintaining porosity apparently causes the same effects as halving the porosity while maintaining the tortuosity factor (Fig. 4.6). The modification results in halving the soil-specific diffusion coefficient, i.e. the initial flux is halved. However, since the open pore volume remains the same, the resulting concentrations are smaller, thus gradients become steeper. Overall, this results in oxygen fluxes that are larger than 50 % of the flux in the reference system. When oxygen is consumed by pyrite oxidation, the gradients continue to increase up to values between 60 and 70 %. Halving the tortuosity factor causes the opposite effect, resulting in an increase of the initial pyrite turnover to 150 % of the reference value.

If the relation between effective porosity and tortuosity factor is taken into consideration and the two parameters are modified accordingly, the resulting total change in turnover is the product of the two single changes in turnover. Halving the porosity coupled with duplication of tortuosity factor results in a decrease of initial flux to approximately 50 % (Fig. 4.7) of the reference flux.

For the examined systems, an approximated factor results that describes the total change in flux according to the change in tortuosity factor and effective porosity:

$$F = \sqrt{\frac{\theta_s^2 \cdot \varphi_e^v}{\theta_v^2 \cdot \varphi_e^s}} \tag{8}$$

$F$ flux change factor,

$\theta_s^2$ tortuosity factor – base value,

$\theta_v^2$ changed tortuosity factor,

$\varphi_e^s$ effective porosity – base value,

$\varphi_e^v$ changed effective porosity.

Since porosity and tortuosity factor are coupled according to Eq. (4), the correct effect of change in porosity regarding the associated change in tortuosity factor may be calculated by combining Eqs. (4) and (8). The resulting equation reads:

$$F_\varphi \approx \sqrt{\frac{(1-2\ln(\varphi_e^s)) \cdot \varphi_e^v}{(1-2\ln(\varphi_e^v)) \cdot \varphi_e^s}} \tag{9}$$

$F_\varphi$ coupled change in flux factor as a function of effective porosity for fine-grained sediments (after Eq. (4)).

The model calculations show that the soil-physical parameters strongly influence the pyrite decomposition rates and the discharge since these parameters have a direct impact on the amount of transported oxygen. Any change in the characteristics of oxygen transport will result in the change of the pyrite decomposition. While the total potential of acid production remains unchanged, the duration of pyrite weathering processes changes.

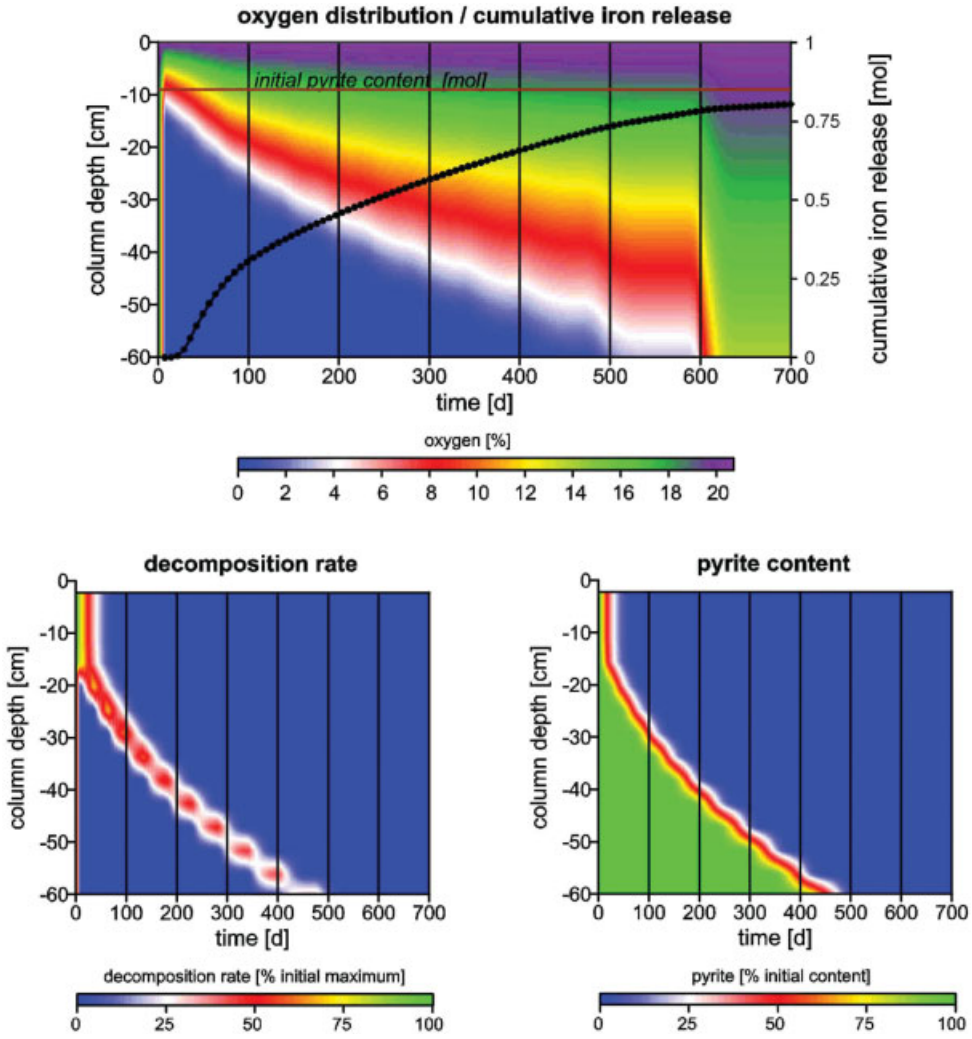


Figure 4.7: Modelled time-depth distribution of oxygen concentrations, pyrite decomposition rates and pyrite contents; cumulative iron release; halved diffusion-effective porosity and coupled duplication of tortuosity factor with regard to modelled column experiment.

A halving of the specific pyrite surface or the pyrite oxidation rate is associated with little effects on the turnover of pyrite and the discharge of reaction products. Both parameters have the same influence, because they both determine the pyrite turnover in moles per time and mass. The effect of halving the parameters (compared to the reference calculation) on the oxygen time-depth-distribution and the discharge is shown in Fig. 4.8.

It is shown that initial turnover and discharges remain almost unchanged, even though the oxygen distribution is strongly affected (doubled penetration depth). Since

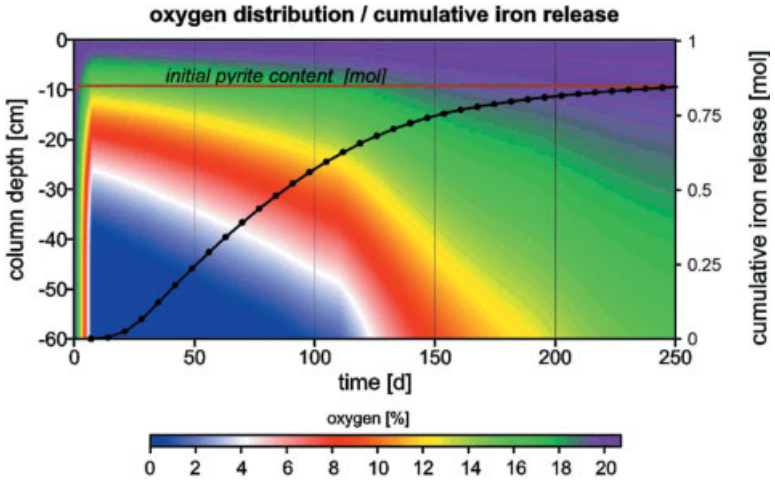


Figure 4.8: Modelled oxygen time-depth distribution and cumulative iron release; changes with regard to modelled column experiment. Halved pyrite oxidation rate (resp. specific pyrite surface).

the pyrite surface and the oxidation rate affect only the thickness of the pyrite oxidation front, in large natural systems the modifications result in a slight shift in depth distribution of reaction products. Doubling the specific pyrite surface or the pyrite oxidation rate causes a halved penetration depth, without great effects on pyrite decomposition and discharge of reaction products.

Modifying the pyrite content of the material has a strong influence on the total turnover of the system. Maintaining all other parameters constant, a duplication of the pyrite quantity results in doubling of the reactive surface, causing a 50 % decrease in the initial oxygen penetration depth (compare Fig. 4.9). The maximum concentrations, indicated by the increased gradient of the discharge curve, are only slightly larger than in the reference calculation. However, due to the increased pyrite quantity the release persists twice as long. The thickness of the pyrite decomposition front is half as thick as in the reference calculation and the time needed for a certain section of the system to become pyrite-free is doubled. The duration of the release of reaction products and their discharge is doubled whereas the seepage water concentration is similar to the reference results. The different stages of the discharge curve show the same features as the curve for halved permeability (Fig. 4.6), since this also results in a smaller thickness of both the initial pyrite weathering zone and the decomposition front.

The effect of halving the pyrite content is inverse. The total potential of acid production is halved as well as the reactive pyrite surface. Thus, the oxygen initially penetrates twice as far into the system. Compared to the reference system the concentrations are slightly smaller, but the total depyritization is completed twice as fast.

Therefore a modification of the pyrite content has strong effects on the time-depth distribution of oxygen and the total potential of acid production. The maximum concentrations in seepage water are not affected significantly.

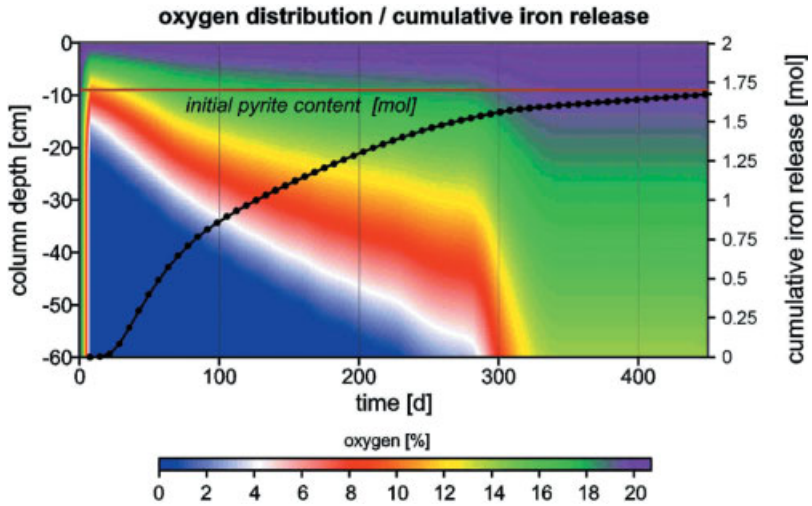


Figure 4.9: Modelled oxygen time-depth distribution and cumulative iron release. Duplication of pyrite content.

### 4.3.6 Field Test

The experience gained from column experiments was transferred to field scale. An approximately 43 year old dump body in the Lower Lusatian lignite district was chosen in order to examine the depyritization that has occurred already, and to predict the potential formation of acid mine drainage that remains. The investigations were carried out south of the residual lake 111 in a tailing of the abandoned open cast lignite mine Plessa, Germany, which has been dumped in 1956/57. In this mine, the world's first conveyor belt bridge was installed in 1929. This mining technique results in a rib structure of the tailings that is typical for the East German lignite-mining district (Klein, 1935). The dewatering of the open pit mine was stopped in 1959, after the mine had been closed in 1958, and the conveyor belt bridge was torn down.

At first, the model was used to predict the position of the depyritization front within the unsaturated zone. With estimates for the pyrite content of the material (mean approximately 1 [wt.%], personal communication) and the effective porosity (approx. 0.3, Hüttl et al., 2000) a first model calculation was executed. The result indicated a depyritization depth of approximately seven meters. In a field test, a well was sunk to a depth of 7.8 m and samples were taken from every meter. In the borehole, an array of optical oxygen sensors was installed with a sensor-to-sensor distance of one meter. After filling the borehole, quasi-stable conditions in oxygen distribution were reached already after 3.5 h (Fig. 4.10). The oxygen concentration decreases from 20.7 % (ambient oxygen) to values of 3–4 % at a depth of 6 to 8 m. The continuous decrease indicates that oxygen consumption at this depth is causing a recharge flux into this layer. The oxygen distribution by itself does not allow the prediction in which zone exactly

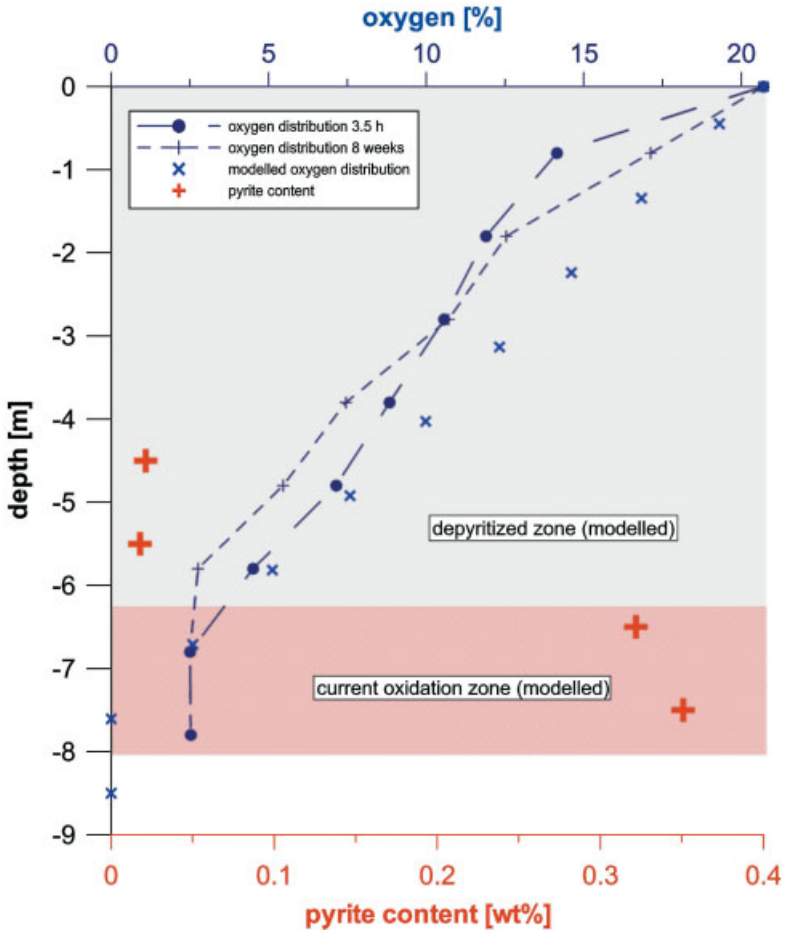


Figure 4.10: Measured oxygen and pyrite distribution in approx. 43 years old pyrite bearing dump body; modelled oxygen distribution, current oxidation zone and depyritization depth.

oxygen consumption takes place (cf. Section 4.3.3). The model conception implemented in DiffMod7 allows the interpretation of the profile regarding its emergence over time and the identification of the current pyrite oxidation zone and the depyritization depth (Fig. 4.10). The measurements immediately after installation of the sensors show that the first prediction of depyritization depth of approx. 7 m is reasonable.

The fact that measured oxygen concentrations do not decrease to zero is not clarified yet. However, the general shapes of the oxygen profiles – especially the parts where gradients change – remain untouched. The second measurement approximately 8 weeks after installation of the sensors revealed that the oxygen depth distribution had not changed significantly (Fig. 4.10). Higher concentrations were found in the uppermost layers. This is probably due to lower microbial activity in the upper soil resulting from lower ambient temperatures (Schachtschabel et al., 1992) during the measure-

ment eight weeks after installation of the sensors (temp. difference: 6 °C). In the lower part of the profile, oxygen concentrations had equilibrated with the surrounding gaseous phase. Oxygen concentrations were constantly low below a depth of 5.8 m. The initial model run could be refined using a better approach to the soil-physic parameters and the measured oxygen concentrations. The resulting modelled oxygen depth distribution matches the measured depth distribution (Fig. 4.10). Soil samples from below 6 m contain significant amounts of pyrite (0.3–0.4 wt.%) whereas the upper layers are pyrite-free (Fig. 4.10). Using the initial and current pyrite distribution data and the current oxygen distribution, the residual oxidation potential of the tailing and the release of reaction products over time may be modelled.

The seepage water concentrations that result from the model calculation are a worst-case prediction, as secondary mineral reactions are not included in DiffMod7. Neglecting buffer reactions does not introduce a great error in this case, because the acid neutralizing capacity of the overburden material is very low.

The processes included in the model calculation seem to be sufficient to explain the observed data, although convective gas transport by groundwater fluctuations, wind pressure, infiltration, air pressure changes as well as variations in temperature are not integrated in the model. This is due to different facts. The sampling point is located in a small forested plain, which is – in contrast to open dumps – not exposed to heavy wind pressure (see Section 4.4). During the operation of the mine, the ground water table was lowered by approximately 20 m. The dewatering was stopped one year after the mine was closed; another nine years later quasi-stable groundwater conditions had been reached (personal communication). At the sample location, groundwater recharge and fluctuations of the water table are small, and flow velocities are low (Hüttl et al., 2000). Thus, significant convective gas movement is not induced by these processes.

## 4.4 Discussion

The simulations presented above indicate that the basic processes of diffusive oxygen recharge and oxygen consumption in systems affected by pyrite oxidation are well implemented in DiffMod7. Some of the processes that have been neglected so far are of minor importance for the simulation results, whereas others should be subject to future improvements of DiffMod7:

There are various processes that induce convective gas transport that have not been considered, yet. Their impact on gas transport in soil is generally low (Wild, 1993). After Mattheß (1991), the proportion of gas exchange in the unsaturated zone that is caused by seepage water movement and subsequent displacement of ground air is in the range of 1/12 to 1/16 of the total gas exchange. Mattheß (1991) gives a value of 1/1000 of the total gas exchange for wind pressure effects in natural systems. Variations in ambient air pressure cause ground air movement. After Farrier and Massmann

(1992), ambient air pressure regionally varies slightly around an average value. The shift of ground air is quickly balanced by diffusive processes. The effects of water table fluctuations are similar to those of air pressure variations.

The time-depth distribution of the reaction products within and below the decomposition zone may be simulated using DiffMod7. Since secondary mineral reactions and adsorption/desorption are not implemented, the maximum extension of the acid plume is predicted. An estimation of the influences of these processes is difficult, as their importance varies depending on the system of interest. The mineralogical composition – especially the distribution of buffer minerals – and the distribution of sorbed matter might have a great influence. There are several alternative ways of extending DiffMod7 in order to be able to investigate these influences. One possibility is to couple the model to a thermodynamic equilibrium model, such as PHREEQC (Parkhurst and Appelo, 1999). Another way is to combine the diffusion/pyrite-oxidation model DiffMod7 with a transport-reaction model, such as CoTReM (Landenberger, 1998; Adler, 2000), that considers geochemical processes and transport of dissolved products. In both cases, it is questionable if the expected additional results will justify the additional computational effort. Secondary processes, such as the formation of iron and sulfate-storing minerals, are known to have a considerable effect on solute concentrations. However, thermodynamic quantification is difficult due to variable compositions of the minerals and the associated varieties of thermodynamic parameters (e.g. schwertmannite (Yu et al., 1999)). As these secondary minerals are usually meta-stable, they cause a retardation of the transport of primary reaction products by temporarily decreasing solute concentrations. Sorption and desorption, as well as reactions with buffer minerals are of minor importance, especially in mature systems. The release of sodium, potassium, calcium, magnesium, etc. from clay mineral exchange sites results in high solute concentrations, whereas the acid neutralizing effect is small. As these components do not impose any direct hazards, their further behaviour is usually of minor interest. The mobilization of heavy metals or the release of large quantities of aluminium is more important, because of their high eco-toxicity. The behaviour of these components in the course of pyrite decomposition may be well predictable without coupled thermodynamic equilibrium calculations, because of the extreme geochemical settings. For accurate predictions of the behaviour of the different reaction products of pyrite decomposition, and for quantification of subsequent processes, separate calculations using thermodynamic equilibrium models are recommended.

The scope of one-dimensional model calculations is limited. Natural and man-made systems are in general characterized by inhomogeneous structures. Therefore the available data is often just valid over short distances. This fact may be met by an extension of the model to a two-dimensional approach. Many systems characterized by pyrite decomposition processes show complex, however regular structures. In dump bodies of lignite open cast mines, in which conveyor belt bridges are used to transport the overburden material to the dump side of the pit, characteristic depositing structures evolve that strongly influence the soil-physical parameters (Hüttl et al., 2000). Repeating nested structures develop perpendicular to the edge of the pit. Due to the temporal sequence of deposition, different zones of the dump body have been exposed to ambient air for different periods of time. Each period of exposal is associated with the evolvement of a new pyrite decomposition front. As a consequence, different incoher-

ent stages of pyrite decomposition can be found within one dump body, but there is only one currently active decomposition front. This situation is accompanied by a complex distribution of reaction products in seepage water. In order to obtain a basic simulation of these processes and their effects, an extension of the available model to a two-dimensional scheme and a better implementation of seepage water movement is necessary. The higher computational effort would be justified by the very valuable additional information on closer-to-reality systems.

## 4.5 Summary

The model gives a good insight into the relations between soil-physical parameters, pyrite decomposition rates, seepage water velocity, time, depth and seepage water concentrations in the context of pyrite decomposition processes in the unsaturated zone. The model runs show that the majority of the relevant processes in the examined systems were identified and implemented appropriately. The soil-physical parameters porosity and tortuosity factor, as well as the initial pyrite content of the material are crucial for the release of acid reaction products. Pyrite grain size and pyrite surface, as well as pyrite oxidation rates, are less important for the overall turnover rates and the release of reaction products. Lower reaction rates and/or a smaller amount of available pyrite surface per volume results in an increased thickness of the reaction zone, while the change in release is small. Referring to lignite open mining dumps, material characterised by low permeability and/or low pyrite content should be dumped in locations where increased exposure time is expected. Once more, it is shown that selective dumping must be suggested.

Deviations between model results and chemical analysis of real systems are particularly due to the fact that an implementation of the associated secondary reactions is missing. The model may easily be enhanced by including several other convective transport processes. Moreover, it is suggested to extend the programme towards two-dimensional calculations, in order to give a more accurate picture of real world systems. However, this implies that base data is available at a sufficient level of accuracy.

The programme DiffMod7 was applied to predict the oxygen penetration depth and the associated depyritization depth of a 43 year old dump body. In situ measurements of the oxygen distribution and the determination of pyrite contents within the dump body supported the model results.

One advantage of the model is its ability to run different scenarios to see the effects of different parameter modifications, supporting almost instantaneous graphical feedback. This way, different strategies to prevent or decrease the formation of acid mine drainage may be evaluated and compared.

# 4.6 References


Adler, M. (2000): Modelling of one-dimensional transport in porous media with respect to simultaneous geochemical reactions in CoTRem. *Ber. FB Geowiss. Univ. Bremen* **166**.

Appelo, C. A. J.; Postma, D. (1994): Geochemistry groundwater and pollution, A. A. Balkema, Rotterdam.

Berner, R. A. (1980): Early Diagenesis: A Theoretical Approach, Princeton Univ. Press, Princeton.

Boudreau, B. P. (1997): Diagenetic Models and Their Implementation – Modelling Transport and Reactions in Aquatic Sediments, Springer-Verlag, Berlin/Heidelberg.

Carman, P. C. (1937): Fluid flow through a granular bed. *Trans. Inst. Chem. Eng.* **15**, 150–156.

Davis, G. B.; Ritchie, A. I. M. (1986): A model of oxidation in pyritic mine wastes 1 – Equations and approximate solution. *Appl. Math. Modell.* **10**, 314–322.

Evangelou, V. P. (1995): Pyrite oxidation and its control, CRC Press Inc., Boca Raton, Florida.

Farrier, D. F.; Massmann, J. (1992): Effects of atmospheric pressure on gas transport in the vadose zone. *Water Resour. Res.* **3**, 777–791.

Friedrich, G.; Dohrmann, R.; Jochum, J.; Echle, W.; Wiechowski, A.; Lang, R.; Riebeiro-Rodrigues, L. C. (1999): Mineralinhalt und Spurenelementverteilung im Neurather Sand – Ihre Bedeutung für die Freisetzung umweltrelevanter Metalle beim Braunkohleabbau im Niederrheinischen Revier. *Z. angew. Geol.* **45**(1), 37–48.

Gerke, H. H.; Molson, J. W.; Frind, E. O. (1998): Modelling the effect of chemical heterogeneity on acidification and solute leaching in overburden mine spoils. *Journal of Hydrology* **209**, 166–185.

Grathwohl, P. (1998): Diffusion in natural porous media: Contaminant Transport, Sorption/Desorption and Dissolution Kinetics, Kluwer Academic Publishers, Bosten/Dordrecht/London.

Hecht, H.;Kölling, M. (accepted): Investigation of pyrite weathering processes in the vadose zone using optical oxygen sensors. *Environmental Geology*.

Holst, G.; Kühl, M.; Klimant, I. (1995): A novel measuring system for oxygen micro-optodes based on a phase modulation technique. *Proc. SPIE* **2508**(45), 387–398.

Hüttl, R. F.; Weber, E.; Klem, D. (Eds.) (2000): Ökologisches Entwicklungspotential der Bergbaufolgelandschaften im Niederlausitzer Braunkohlerevier, B. G. Teubner, Stuttgart/Leipzig/Wiesbaden.

Klein, G. (1935): Handbuch für den deutschen Braunkohletagebau, Verlag W. Knapp, Halle/Saale.

Kölling, M. (1990): Modellierung geochemischer Prozesse im Sickerwasser und Grundwasser. Beispiel: Die Pyritverwitterung und das Problem saurer Grubenwässer. *Ber. FB Geowiss. Univ. Bremen* **8**.

Landenberger, H. (1998): CoTReM, ein Multi-Komponenten Transport- und Reaktions-Modell. *Ber. FB Geowiss. Univ. Bremen* **110**.

Mattheß, G. (1991): Lehrbuch der Hydrogeologie. Band 2: Die Beschaffenheit des Grundwassers, Gebr. Borntraeger, Berlin/Stuttgart.

Mitchell, A. R.; Griffiths, D. F. (1980): The Finite Difference Method in Partial Differential Equations, Wiley, Chichester.

Nordstrom, D. K. (1982): Aqueous pyrite oxidation and the consequent formation of secondary iron minerals. In: Acid sulfate weathering: Pedogeochemistry and Relationship to Manipulation of Soil Materials (Eds.:Kittrick, J. A.; Fanning, D. F.; Hossner, L. R.), Soil Sci. Soc. of America, Madison, Wisconsin. pp. 37–56.

Parkhurst, D. L.; Appelo, C. A. J. (1999): PHREEQC (Version 2) – A computer program for speciation, batch-reaction, one-dimensional transport and inverse geochemical calculations. Water-Resources Investigations Report 99–4259, U.S. Department of the Interior, U.S. Geological Survey, Denver, Colorado.

Prein, A. (1994): Sauerstoffzufuhr als limitierender Faktor für die Pyritverwitterung in Abraumkippen von Braunkohletagebauen. *Mitteilungen, Institut für Wasserwirtschaft, Hydrologie und Landwirtschaftlichen Wasserbau der Universität Hannover* **79**.

Puura, E.; Neretnieks, I.; Kirsimäe K. (1999): Atmospheric oxidation of the pyritic waste rock in Maardu, Estonia – 1. field study and modelling. *Environmental Geology* **39**(1), 1–19.

Schachtschabel, P.; Blume, H.-P.; Brümmer, G.; Hartge, K.-H.; Schwertmann, U. (1992): Scheffer/Schachtschabel: Lehrbuch der Bodenkunde, Ferdinand Enke Verlag, Stuttgart.

Schulz, H. D. (2000): Quantification of Early Diagenesis: Dissolved Constituents in Marine Pore Water. In: Marine Geochemistry (Eds.: Schulz, H. D.; Zabel, M.), Springer-Verlag, Berlin/Heidelberg, pp. 85–128.

Schulz, H. D.; Reardon, E. J. (1983): A combined mixing cell/analytical model to describe two-dimensional reactive solute transport for unidirectional ground water flow. *Water Resour. Res* **19**, 493–502.

Volkov, I. I.; Zhabina, N. N. (1977): Determination of Pyritic Sulfur with Metallic Chromium and Chromium (II) Solution. In: Chemical Analysis of Marine Sediments (Ed.: Ostroumov, E. A.), Nauka, Moscow, pp. 5–14.

Wild, A. (1993): Soil and the environment: an introduction, Cambridge Univ. Press, Cambridge.

Wunderly, M. D.; Blowes, D. W.; Frind, E. O.; Ptacek, C. J. (1996): Sulfide mineral oxidation and subsequent reactive transport of oxidation products in mine tailings impopundments: A numerical model. *Water Resour. Res.* **32**, 3173–3187.

Xu, T.; White, S. P.; Preuss, K. ; Brimhall, G. H. (2000); Modeling of Pyrite Oxidation in Saturated and Unsaturated Subsurface Flow Systems. *Transport in Porous Media* **39**, 25–56.

Yu, J.-Y.; Heo, B.; Choi, I.-K.; Cho, J.-P.; Chang, H.-W. (1999): Apparent solubilities of schwertmannite and ferrihydrite in natural stream waters polluted by mine drainage. *Geochim. Cosmochim. Acta* **63**(19/20), 3407–3416.

# 5 Speciation and Sorption for Risk Assessment: Modelling and Database Applications

Vinzenz Brendler*, Thuro Arnold, Sture Nordlinder, Harald Zänker and Gert Bernhard

## Abstract

The paper summarizes efforts started to deliver a profound chemical base for risk assessment, namely to properly take into account the physico-chemical phenomena governing the contamination source term development in time and space. One major aspect there is the substitution of conventional distribution coefficients ($K_d$ values) for the empirical description of sorption processes by surface complexation models, in combination with other thermodynamic concepts. Thus, the framework of a "Smart $K_d$" is developed for complex scenarios with a detailed explanation of the underlying assumptions and theories. It helps to identify essential processes and the associated most critical parameters, easing further refinement studies. The presented case studies cover a broad spectrum of contamination cases and successfully demonstrate the applicability of the methodology. The necessity to create a mineral-specific sorption database to support the "Smart $K_d$" approach is derived and a first prototype for such a digital database introduced, combining numeric data with a knowledge base about the relevant theories, experimental methods, and structural information.

## 5.1 Introduction

World-wide activities focus on the remediation of radioactively contaminated sites. Part of such efforts were projects funded by the DFG (Deutsche Forschungsgemeinschaft): "Characterization of colloidal particles in drainage systems of abandoned Saxonian mines" and "Investigation of mechanisms of uranium(VI) sorption onto rock and mineral surfaces. Identification and modelling of sorbed surface species on a molecular level" and funded by the EC: "Restoration Strategies for radioactively contaminated sites and their close surroundings". One common aim was to deliver a more pro-

*Institut für Radiochemie, Forschungszentrum Rossendorf e. V., Postfach 51 01 19, 01314 Dresden; e-Mail: brendler@fz-rossendorf.de



*Geochemical Processes: Conceptual Models for Reactive Transport in Soil and Groundwater. Research Report.* Deutsche Forschungsgemeinschaft (DFG).
 ISBN: 978-3-527-27764-3

found chemical base for risk assessment, namely to properly take into account the physico-chemical phenomena governing the contamination source term development in time and space. This requires to extend the knowledge about these phenomena and the underlying basic processes and interactions to finally allow a better integration of chemical speciation into existing risk assessment codes. Major parts of this paper originate from those projects.

## 5.2 Geochemical Speciation and Sorption

A contaminant can occur in many different forms in an environmental compartment, each of them having different mobility, transfer coefficients to and between living matter, and even toxicity. This variety of existing forms for a given element is termed chemical speciation, defined as the distribution of one or more elements between all its possible species[1] (distinct chemical entities) in a given system[2]. It should be noted that the term "speciation" is also used in another context to describe all the experimental methods applied to investigate the above discussed species distribution.

Species distributions determine whether a contaminant is mainly a mobile component – and thus easily transported and taken up – or is immobilized through precipitation or adsorption onto a surface. Therefore, changes in speciation can either accelerate or slow down radionuclide migration. Moreover, speciation also strongly influences the degree of transfer between the environment and living systems, the distribution of contaminants inside organisms, and their biological consequences. Physico-chemical processes affecting the speciation are listed below. Their importance may vary, so the order should not be considered a ranking:

- radioactive decay,
- complexation reactions (with organic and inorganic ligands) through:
  - hydrolysis
  - dissociation
  - association/polymerization
  - oxidation state changes/redox reactions
- precipitation and dissolution of solid phases,
- co-precipitation (inclusion and surface precipitation) of trace components,
- physical and chemical sorption onto mineral surfaces or colloids,
- formation of solid solutions (mixed mineral phases),

[1] Simple ions or neutral molecules, ion pairs, associates, complexes, hydrolysis products, pure minerals, solid solutions, gases, surface complexes.
[2] Aqueous solution in contact with all solid phases and the gas phase, maybe also other fluid phases (organics), colloids and aerosols.

- ion exchange,
- extraction (in case of several fluid phases),
- formation of colloids,
- formation of aerosols,
- processes involving biological material, such as biosorption, biologically catalyzed redox reactions, enzymatic reactions, metabolisms.

The various processes listed above can be described quantitatively by their respective functional terms, each requiring a unique set of parameters. Fortunately, many parameters are used simultaneously for many or all of the above reactions, like temperature or concentrations. In general, the parameters can be divided into system-specific parameters (subdivided into the stationary state and the dynamic evolution) and into reaction-specific parameters. Many of these parameters also depend on the chemical or physical models applied to the system. The resulting very complex pattern usually has to be simplified when it comes to integrated modelling exercises of contaminant reaction paths and migration, based on coupled transport codes.

Whereas the simplest (and older) sorption models do not distinguish between the basic processes contributing to the overall sorption, newer model approaches try to address all relevant processes separately, namely physisorption, chemisorption, co-precipitation, inclusion, diffusion, surface-precipitation, or the formation of solid solutions. Sorption models in a strict sense are usually grouped into two classes, the phenomenological models, and the surface complexation models.

Phenomenological adsorption models comprise different flavours of the afore mentioned distribution coefficient ($K_d$) model. The $K_d$ framework is built on the concept of distribution (or retardation) coefficients. This is defined as the experimentally determined ratio of the sorbed (fixed, immobilized) and unsorbed (free, truly dissolved) fraction of a component (chemical element) under equilibrium conditions.

Sorption isotherms at constant pH (most often used types are Langmuir, Freundlich, and Frumkin) are a step toward a more realistic description of surface phenomena, expressing the $K_d$ as a function of sorbent concentration. Their to the best semi-empirical foundations allow them to be rather simple in terms of defining equations and amount of model parameters. Of course this often does not reflect reality with the necessary accuracy, so their usefulness is restricted to only a few cases.

Up to now, the physico-chemical phenomena were considered in risk assessment (if at all) by applying distribution coefficients ($K_d$) in order to model the distribution of a contaminant between solid and aqueous phases. It follows a discussion of the shortcomings of such a model and how it could be improved.

### 5.2.1 The Concept of "Smart $K_d$"

In the literature there are many attempts to describe the interactions between ions in solution and a mineral surface in contact with them. The resulting interactions can be grouped into various phenomena, such as physisorption, chemisorption, co-precipitation, inclusion, diffusion, surface-precipitation, or even formation of solid solutions.

The subsuming of many physico-chemical processes into one parameter is a severe weakness of the $K_d$ principle (Hayes et al., 1991; Puigdomenech and Bergström, 1994; Wilhelm and Beam, 1999). Distribution coefficients are very difficult to measure with a good precision and accuracy. Literally by definition, because of their incorporation of very different basic physico-chemical phenomena, they are dependent on so many parameters that even slight changes in one system parameter (say the $E_H$ or the content of a major cation, or the occurrence of a new mineral phase, etc.) can drastically change the distribution coefficient. To measure the effect of all combinations of these parameters is impossible. That means, all $K_d$ values used nowadays in risk assessment or other prognostic studies are just snapshots for specific locations of the site, valid only for the time of the measurement. This in turn assigns them very large uncertainties.

A much better strategy is the decomposition of the $K_d$ value into the main basic processes defining it. Such an approach will unfold the single value $K_d$ into a vector of parameters, such as $E_H$, pH, concentrations of the various components, binding site densities, surface areas, and temperature. Apparently this is a step backwards. But it has the great advantage that all these parameters can be measured with more reliability and precision. Knowing the functional relationships between these processes and how they contribute to the $K_d$ allows a computation of $K_d$ rather than a measurement. Moreover, simulations with variable parameter values, even for hypothetical conditions, may easily yield a $K_d$ surface as a function of the "primary" parameter vector: $K_d = \boldsymbol{f}(E_H, pH, p_{CO2}, T, ...)$. Usually, the function $\boldsymbol{f}$ can not be expressed as an explicit function but contains implicit formulations only accessible through numeric iterations. Also, some long-term effects that can render conventional distribution coefficients meaningless (co-precipitation, diffusion of the trace element into crystal lattices ) can be accounted for in a better way. Another application is expressing $K_d$ as a function of time, related to better-defined time dependencies of other basic parameters. Furthermore, it becomes possible to identify those parameters affecting the $K_d$ strongest. Consequently, extra measurements can be designed efficaciously to reduce the $K_d$ uncertainty. And last but not least the formal keeping of the used $K_d$ paradigm renders it easy to couple a "smart $K_d$" framework with already existing contaminant transport and risk assessment codes, enhancing its acceptance.

Applications of simple variants of such an approach have already been proved successfully (Tessier et al., 1996). Further example cases will be given in the following paragraphs of this chapter.

The unfolding of $K_d$ values leads to modern concepts that treat surface reactions as complexation reactions analogous to such reactions in homogeneous aqueous solutions. Therefore these models are called Surface Complexation Models (SCM), for details refer to, e.g., Stumm, 1992. This requires the definition of surface sites with a finite concentration. Usually such surface sites are represented as SOH-groups with S denoting a metal from the solid structure, located at the solid-liquid interface. Many mineral surfaces, but especially colloids carry a significant surface charge, creating an electrostatic potential extending into the aqueous solution. To account in a proper way for this charge effect, additional terms have been introduced into adsorption models, modifying the activity of sorbate ions. These terms describe the electrical work necessary to penetrate the zone of electrostatic potentials, resulting in a difference between

the activity of ions $\mathbf{M_s}$ with the charge $z^+$ near the surface and the same ions **M** in the bulk solution.

The main models used at present are sorted here according to the increasing number of required electrostatic model parameters:

- The Diffuse Double Layer Model (DDL) (Stumm et al., 1970; Dzombak and Morel, 1990): Here, the total charge of the double layer is defined as a function only of charge and ionic strength. Thus, an important advantage of this rather simple approach is, that there are no electrostatic parameters required at all. This reduces data needs and consequently data uncertainty.

- The Constant Capacitance Model (CC) (Schindler and Gamsjäger, 1972): The constant capacitance model assumes only one layer or plane between surface and bulk solution. All specifically adsorbed ions contribute to the surface charge in this layer. Actually, this model is just a special case of the diffuse layer model for solutions of higher ionic strength ($I > 0.01$ mol/L) and surfaces of low potential. It is strongly dependent on the ionic strength, and requires one electrostatic parameter, the capacity **C**.

- The Triple Layer Model (TL) (Yates et al., 1974; Davis et al., 1978): Two different planes are assumed for the surface: The innermost or o-plane does only incorporate protonation or deprotonation of surface sites. All other specifically adsorbed ions are assigned to the outer or b-plane. Therefore, each plane has its own charge and potential. The third layer (to justify the name of the model) is as in the above models the diffuse layer. In summary, this would give two electrostatic parameters (Capacities $\mathbf{C_1}$ and $\mathbf{C_2}$), but to reduce further the number of variable model parameters, $\mathbf{C_2}$ is generally fixed to 0.2, whereas $\mathbf{C_1}$ is a fitting parameter inside a range between 0.1 and 2.0, which is supported by theoretical considerations.

- The Non-Electrostatic (NE) surface complexation model (Davis et al., 1998; Stumm et al., 1976): This is the simplest approach, neglecting any contributions from electrostatic interactions. The sorption is considered to be purely chemical, thus only reaction constants serve as fitting parameters.

An extension in principle applicable to every model is the concept of strong and weak binding sites according to Dzombak and Morel, 1990, and the 1-pK approach by Bolt and Van Riemsdijk, 1982.

#### 5.2.1.1 Application Case: Sorption onto Rocks

The SCM concept combined with a powerful sorption database allows a straightforward extension towards rocks and soils composed of several minerals. Their sorption behaviour should be predicted from the weighted superposition of the sorption processes for all constituting minerals. The number of important rock-forming minerals is rather limited, more then 95 % of the known rocks in the earth's crust consist of only about 20 minerals and mineral groups (Ronov and Yaroshevsky, 1967). Thus we hypothesized that the sorption behaviour of uranium(VI) onto rocks can be described

in an additive fashion based on the sorption onto its mineralogical components and onto possibly forming secondary minerals. To verify this hypothesis, we carried out a large number of batch sorption experiments with uranium(VI), acid base titration, and adsorption isotherms with phyllite, quartz, chlorite, muscovite, albite, and ferrihydrite. Furthermore, we probed for the possible formation of secondary Fe phases by Mössbauer spectroscopy and centrifugation experiments. A detailed description of the experimental conditions is given in Arnold et al., 2001.

The studied phyllite is composed of 48 vol.% quartz, 25 vol.% chlorite, 20 vol.% muscovite, 5 vol.% albite feldspar, and 2 vol.% opaque material, mostly rutile, magnetite, and traces of hematite. The basis for the successful interpretation of the experimental sorption data of uranium(VI) on phyllite were:

- the determination of surface complex formation constants of uranium(VI) with quartz, chlorite, muscovite, albite, and ferrihydrite in individual batch sorption experiments, shown in Table 5.1,
- the determination of surface acidity constants of quartz, chlorite, muscovite, and albite, obtained from separate acid base titration (Arnold et al., 2001; Zorn, 2000),
- the determination of surface site densities of quartz, chlorite, muscovite and albite evaluated independently of each other with adsorption isotherms and
- the quantification of the secondary phase ferrihydrite, which formed during the batch sorption experiments with phyllite.

The surface complex formation constants and the protolysis constants were optimized by using the experimentally obtained data sets and the computer code FITEQL (Herbelin and Westall, 1996). Surface site densities were evaluated from adsorption isotherms at pH 6.5 and a total uranium concentration of $1\times10^{-4}$ M. The formation of ferrihydrite during the batch sorption experiment was identified by Mössbauer spec-

Table 5.1: Surface complex formation constants (I = 0) of uranium(VI) with mineralogical components of phyllite. Values are taken from Arnold et al., 2001 (Reference A) and Waite et al., 1994 (Reference B).

| Mineral | Reaction | log K | Reference |
|---|---|---|---|
| Quartz | $X(OH)_2 + UO_2^{2+} = (XO_2UO_2) + 2H^+$ | –5.51 | A |
| Chloride | $XOH + UO_2^{2+} = (XO^-UO_2^{2+}) + H^+$ | 4.71 | A |
| Muscovite | $X(OH)_2 + UO_2^{2+} = (XO_2UO_2) + 2H^+$ | –0.55 | A |
| | $XOH + UO_2^{2+} = (XO^-UO_2^{2+}) + H^+$ | –5.75 | A |
| Albite | $XOH + UO_2^{2+} = (XO^-UO_2^{2+}) + H^+$ | 1.54 | A |
| Ferrihydrite | $Fe_s(OH)_2 + UO_2^{2+} = Fe_sO_2UO_2 + 2H^+$ | –3.18 | A |
| | $Fe_s(OH)_2 + UO_2^{2+} = Fe_sO_2UO_2 + 2H^+$ | –6.31 | A |
| | $Fe_s(OH)_2 + UO_2^{2+} + CO_3 = Fe_sO_2UO_2CO_3 + 2H^+$ | 3.67 | B |
| | $Fe_s(OH)_2 + UO_2^{2+} + CO_3 = Fe_sO_2UO_2CO_3 + 2H^+$ | –0.42 | B |

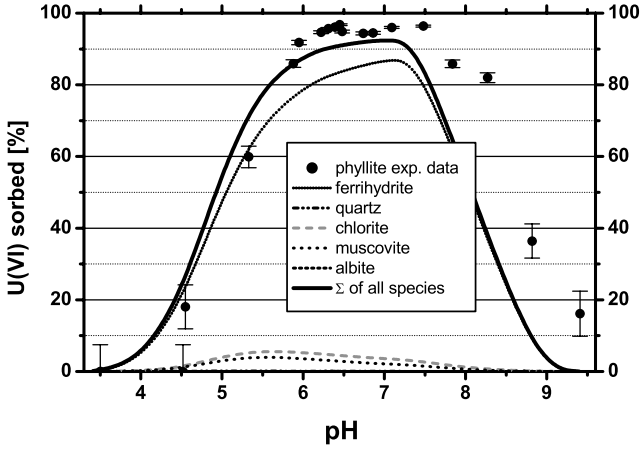


Figure 5.1: Modelled uranyl(VI) sorption on phyllite and its components together with experimental uranyl(VI) sorption data on phyllite.

troscopy, showing a 2.8 percent increase of $Fe^{3+}$ in the phyllite powder. The newly formed ferrihydrite was present as Fe nano-particles or agglomerates with diameters ranging from 6–25 nm.

FITEQL calculations were carried out for a composite phyllite which was constructed from the respective mineral components quartz, chlorite, muscovite, and albite in their relative proportion within the phyllite, and in addition with the newly forming phase ferrihydrite.

Figure 5.1 shows the modelled sorption curve together with the experimental sorption data of phyllite. It is noteworthy that the calculated sorption curve of the phyllite is based exclusively on surface complex formation and surface acidity constants obtained from individual batch experiments with pure mineral phases. No experimental data of phyllite were used for the optimization procedure. The modelling of the associated aqueous phase speciation of uranium(VI) was based on the recommended NEA data set (Grenthe et al., 1992).

The modelling indicated that uranium(VI) sorption to ferrihydrite clearly dominates the uranium(VI) sorption on phyllite showing the great importance of secondary iron phases for sorption studies.

### 5.2.1.2 Application Case: Colloids in Mines

Geochemical modelling including surface complexation were used to interpret observations of pH dependence of the distribution of uranium in complex water samples from the mine gallery “Rothschönberger Stolln” at Freiberg/Saxony. The major obstacle is the lack of an appropriate sorption database covering all occurring elements in good quality.

Risk assessment studies and the planning of restoration measures for contaminated water supplies have to rely on conservative assumptions on the mobility of the

potentially hazardous compounds. In many cases this is not only determined by solubility products and the complexation in the aqueous phase, but also by migration pathways in colloidal form, either pseudo- or eigencolloids. This study will explore to which degree such phenomena observed on water samples from the "Rothschönberger Stolln" mine drainage gallery in Freiberg/Saxony can be explained by surface complexation models (SCM). The respective analytical results and the colloid characterization (mainly hydrous ferric oxide – ferrihydrite) were presented in previous articles by Zänker et al., 2000.

The MINTEQA2 (Allison et al., 1991) geochemical speciation software was used for the modelling. From the various data sets available in the literature, only two, both based on the Diffuse Double Layer Model (DDL), incorporate uranium(VI) surface species. The first one originates from Dzombak and Morel, 1990, where the uranium(VI) surface species is not correctly described (Scenario 1), sorption of carbonate is missing and no ternary uranium–carbonate-surface species are included. The second one was published by Arnold et al., 1998 (Scenario 2) and is lacking data for competing sorption reactions of the other major solution components. To discriminate the effects caused by the binary and ternary carbonate surface species, in a third scenario the data set from Dzombak and Morel, 1990 has been stripped off of all reactions containing ions other than uranium. The idea of a combined database from Dzombak and Morel, 1990 and Arnold et al., 1998 has to be abandoned due to different surface site densities (SSD) and surface protolysis constants applied in the two basic data sets, rendering them mutually inconsistent.

From the species distribution between colloids and aqueous phase shown in Fig. 5.2 it is obvious that the analytical determined distribution is not properly reflected by the modelling results. This can have several reasons:

- In the acidic range (pH 3–5), all data sets heavily underestimate the effect of sorption. Even a tenfold increasing of the surface site densities did not reverse this effect, so the reason must be some missing (ternary?) surface complexes of uranium. There are enough free surface sites available, see Fig. 5.3.
- At the highest investigated pH, the inclusion of ternary uranyl–carbonate surface species overcompensates the carbonate sorption in Arnold et al., 1998 and yields too much sorption. Most probably a strong competing surface species is missing.
- The addition of competing surface reactions in Dzombak and Morel, 1990 for the other major cations in solution reduces the uranium(VI) sorption too much. The same effect transferred to the data from Arnold et al., 1998 would also give too strong a reduction in uranium(VI) sorption. A closer look on the speciation shows that mainly lead and zinc bind to the strong binding sites, but the weak binding sites are occupied only to a small amount, similar to Fig. 5.3.

This work very distinctly demonstrates the need for comprehensive and consistent sets of SCM data when real-world scenarios with their complexity of chemical interactions have to be modelled. The last parts of this chapter will address this issue again.

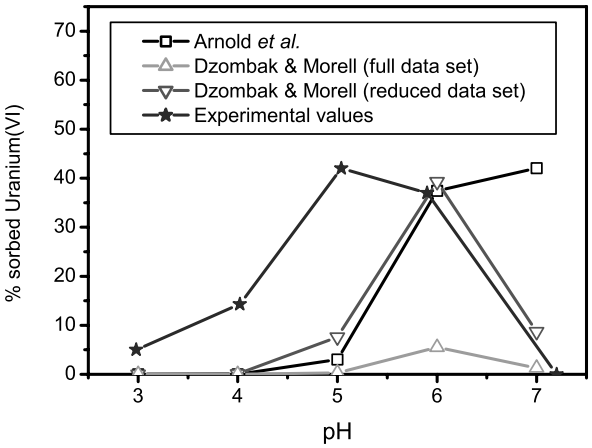


Figure 5.2: Comparison of experimentally determined uranium sorption onto hydrous ferric oxide colloids from the gallery "Rothschönberger Stolln" with various speciation models.

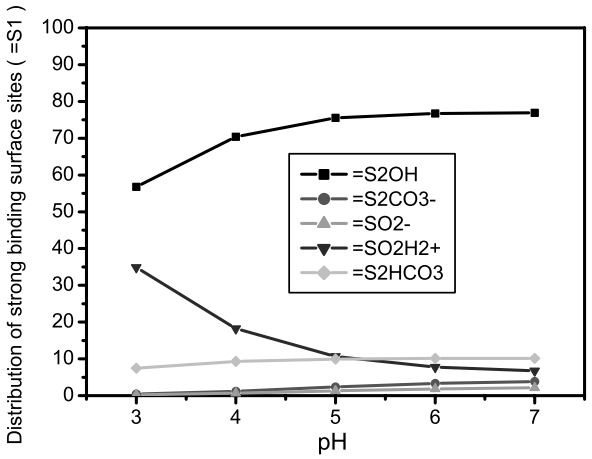


Figure 5.3: Distribution of strong surface binding sites of hydrous ferric oxide colloids.

### 5.2.1.3 Application Case: Uranium Migration

An EU project "**RE**storation **STRAT**egies for radioactively contaminated sites and their close surroundings – RESTRAT" (Zeevaert et al., 2001) developed a generic methodology for ranking of restoration techniques. The risk assessment model used for RESTRAT is based on two programmes:

(1) PRISM (Gardner et al., 1983) as outer shell performs uncertainty analysis, using the Latin Hypercube Sampling for input parameters, allowing arbitrary parameter distributions and correlations;

(2) BIOPATH (Befrgström et al., 1982) computes the contaminant transport in geo- and biosphere based on compartment theory, and the subsequent radiological doses to critical groups. It applies first order differential equations for kinetics.

A realization of this concept requires the integration of a geochemical speciation programme, such as MINTEQA2 (Allison et al., 1991), into the risk assessment code PRISM/BIOPATH. Thus, our strategy was as follows: Leaving the original codes for both risk assessment and chemical speciation mainly unchanged, an interface was created to connect them, together with software to handle the input setup. MINTEQA2 covers all chemical reactions in homogeneous aqueous solutions, including redox reactions, handles precipitation and dissolution equilibria, and incorporates surface complexation models (SCM) for the most important sorption process (Dzombak and Morel, 1990). MINTEQA2 delivers a computed $K_d$ whenever required, see Fig. 5.4 for the internal flow of information and the relationships between the various software modules.

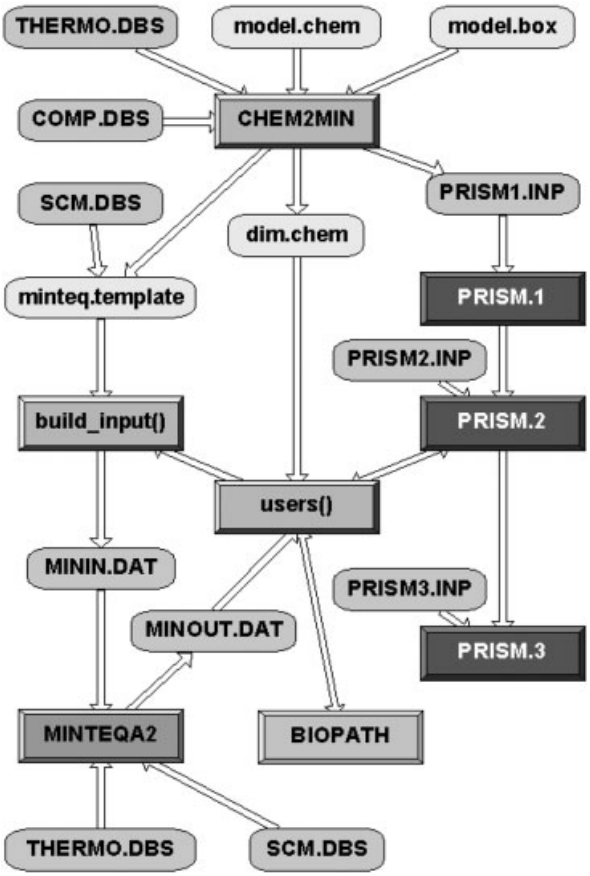


Figure 5.4: Data flow between PRISM, BIOPATH and MINTEQA2 in the coupled model. Rectangular boxes are programme modules, rounded boxes are data files.

The chemical model is defined in a separate file that must be written by the user. It creates the input file for PRISM and a template for the speciation code, assuring a model description consistent for all parts of the modelling. The input file has a well defined, line-oriented structure. Detailed chemical data for each compartment includes the selected SCM with its intrinsic surface parameter, also pH, $E_H$ and the concentrations for all components. Default reaction constants (for complexation, precipitation/dissolution, sorption) can be modified, and reactions can also be suppressed totally.

The first application of the new model approach was to the Ranstad Tailing site in Sweden, a former uranium milling facility. Figures 5.5 and 5.6 illustrate the derivation of a compartmental structure for this site. The tailing layer (**T**) is situated above a moraine layer (**M**) and a limestone layer (**L**). It is surrounded by a collecting ditch that

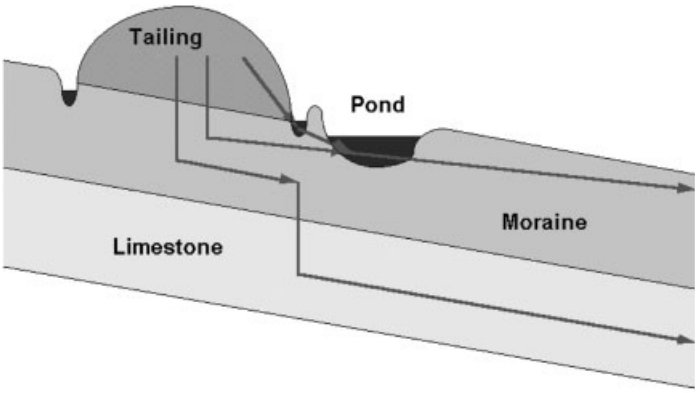


Figure 5.5: Schematic cut through the Ranstad Uranium Mill Tailing Site showing major water pathways.

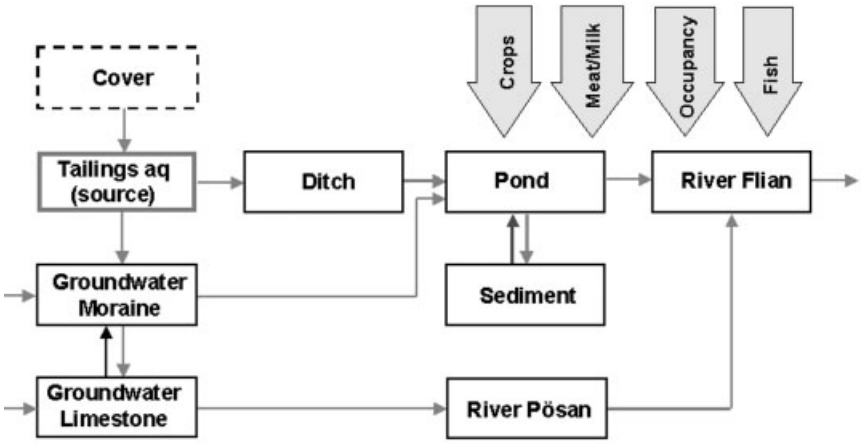


Figure 5.6: BIOPATH compartment structure for the Ranstad Site, together with the major contamination pathways for uranium.

drains into a storage pond (**P**) and then into a river. Additionally, both moraine and limestone layers are aquifers. The main contaminant is uranium.

Samples from the site contained considerable amounts of freshly precipitated iron hydroxides. Their transformation into thermodynamically more stable minerals such as goethite or hematite has a very slow kinetics, thus ferrihydrite was chosen as the major adsorbing surface. The Diffuse Double Layer model (Dzombak and Morel, 1990) was selected to describe surface complexation. The respective intrinsic surface parameters and the reaction constants for the ions competing with uranium(VI) for sorption sites were taken from a database mainly based on Dzombak and Morel, 1990, with the uranium(VI) sorption parameters as determined by Dicke and Smith, 1996. The results, based on runs with 1000 varied parameter sets, are summarized in Table 5.2.

As expected, all $K_d$ values exhibit a clear lognormal distribution. The calculated distribution coefficients ($K_d$ values) for all contaminants fall well into the range used so far for the modelling of the sites (Puigdomenech and Bergström, 1994), but exhibit much smaller uncertainties. Moreover, those parameters were identified contributing most to the uncertainty of the various computed $K_d$ values: pH, the carbonate content $C_{HCO3-}$, and the solid concentration $C_{solid}$. The first two parameters determine the contaminant speciation in solution, controlling the amount of hydrolysis species and carbonate complexes that reduce the respective sorbed portion. The uncertainty in the solid concentration is mainly assigned to the sediment composition (ferrihydrite content), but in case of aquifers it reflects also the uncertainty of the rock porosity. Also the portion of rock which is not accessible to sorption processes inside the various layers is not well known.

These results for the Ranstad Tailing (Sweden) prove the applicability of the concept of unfolding the $K_d$ and its software implementation. As a next step, the variation of the $K_d$ due to the time-dependence of its determining parameters will be included. The established database of mineral specific surface complexation parameters will be steadily expanded, combined with an increased user-friendliness and flexibility. Exhaustive information is available on the internet under: http://www.fz–rossendorf.de/RESTRAT/.

Table 5.2: Computed $K_d$ values for the Ranstad Tailing site compartments (for abbreviated compartment labels see text) with the major uncertainty factors and how they contribute to the overall uncertainty.

| Compartment | $K_d \pm s$ | 1st Factor | 2nd Factor |
|---|---|---|---|
| T | $(2.0\pm0.8) \times 10^{-2}$ | pH: 76.4 % | $C_{solid}$: 11.8 % |
| M | $(5.2\pm1.1) \times 10^{-2}$ | $C_{solid}$: 38.6 % | pH: 34.2 % |
| L | $(3.5\pm1.3) \times 10^{-3}$ | pH: 70.2 % | $C_{solid}$: 18.6 % |
| P | 2.37±0.43 | $C_{solid}$: 50.7 % | pH: 13.2 % |

### 5.2.2 Mineral-Specific Sorption Database

As to the knowledge of the author, there is no digital thermodynamic database for surface complexation equilibria existing world-wide, despite the vast amount of available data. This induces several severe drawbacks:

- There is a lack of systematic screening and filling of data gaps.
- Only rarely critical reviews of alternative (and sometimes mutually excluding) data sets exist. Consequently, no broadly accepted set of recommended values exists, complicating comparisons of sorption experiments or modelling results.
- Every sorption problem relies on its own case-specific and often incomplete or inconsistent data set.
- Only very few of the abundant surface complexes proposed in the literature (mostly resulting just from best-fit considerations) are actually validated by spectroscopic evidence or supported by theoretical (quantum-chemical) calculations.

Therefore, a prototype of a digitized version of a thermodynamic sorption database has been implemented as a relational database with MS Access: "RES$^3$T – Rossendorf Expert System for Surface and Sorption Thermodynamics". It is mineral-specific and can therefore also be used for additive models of more complex solid phases such as rocks or soils. An integrated user interface helps users to access selected mineral and sorption data, to extract internally consistent data sets for sorption modelling, and to export them into formats suitable for other modelling software.

The data records contain information about:

- chemical ligands which can be both inorganic or organic ones: constituting elements, stoichiometry, charge, radius, redox state, molar mass;
- minerals: names (official and trivial ones), formula, density, molar mass, reaction paths (aging, weathering, secondary phase formations) with chemical equation, thermodynamic and kinetic constants;
- mineral surface properties: specific surface area (with associated grain size fraction), point of zero charge;
- surface binding sites: concentration, affinity or coordination type, protolysis constants, applied SCM type, capacitance values, ion exchange capacity;
- surface complexes: species, spectroscopic or theory-based evidence, reaction equation, formation constant, chemical structure.

For any value the used experimental method is stored, together with the respective ionic strength, the background media, and other information necessary to evaluate the data or derive other values. If published, errors for numerical data are included as a prerequisite for sensitivity and uncertainty analysis.

In addition to such "hard" data items an extensive bibliography is provided with both original citations and secondary literature references. The cited literature comprises also model evaluations with respect to theoretical limitations, thermodynamic consistency and parameter sensitivity. Moreover, it covers questions of experimental methods (design, error ranges and application areas) and interpretation of results from sorption experiments. All this means a transition from a pure data collection towards a "smart" database, that finally will turn into a sorption expert system. This is supported by a broad variety of offered user interactions:

- Users can easily extract specific data sets, e.g. all records relevant for the combination of a specific mineral and a specific SCM, or all sorption data available for a certain element, ligand, ion, or all published surface area data of a mineral, with output to screen or printer.
- Data selections can be exported into a file to be used in other geochemical speciation or reactive transport codes. Then, the output format will automatically be adapted to the specific requirements of the different software packages.
- Original bibliographic references can be traced back with access to other parameter sets originating from the same source.
- Each data record has a time stamp and editing remarks. Thus it is easy to reconstruct past data set assemblages at any later time, or to compare alternative data sets for a given scenario.
- The user is supplied with an integrated online help in addition to a printed documentation.

As of April 2002, the database contains 355 specific surface area values, 489 surface site property data sets, and 1168 records for surface complexation reactions for a total of 77 solid phases.

Major future development directions are towards the implementation of a world wide web (www) gateway to allow easy external access to the database via the internet, and towards an automatic data conversion between various units or reaction formulations.

## Acknowledgements

Financial support from the Deutsche Forschungsgemeinschaft under grants DFG ZA 238/1–3 and NI 210/6–1 and from the Nuclear Fission Safety Programme of the European Commission under contract FI4P–CT95–0021a is gratefully acknowledged. Furthermore, we would like to thank our colleagues Torsten Zorn and Yvonne Stiglund for their valuable contributions.

# 5.3 References


Allison, J. D.; Brown, D. S.; Novo-Gradac, K. J. (1991): MINTEQA2/PRODEFA2 Version 3.0 user's manual. U.S. EPA, Environ. Res. Lab., EPA/600/3–91/021.

Arnold, T.; Zorn, T. ;Bernhard, G.; Nitsche, H. (1998): Sorption of uranium(VI) onto phyllite. *Chemical Geology* **151**, 129–141.

Arnold, T.; Zorn, T.; Zänker, H.; Bernhard, G.; Nitsche H. (2001); Sorption behaviour of U(VI) on phyllite: experiments and modeling. *Journal of Contaminant Hydrology* **47**, 219–231.

Bergström, U.; Edlund, O.; Evans, S.; Röjder, B. (1982): Studsvik Energiteknik AB, Report NW–82/261, Nyköping.

Bolt, G. H.; van Riemsdijk, W. H. (1982): In: Soil Chemistry, B. Physico–chemical models (Ed.: Bolt, G. H.), Elsevier, Amsterdam.

Davis, J. A.; Coston, J. A.; Kent, D. B.; Fuller, C. C. (1998): Application of the surface complexation concept to complex mineral assemblages. *Environmental Science and Technology* **32**, 2820–2828.

Davis, J. A.; James, R. O.; Leckie, J. O. (1978): Surface ionization and complexation at the oxide/water interface. I. Computation of electrical double layer properties in simple electrolytes. *Journal of Colloid and Interface Science* **63**, 480–499.

Dicke, C. A.; Smith, R. W. (1996): Surface complexation modeling of uranium adsorption on naturally occurring iron coated sediments, ACS Meeting, New Orleans.

Dzombak, D. A.; Morel, F. M. M. (1990); Surface complexation modeling. Hydrous ferric oxide, Wiley; New York.

Gardner, R. H.; Röjder, B.; Bergström, U. (1983): Studsvik Energiteknik AB, Report NW–83/555, Nyköping.

Grenthe, I.; Fuger, J.; Lemire, R. J.; Muller, A. B.; Nguyen-Trung, C.; Wanner, H. (1992): Chemical Thermodynamics of Uranium, Elsevier, Amsterdam.

Hayes, K. F.; Redden, G.; Ela, W.; Leckie, J. O. (1991): Surface Complexation Models: An evaluation of model parameter estimation using FITEQL and oxide mineral titration data. *Journal of Colloid and Interface Science* **142**, 448–469.

Herbelin, A. L.; Westall, J. C. (1996): FITEQL – A computer programme for the determination of chemical equilibrium constants from experimental data. Version 3.2 Report 96–01, Dep. of Chem., Oregon State University, Oregon.

Puigdomenech, I.; Bergström, U. (1994): SKB Technical Report 94–32, Stockholm.

Ronov, A. B.; Yaroshevsky, A. A. (1967): Chemical structure of the earth's crust. *Geochemistry International* **4**, 1041–1066.

Schindler, P. W.; Gamsjäger, H. (1972): Acid–base reactions of the $TiO_2$(Anatase) – water interface and the point of zero charge of $TiO_2$ suspensions. *Kolloid–Z.Z.Polymere* **250**, 759–763.

Stumm, W. (1992): Chemistry of the solid–water interface, Wiley, New York.

Stumm, W.; Hohl, H.; Dalang, F. (1976): Interaction of metal ions with hydrous oxide surfaces. *Croatica Chemica Acta* **48**, 491–504.

Stumm, W.; Huang, C. P.; Jenkins, S. R. (1970): Specific chemical interaction affecting the stability of dispersed systems. *Croatica Chemica Acta* **42**, 223–245.

Tessier, A.; Fortin, D.; Belzile, N.; DeVitre, R.R.; Leppard, G. G. (1996): Metal sorption to diagenetic iron and manganese oxyhydroxides and associated organic matter: Narrowing the gap between field and laboratory measurements, *Geochimica et Cosmochimica Acta*, **60**, 387–404.

Waite, T.; Davis, J. A.; Payne, T. E.; Waychunas G. A.; Xu, N. (1994): Uranium(VI) adsorption to ferrihydrite: Application of a surface complexation model. *Geochimica et Cosmochimica Acta* **58**, 5465–5478.

Wilhelm, R. G.; Beam, P. (Eds.) (1999): Understanding variation in partition coefficient, $K_d$, values. EPA Report 402–R–99–004A, Washington.

Yates, D. E.; Levine, S.; Healy, T. W. (1974): Site–binding model of the electrical double layer at the oxide/water interface. *Journal of the Chemical Society, Faraday Transactions 1* **70**, 1807–1818.

Zänker, H.; Richter, W.; Brendler, V.; Nitsche, H. (2000): Colloid–borne uranium and other heavy metals in the water of a mine drainage gallery. *Radiochimica Acta* **88**, 619–624.

Zeevaert, T.; Bousher, A.; Brendler, V.; Jensen, P. H.; Nordlinder, S. (2001): Evaluation and ranking of restoration strategies for radioactively contaminated sites. *Journal of Environmental Radioactivity* **56**, 33–50.

Zorn, T. (2000): Untersuchungen der Sorption von Uran(VI) an das Gestein Phyllit zur Bestimmung von Oberflächenkomplexbildungskonstanten (Investigations of the sorption of uranium(VI) onto the rock phyllite to determine surface complex formation constants) PhD Thesis, Technical University Dresden (in German).

# 6 New Geochemical Simulator Rockflow-RTM: Development and Benchmarking

Abderrahamne Habbar*, Olaf Kolditz and Werner Zielke

## Abstract

A number of environmentally relevant problems require the analysis of reactive contaminant transport in subsurface systems, e.g. disposal of hazardous waste in rock formations or infiltration of leachates from landfills. Biological degradation or radioactive decay are transformation processes that may play an important role in the prediction of the migration of subsurface contaminants. Understanding this transformation processes can be important for the design of a permeable reactive barrier (treatment walls) or for the prediction of contaminant migration in the environmental system. This paper deals with the transport of chemically reactive components in porous and fractured media. We investigate transport processes where chemical reactions occur either under equilibrium or under nonequilibrium conditions. Especially the problem of radionuclide chain decay and the problem of the degradation of some organic contaminants will be treated here. The mathematical description of reactive transport processes is given in a set of linear/nonlinear partial differential equations, which are discretized by using the finite element method in combination with different time-stepping schemes. The new finite element (FE) kernels RTM (Reactive Transport Modul) for the numerical simulation of reactive transport processes is embedded in the more general simulator Rockflow. We present benchmark studies for the verification of the numerical code. Further, nitrification and trichloroethylene desintegration reactions as transformation processes are presented. Finally, we present a calculation to demonstrate the impact of nonequilibrium sorption in degradation processes in fractured porous media.

* Institut für Strömungsmechanik und ERIB, Universität Hannover, Appelstr. 9a, 30167 Hannover; e-Mail: habbar@hydromech.uni-hannover.de



*Geochemical Processes: Conceptual Models for Reactive Transport in Soil and Groundwater. Research Report.* Deutsche Forschungsgemeinschaft (DFG).
 ISBN: 978-3-527-27764-3

## 6.1 Introduction

A large amount of works about transformation reaction has been done by a number of researchers. Transformation reactions that occur during the transport of some subsurface contaminants in porous and fractured porous media are of interest. Biological degradation or radioactive decay are transformation processes that may play a very important role in the prediction of the migration of such transformation products. Analytical and semianalytical solutions have been developed for the nonreactive and the reactive transport with sequentially decaying reaction products (Cho, 1971; Sudicky and Frind, 1984; Khandelwal and Rabideau, 1999; Cormenzana, 2000). They are all based on analytical and semi-analytical solutions but none of them considers the nonequilibrium sorption reaction of migration in fractured porous media. For long time predictions or for sensitivity analysis the analytical solutions for homogenous media are efficient; but there are several engineering problems where heterogeneity, complex geometry and time dependent parameters such as boundary conditions must be considered. A three-dimensional numerical model describing migration of one or more reactive solutes in fractured porous media incorporating advection, dispersion, matrix diffusion, equilibrium or nonequilibrium sorption, and sequentially decay in the aqueous and/or the sorbed phases will be presented in this paper. Finally, the verification and validity of the new numerical simulator Rockflow-RTM (RF-RTM) will be illustrated through a series of examples.

## 6.2 Governing Equations

### 6.2.1 Nonequilibrium Equations

From the large number of mathematical models for the transport of transformation products with kinetic reactions that can be considered in the Rockflow system we have chosen a first-order chemical nonequilibrium model to simulate the sorption reaction. It can be described by the governing solute transport equation with rate-limited sorption and first-order decay in aqueous and sorbed phases. This model includes the processes of advection, dispersion, sorption, biological degradation or radioactive decay of the contaminant in the aqueous and/or sorbed phases. Figure 6.1 illustrates the conceptual model for sequential decay of a reactive species.

The set of equations in a three-dimensional Cartesian coordinate system can be written as:

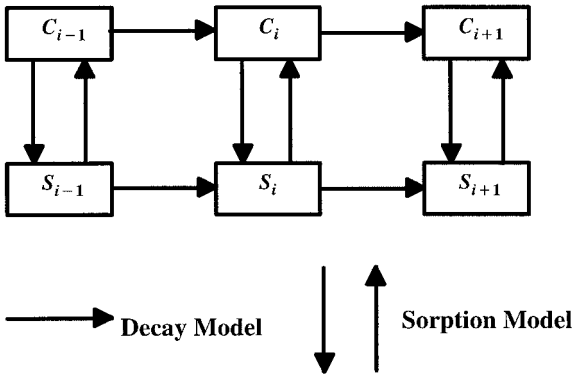


Figure 6.1: Conceptual model for sequential decay including sorption processes ($C_i$– dissolved components, $S_i$ – sorbed components).

$$\theta \frac{\partial C_i}{\partial t} + \rho_b \frac{\partial S_i}{\partial t} + q_\alpha \frac{\partial C_i}{\partial x_\alpha} = \theta \frac{\partial}{\partial x_\alpha}\left( D^i_{\alpha\beta} \frac{\partial C_i}{\partial x_\beta} \right)$$

$$+\lambda_{w,i-1}\theta C_{i-1} - \lambda_{w,i}\theta C_i + \lambda_{s,i-1}\rho_b S_{i-1} - \lambda_{s,i} S_i, \ \left(i = 1,2,\ldots,n\right) \tag{1a}$$

$$\frac{\partial S_i}{\partial t} = \alpha_i \left[ f_i\left(C_i\right) - S_i \right] + \lambda_{s,i-1} S_{i-1} - \lambda_{s,i}\rho_b S_i, \ \left(i = 1,2,\ldots,n\right) \tag{1b}$$

where $C_i$ is the i-th aqueous solute concentration [M/L$^3$], $S_i$ is the i-th sorbed phase concentration [M/M], $\rho_b$ is the soil bulk density of the porous medium [M/L$^3$], $\theta$ is the porosity [L$^3$/L$^3$], $D^i_{\alpha\beta}$ is the i-th local hydrodynamic dispersion tensor [L$^2$/T], $\rho_\alpha$ is the Darcy velocity [L/T], $\lambda_{w,i}$ and $\lambda_{s,i}$ is the i-th first-order decay rate coefficient in the aqueous and sorbed phase, respecively [1/T], $\alpha_i$ is the i-th sorption rate coefficient [1/T], $x$ is the distance [L] and $t$ is the time [T]. The dispersion tensor $D^i_{\alpha\beta}$ is given as follows (Bear, 1972):

$$\theta D^i_{\alpha\beta} = \left(\alpha_T q + D^i_m \tau\right)\delta_{\alpha\beta} + \left(\alpha_L - \alpha_T\right)\frac{q_\alpha q_\beta}{q}, \ \ \left(\alpha,\beta = 1,2,3\right) \tag{2}$$

where $\alpha_L$ and $\alpha_T$ are the longitudinal and transverse dispersivities, $D^i_m$ is the i-th solute molecular diffusion coefficient, $\tau$ is the tortuosity, and $\delta_{\alpha\beta}$ is the Kronecker delta symbol.

Note that for $i$ =1, $C_{i-1}$ is assumed to be zero, and

$$\lambda_{w,0} = \lambda_{s,0} = 0 \tag{3}$$

In Eq. (1a) the terms on the left side represent the rate of change of total dissolved and adsorbed mass as well as advection. The terms on the right describe the mechanical dispersion in the related direction, and the mass change due to decay. Equation (1b) describes the kinetic submodel for the chemical nonequilibrium model. It gives the time rate for the change of the adsorbed phase. One needs this equation to close the problem.

Table 6.1: Frequently used equilibrium sorption models.

| Model (L/N) L: linear, N: nonlinear | Isotherm equation |
|---|---|
| Henry (L) | $S = k_1 C$ |
| Freundlich (N) | $S = k_1 C^{k_2}$ |
| Langmuir (N) | $S = \frac{k_1 \ C}{1 + k_2 C}$ |
| Freundlich-Langmuir (N) | $S = \frac{k_1 \ C^{k_3}}{1 + k_2 C^{k_3}}$ |

If the reaction is considered to be in equilibrium, then one can take it into consideration by setting the parameter equal to infinity. Only steady state water flow is considered. Further, it is assumed that the transport of the solute takes place in saturated porous media, and any effect of concentration on the fluid properties is neglected.

The function $f(C)$ represents any sorption isotherm for a chemical species (linear or nonlinear). The most frequently encountered equilibrium sorption models are listed in Table 6.1 (Simunek et. al., 1999; Selim et. al.; 1990)

### 6.2.2 Equilibrium Equations

In case of an equilibrium model Eqs. (1a)–(2) reduce to:

$$R_i \frac{\partial C_i}{\partial t} + v_\alpha \frac{\partial C_i}{\partial x_\alpha} = \frac{\partial}{\partial x_\alpha}\left( D^i_{\alpha\beta} \frac{\partial C_i}{\partial x_\beta} \right)$$

$$+\lambda_{w,i-1} C_{i-1} - \lambda_{w,i} C_i + \lambda_{s,i-1} \frac{\rho_b}{\theta} S_{i-1} - \lambda_{s,i} \frac{\rho_b}{\theta} S_i, \ \left(i = 1,2,\ldots,n\right) \tag{4}$$

with:

$$R_i = 1 + \frac{\rho_b}{\theta} \frac{\partial S_i}{\partial C_i} \tag{5}$$

where $R_i$ is the retardation factor for the solute $i$ and $v_\alpha = \frac{q_\alpha}{\theta}$ is the pore water velocity.

Assuming linear equilibrium sorption conditions and if the decay constants for the i-th species are identical in the aqueous and sorbed phases ($\lambda_{w,i} = \lambda_{s,i} = \lambda_i$), the above equations reduce to that equations given by van Genuchten (1985) as follows:

Table 6.2: Kinetic models of Rockflow-RTM.

| Kinetic reaction | Formulation |
|---|---|
| mass transfer | $\frac{\partial S}{\partial t} = \alpha \left( f(C) - S \right)$ |
| first order reaction | $\frac{\partial S}{\partial t} = k_1 \frac{\theta}{\rho_b} C - k_2 S$ |
| n-th order reaction | $\frac{\partial S}{\partial t} = k_1 \frac{\theta}{\rho_b} C^n - k_2 S$ |
| reaction with Langmuir kinetic | $\frac{\partial S}{\partial t} = k_1 \frac{\theta}{\rho_b} C \left( S_{\max} - S \right) - k_2 S$ |

$$R_i \frac{\partial C_i}{\partial t} + v_\alpha \frac{\partial C_i}{\partial x_\alpha} = \frac{\partial}{\partial x_\alpha} \left( D^i_{\alpha\beta} \frac{\partial C_i}{\partial x_\beta} \right) + \lambda_{i-1} R_{i-1} C_{i-1} - \lambda_i R_i C_i, \ \left( i = 1, 2, \ldots, n \right) \tag{6}$$

and:

$$R_i = 1 + \frac{\rho_b}{\theta} K^i_D \tag{7}$$

Details of the given mathematical model can be found in Habbar (2001). For simplicity only we have formulated the above equations with a mass transfer nonequilibrium kinetic type. Rockflow-RTM can support several nonequilibrium models. Some of them are listed in Table 6.2.

## 6.3 Numerical Method

The Galerkin method is applied with linear finite elements. The weak formulation of Eqs. (1a) and (1b) is obtained by taking simultaneously the products of the equations with appropriate test functions and integration by parts of the spatial derivatives. We use a Lagrangian interpolation of the approximate solutions $\tilde{C}$ for the aqueous solute concentration $C_i$ and $\tilde{S}$ for the sorbed phase concentration $S_i$ for every species:

$$\tilde{C} = \sum_{j=1}^{np} \phi_j \left( x, y, z \right) C_j(t), \qquad \tilde{S} = \sum_{j=1}^{np} \phi_j \left( x, y, z \right) S_j(t) \tag{8}$$

where $C_j$ is the solute concentration at node $j$, $\phi_j$ is the associated basis function and $np$ is number of element nodes. Substitution of the approximate functions $\tilde{C}$ and $\tilde{S}$ in the weak formulation of the coupled transport equations leads to the following semi-discrete Galerkin approximation:

$$[\mathbf{A}]\ \frac{\partial}{\partial t}\{C_j\}_i + [\mathbf{S}_1]\ \frac{\partial}{\partial t}\{S_j\}_i + [\mathbf{D}]\ \{\mathrm{C_j}\}_i = \mathbf{r}_1 \tag{9a}$$

$$[\mathbf{S}_2]\ \frac{\partial}{\partial t}\{S_j\}_i + [\mathbf{A}_\mathrm{C}]\ \{C_j\}_i + [\mathbf{A}_\mathrm{S}]\ \{S_j\}_i = \mathbf{r}_2 \tag{9b}$$

where $[\mathbf{A}]$, $[\mathbf{S_1}]$, $[\mathbf{D}]$, $[\mathbf{S_2}]$, $[\mathbf{A_C}]$ and $[\mathbf{A_S}]$ are system matrices and $\mathbf{r}_1$ and $\mathbf{r}_2$ the system vectors. The equation systems can be treated further as a global problem with only one equation system:

$$\begin{bmatrix} [\mathbf{A}] & [\mathbf{S}_1] \\ [\mathbf{0}] & [\mathbf{S}_2] \end{bmatrix} \frac{\partial}{\partial t} \begin{bmatrix} \{\mathbf{C}_\mathrm{j}\} \\ \{\mathbf{S}_\mathrm{j}\} \end{bmatrix}_\mathrm{i} + \begin{bmatrix} [\mathbf{D}] & [\mathbf{0}] \\ [\mathbf{A}_\mathrm{C}] & [\mathbf{A}_\mathrm{S}] \end{bmatrix} \begin{bmatrix} \{C_j\} \\ \{S_j\} \end{bmatrix}_i = \begin{bmatrix} \mathbf{r}_1 \\ \mathbf{r}_2 \end{bmatrix} \tag{10}$$

We treat the chemical problem separately and solve the coupled problem iteratively.

A finite difference scheme for discretization in time is used at this stage. In order to reduce the set of ordinary differential equations to algebraic equations, a time weighting coefficient is introduced, that allows to use several schemes: explicit, implicit or the Crank-Nicolson scheme.

The finally resulting equations, including the global matrices assembled from the element contributions and all specified boundary conditions, can be solved with the several solver algorithms allowed in the Rockflow system. We use an iterative scheme to solve the coupled equations: we start with an initial sorbed concentration, then we solve (9a) with the independent variable $C_i$. The chemical problem (Eq. (9b)) is subsequently solved separately with the new estimate concentration to get an improved value for the sorbed concentration. This scheme is repeated iteratively until a convergence is reached. Details of the numerical methods can be found in Habbar [2001].

## 6.4 Software Concept

The FE kernel RTM described below is embedded in the simulator ROCKFLOW-3. This finite element programme has been developed to simulate flow and transport processes of one and more fluid phases in subsurface hydrosystems (Kolditz et al., 1999).

The software is completely in ANSI-C. Dynamic memory allocation and pointer technique are particularly important for the utilization of automatic grid adaptation and the coupling of different FE kernels. The code consists of several FE kernels, which assemble the matrix equations for the specific partial differential equations of a physico-chemical problem, e.g. saturated groundwater flow, gas flow, multiphase flow, tracer transport and reactive transport. These FE kernels may be connected to each other via internal interfaces (so-called models) and with the common libraries to simu-

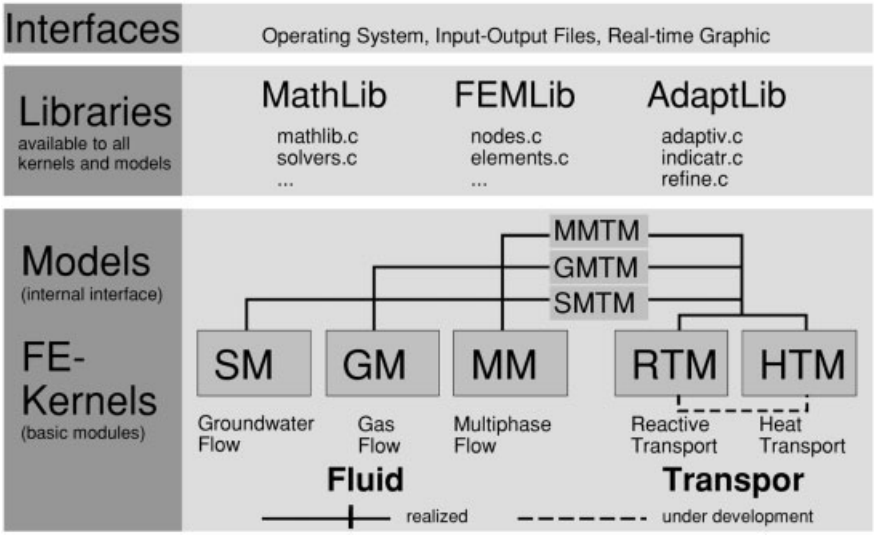


Figure 6.2: Coupling of FE kernels in the Rockflow system.

late coupled problems such as contaminant transport by saturated groundwater, gas or multiphase flow. The concept of an internal interface allows the independent development of specific FE kernels. Therefore, the code may be easily extended to other problems. Furthermore, the internal interface is important for the code development by several programmers. The external interface has different functions: import geometry files from external mesh generators (e.g. RF-HGM, Rother et al., 2000) and export simulation results for data visualization (e.g. Tecplot).

As the software concept allows the coupling of several FE kernels (see Fig. 6.2), chemical processes can be simulated for different hydrological systems, e.g. reactive components can be transported by saturated groundwater, gas, or multiphase flow.

## 6.5 Examples

The following examples illustrate the variety of geochemical problems treated with the numerical simulator. We first consider geochemical processes in porous media: nitrification (Example 1), validation of the nonequilibrium model (Example 2) and TCE transformation (Example 3). After that we treat the same problems in fractured porous media: matrix diffusion (Example 4), two-member decay chain (Example 5). Finally, Example 5 is extended to demonstrate the influence of parameter variation for the concentration distribution that occurs either under equilibrium or nonequilibrium conditions (Example 6).

### 6.5.1 Nitrification Process in a Porous Column

*Example 1*: Cho (1971), van Genuchten (1985)

The first example demonstrates the nitrification problem in a porous medium. We only consider the three-species nitrification chain (Cho, 1971; van Genuchten, 1985):

$$NH_4^+ \rightarrow NO_2^- \rightarrow NO_3^-$$

Cho derived an analytical solution for this transformation reactions. He made some assumptions to derive a simplified version for the transformation problem. The main assumption is the linear equilibrium condition for cation exchange reactions of $NH_4^+$. Writing Eq. (6) for the three species $NH_4^+$ ($C_1$), $NO_2^-$ ($C_2$) and $NO_3^-$ ($C_3$) in one-dimensional form with the assumption of constant solution flow and constant dispersion value for the species, yields (van Genuchten, 1985):

$$R_1 \frac{\partial C_1}{\partial t} + v \frac{\partial C_1}{\partial x} = D \frac{\partial^2 C_1}{\partial x^2} - \lambda_1 R_1 C_1 \tag{11a}$$

$$\frac{\partial C_2}{\partial t} + v \frac{\partial C_2}{\partial x} = D \frac{\partial^2 C_2}{\partial x^2} + \lambda_1 R_1 C_1 - \lambda_2 C_2 \tag{11b}$$

$$\frac{\partial C_3}{\partial t} + v \frac{\partial C_3}{\partial x} = D \frac{\partial^2 C_3}{\partial x^2} + \lambda_2 C_2 - \lambda_3 C_3 \tag{11c}$$

Further, if we define the following expressions:

$$k_1 = \lambda_1 R_1,\ k_2 = \lambda_2 \ and\ k_3 = \lambda_3$$

the above equations reduce to that equations given by Cho (1971):

$$\frac{\partial C_1}{\partial t} = D^* \frac{\partial^2 C_1}{\partial x^2} - v^* \frac{\partial C_1}{\partial x} - k^* C_1 \tag{12a}$$

$$\frac{\partial C_2}{\partial t} + v \frac{\partial C_2}{\partial x} = D \frac{\partial^2 C_2}{\partial x^2} + \lambda_1 R_1 C_1 - \lambda_2 C_2 \tag{12b}$$

$$\frac{\partial C_3}{\partial t} + v \frac{\partial C_3}{\partial x} = D \frac{\partial^2 C_3}{\partial x^2} + \lambda_2 C_2 - \lambda_3 C_3 \tag{12c}$$

where:

$$D^* = \frac{D}{R_1}, v^* = \frac{v}{R_1} and\ k^* = \frac{k_1}{R_1}.$$

The solution is initially free of nitrogen components (initial conditions),

$$C_i(x, t=0) = 0 \tag{13}$$

and the inputs are constant concentrations at (boundary conditions),

$$C_1 = C_1^0, C_2 = C_2^0, C_3 = C_3^0. \tag{14}$$

The example presented here only involves application of the parent component ($C_1$). Further input parameter values are:

$$v = 1 \ cm \ \ h^{-1}, D = 0.18 \ cm^2 \ \ h^{-1}, R_1 = 2.0$$

$$k_1 = 0.01 \ h^{-1}, k_2 = 0.1 \ h^{-1}, k_3 = 0.0 \ h^{-1}$$

Figure 6.3 shows the numerical results compared with the analytical solution of Cho (1971). The calculated concentration distributions for the three species $NH_4^+$, $NO_2^-$ and and $NO_3^-$ and and at t = 200 h are identical to those of the analytical solution.

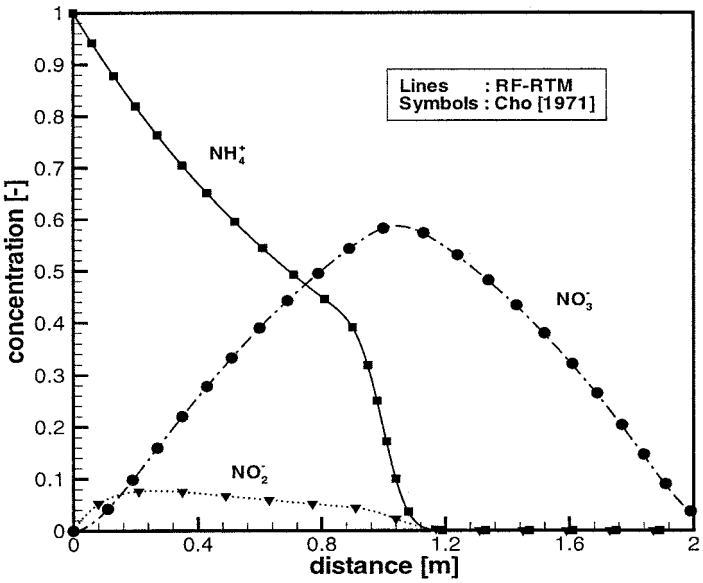


Figure 6.3: Concentration distributions for nitrogen transformations at t = 200 h.

### 6.5.2 Geochemical Nonequilibrium Effects

*Example 2*: Validation of the nonequilibrium model

The purpose of the next example is to illustrate the influence of the reaction parameter (see Eq. (1b)) on the transport of the solute. The decay terms are neglected here. The value of $\alpha$ can be applied in order to control the conditions for which the reactions are in equilibrium or not. While for large values of $\alpha = 10^{-5}$ 1/*s* the processes take place at equilibrium conditions (the curves C/C0 and S/S0 overlap each other (Fig. 6.4)), for $\alpha = 10^{-8}$ 1/*s* (the smallest value of $\alpha$) a typical nonequilibrium case is considered. The sorbed concentration is much lower than the solute concentration (Fig. 6.4). This indicates, the geochemical system is far from equilibrium.

Further values for the example are listed in the following Table 6.3.

Table 6.3: Simulation parameters.

| | | |
|---|---|---|
| length | $L$ | 100.0 m |
| porosity | $\theta$ | 0.2 $m^3/m^{-3}$ |
| Darcy velocity | $q$ | 0.1 $m/d^{-1}$ |
| dispersion | $D$ | 5.0 $m^2/s^{-1}$ |
| bulk density | $\rho_b$ | 1660.0 $kg/m^{-3}$ |
| equilibrium distribution coefficient | $K_d$ | 6.8 $10^{-4}$ $m^3/kg^{-1}$ |
| first-order transfer coefficient | $\alpha$ | $10^{-8}$ to $10^{-5}$ $L/s^{-1}$ |

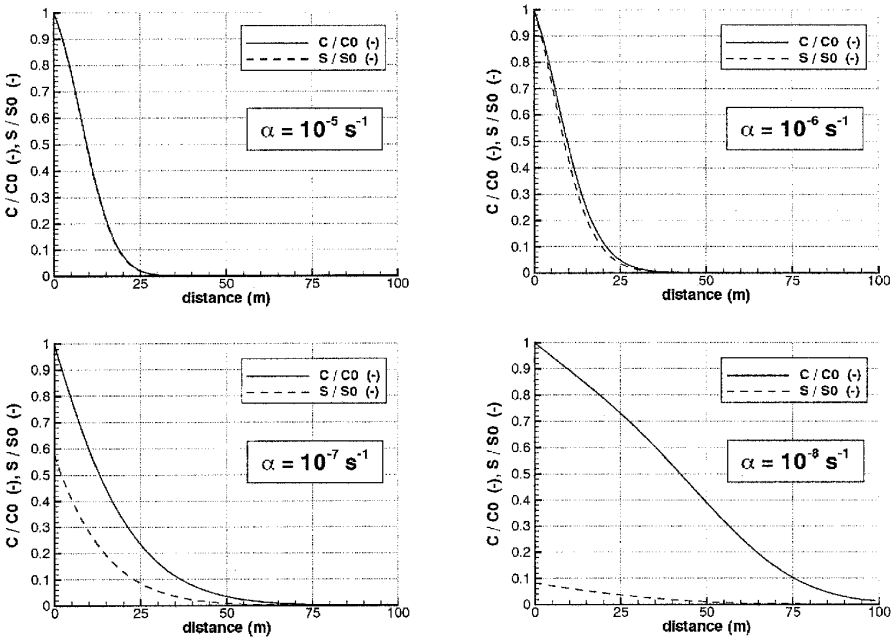


Figure 6.4: Kinetic model – concentration distributions in aqueous and sorbed phases for various rates of reactions $\alpha$.

### 6.5.3 TCE Transformation

*Example 3*: Khandelwal and Rabideau (1999)

Transformation processes are very important for the treatment of many organic contaminants with permeable reactive barriers. The components and their products undergo sorption reactions. This sorption reactions may be either in equilibrium or nonequilibrium. Desintegration of tetrachloroethene or trichloroethylene are two of many examples, that can be treated with this permeable reactive barriers. Khandelwal and Rabideau (1999) developed analytical and semi-analytical solutions for this problem. They consider the sorption reaction with a nonequilibrium model. We verified the numerical RF-RTM model with their analytical solution.

This example shows the migration and degradation of TCE (trichloroethylene) and its reaction products c12DCE (c-1,2-dichloroethene) and VC (vinyl chloride) in a zero-valent iron PRB (permeable reactive barrier) (Kandelwal and Rabideau, 1999):

$$\text{TCE} \rightarrow \text{c12DCE} \rightarrow \text{VC}$$

The simulations were performed for a 1 m thick wall. The apparent velocity and dispersion factor are:

$$v = 1 \ m\,d^{-1}, D = 0.1 \ m^2\,d^{-1},$$

Other characteristic values are listed in the following Table 6.4.

Figure 6.5 shows the relative concentrations across a 1-m treatment wall for the migration of the parent product TCE and its reaction products c12DCE and VC. The simulation is achieved with the equilibrium sorption reaction model. The results are identical to that analytically calculated by Khandelwal and Rabideau (1999).

Figure 6.6 shows the simulation of the transport of the second daughter product (VC). It is calculated for different sorption rate constants. The nonequilibrium effect can be specified with the Damkohler number $Da = \alpha\, L/v$, where $L$ denotes the thickness of the treatment wall. The Damkohler number as mentioned by Domenico and Schwartz (1990) may be taken as a measure of tendency for reaction related to the tendency for transport.

Table 6.4: Solute reaction characteristics.

| Parameters | TCE | C12DCE | VC |
|---|---|---|---|
| $\lambda$, $d^{-1}$ | 23.4 | 2.46 | 3.0 |
| $f$, – | 0.03 | 1.0 | 1.0 |
| $K_d$, $cm^3g^{-1}$ | 10.0 | 4.0 | 6.0 |
| $C_0$, $mgm^{-3}$ | 1.0 | 0.0 | 0.0 |

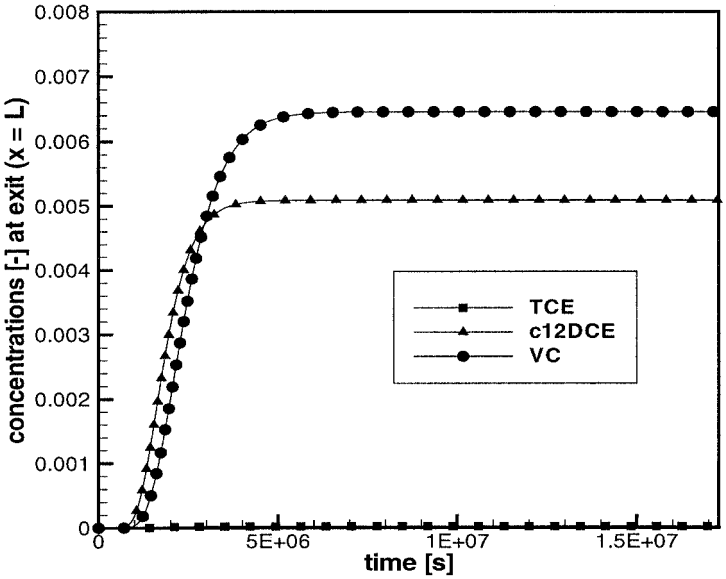


Figure 6.5: Predicted relative concentrations across a permeable reactive barrier exit for the migration of trichloroethylene and reaction products (equilibrium model).

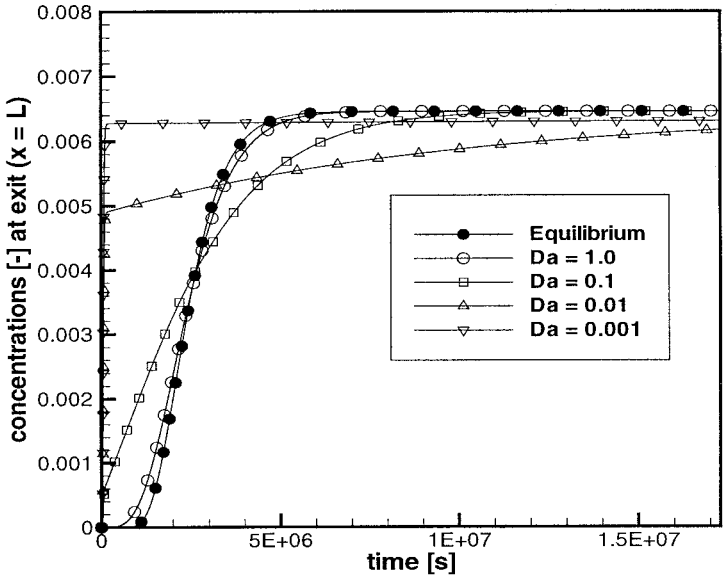


Figure 6.6: Predicted vinyl chloride relative concentration across a permeable reactive barrier exit for various sorption rate constants (nonequilibrium model).

### 6.5.4 Matrix Diffusion

*Example 4*: Tang et al. (1981)

The importance of matrix diffusion for solute transport in fractured-porous media is recognized by many researchers. Prediction of migration processes of radionuclides in a hard rock formation may be more complicated, when the matrix diffusion must be considered. Not only the transport along the fracture is of interest, but the interaction between fracture and matrix must be considered. We begin with an example that allows us to demonstrate how Rockflow can treat the transport of contaminant in a fracture with diffusion in an adjacent matrix. Grisak and Pickens (1980) presented a numerical model to describe solute transport through fractured media. They show the important role of diffusion from the fracture into the matrix and so the net effect of retardation of solute arrival at any point of the fracture. Tang et al. [1981] developed an anytical solution for the same problem. The physical system consists of a single fracture located in a saturated porous rock (see Fig. 6.7). A contaminant source of constant strength is released at the origin of the fracture. To get a more detailed description of the physical system see Grisak and Pickens (1980) or Tang et al. (1981). The main processes are advective and diffusive transport in the fracture and transverse diffusion at the interface fracture-matrix.

The simulation parameters are following in Tables 6.5 and 6.6.

The problem of matrix diffusion is treated with one of several discretization techniques of the matrix and coupling of the elements with different dimensions

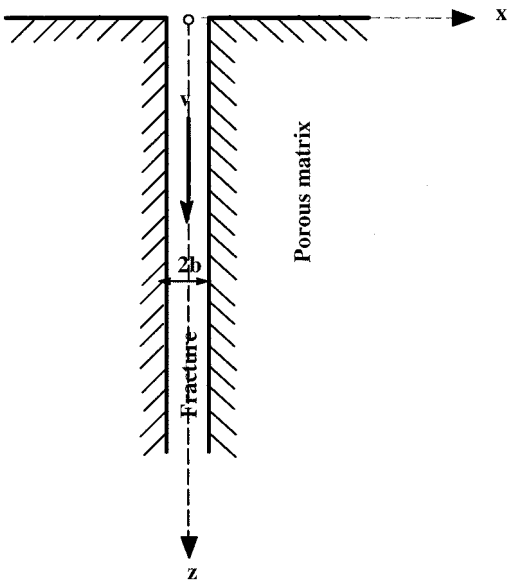


Figure 6.7: Sketch of the fracture-matrix system.

Table 6.5: Fracture characteristics.

| Fracture | | |
|---|---|---|
| length | $L$ | 1.0 m |
| porosity | $\theta$ | 1.0 $m^3/m^{-3}$ |
| Darcy velocity | $q$ | 0.75 $m/d^{-1}$ |
| molecular diffusion | $D_m$ | 0.0 $m^2/s^{-1}$ |
| dispersion parameter | $\alpha_1$ | 0.76 m |

Table 6.6: Matrix characteristics.

| Matrix | | |
|---|---|---|
| length | $L$ | 1.0 m |
| porosity | $\theta$ | 0.35 $m^3/m^{-3}$ |
| Darcy velocity | $q$ | 0.0 $m/d^{-1}$ |
| molecular diffusion | $D_m$ | $10^{-10}$ to $10^{-14}$ $m^2/s^{-1}$ |
| tortuosity | $\tau$ | 1.0 [–] |

(see Fig. 6.8). The one-dimensional element represents the fracture and all physical and chemical parameter can be assigned. The two-dimensional element is the adjacent matrix and allows us not only to simulate diffusion processes within the matrix but the consideration of the advection processes in case of no negligible permeability of the rock matrix as well. This may be an important effect that must be considered in certain cases.

Figure 6.9 shows the schematic discretization of the region used in the following examples which include matrix diffusion processes.

Figure 6.10 shows a comparison of the concentration given by the analytical solution of Tang et al. (1981) and the numerical solution by Rockflow-RTM. It can be observed that the numerical solutions are identical to those calculated analytically even when the diffusion coefficient takes a considerable value.

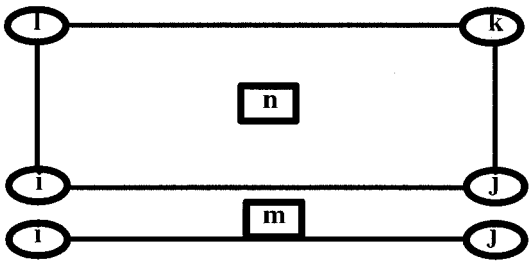


Figure 6.8: Coupling of elements in Rockflow system: 1D element m represents the fracture and the 2D element n the matrix.

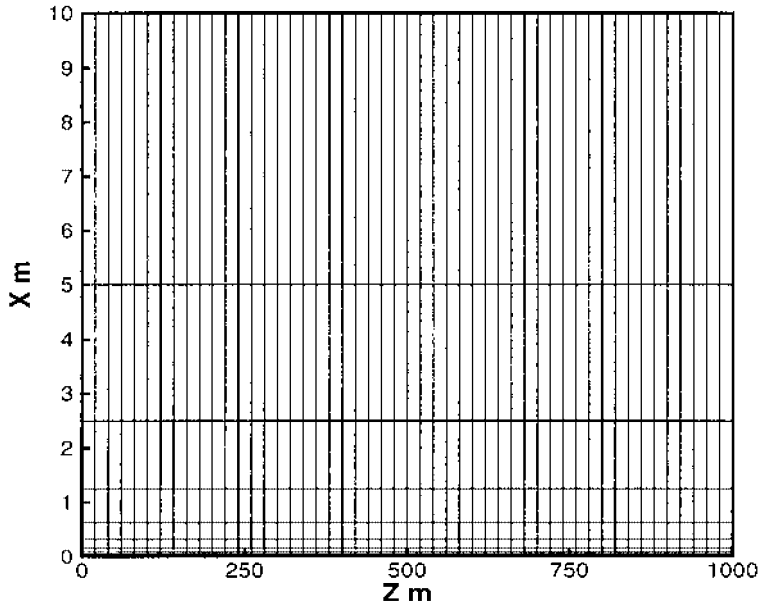


Figure 6.9: Schematic discretization of the modelled region with isoparametric finite elements (fracture: z = 0, matrix: z > = 0).

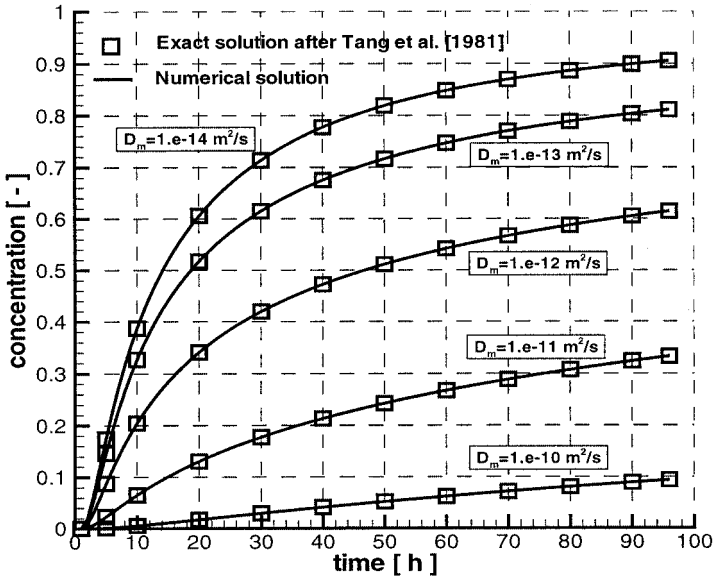


Figure 6.10: Comparison with analytical solution of Tang et al. (1981). Breakthrough curves for fracture at x = 0.76 m, for values of $D^m$ in the range of $10^{-10}$ to $10^{-14}$ $m^2\,s^{-1}$.

### 6.5.5 Two-Member Decay Chain in Fracture-Matrix System

*Example 5*: Sudicky and Frind (1984), Cormenzana (2000)

We will use the analytical solution to verify the numerical solution given first by Sudicky and Frind (1984) and later corrected by Cormenza (2000). This example illustrates the migration of two-member decay chain in fracture-matrix system. Both member, parent and daughter, of the decay chain have the same properties except that the half-lives are different. Since the evaluation of the analytical solution given by Sudicky and Frind (1984) was incorrect, we can confirm the correct solution given by Cormenzana (2000).

The physical system consists of a single fracture located in a saturated porous rock (Fig. 6.7). The properties of the fracture and the porous matrix and the radionuclide properties are listed in Tables 6.7 and 6.8.

Note that no sorption reactions have been assumed, so all retardation factors are equal to unity. A contaminant source containing radionuclides is released instantaneously at the origin of the fracture at time t = 0 (a first-type Dirac delta inlet condition). To get a more detailed description of the physical system see Sudicky and Frind (1984) or Cormenzana (2000).

While this problem admits only advection in the fracture we use an upwind scheme to avoid oscillations in the numerical solution (Hughes and Brooks, 1982). Figure 6.11 gives plots versus distance along the fracture of the concentration distributions of the parent (solid lines) and daughter product (dashed lines) at t = 1000 days and t = 10 000 days. The analytical solution of Cormenzana (2000) and the numerical solution of Rockflow fit very well.

Table 6.7: Fracture characteristics and radionuclide properties in the fracture.

| Fracture | | |
|---|---|---|
| length | $L$ | 1000.0 m |
| fracture aperture | $2b$ | 1.00 µm |
| porosity | $\theta$ | 1.0 $m^3/m^{-3}$ |
| Darcy velocity | $q$ | 0.1 $m/d^{-1}$ |
| dispersion | $D$ | 0.0 $m^2/s^{-1}$ |

Table 6.8: Matrix characteristics and radionuclide properties in the porous matrix.

| Matrix | | |
|---|---|---|
| length | $L$ | 1000.0 m |
| porosity | $\theta$ | 0.01 $m^3/m^{-3}$ |
| Darcy velocity | $q$ | 0.0 $m/d^{-1}$ |
| molecular diffusion | $D_{m1} = D_{m2}$ | 8.64 $10^{-5}$ $m^2/s^{-1}$ |
| tortuosity | $\tau$ | 0.1 [–] |

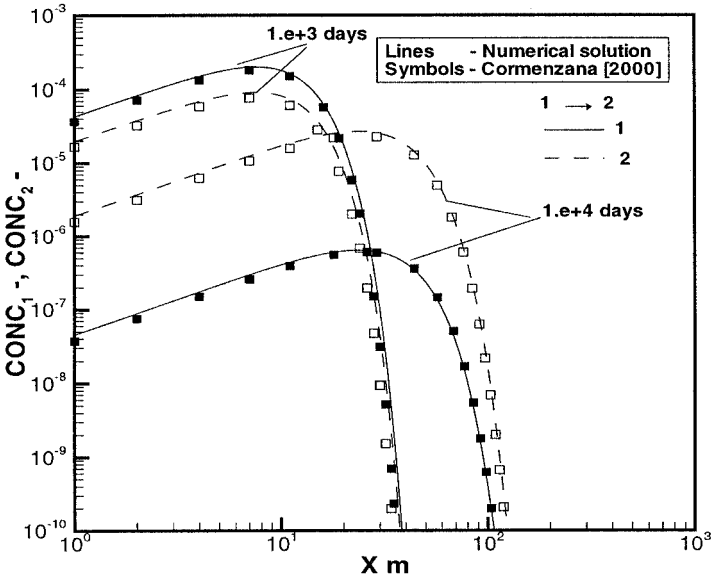


Figure 6.11: Concentration profiles along the fracture for a two-member decay chain. All parameter are equal except the half-lifes.

### 6.5.6 Two-Member Decay Chain in Fracture–Matrix System

*Example 6*: Extented Cormenzana (2000) (Equilibrium/Nonequilibrium model)

We extend the example of Sudicky and Frind (1984) and Cormenza (2000) to illustrate which processes can influence the migration of the daughter product along the fracture. For the first two cases we assume that chemical reactions occur under equilibrium. Only for the last case we use the nonequilibrium first-order reaction model as mentioned above.

Figure 6.12 shows the concentration distribution along the fracture for the identical case study as above (Example 5) except that the diffusion coefficient for the parent and daughter member are different. Further the same half-life for both members is assumed.

Clearly, that while the two-members have the same properties in the fracture the daughter member can penetrate further along the fracture than the parent, only when they possess different effective diffusion values. This is achieved when different molecular diffusion coefficients are used (Fig. 6.12) or when different sorption reactions for the species occur in the matrix (Fig. 6.13).

In case of nonequilibrium reactions, the same effect can be obtained as above when different transfer rate coefficients are assumed, as we see in Fig. 6.14. Numerical modelling of the decay chain reactions in fractured porous media with a nonequilibrium sorption model is treated for the first time. Further there exists no analytical solution for this type of model.

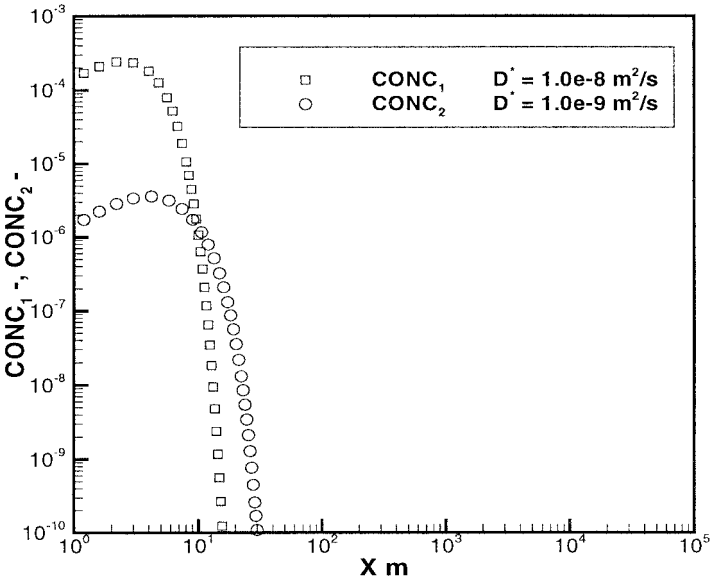


Figure 6.12: Concentration profiles along the fracture for a two-member decay chain. Variation of the molecular diffusion coefficient.

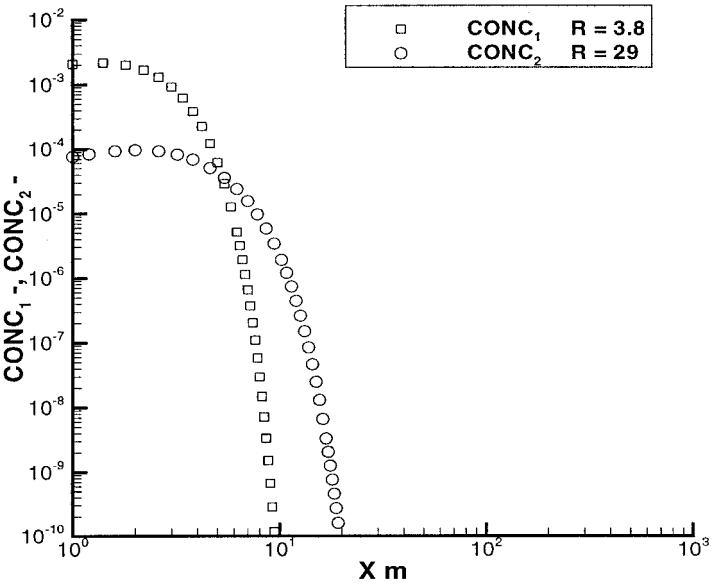


Figure 6.13: Concentration profiles along the fracture for a two-member decay chain. Variation of the retardation factor coefficient.

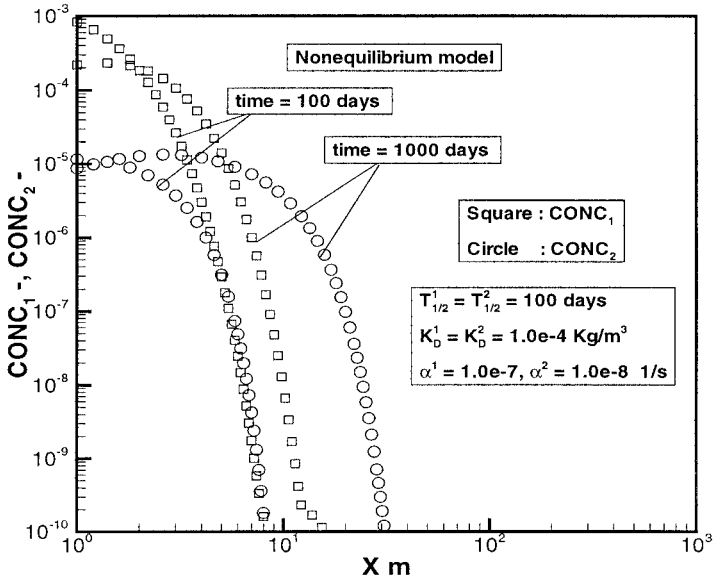


Figure 6.14: Effect of nonequilibrium sorption reactions for concentration distribution along the fracture for a two-member decay chain. Variation of the transfer parameter.

## 6.6 Conclusions

A new numerical solver RF-RTM for the reactive transport in fractured porous media was investigated. The simulator RF-RTM is a three-dimensional model, that can consider several nonequilibrium kinetic type models. This paper illustrates the accuracy with the finite element model for simulating decay reactions in fractured porous media. The presented results show the capability of RF-RTM to simulate transport of one or more species. The finite element model RF-RTM was verified for several situations: when sorption occurs under equilibrium conditions such as in Example 1 and 5, or in case of matrix diffusion such as in Example 4. Validation of the nonequilibrium model was shown in Example 3. The nonequilibrium model is verified only for homogenous media. Numerical modelling of the decay chain reactions in fractured porous media with a nonequilibrium sorption model is treated for the first time. Especially the different penetrations of decay chain components in a fracture-matrix system was illustrated through a series of simulations (see Example 6). Further research is needed to quantify the effect of nonlinear sorption in the migration of the contaminants with sequentially decaying processes in fractured porous media.

## Ackowledgement

The work presented in this paper was supported by the DFG (Deutsche Forschungsgemeinschaft) under grant ZI 202/12–1/2. The authors appreciate the support of the groundwater research group (Thorenz, C.; Kaiser, R. and Rother, T.). Special thanks are extended to Ratke, R.

## 6.7 References

Bear, J. (1972): Dynamics of Fluids in Porous Media, Elsevier.

Cho, C. M. (1971): Convective transport of ammonium with nitrification in soil. *Can. J. Soil. Sci* **51**, 339–350.

Cormenzana, J. (2000): Tranport of a two-member decay chain in a single fracture: Simplified analytical solution for two radionuclides with the same transport properties. *Water Resour. Res.* **36**(5), 1339–1346.

Domenico, P. A.; Schwartz, F. W. (1990): Physical and chemical hydrogeologie, John Wiley, New York.

Grisak, G. E.; Pickens, J. F. (1980): Solute transport through fractured porous media: 1) The effect of matrix diffusion. *Water Resour. Res.* **16**(4), 719–730.

Habbar, A. (2001): Direct and Inverse Modelling of Reactive Transport in Porous and Fractured Media, PhD Thesis, Hannover.

Higashi, K.; Pigford, T. H. (1980): Analytical models for migration of radionuclides in geologic sorbing media. *J. Nucl. Sci Technol.* **17**, 700–709.

Hughes, T. J. R.; Brooks, A. N. (1982): Streamline Upwind/Petrov-Galerkin Formulations for Convection Dominated Flows with Particular Emphasis on the Incompressible Navier-Stokes Equations. *Computer Methods in Applied Mechanics and Engineering* **32**, 199–259.

Khandelwal, A.; Rabideau, A. J. (1999): Transport of sequentially decaying reaction products influenced by linear nonequilibrium sorption. *Water Resour. Res.* **35**(6), 1939–1945.

Kolditz, O.; Kaiser, R.; Thorenz, C.; Habbar, A (1999): ROCKFLOW – Theory and Users Manual, Release 3.4, Institut für Strömungsmechanik und ERIB, Universität Hannover.

Rother, T; Kolditz, O.; Taniguchi, T. (2000): Grid Generation of Fractured-Porous Aquifers. In: Proc. 7th International Conference on Numerical Grid Generation in Computational Field Simulations, Whistler, British Columbia, Canada, Sept. 25–28.

Selim, H. M.; Amacher, M. C.; Iskandar, I. K. (1990): Modelling the Transport of Heavy Metals in Soils, Monograph 90–2, U.S. Army Corps of Engineers.

Simunek, J.; Sejna, M.; van Genuchten, M. Th. (1999): The HYDRUS-2D Software Package for Simulating the Two-Dimensional Movement of Water, Heat, and Multiple Solutes in Variably-Saturated Media, Version 2.0, U. S. Salinity Laboratory, USDA, ARS.

Sudicky, E. A.; Frind, E. O. (1984): Contaminant transport in fractured porous media: Analytical solution for a two-member decay chain in a single fracture. *Water Resour. Res.* **20**(7), 1021–1029.

Tang, D. H.; Frind, E. O.; Sudicky, E. A. (1981): Contaminant transport in fractured porous media: Analytical solution for a single fracture. *Water Resour. Res.* **17**(3), 555–565.

van Genuchten, M. Th. (1985): Convective-dispersive transport in sequential first-order decay reactions. *Computers & Geosciences* **11**(2), 129–147.

# 7 Modelling Reactive Transport of Organic Solutes in Groundwater with a Lagrangian Streamtube Approach

Michael Finkel*, Rudolf Liedl and Georg Teutsch

## Abstract

Spreading of organics in groundwater is modelled by a numerical streamtube approach providing a computationally efficient alternative to conventional finite difference and finite element techniques due to a decoupling of conservative transport and physico-chemical processes. The streamtube model is designed as a forward modelling tool, i.e. the input data set describing groundwater flow, transport and reactions only contains parameters which may be determined by field or laboratory experiments. The model accounts for equilibrium as well as nonequilibrium retardation. Sorption/desorption kinetics are described as intra-particle diffusion of chemicals inside the grain particles of porous aquifer material which may consist of different lithological components and/or grain size fractions.

The applicability of the model is demonstrated by a parameter study focusing on the remediation of a PAH contaminated site with the help of surfactants. It is found that the spreading and the removal of the contaminant (phenanthrene) are strongly affected by the grain size distribution and the surfactant concentration, respectively.

## 7.1 Introduction

Modelling in the field of soil and groundwater remediation usually requires to deal with a complex system of processes and interactions among a mixture of reactive solutes as well as between the solutes and the solid phase. In hardly any case this system is completely known. And, therefore, mathematical models must use simplified approaches. Most of the models are based on descriptions including parameters that cannot be measured or directly derived from site characteristics relevant to contami-

* Institut und Museum für Geologie und Paläontologie, Universität Tübingen, Sigwartstr. 10, 72076 Tübingen; e-Mail: michael.finkel@uni-tuebingen.de



*Geochemical Processes: Conceptual Models for Reactive Transport in Soil and Groundwater. Research Report.* Deutsche Forschungsgemeinschaft (DFG).
 ISBN: 978-3-527-27764-3

nant transport but must be fitted in accordance with the spatial or temporal scale of the specific problem considered (e.g. macrodispersivity or first-order rate coefficients). Hence, these models are of limited use for predictions. To overcome this problem, we propose a modelling strategy together with an appropriate model concept that is intended to be especially useful for 'forward simulations' in order to predict the transport organic contaminants in groundwater. In this paper, we present the approach within the context of the transport of polycyclic aromatic hydrocarbons (PAHs) being retarded under nonequilibrium conditions and solubilised by means of surface active agents (surfactants). The occasion to this work is given by the fact that conventional remediation techniques such as pump-and-treat are not suitable for the highly hydrophobic PAHs (low water solubilities) as clean up cannot be achieved within reasonable periods of time. Surfactants may influence the transport of PAH and thus are expected to enhance the remediation of PAH-contaminated sites. Therefore, several investigations on the use of surfactants to cleanup soils at the laboratory scale (e.g. Burris and Antworth, 1992; Edwards et al., 1994A; Grimberg et al., 1995) as well as some field demonstration projects, especially in the United States (U. S. Environmental Protection Agency, 1995) commenced in the 90's.

The proposed modelling strategy aims at two main goals. Firstly, in order to avoid fitting parameters, all relevant reactive processes should be described with mathematical formulations that need only measurable parameters or parameters that can be related to measurable aquifer properties as input. Secondly, the model concept should allow for an implementation of even complex reactive process formulations and, furthermore, it should be easy to handle and computationally efficient in order to examine the influence of a number of processes and parameters on the contaminant behaviour in groundwater. Putting these idea into a model concept requires a co-ordinated research of laboratory and modelling groups (Finkel et al., 1998; Danzer and Grathwohl, 1998). Furthermore, with regard to the identification of reactive processes being most relevant to coupled transport of PAHs and surfactants and to obtain measured parameters, we utilise the results of numerous experimental studies carried out in the last decade (Grathwohl, 1992, 1998; Grathwohl and Kleineidam, 1995; Kleineidam, 1998; Kleineidam et al., 1999; Rügner et al., 1997, 1999; Rügner, 1998; Danzer and Grathwohl, 1998; Danzer, 1999).

The concept of the transport model is based on a Lagrangian description of solute transport in groundwater. The Lagrangian concept has mostly been used to develop analytical solutions for three-dimensional reactive transport in heterogeneous porous aquifers, either presented as streamtube approach (e.g. Simmons et al., 1995; Berglund and Cvetkovic, 1995; Ginn et al., 1995; Dagan and Cvetkovic, 1996; Ginn, 2001) or as transfer-function approach (e.g. Jury, 1982; Jury et al., 1986; Jury and Roth, 1990; Roth and Jury, 1993). While useful for verifying the accuracy of numerical models based on the Eulerian description of solute transport in groundwater by means of the advection-dispersion equation (Yabusaki et al., 1998), these analytical solutions are limited to nearly uniform flow fields and rather simple reactive transport problems, e.g. for individual processes or single components. By consequently converting this approach into a numerical model as presented here with the programme SMART (Streamtube Model for Advective and Reactive Transport), these limitations can be overcome and even complex situations can be addressed. This refers to flow conditions as well as to the reactive processes involved.

Beside the presentation of the SMART concept, the objectives of this paper are (i) to examine how organic contaminant transport is influenced by properties of natural aquifer material and (ii) to show how surfactants may enhance the remediation of sites contaminated with polycyclic aromatic hydrocarbons (PAH). This is done in an exemplary way by applying the transport model to a simplified field-scale remediation scenario where Phenanthrene (PHE) and the non-ionic surfactant Terrasurf G50 (TG50) are considered as solutes.

## 7.2 Reactive Transport Model SMART

### 7.2.1 Streamtube Approach

According to the Lagrangian concept conservative transport is quantified with respect to the travel time $\tau$ of an inert tracer. In particular, a probability density function (pdf) of travel times $g(\tau,x)$ is used to model the transport of a conservative solute between an injection plane and a control plane which are a distance $x$ apart from each other and are both oriented normal to the mean flow (Fig. 7.1). As a consequence, the pdf $g(\tau,x)$ completely reflects the hydraulic heterogeneity of the aquifer domain considered. The modelling approach is based on the assumptions that (i) the flow field is time-invariant, (ii) hydraulic heterogeneity is completely described by the variability of the velocity field, and (iii) 'dispersive' spreading of a plume can be attributed to macroscopic hydraulic heterogeneities, i.e. pore-scale dispersion and molecular diffusion can be neglected. Following these assumptions no mass transfer between

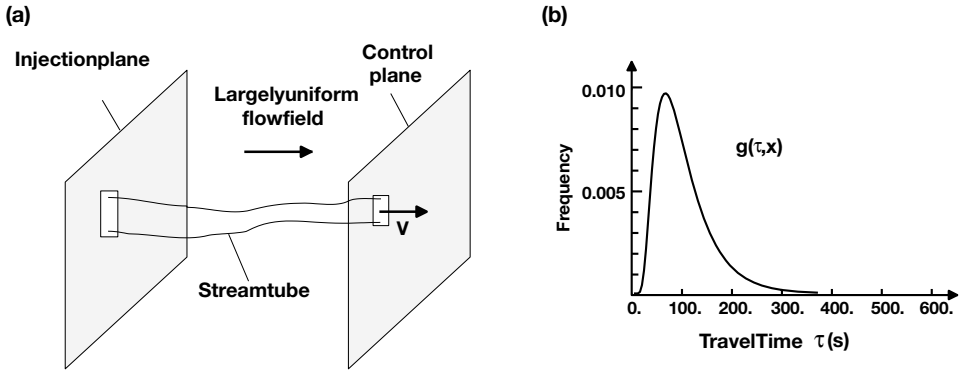


Figure 7.1: Conceptual basis of the streamtube approach: (a) aquifer domain between an injection and a control plane, (b) pdf of travel time as description of flow field variability in the aquifer domain.

streamtubes is taking place and the streamtubes can be regarded independently from each other. Even though the assumption of diffusion-free behaviour is generally unrealistic, it is a valid approximation for many advection-dominated situations such as near injection or extraction wells commonly employed in field remediation (Charbeneau, 1981).

In the numerical streamtube model, the restriction to nearly uniform flow fields, commonly associated with the streamtube approach, is eliminated by introducing non-planar injection and control surfaces which are perpendicular to the mean flow direction, thus accounting for non-uniform velocity fields (Fig. 7.2). Furthermore, the numerical approach allows to consider even complex physico-chemical relationships among the solutes regarded as well as between the solute and the solid phase.

Some examples illustrating possible arrangements of injection and control surfaces are given in Fig. 7.3. The model concept can be applied to field-scale situations but as well to small-scale problems, for example laboratory columns (Fig. 7.3a). In a

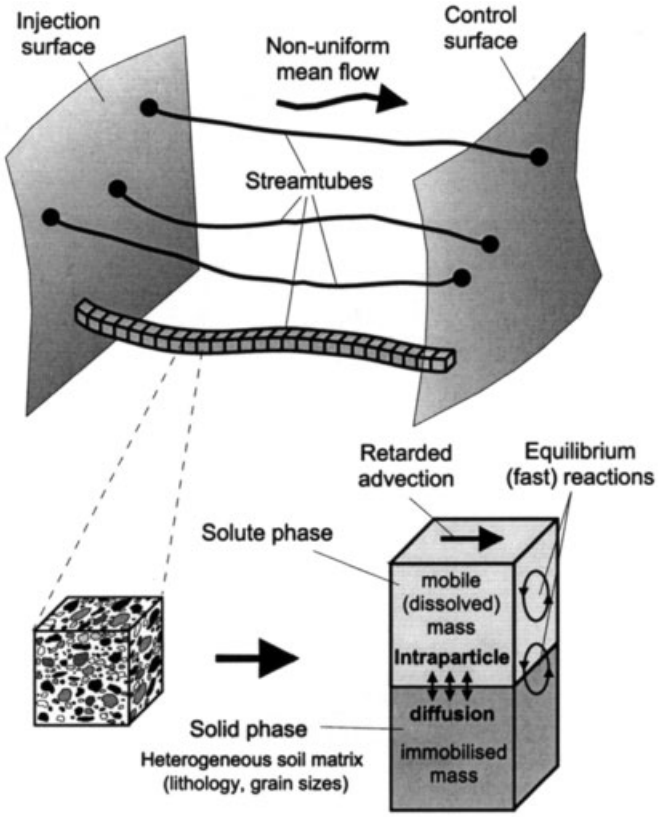


Figure 7.2: General scheme of the conceptual transport model: ensemble of streamtubes representing the heterogeneous flow field between an injection and a control surface; solutes are undergoing various processes; solute-solid phase-interactions depend on soil heterogeneity.

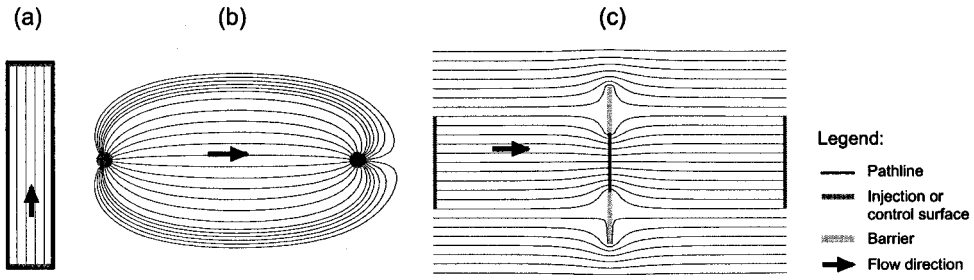


Figure 7.3: Cross-sections illustrating the definition of injection and control surfaces.

double well system the well screens may be taken (Fig. 7.3b). In the case of a funnel-and-gate system, the cross-section of the gate (reactor) is a possible choice for both the injection and the control surface (Fig. 7.3c). The pdf may be directly determined from tracer experiments or estimated by simulation of groundwater flow and conservative transport using appropriate analytical or numerical models.

### 7.2.2 Accounting for Reactive Processes

A vital feature of the streamtube approach is that the influence of physico-chemical reactions on transport of reactive solutes in groundwater can be considered separately from the impact of hydraulic heterogeneities or non-uniform groundwater flow. Here, reactive processes can be described by a single reaction function $\Gamma(\tau,t)$. For any fixed time $t$, this function represents a normalised concentration profile where $\Gamma(\tau,t)$ refers to all positions within the streamtubes that have been reached by a conservative tracer after a travel time $\tau$. The use of a single reaction function is synonymous to the assumption that all parameters relevant to reactive processes are homogeneously distributed within the aquifer domain of interest, i.e. a single reaction path can be regarded 'representative' for all solute trajectories with respect to the reactions they are undergoing.

This assumption, however, is a reasonable approximation even for situations where the distribution of physico-chemical parameters is heterogeneous to some extent, in particular if the scale of physico-chemical heterogeneity is considerably smaller than the transport distance or if inter-connectivity of high permeable areas is low, i.e. all fluid particles reside on their way from input to control surface approximately the same time in low as well as in high permeability areas. This is demonstrated by Peter et al. (chapter 14) by means of a comparison of SMART and the well-known transport code MT3D (Zheng, 1990).

If large-scale physico-chemical heterogeneities are present and the individual solute particles encounter quite different physicochemical properties of the aquifer material along their flowpaths, reactive transport must be computed explicitly in terms of $\Gamma$ along each and every streamtube (see below and Thiele et al., 1995A, B).

### 7.2.3 Numerical Evaluation of Breakthrough Curves

In order to evaluate the reaction function, simulations of one-dimensional advective-reactive transport expressed in terms of the travel time $\tau$ must be conducted. A series of concentration profiles with respect to $\tau$ calculated at distinct times $t_i$ ($i$ = 1,2,...,$n$) approximate the reaction function $\Gamma$ (Fig. 7.4). The 'length' of the streamtube is given

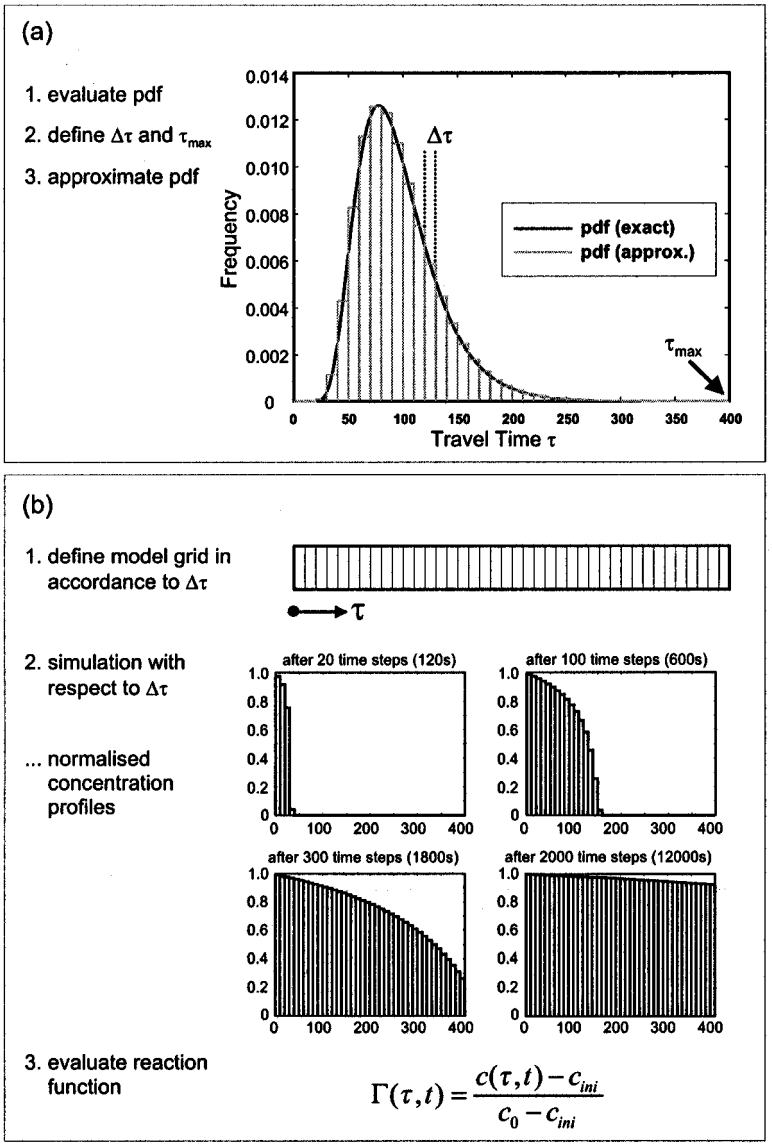


Figure 7.4: Steps in decoupled modelling of conservative transport and reactions.

by the maximum travel time $\tau_{max}$ of the 'slowest' fluid particle between the input and control surface. Furthermore, a travel time increment $\Delta\tau$ must be chosen that is appropriate to approximate the pdf and also serves as the model discretisation to evaluate the reaction function $\Gamma$.

If the assumption of a 'representative' streamtube is valid, the normalised breakthrough curve (BTC) of a reactive tracer at the control surface (Fig. 7.5) is then given by:

$$c(x,t) = \int_0^{\tau_{max}} g(\tau,x)\ \Gamma(\tau,t)\ d\tau \tag{1}$$

The integral in Eq. (1) is evaluated numerically by replacing the integral by a finite sum (see Fig. 7.5).

If a separate consideration of an ensemble of single streamtubes should be required due to large-scale physico-chemical heterogeneities, the model discretisation must be chosen in accordance with the residence times of a conservative tracer in the homogeneous sub-regions (zones) of the aquifer domain considered (Fig. 7.6). In this case, a definite value of the total travel time $\tau_{C,tot}(k)$ of a conservative tracer along each

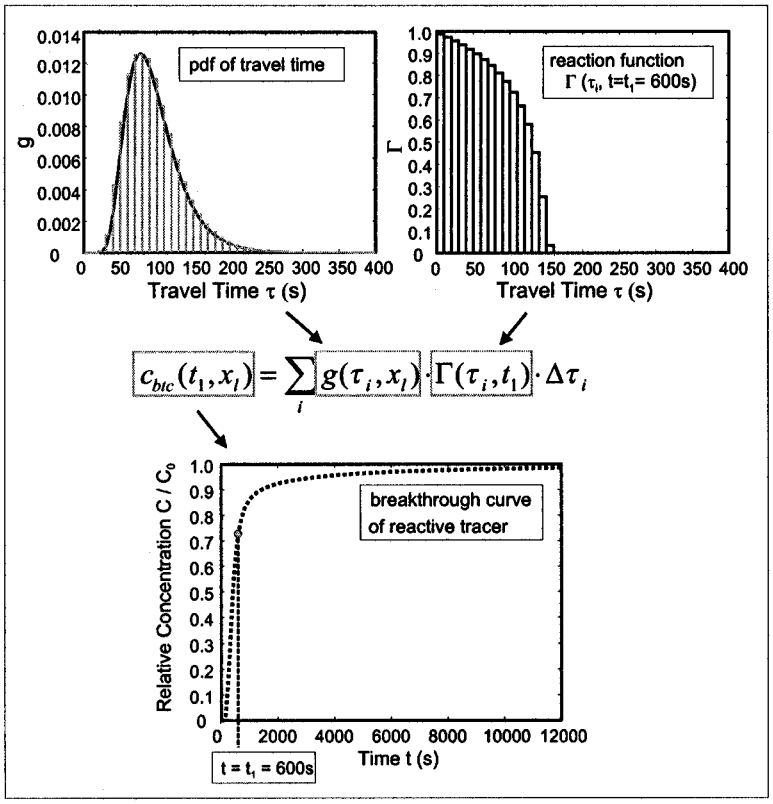


Figure 7.5: Numerical integration to evaluate the breakthrough curve of the reactive tracer.

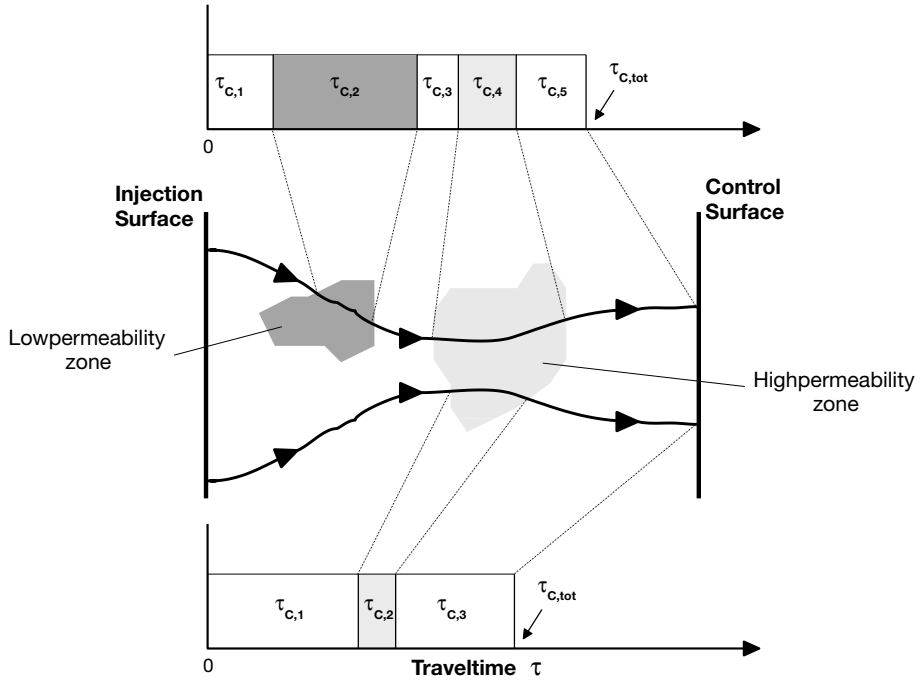


Figure 7.6: Travel time parameterisation in case of large-scale heterogeneities in the aquifer domain.

streamtube $k$ is obtained and gives the 'length' of the 1D model to calculate the reaction function for streamtube $k$. Since $g$ is reduced here to one value $\tau_{C,tot}(k)$, the integration of $g \cdot \Gamma$ with respect to $\tau$ is performed by simply setting the BTC $c_k(\boldsymbol{x},t)$ of a reactive solute at the control surface for streamtube $k$ equal to $\Gamma_k(\tau_{C,tot}(k),t)$. The ensemble BTC $c(t)$ at the control surface can then be determined by averaging the BTCs for all of the $m$ single streamtubes:

$$c(t) = \frac{1}{m}\sum_{k=1}^{m} c_k(\mathbf{x},t) \tag{2}$$

In case of nonequilibrium conditions or a complex system of reactive processes, each reaction function $\Gamma(\tau_{tot,k},t)$ has to be evaluated by means of a numerical simulation. A special case is given if no inter-solute and no kinetic reactions have to be taken into account, e.g. in case of 'fast' or equilibrium sorption. In this case the reaction function $\Gamma$ can be calculated analytically by

$$c_k(x,t) = \Gamma(\tau_{C,tot}(k),t) = H\left[\frac{t}{R_{eff}} - \tau_{C,tot}(k)\right] \tag{3}$$

where $H$ is the Heaviside step function and $R_{eff}$ is the effective retardation factor of the reactive solute considered. $R_{eff}$ is described as

$$R_{eff}(k) = \frac{\tau_{R,tot}(k)}{\tau_{C,tot}(k)} \tag{4}$$

with $\tau_{R,tot}(k)$ as the travel time of the reactive solute along streamtube $k$, that is

$$\tau_{R,tot}(k) = \sum_{i=1}^{n} \tau_{C,i}\, R_i \tag{5}$$

where $R_i$ is the retardation factor in sub-region $i$ and $n$ is the number of sub-regions encountered by streamtube $k$.

## 7.3 Reactive Transport of Phenanthrene and Terrasurf G50

### 7.3.1 Conceptual Model of Relevant Processes

The conceptualisation of the system of reactive processes that must be considered to properly describe coupled transport of PAHs and surfactants in groundwater comprises the results of numerous experimental investigations (e.g. Kile and Chiou, 1989; Kan and Tomson,1990; Edwards et al., 1991; Burris and Antworth, 1992; Wagner et al., 1994; Edwards et al., 1994B; Grimberg et al., 1995; Kleineidam, 1998; Rügner, 1998; Danzer and Grathwohl, 1998; Danzer, 1999) and, to our knowledge, coincides with the latest state of research. As shown in Fig. 7.7 the following processes are considered: (i) PAH sorption onto soil grain surface (easy accessible sorption sites), (ii) retarded diffusion of PAH into intra-particle pores, (iii) formation of surfactant micelles, (iv) sorption of surfactant monomeres onto soil grain surface, (v) PAH solution into surfactant micelles, and (vi) PAH sorption onto sorbed surfactant hemi- and admicelles. According to experimental research studies mentioned above, all processes except of (ii) are ‘fast’ (seconds to minutes) in relation to the time scale of field-scale problems. Therefore, processes (i), (iv), (v) and (vi) are modelled by means of equilibrium approaches (distribution coefficients as indicated in Fig. 7.7). The formation of micelles (iii) is described by a threshold function with critical micelle concentration (*CMC*) as threshold value: for dissolved surfactant concentration $C_{S,diss}$ below *CMC* no micelles exist, if $C_{S,diss}$ is beyond *CMC* the concentration of micelles equals $C_{S,diss}$ - *CMC*. The retarded diffusion of PAH into intra-particle pores is expressed as time-variant diffusion into spherical grains (Crank, 1975). In SMART this can be done alternatively either by an analytical approach (Finkel and Liedl, 1998) or by a numerical solution (Jaeger and Liedl, 2000).

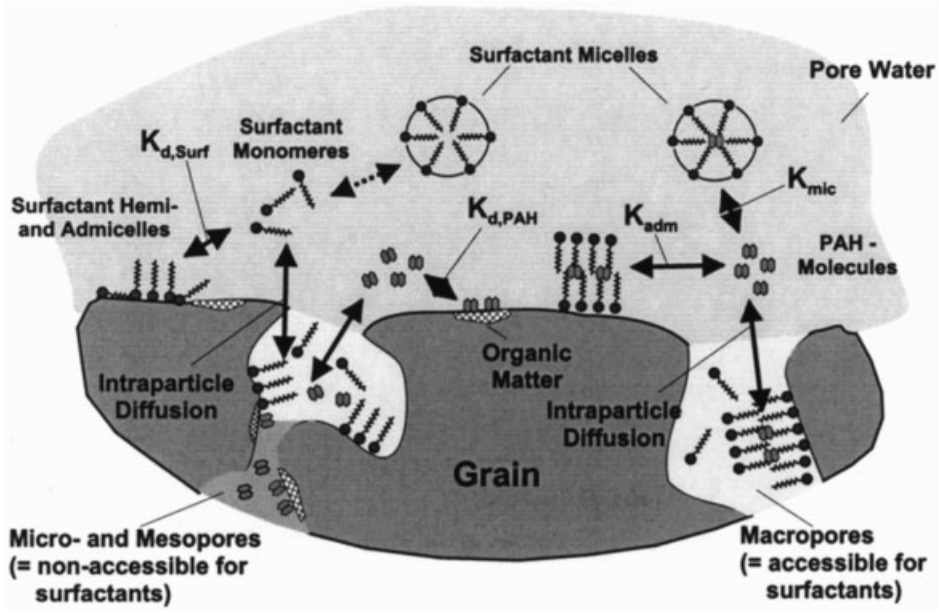


Figure 7.7: Conceptual model of processes for the coupled transport of PAH and surfactants.

An important feature of the model concept is that sorption processes are described as the sum of litho- and/or grain-size-specific processes (Finkel, 1999). This is done in accordance with the results of experimental studies revealing that PAH sorption distribution coefficients vary with lithological type of solid material, and that PAH intra-particle diffusion and surfactant sorption depend on both the grain size and the lithological type of solid material (e.g. Kleineidam, 1998; Kleineidam et al., 1999; Rügner et al., 1997, 1999; Rügner, 1998). Consequently, physico-chemical soil heterogeneity is addressed by a matrix of mass fractions of different lithological sub-units and grain size classes (Fig. 7.8) and process descriptions are based on lithocomponent- and grain-size-specific parameters. By doing this, we expect to transfer process-relevant parameters, as measured in the laboratory, to the field where it is then sufficient to determine the lithological fractions and grain size distributions (effective or average values).

Since a comprehensive discussion of the conceptual model of processes is beyond the scope of this paper, the reader is referred to Finkel et al. (1998) and Finkel (1999) for more details. The behaviour of surfactants and their possible influences on organic substances is well described e.g. in West and Harwell (1992), Danzer and Grathwohl (1998), and Danzer (1999).

The model described above was verified and validated with regard to column experiments at the laboratory scale (Finkel, 1999; Finkel et al., 1998). The results provide evidence that the conceptual model of processes (Fig. 7.7) is appropriate to represent all relevant processes and interactions occurring when PAH and surfactants migrate in the groundwater (Finkel et al., 1998).

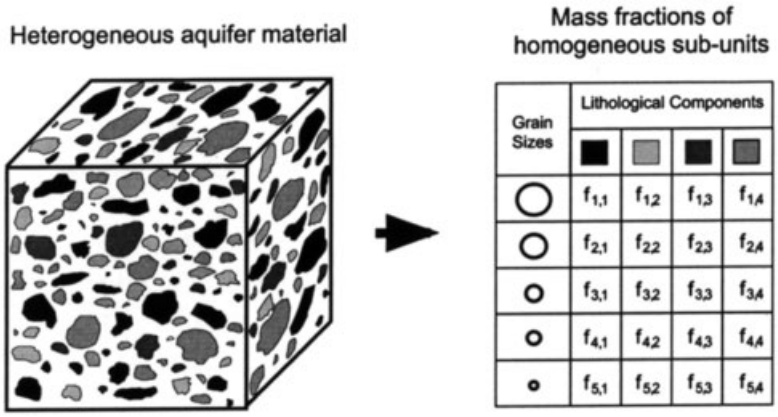


Figure 7.8: Detailed consideration of physico-chemical aquifer material heterogeneity by means of a matrix of mass fractions $f_{i,j}$ of different lithological sub-units and grain size classes.

## 7.3.2 Remediation Scenario

The following simplified field-scale remediation scenario is considered in this study: phenanthrene (PHE) is emitted from a NAPL source with a constant concentration of 200 µg/L and the contaminant plume is captured by an extraction well 25 meters downstream the source zone (Fig. 7.9).

It is assumed that the aquifer is confined and hydraulically homogeneous (average hydraulic transmissivity $T = 10^{-1}$ m$^2$/s, gradient of the natural uniform flow field $I = 0.2$ %) and composed of Neckar river alluvial (NRA). The lithological composition and grain size distribution of NRA (Tab. 7.1), as determined by Rügner et al. (1997), is

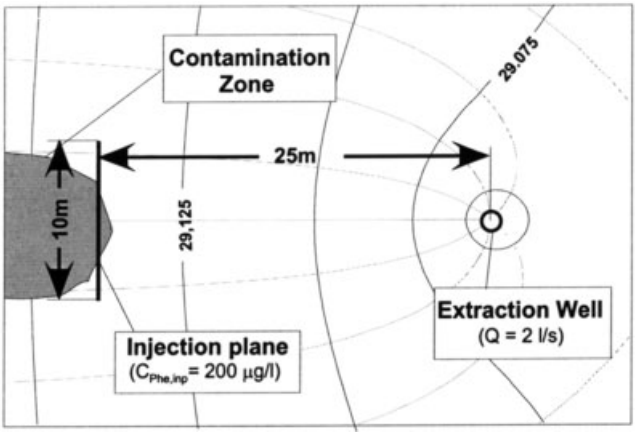


Figure 7.9: Simplified remediation scenario: extraction well in uniform flow field.

Table 7.1: Lithological composition and grain size distribution of Neckar river alluvial (NRA).

| Grain Size (d in mm) | Quartz | 'Stuben' Sandstone | Jurassic Limestone | Triassic Limestone | NRA Sample |
|---|---|---|---|---|---|
| Mass fractions of homogeneous sub-units (in %) | | | | | |
| > 16 | 0 | 10 | 10 | 30 | 50 |
| 8–16 | 0 | 1 | 13 | 6 | 20 |
| 4–8 | 0 | 1 | 6.5 | 2.5 | 10 |
| 2–4 | 1 | 0.5 | 2.5 | 1 | 5 |
| 1–2 | 8.25 | 0.75 | 3.75 | 2.25 | 15 |
| Sample | 9.25 (~10) | 13.25 (~15) | 35.75 (~35) | 41.75 (~40) | 100 |
| Mean grain diameters of lithological subcomponents (in mm) | | | | | |
| Mean | 1.7 | 16.6 | 16.6 | 11.4 | 13.3 |

assumed to be the same in the whole model area. In order to get an estimate on how an application of surfactants may enhance transport of PHE organic contaminants, in the second part of this study it is further assumed that the non-ionic surfactant TG50 (Dow Chemicals) is injected into the aquifer such that TG50 is present in the entire capture zone of the remediation well with a constant concentration and that changes in the flow field caused by the injection are negligible. Although these assumptions are obviously strong simplifications of reality, they should be admissible when trying to get a first estimate on the possible enhancement that can be achieved with a certain type of surfactant as it is done for TG50 in this study.

### 7.3.3 Process Parameters

All process parameters for the different lithological sub-units are listed in Table 7.2. Intra-particle porosity and sorption parameters have been measured by Rügner et al. (1997). The maximal sorbed TG50 concentrations $q_{max,TG50}$, the critical micelle concentration *CMC* (~ 100 mg/L) and the parameters of PHE partitioning into the admicellar phase ($K_{adm}$ = 18 300 l/kg$_{TG50}$) and the micellar phase ($K_{mic}$ = 11 000 l/kg$_{TG50}$) were also independently measured in the laboratory (Danzer and Grathwohl, 1998).

Table 7.2: Measured process parameters.

| Parameter | Unit | Quartz | 'Stuben' Sandstone | Jurassic Limestone | Triassic Limestone |
|---|---|---|---|---|---|
| Intraparticle Porosity | % | 0.5 | 8.8 | 1.2 | 0.7 |
| $K_{d,PHE}$ [1)] | L/kg | 1.2 | 5.0 | 13.5 | 31.0 |
| Equilibrium Fraction [2)] | % | 2 | 0.5 | 0.5 | 0.5 |
| $q_{max,TG50}$ | mg/kg | 40 | 770 | 400 | 170 |

[1)] Result of a linearisation of the associated *Freundlich* isotherm with respect to $C_{PHE,inp,}$
[2)] Tantamount to rate of easy accessible sorption sites (approximated via ratio of inner and outer grain surface).

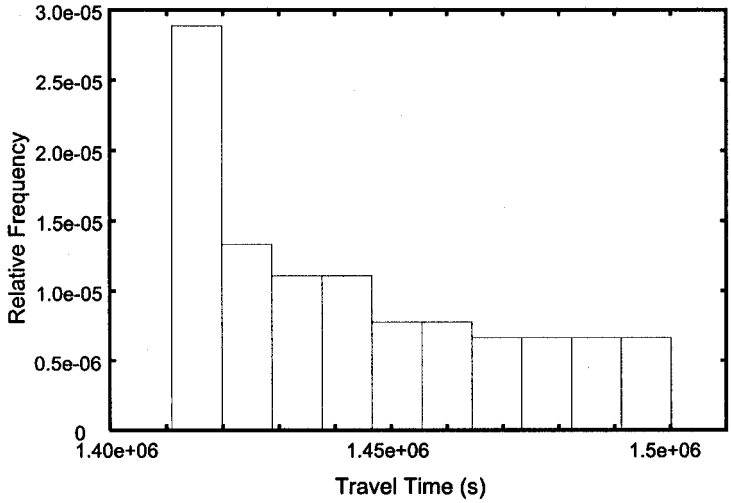


Figure 7.10: Approximated pdf of travel time of a conservative tracer between injection plane and remediation well.

### 7.3.4 Conservative Transport Description

Conservative transport has been modelled using standard software. The flow field for the remediation scenario described above has been calculated by MODFLOW (McDonald and Harbaugh, 1984). The particle-tracking software MODPATH (Pollock, 1988, 1994) has been used to calculate total travel time of each particle from the injection plane to the well screen. The simulation of conservative transport leads to the pdf of travel time as shown in Fig. 7.10.

### 7.3.5 Reactive Transport Simulations

#### 7.3.5.1 Influence of Aquifer Properties on Transport of PHE

It is obvious that it is practically not feasible to exactly quantify the physico-chemical aquifer properties but estimates and simplifications, e.g. average or effective values must be applied. In view of an application of the SMART modelling strategy and concept for transport predictions, it is important to know how wrong estimates of the physicochemical properties of the aquifer material will take effect on the simulation results. Therefore, the objective of a first suite of simulations is to assess the impact of the composition of the aquifer material and its physicochemical properties on the transport of PHE and to examine the sensitivity of lithological composition and grain

size distribution of the aquifer material. The results of these PHE transport simulations are shown in Fig. 7.11a to Fig. 7.11c.

In a first step, in order to reveal the specific characteristic of the litholological sub-units, it is investigated what PHE breakthrough would be observed at the control surface if the aquifer material purely consisted of a single sub-unit assuming an averaged grain size of 13.3 mm as determined for NRA (Tab. 7.2). As it is shown in Fig. 7.11a, the calculated BTCs differ considerably from the BTC obtained for the composed material. Figure 7.11a also depicts the general relationships between sorption parameters and the shape of the BTC: (i) the $K_d$ value, a measure of the sorption capacity, mainly determines the tailing (the lower the $K_d$ value the less the tailing), (ii) a low $K_d$ value and a high intra-particle porosity promote the intra-particle diffusion (enhanced sorption process) and cause a later breakthrough (see BTC for 'Stuben' sandstone for example).

In order to assess the effect of deviations in the lithological composition, two hypothetical compositions with different mass fractions of the lithological sub-units compared to the NRA sample were introduced (Tab. 7.3). It is assumed that the mass fractions of the less sorbing components Quartz and Stuben sandstone are overestimated against an underestimation of the mass fractions of Jurassic and Triassic limestone. The resulting lithological compositions have lower averaged $K_d$ values compared to the NRA sample (Tab. 7.3). Two cases are examined: a deviation of 10 % (moderate), and a deviation of 20 % (strong). At first sight, the results of the simulations (Fig. 7.11b) are surprising. According to the decreased averaged $K_d$ values also a decreased retardation could be expected. Instead, an increased retardation can be observed for the modified compositions within the time range of 800 days. This is due to the fact that intra-particle diffusion (kinetic sorption) is faster into lithological sub-units Quartz and Stuben sandstone (see Fig. 7.11a). Accordingly, as indicated by a less pronounced tailing of the BTCs (steeper slope at t = 800 days), complete breakthrough (relative concentration $C/C_{PHE,inp} = 1.0$) will be approached faster as compared to the NRA sample. Generally, it is worth to note that the differences in the BTCs are not as big as it would have been expected on the basis of the associated mean $K_d$ values of the compositions (Tab. 7.3).

Table 7.3: Changes in aquifer material properties to assess their influence on the transport of PHE.

| Composition | Mass fractions of lithological subunits (%) | | | | Averaged $K_d$ value |
|---|---|---|---|---|---|
| | Quartz | 'Stuben' Sandstone | Jurassic Limestone | Triassic Limestone | |
| NRA sample | 10 | 15 | 35 | 45 | 18.1 |
| 'moderate' deviations [1)] | 20 (+10) | 25 (+10) | 25 (–10) | 35 (–10) | 14.3 |
| 'strong' deviations [1)] | 30 (+20) | 35 (+20) | 15 (–20) | 25 (–20) | 10.4 |

[1)] Deviation (in %) from NRA sample in parentheses.

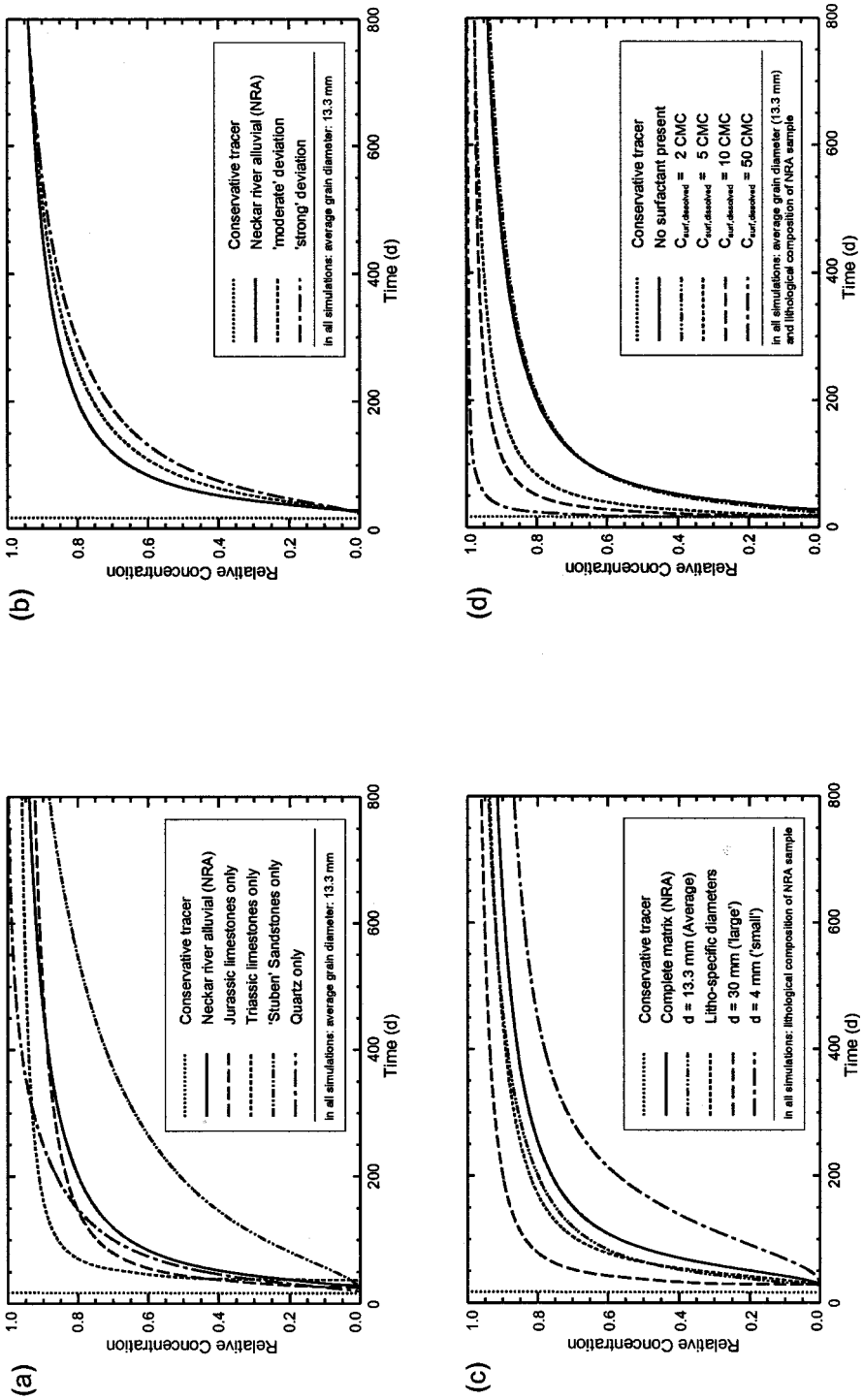


Figure 7.11: (a) Breakthrough of phenanthrene in the extraction well: comparison of NRA and its lithological sub-units; (b) effect of lithological soil composition on breakthrough of phenanthrene in the extraction well; (c) effect of the mean diameter of soil grains on breakthrough of phenanthrene in the extraction well; (d) effect of Terrasurf G50 on breakthrough of phenanthrene in the extraction well.

Another parameter that influences the sorption of organic contaminants is the size of the soil grains (diffusion length): the finer the aquifer material the faster the kinetics described by the intra-particle diffusion process. Therefore, in the context of modelling, it is important to know the necessary degree of detail the grain size distribution of the aquifer material must be considered with, in order to adequately describe the contaminant transport. The issue was investigated by comparing the following cases: (i) 'complete' description of the grain size distribution by five different grain size classes (Tab. 7.1), (ii) approximated description through an average grain size (13.3 mm), and (iii) accounting for different litho-specific mean grain diameters (Tab. 7.1). Two more calculations have been done, in order to estimate the impact of the grain size in general by assuming average grain diameters of 4 mm (case 'small'), and 30 mm (case 'large'), respectively. Figure 7.11c shows that mean values lead to an underestimation of the retardation. The two main characteristics of the BTC, the early breakthrough and the tailing are not described properly, because the small and large grain size fractions that are mainly responsible for these characteristics are not considered separately. The considerable differences in the shape of the BTCs obtained for different simplified descriptions of the grain size distribution in comparison to a detailed consideration (complete matrix) support the general finding that nonequilibrium transport of PHE is more sensitive to the grain size distribution of the aquifer material than to its lithological composition.

#### 7.3.5.2 Impact of Non-Ionic Surfactant TG50 on Transport of PHE

The enhancing impact (solubilising effect) an application of TG50 may have on the transport of PHE within the framework of the remediation scenario described above, depends on $C_{surf,dissolved}$, the established concentration of TG50 in groundwater. For low TG50 concentration ($C_{surf,dissolved} \leq CMC$) partitioning of PHE onto sorbed ad- and hemimicelles leads to an increased retardation of PHE (adsolubilisation). Only if $C_{surf,dissolved}$ is well above *CMC,* and partitioning of PHE into the mobile surfactant phase (micelles) dominates PHE partitioning onto sorbed ad- and hemimicelles, a solubilisation of PHE can be achieved. To examine the relationship between $C_{surf,dissolved}$ and the extent of the resulting PHE solubilisation, simulations of coupled transport of PHE and TG50 with different values of $C_{surf,dissolved}$ (2, 5, 10, and 50 times the CMC) have been carried out.

Figure 7.11d shows that for $C_{surf,dissolved} = 2\ CMC$ hardly any change in the BTC of PHE can be observed. In this case, solubilisation and adsolubilisation level each other out. If $C_{surf,dissolved}$ is increased to 5 *CMC* considerable solubilisation of PHE is seen. For even higher values of $C_{surf,dissolved}$ 'early' breakthrough of PHE approaches the BTC of a conservative tracer.

## 7.4 Summary and Conclusions

The multi-component transport model SMART has been developed to describe transport of organic contaminants in heterogeneous porous media. The model is based on the streamtube approach allowing for separate treatment of conservative transport and reactive processes. It accounts for the hydraulic as well as for the physico-chemical heterogeneity of porous aquifers. Both equilibrium and kinetic processes may be considered. The model is concepted as a forward model by addressing the chemical non-uniformity of the aquifer material by means of a matrix of different grain size classes and lithological components, and by using independently measured parameters only. The model has been applied to a simple pump-and-treat remediation scenario to show how the physico-chemical properties of aquifer material and its description within the model are influencing the transport of organic contaminants. Simulations have been done for the PAH phenanthrene and are based on measured input parameters from Rügner et al. (1997) and Danzer and Grathwohl (1998). Additionally, it has been investigated how the fate and transport of phenanthrene may be altered in the presence of a non-ionic surfactant (Terrasurf G50).

The results show that the composition of the aquifer material strongly determines the transport of organic contaminants and that the quality of the results obtained from mathematical modelling depends on the degree of detail the aquifer material is decribed with. Furthermore, the results indicate that the influence of the grain size predominates the impact of the lithological composition (Fig. 7.11a to 7.11c). The simulations with regard to a surfactant application reveal that, for moderate to high concentrations of Terrasurf G50, a considerable enhancement of the phenanthrene transport (near to conservative conditions) may be achieved (Fig. 7.11d).

SMART is applicable if integral information on contaminant behaviour in groundwater is sufficient. If point information is needed a conventional FD or FE model has to be used. Although it is obvious that the streamtube approach is not as flexible as ‘real 3D models’, decoupling of conservative transport and physico-chemical processes allow to model three-dimensional contaminant transport in a convenient and computationally efficient way, especially if only one ‘representative’ streamtube must be modelled. Computation times, as observed by Peter et al. (chapter 14) are much lower compared to MT3D simulations. It should also be mentioned, that the streamtube approach possesses some advantages compared to ‘real 3D models’ even if each and every streamtube has to be modelled by means of a numerical model in order to evaluate $\Gamma$. Since only one dimensional advective-reactive transport must be modelled, numerical solutions based on ‘discrete’ or ‘mechanistical’ approaches, free of numerical dispersion, can be applied. In SMART this is done by a so-called ‘parcel-tracking’ approach where contaminant transport is described by means of a continuous series of water volumes (‘parcels’) as described in Finkel et al. (1998).

## Acknowledgements

We would like to thank the Federal Ministry of Education and Research (BMBF) for funding of this research. We would also like to thank the reviewer for his helpful comments which considerably improved this paper.

## 7.5 References

Berglund, S.; Cvetkovic, V. (1995): Pump-and-treat remediation of heterogeneous aquifers: Effects of rate-limited mass transfer. *Ground Water* **33** (4), 675–685.

Burris, D. R.; Antworth, C. P. (1992): In situ modification of an aquifer material by a cationic surfactant to enhance retardation of organic contaminants. *Journal of Contaminant Hydrology* **10**, 325–337.

Charbeneau, R. (1981): Groundwater contaminant transport with adsorption and ion exchange chemistry: Method of characteristics for the case without dispersion. *Water Resour. Res.* **17** (3), 705–713.

Crank, J. (1975): The Mathematics of Diffusion, Oxford University Press, 2nd edition.

Dagan, G.; Cvetkovic, V. (1996): Reactive transport and immiscible flow in geological media. I. General theory. *Proc. R. Soc. Lond.* **A 452**, 285–301.

Danzer, J. (1999): Surfactant Transport and Coupled Transport of Polycyclic Aromatic Hydrocarbons (PAHs) and Surfactants in Natural Aquifer Material – Laboratory Experiments. Tübinger Geowissenschaftliche Arbeiten (TGA), Reihe C, Nr. 49, p. 75, PhD thesis.

Danzer, J.; Grathwohl P. (1998): Coupled transport of PAH and surfactants in natural aquifer material. *Physics and Chemistry of the Earth* **23**(2), 237–243.

Edwards, D. A.; Adeel, Z.; Luthy, R. G. (1994A): Distribution of nonionic surfactant and phenanthrene in a sediment/aqueous system. *Environ. Sci. and Technol*. **28**(8), 1550–1560.

Edwards, D. A.; Liu, Z; Luthy, R. G. (1994B): Experimental data and modeling for surfactant micelles, HOCs, and soil. *Journal of Environmental Engineering* **120**(1), 23–41.

Edwards, D. A.; Luthy, R. G.; Liu, Z. (1991): Solubilization of polycyclic aromatic hydrocarbons in micellar nonionic surfactant solutions. *Environ. Sci. Technol.* **25**(1), 127–133.

Finkel, M. (1999): Quantitative Beschreibung des Transports von polyzyklischen aromatischen Kohlenwasserstoffen (PAK) und Tensiden in porösen Medien (Quantitative description of the transport of polycyclic aromatic hydrocarbons (PAH) and surfactants in porous media), Tübinger Geowissenschaftliche Arbeiten (TGA), Reihe C, Nr. 47, p. 98, PhD thesis.

Finkel, M.; Liedl, R. (1998): Retarded intraparticle diffusion in heterogeneous aquifer material. In: Water-Rock Interaction, Proc. 9th Intern. Symp. (Eds.: Arehart, G. B.; Hulston, J. R.), Taupo, New Zealand, 219–222.

Finkel, M.; Liedl, R.; Teutsch, G. (1998): Modelling surfactant influenced PAH migration. *Physics and Chemistry of the Earth* **23**(2), 245–250.

Ginn, T. R. (2001): Stochastic-convective transport with nonlinear reactions and mixing: Finite streamtube ensemble formulation for multicomponent reaction systems with intra-streamtube dispersion. *J. Hydrol.* **47**, 1–28.

Ginn, T.; Simmons C.; Wood, B. (1995): Stochastic-convective transport with nonlinear reaction: Biodegradation with microbial growth. *Water Resour. Res.* **31**(11), 2689–2700.

Grathwohl, P. (1992): Die molekulare Diffusion als limitierender Faktor bei der Sanierung von Boden- und Grundwasserkontaminationen (The molecular diffusion as limiting factor for the remediation of soil and groundwater contaminations). *Z. Umweltchem. Okotox.* **4**(4), 231–236.

Grathwohl, P. (1998): Diffusion in Natural Porous Media: Contaminant Transport, Sorption/Desorption and Dissolution Kinetics, Kluwer Academic Publishers, Boston, p. 224.

Grathwohl, P.; Kleineidam, S. (1995): Impact of heterogeneous aquifer materials on sorption capacities and sorption dynamics of organic contaminants. In: Groundwater Quality: Remediation and Protection (Eds.: Kovar, K.; Krasny, J.). *IAHS Publ.* **225**, S.79–86.

Grimberg, S. J.; Nagel, J.; Aitken, M. D. (1995): Kinetics of phenanthrene dissolution into water in the presence of nonionic surfactants. *Environ. Sci. and Technol.* **29**, 1480–1487.

Jaeger, R.; Liedl, R.. (2000): Prognose der Sorptionskinetik organischer Schadstoffe in heterogenem Aquifermaterial (Predicting sorption kinetics of organic contaminants in heterogeneous aquifer material). *Grundwasser* **5**(2), 57–66.

Jury, W. (1982): Simulation of solute transport using a transfer function model. *Water Resour. Res.* **18**(2), 363–368.

Jury, W.; Roth, K. (1990): Transfer Functions and Movement Through Soil: Theory and Applications, Birkhäuser Verlag, Basel/Boston/Berlin, p. 226.

Jury, W.; Sposito, G.; White, R. (1986): A transfer function model of solute transport through soil: 1. Fundamental concepts. *Water Resour. Res.* **22**(2), 243–247.

Kann, A. T.; Tomson, M. B. (1990): Groundwater transport of hydrophobic organic compounds in the presence of dissolved organic matter. *Environ. Toxicol. Chem.* **9**, 253–263.

Kile, D. E., Chiou, C. T. (1989): Water solubility enhancement of DDT and trichlorbenzene by some surfactants below and above the critical micelle concentration. *Environ. Sci. Technol.* **23**, 832–838.

Kleineidam, S. (1998): Der Einfluß von Sedimentologie und Sedimentpetrographie auf den Transport gelöster organischer Schadstoffe im Grundwasser (Influence of sedimentology and sedimentpetrography on transport of organic solutes in groundwater), Tübinger Geowissenschaftliche Arbeiten (TGA), Reihe C, Nr. 41, p. 82, PhD thesis.

Kleineidam, S.; Rügner, H.; Grathwohl, P. (1999): Impact of grain scale heterogeneity on slow sorption kinetics. *Environ. Tox. Chem.***18**(8), 1673–1678.

McDonald, M. G.; Harbaugh, A. W. (1984): MODFLOW, A modular three-dimensional finite-difference ground-water flow model, U. S. Geological Survey, Open-File Report 83–875.

Pollock, D. W. (1988): Semianalytical computation of path lines for finite difference models. *Ground Water* **26**(6), 743–750.

Pollock, D. W. (1994): User's guide for MODPATH/MODPATH-PLOT, version 3: A particle tracking post-processing package for the finite-difference ground-water flow model MODFLOW. Reston, V.A., U. S. Geological Survey.

Roth, K.; Jury, W.A. (1993): Linear transport models for adsorbing solutes. *Water Resour. Res.* **29**(4), 1195–1203.

Rügner, H. (1998): Einfluß der Aquiferlithologie des Neckartals auf die Sorption und Sorptionskinetik organischer Schadstoffe (Influence of aquifer lithology of the Neckar river valley on sorption and sorption kinetics of organic contaminants), Tübinger Geowissenschaftliche Arbeiten (TGA), Reihe C, Nr. 39, p. 78, PhD thesis.

Rügner, H.; Kleineidam, S.; Grathwohl, P. (1997); Sorptionsverhalten organischer Schadstoffe in heterogenem Aquifermaterial am Beispiel des Phenanthrens (Sorption behaviour of organic contaminants in heterogeneous aquifer material demonstrated for phenanthrene). *Grundwasser* **2**(3), 133–138.

Rügner, H.; Kleineidam, S.; Grathwohl, P. (1999): Long term sorption kinetics of phenanthrene in aquifer materials. *Environ. Sci. Tech.* **33**(10), 1645–1651.

Simmons, C. S.; Ginn, T.; Wood, B. (1995): Stochastic-convective transport with nonlinear reaction: Mathematical framework. *Water Resour. Res.* **31**(11), 2675–2688.

Thiele, M.; Blunt, M.; Orr Jr., F. (1995A): Modeling flow in heterogeneous media using streamtubes, I – Miscible and immiscible displacements. *In Situ* **19**(3), 299–339.

Thiele, M.; Blunt, M.; Orr Jr., F. (1995B): Modeling flow in heterogeneous media using streamtubes, II – Compositional displacements. *In Situ* **19**(3), 367–391.

U.S. Environmental Protection Agency, EPA (1995): In situ remediation technology status report: surfactant enhancements. EPA542–K–94–003.

Wagner, J.; Chen, H.; Brownawell, B. J.; Westall, J. C. (1994): Use of cationic surfactants to modify soil surfaces to promote sorption and retard migration of hydrophobic organic compounds. – *Environ. Sci. Technol.* **28**(1), S. 231–237.

West, C. W.; Harwell, J. H. (1992): Surfactants and subsurface remediation. *Environ. Sci. Technol.* **26**(12), 2324–2330.

Yabusaki, S.; Steefel, C.; Wood, B. (1998): Multidimensional, multicomponent, subsurface reactive transport in nonuniform velocity fields: Code verification using an advective reactive streamtube approach. *J. Contam. Hydrol.* **28**(2), 299–331.

Zheng, C. (1990): MT3D, A modular three-dimensional transport model for simulation of advection, dispersion and chemical reactions of contaminants in groundwater systems. Report to the U.S. Environmental Protection Agency, p. 170.

# 8 Conception of a GIS-Based Data Model for Combined Hydrochemical and Hydraulic Balance Calculations in Pleistocene Landscapes – an Approach of Regionalization

Christoph Merz*, Peter Schuhmacher, Jörg Steidl and Andreas Winkler

## Abstract

In the pleistocene landscape of NE Germany the discharge of groundwater from quaternary deposits into rivers and ditches is one of the main components needed to describe the water and substance balance. Therefore, estimation of substance flux in the landscape requires the development of a conceptional database model in a regional scale which is prerequisite for modelling the groundwater and substance flow.

Facing hydrochemical and hydraulic process studies, investigations were carried out for different typical landscape units of NE Germany. Process studies in combination with common deterministic modelling tools and a conceptional regional modelling approach allow to describe the hydrogeological conditions and substance dynamics of pleistocene aquifer systems in the upper mesoscale (50 $km^2$ to 2500 $km^2$). Using common available hydrogeological data, the resulting data models are sufficiently accurate considering the heterogeneity of the aquifer- and the drainage systems.

The method was validated by hydraulic calculations carried out in a pleistocene aged watershed covering 220 $km^2$ (Stoebber river) and applied for the calculation of groundwater residence times in the mesoscale watershed of the Ucker river (covering 2400 $km^2$) and planned for modelling substance balance in the Oderbruch region (800 $km^2$).

* Institut für Landschaftswasserhaushalt, Zentrum für Agrarlandschafts- und Landnutzungsforschung (ZALF) e. V., Eberswalderstr. 84, 15374 Müncheberg; e-Mail: cmerz@zalf.de



*Geochemical Processes: Conceptual Models for Reactive Transport in Soil and Groundwater. Research Report.* Deutsche Forschungsgemeinschaft (DFG).
 ISBN: 978-3-527-27764-3

## 8.1 Introduction

The calculation of water and substance balances at a regional scale is important for predicting landscape developments and management strategies. Under the given specific geologic conditions of the younger Pleistocene of NE Germany, the flow and discharge of groundwater are the main components in understanding the hydrologic and substance system. Common complex deterministic models such as PHREEQC or FEFLOW can be used to describe hydrochemical processes and analyse the groundwater flow component in the field scale. At the regional scale, only simplified models based on Darcy's law/Piston flow approach and hydrochemical budget calculations can be useful. However, all deterministic modelling concepts require detailed information of the extremely complex hydrochemical and geologic situations. In the glacially formed pleistocene watersheds, a large amount of data (boreholes, profiles, measurements etc.) is required to obtain a detailed description of the complex hydraulic and hydrochemical situation. The large number of spatially distributed parameters which must be considered in a regional scale suggest, that field investigations and direct-measurement methods are too expensive and time-consuming for this assessment. An alternative to field measurements is the combination of process studies in a field scale with existing hydrogeologic and hydrochemical thematic informations and additionally, a systematic reducing of scale-dependent parameters to create a conceptional data model in a GIS environment. This approach, the support of GIS technology in combination with common deterministic modelling tools, allows to describe the hydraulic and hydrochemical properties of groundwater systems in a mesoscale region.

## 8.2 Material and Methods

The process of regionalization includes a conceptual replication of complex geologic and hydrologic conditions to serve as a base for numeric modelling of the hydraulic and chemical processes occurring in the aquifer. All required geographic and basic hydrological information are digitized data from thematic maps in combination with available data from public institutions, for example Geological Surveys and Environmental Offices. In addition, chemical analysis data and results of point measurements can be used and regionalized by geostatistic approaches (Davis, 1986; Schafmeister, 1999). All digitized information was converted from vector to grid format. The grid format represents a compromise between the requirements for resolving and the amount of information needed by the calculations. The main steps of further processing are:

- classification of the geologic, hydrochemic and hydraulic parameters and assignment to all grid points in the data model,
- reducing the spatial heterogeneity and aggregation of the parameters by a systematic schematization of the structure by GIS data model processing,
- deriving the regional data model from the aggregated and spatial connected parameter records and verification of the hydrogeologic plausibilities by GIS visual functions.

For hydraulic calculations, carried out in the Stoebber river watershed and in the Ucker river watershed, the required digitized topographic information was generated from existing topographic maps. The following classified geohydrologic information was digitized from a hydrogeologic map developed by the Central Geological Survey of the GDR (Hydrogeologische Karte HYKA 50, scale 1:50,000) to provide an area-wide overview of the hydraulic conditions of the different aquifers in the mesoscale region:

- distribution, thickness, and hydraulic conductivity of the existing aquifers,
- stratigraphic structure of the aquifers and barrier layers (aquitards),
- the thickness of the unsaturated zone,
- the equipotential surface of groundwater,
- identification of unconfined and confined groundwater conditions,
- identification of the hydraulic connections between different aquifers.

The spatial distribution of aquifer structure was determined by an estimation of the depth of the bases of the hydrogeologic units from the digital topographic information and the classified thickness of the unsaturated and saturated zones (Fig. 8.1).

The depth was controlled by the calculated groundwater head, the water and pressure conditions in the aquifer as well as by known drilling profiles. Hydraulic parameters, for example the classified hydraulic conductivity, were assigned to each layer of this geometric model from maps and additional measurements.

The information from the maps is not sufficient to assign all the parameters needed in the model. Some parameters, such as thickness of aquitards and aquifuges are not available from the HYKA 50 and were supplemented by data from drilling profiles and expert knowledge. Unknown hydraulic parameters like the effective porosity, which is an essential parameter for each grid element, can be calculated from the saturated hydraulic conductivity based on functions and algorithms (Busch et al., 1993; Abbott and Refsgard, 1996).

The spatial distribution of the potential head was calculated based on geostatistics from thematic point information and measurements from observation wells (Hutchinson, 1989). The potential head was used to define the groundwater divides, the 1$^{st}$ and 2$^{nd}$ order boundary conditions and the initial conditions of the groundwater modelling.

In addition, combining spatial digital topographic information enables the spatial construction of unknown parameters, e.g. the calculation of the depth to the groundwater table from the ground surface and the groundwater surface level. The digitized information was converted from vector to grid format. Due to the map scale of 1:50,000, a grid size of 50 m seemed to be adequate.

From this thematic information, a geohydrologic data model was developed to be used by both the groundwater modelling system FEFLOW (Diersch, 1993) and the groundwater component of the integrated hydrologic modelling system MIKE-SHE (Abbott et al. 1986). Calibration was achieved using a steady-state solution of the groundwater flow.

In order to use the data model with FEFLOW, MODFLOW or MIKE-SHE the geologic layers and aquifers must be transformed into representative layers subject to mathematical calculation. The transformation is mainly managed by the GIS data

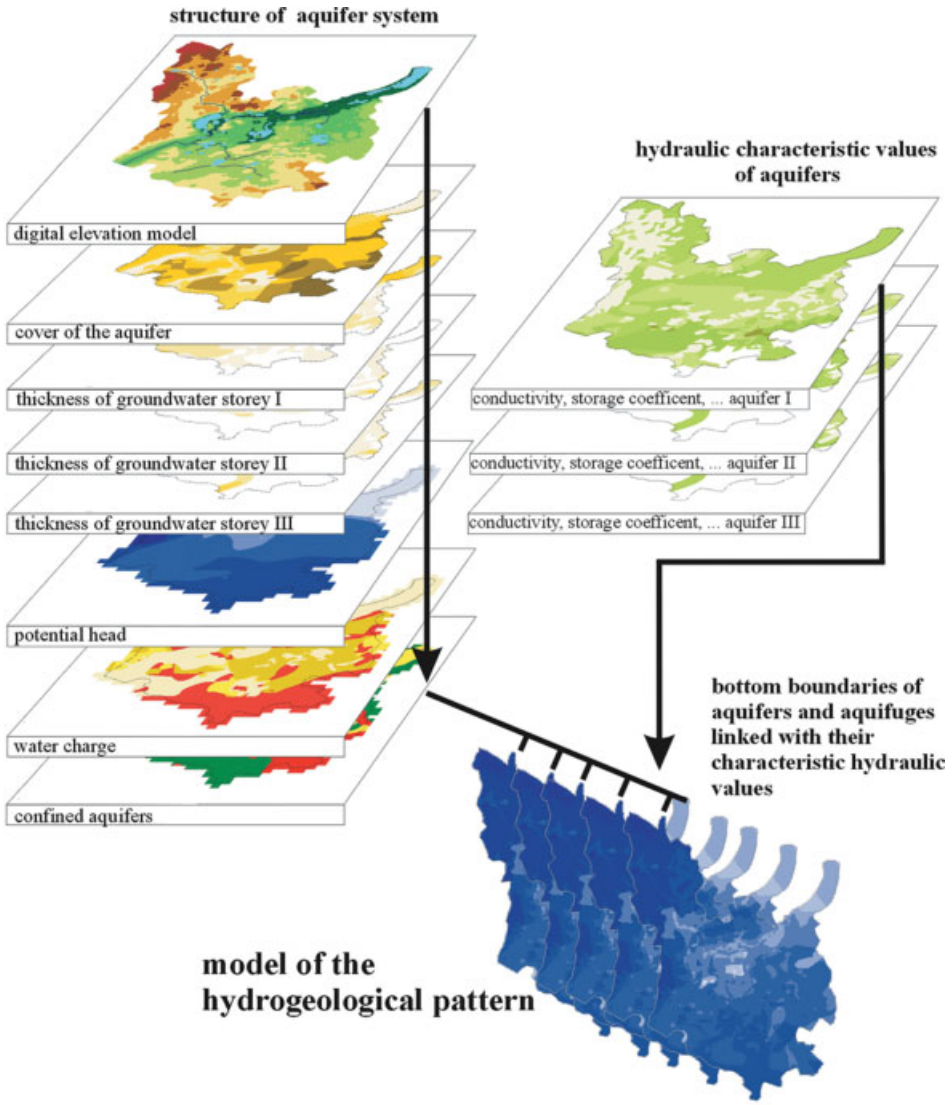


Figure 8.1: Deriving the hydrogeologic data model for the Stoebber watershed (220 km$^2$).

model. GIS was used as well to resample the grid size and the aggregation level by several schematization steps without the loss of essential information.

The derived hydrogeologic data model is very complex due to the natural conditions of the pleistocene lowlands. Therefore, the model must be adjusted to the complexity of the questions to be answered, as well as to the requirements of the deterministic models with respect to their structure and numeric format. The data models have to be synthesized taking the different calculation algorithms (finite element models and grid-oriented finite difference models) into account. This means to adjust the discretization structure according to irregular triangles of different densities or regular grid elements. Moreover, MIKE-SHE as a complex integrated watershed model with coupled saturated and unsaturated zones requires a number of additional complex parameters (Steidl et al., 1997). FEFLOW needs more respect to the structure of the numeric-geologic slice model to avoid errors during the interpolation between calculation layers with high gradients (for example sudden change of the hydraulic conductivity).

## 8.3 Results

### 8.3.1 Stoebber Watershed

Initial investigations were carried out in the Stoebber river watershed located 50 km east of Berlin. The river valley lies between end moraines deposited 15,000 years ago during the Weichsel glaciation. The glacial deposits here are very complex, as are most of the younger pleistocene sediments of NE Germany. Six hydrologically distinct aquifers are present in the watershed. Extremely intense hydraulic interchanges, especially between the three youngest aquifers, result from erosional processes which strongly altered the marly sediments of the aquitards. In the valley, the aquifer is covered only by a thin layer of sandy sediments. Taking the short flow times and minor protection into consideration, these regions are very sensitive with respect to land use changes and their influence on groundwater quality (Wurbs et al., 1999).

The calculations with FEFLOW and MIKE-SHE were carried out in the Stoebber watershed based on the derived $50 \times 50$ m data model. In this case a grid size resolution for the groundwater model of $500 \times 500$ m was used. The data model was calibrated based on the known potentiometric surface of the groundwater. The results, lying in between the preset error limits, fit well into the geohydrologic situation showing low gradients in the groundmoraine-dominated tablelands and high gradients in the transition zones towards the river valley (Fig. 8.2). Differences between calculated steady-state and measured values are tolerated up to a value of 2 ‰ in groundwater slope, but not more than 1.0 m in groundwater heads. In the case of higher deviations corrections and adaptations in the data model are generally made by varying the hydraulic conductivity and/or revising the hydrogeologic model (for example variation of the aquifer and aquitard thicknesses until the model converges with the known values).

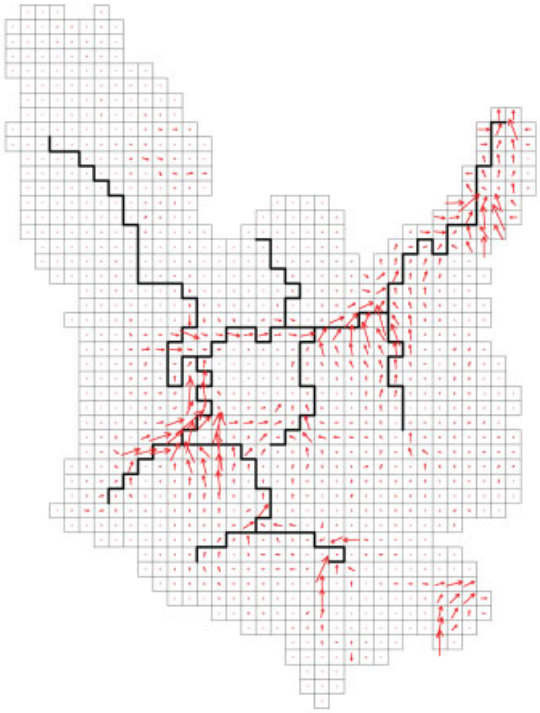

Figure 8.2: Groundwater velocities in the Stoebber watershed, calculated with MIKE-SHE.

## 8.3.2 Oderbruch

### 8.3.2.1 Introduction

The Oderbruch with an area of almost 800 km$^2$, is the largest river polder area of Germany. The majority of the area is intensively used for agriculture. In the east, the boundary of the polder is the Oder river, and in the west, the ground moraine of the Barnim/Lebus plateau.

Since the diking of the Oder 250 years ago, the polder area is at a lower level than the main river and water from the Oder infiltrates the groundwater table year-round. The groundwater from the Oder as well as inflowing water from the plateau is led out of the polder area by a drainage ditch network stretching over the entire Oderbruch. This drainage ditches provide a matter sink/source for heavy metals under exfiltrating conditions.

In the context of the DFG priority programme “Geochemical processes with long-term effects in anthropogenically affected seepage and groundwater”, numerous investigations have been carried out within the last five years concerning chemical

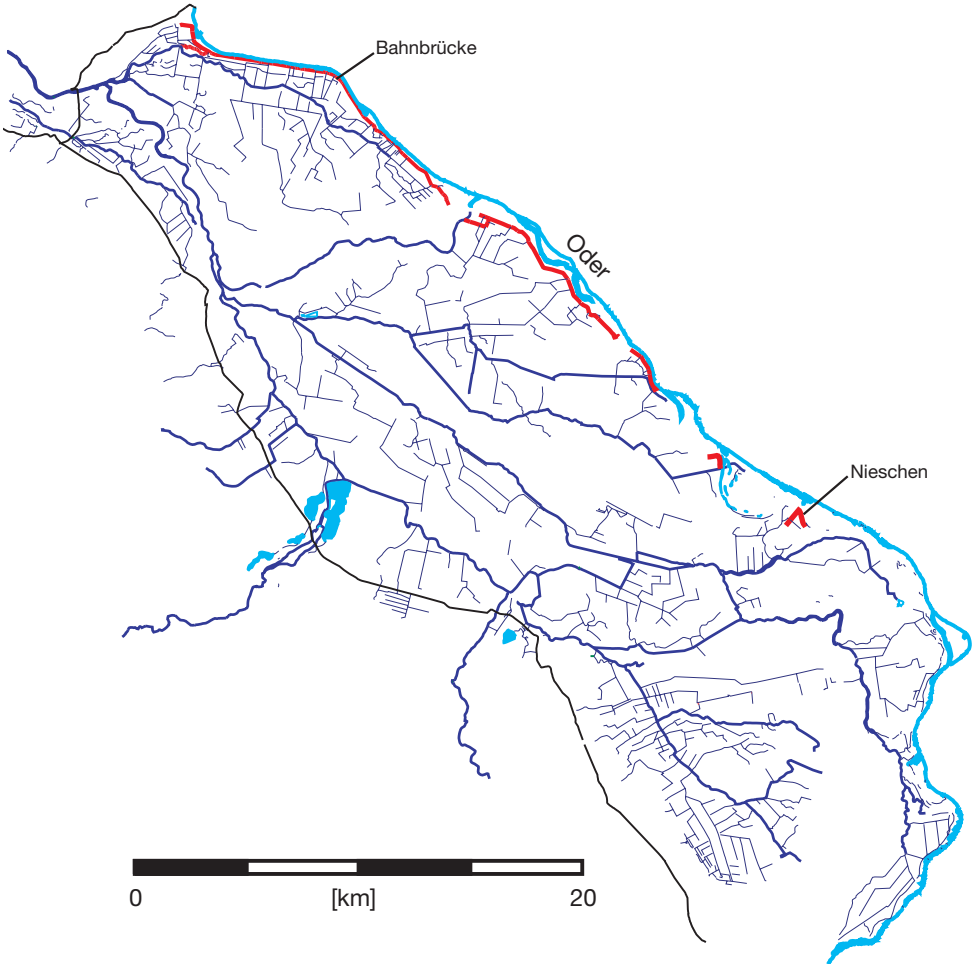


Figure 8.3: Regional map of the Oderbruch with the ditch system and location of the investigation sites. The active ditches behind the dykes are coloured with red lines.

processes in groundwater. Regarding the hydrochemistry and the solid material investigations, the work is centered on the characterization and modelling of the processes at the contact zone between the anoxic aquifer and the oxic ditch systems. The research allows for statements concerning the balancing of the substance dynamics under long-term effects of the anoxic aquifer/oxic ditch system with particular consideration of the migration behaviour of iron and manganese. Given specific hydrogeologic and hydrochemical conditions, the flow and discharge of groundwater into the surface waters is one of the main components in understanding the hydrologic and substance system in the Younger Pleistocene lowlands of NE Germany.

### 8.3.2.2 Material and Methods

*Field Investigations*

The detailed recording of the processes at the contact zone of the anoxic aquifer and oxic surface water were carried out for a ditch with exfiltrating but seasonally dry conditions. The measurements are based on a transect with groundwater observation wells installed at different depth. Sampling was carried out at intervals of 2 months.

The analysis of the sediments at various depths of the aquifer was carried out by using different leaching agents for specific leaching fractions: Na-dithionite and 0.2 M oxalate (oxides and hydroxides), 1 M HCl (acid volatile sulfides), acetic Cr(II) for pyrite (Canfield et al., 1986; Cornell and Schwertmann, 1996; Hsieh and Yang, 1989).

The key processes were identified by the precise analysis of the hydrochemistry in connection with modelled hydraulics. Flow paths and exfiltrating rates needed for the accounting of the substance balance were determined by the hydraulic groundwater model FEFLOW. For the calculation of the geochemical processes, inverse modelling with the thermodynamic programme PHREEQC (Parkhurst, 1995) was used. Like the programme NETPATH (Plummer et al., 1990), PHREEQC offers the possibility to calculate mass transfer along a specific flow path with respect to changes of quality. Additionally, it is possible to consider mixing effects of several initial waters.

### 8.3.2.3 Results

*Hydraulic Modelling*

The calculated flow paths near the transect in *Nieschen* show an increasing influence of the groundwater level raising up towards the ditch floor (Fig. 8.4). Near the eastern edge of the ditch, the influence decreases rapidly. This exfiltration zone is dominated by intensive mixing effects of deep and shallow groundwater. The total exfiltration rate, calculated for 1999, reached 202 $m^3/m^2$.

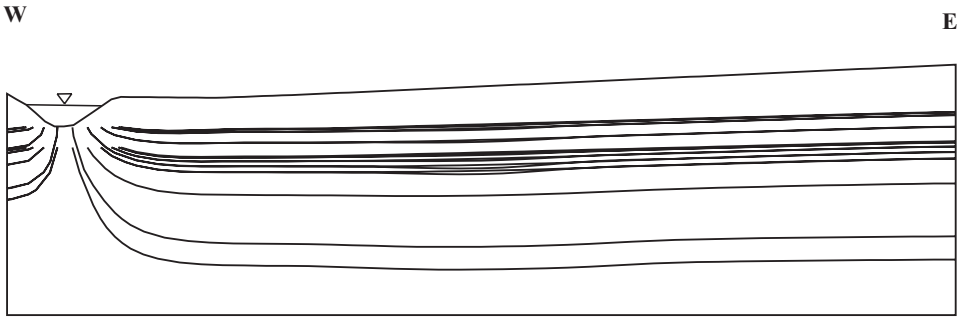


Figure 8.4: 2D-description of the flow path under exfiltrating conditions calculated with FEFLOW using a classified $k_f$-value distribution.

*Geochemical Modelling*

*Exfiltration Phase*. Generally, zones of high substance dynamics can be separated into a zone under the eastern ditch shoulder and in a second zone below a plume of reducing conditions under the ditch floor. Near the eastern ditch edge, a mixing of shallow groundwater and deep, anaerobic groundwater at a ratio of nearly 8:2 can be observed (Fig. 8.5). In a first step the mixing values were calculated on the basis of chloride concentrations. Based on these ratios and the measured chemical parameters in the groundwater observation wells, a inverse modelling with PHREEQC was carried out to determine the chemical processes during the different hydraulic phases. Figure 8.5 shows the schematic description of the flow path, the mixing ratios and of the modelled turnover ratios of iron reactions. During the exfiltration phase, the mixing process is combined with the degradation of the organic matter by iron reduction (Lovley, 1991). Near the eastern ditch edge the model shows iron reduction proceeding with 0.016 mmol Fe/L. Directly below the ditch floor, iron reduction proceeds with 0.004 mmol/L, caused by shallow groundwater and deep groundwater mixing at a ratio of 3:7. In the surface water of the ditch and in the bottom sediments, oxidation processes dominate under nearly neutral pH conditions. Dissolved $Fe^{2+}$ ions with a concentration of 0.024 mmol/L precipitate as $Fe(OH)_3$.

With rising hydraulic gradients, deep groundwater has an increasing influence. The increase of deep groundwater up to a ratio of 9:1 results in a distinct change of thermodynamic equilibrium in the direction of sulfide precipitation. This process is confirmed by the results of the sequentional bounding analysis which show an increasing sulfide fraction. Investigations of $^{34}S/^{32}S$ isotope fractioning should give more detailed information with respect to this process.

*Drying-up Phase.* When water levels in the Oder river drop, the ditch in *Nieschen* runs dry. This change of hydraulic conditions creates a total change in the environmental conditions. The hydraulic gradient in the direction to the ditch changes into a horizontal ground-

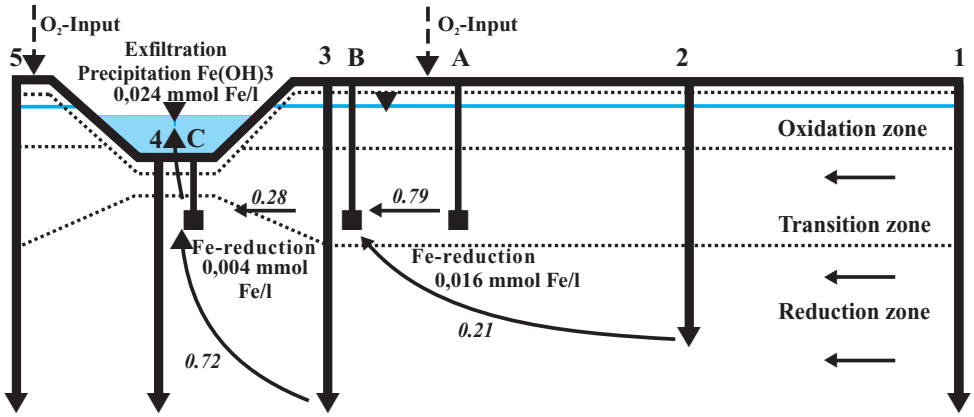


Figure 8.5: Schematic description of the flow path (arrows), mixing ratios (italics) and calculated turnover ratios of iron reactions under exfiltrating conditions.

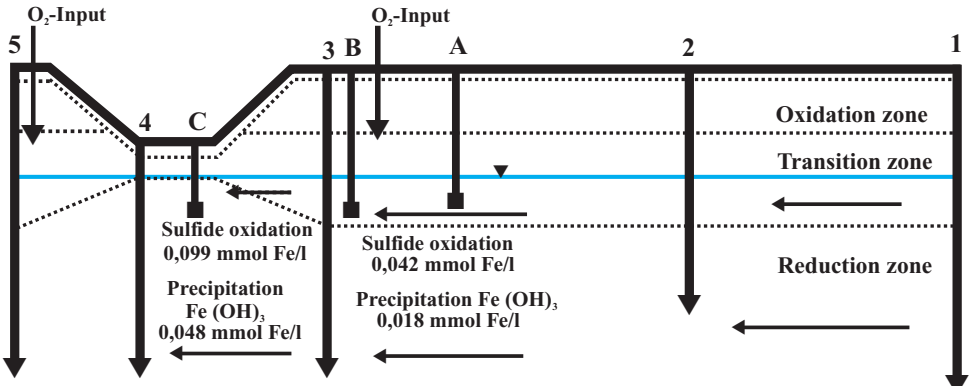


Figure 8.6: Schematic description of the flow path (arrows) and calculated turnover ratios of iron reactions under dry conditions.

water flow under the ditch (Fig. 8.6). A high substance flow can be observed between the groundwater observation wells (GWO) A–B and B–C. Due to the lowering water level, oxygen is diffusing into the aquifer, triggering sulfide oxidation at the outer margin of the reduction zone (see GOW B) and at the anaerobic plume located under the ditch.

The concentrations of dissolved iron and sulfate do not show a stoichiometric ratio, indicating a pyrite solution. The concentration of the sulfide ions is significantly higher. Verifying the $Ca^{2+}$, $Mg^{2+}$ and $SO_4^{2-}$ concentrations, there is no evidence for the influence by seepage water. Therefore, as an explanation, a combination of parallel processes is favoured: the oxidation of pyrite, and subsequently, the precipitation of iron oxides (Appelo and Postma, 1996).

*Balance Calculations*

The regional balance calculation is based on a GIS data model consisting of the geographic distribution of the drainage system and the derived hydraulic and geochemical properties. The regional characterization was carried out by a hydrogeologic mapping and a classification of characteristic ditch types by hydraulic and geochemical parameters. The main investigation is focused on the ditches positioned parallel to the dykes because this zone shows the highest hydraulic and hydrochemical gradients (Fig. 8.3). Three exemplary ditch types could be distinguished: drying up/exfiltrating, permanent exfiltrating and not active.

Regarding the different ditch types, the exfiltrating rates and the geochemical characteristics for the studied processes were determined in two selected exemplary ditch compartments: For the drying up/exfiltrating type a ditch located in the southern part of the Oderbruch with a length of 0.8 km (*Nieschen*) and for the permanent exfiltrating type a ditch compartment in the northern part, named *Bahnbrücke*, with a length of 2.2 km. For calibration, the hydraulic situation was characterized by a relative simple measurement system consisting of 8–10 groundwater observation wells respectively, to derive hydroisohypes and hydraulic gradients between groundwater and the surface water. The exfiltration rates were determined by run off measurements in the ditch compartments using level

analysis and a flow induction meter. At selected sampling points, the hydraulic conductivity of the ditch floor was measured with a high pressure permeameter. The geochemical characterization was carried out by a characterization of the ditch bottom by core sampling and measurements of the iron concentration and detailed process studies in *Nieschen* (Section 8.3.2.3). The connection of the measured parameters with the digital data model was realized by GIS.

The model site *Nieschen* shows a complex geologic structure (Fig. 8.7). Impermeable layers dominate in the southern parts ($k_f$ 1 × $10^{-7}$ m/s) and more sandy layers the northern parts ($k_f$ 5 × $10^{-4}$ m/s). The colmatation layer showed values about 2.2 × $10^{-5}$ m/s. For the sandy parts the exfiltrating rates, calculated with FEFLOW at the transect *Nieschen*, reaches 202 $m^3/m^2$ for 1999. The total discharge for *Nieschen* was calculated regarding the time depending gradients and the spatial distributed hydraulic conductivity and validated by run off measurements. Figure 8.8 shows the exfiltrating rates for 1 day, one year and the accumulated exfiltration values for 35 years.

Assuming an average iron concentration of 0.024 mmol/L $Fe^{2+}$ below the ditch floor in the anoxic aquifer and ignoring precipitation and adsorption potential, more than 6700 kg iron migrates into the surface water for a period of 35 years. But sediment extractions with dithionite and $HNO_3$ show iron concentrations up to 45 g/kg sediment. Regarding the sediment volume below the ditch segment of 1 km length, 6500 kg iron accumulated in the sediments of the ditch. Therefore, more than 90 % of the iron is precipitated mostly as Fe(III)hydroxides under oxidizing conditions. The rest, < 10 %, migrates as colloids into the surface water generating the significantly red precipitations of ferrihydrite.

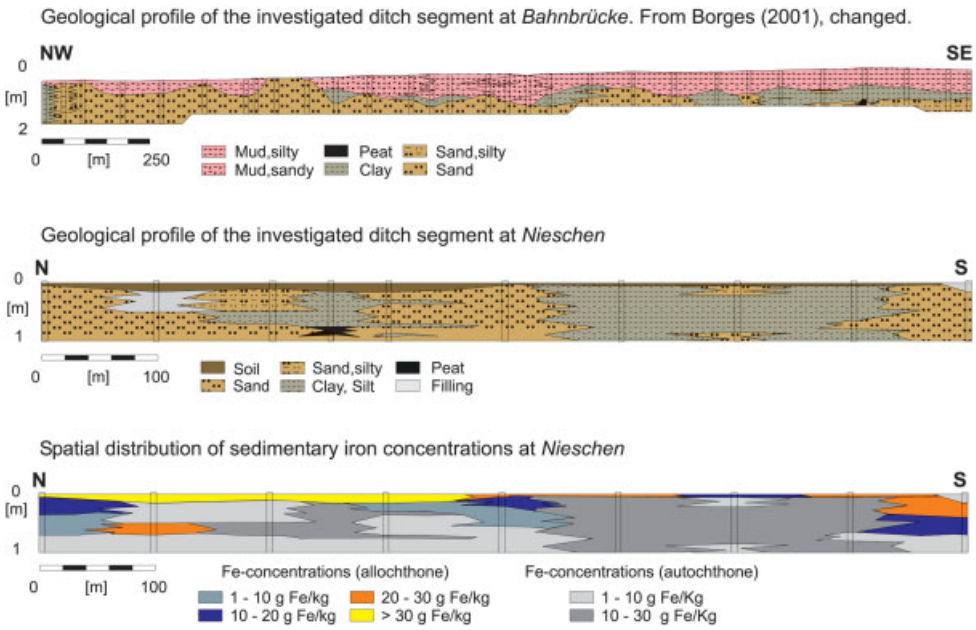


Figure 8.7: Geological profiles of the investigation sites *Nieschen* and *Bahnbrücke.*

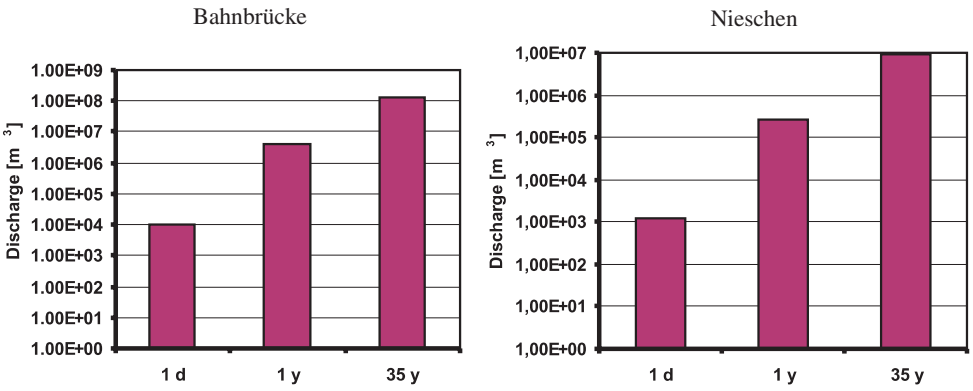


Figure 8.8: Calculated exfiltration rates at *Bahnbrücke* and *Nieschen*.

For manganese, the enrichment reaches 191 kg in the investigated ditch segment (1 km length). With average $Mn^{2+}$ concentration of 0.004 mmol/L in the exfiltrating anoxic groundwater, a potential enrichment of manganese at a magnitude of 31.5 kg occurs. In the context of 35 years, this corresponds to 1100 kg of accumulated manganese. The relatively low enrichment at the sediments below the ditch floor implies that more than 85 % of the manganese is not fixed, rather it is carried immediately into the ditches as dissolved $Mn^{2+}$ ions (Postma and Appelo, 2000). Another explanation is that manganese is carried into the ditches after precipitation as $MnO_2$, reduced by an immediately subsequent oxidation of $Fe^{2+}$ (Matsunaga et al., 1993). Laboratory investigations under controlled environmental conditions with $^{59}Fe$ and $^{54}Mn$ confirm the different fixing rates of manganese and iron, but provide no evidence to the process of manganese migration.

The permanent exfiltrating investigation site *Bahnbrücke* covers a ditch section of 2.2 km length. The width varies between 2.9 and 3.5 m. The structure of the ditch floor is shown in Fig. 8.7. Impermeable layers dominate in the southern parts ($k_f$ values between $5 \times 10^{-6}$ and $5 \times 10^{-8}$ m/s) and more sandy layers the northern parts ($k_f$ $5 \times 10^{-4}$ m/s).The total discharge, regarding the time depending gradients and the spatial distributed $k_f$-values, are shown in Fig. 8.8. With constant $Fe^{2+}$ concentration in the exfiltrating groundwater and constant exfiltration rates of 560 $m^3/a/m^2$, the quantity of iron discharge corresponds to 200 tons exfiltrated iron during a 35-year period. Sediment extractions show iron precipitate concentrations of 19,000 kg in the sediments of the ditch segment (2.2 km length). These results indicate, that less than 10 % of the mobile iron accumulated in the floor sediments of the permanent exfiltrating ditches.

*Processing of the GIS Data Model.* In a final step the mass balances are regionalized and applied for the whole classified ditch system. The spatial heterogeneity of the hydraulic and hydrochemical parameters are reduced by a systematic schematization of the ditch structure by GIS data model processing. The required geographic and basic hydrological information are digitized data from thematic maps of the Oderbruch

region and combined with the available data from the field investigations. The main steps of further processing are:

- aggregation and classification of all available geologic, hydrochemic and hydraulic parameters and assignment to all grid points,
- deriving the regional data model from the aggregated and spatial connected parameter records,
- verification of the plausibilities by GIS visual functions and calibration of the model by run off field measurements.

The digitized information was converted from vector to grid format. The grid format represents a compromise between the requirements for resolving the drainage structures and the amount of information needed by the calculations. GIS processing is carried out by a grid calculation of the whole ditch system near the dykes, length 39 km. Due to the map scale of 1:10,000, a grid size of 100 m seemed to be adequate.

Hydraulic parameters like $k_f$ values and the colmatation layer thickness were derived from measurements, a digitized map of the alluvial soil thickness and geostatistic calculations. The classified parameters were assigned to each grid point of the geometric ditch model. From this information, a specific data model was developed and connected with an uncomplex self constructed model based on the Darcy equation to calculate the exfiltration rates (Fig. 8.9).

The spatial distribution of the hydraulic head was calculated based on measurements and a digitized map of the groundwater contour lines. The hydraulic head of the groundwater was used to define the 1st and the potential head of the ditch as boundary condition 3rd order. For calibration the exfiltration rate (Q) is determined by run off measurements:

$$Q = (Q_{m+1} - Q_m) / L \tag{1}$$

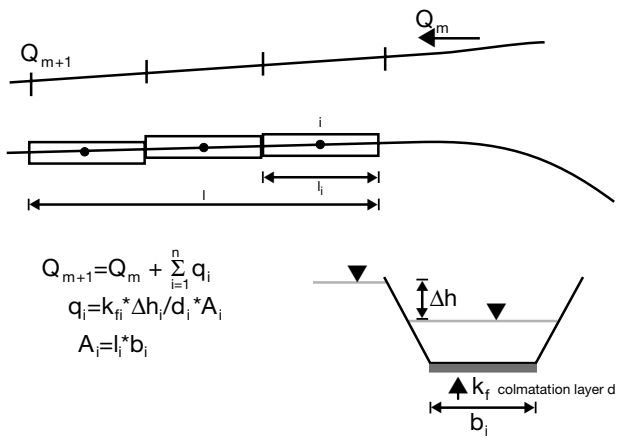


Figure 8.9: Schematic description of the grid model and the numeric calculation of the exfiltration rates. Grid cell size $l_1 \triangleq 50$ m.

In combination with the hydrochemical process studies the mass balance of the trace metals can be calculated for all ditch compartments. For substance balance calculation the spatial distributed parameters of metal enrichment, stratigraphic structure and the permeability of the ditch floor were determined in *Nieschen* and *Bahnbrücke*. They are aggregated by GIS processing and assigned to every classified ditch element.

Validation of the hydraulic model was achieved using a steady-state solution of the groundwater flow and exfiltrating rate calculated by the groundwater modelling system FEFLOW. These calculations are carried out at a transect in *Nieschen* (see Section 8.3.2.3). Detailed geologic and hydraulic data and long term measurements enables an exact parameterization of the exemplary ditch types.

### 8.3.3 Ucker Watershed

In a further case study in the Ucker River basin (2400 $km^2$) in NE Germany, the possibilities of construction and validation of described hydrogeologic data models for modelling the substance transport in pleistocene aquifers is carried out at the regional scale. Following Wendland and Kunkel (1997), first calculations of average effective groundwater velocities were made by self-designed GIS tools, using a simple Darcy approach (Steidl and Dannowski, 1999). The spatial distribution of the derived groundwater slope and the classified hydraulic properties of the upper aquifer served as hydrogeologic input information. Depending on the location, the calculated groundwater field velocities vary between less than 5 m/yr to more than 2000 m/yr and demonstrate the enormous heterogeneity in this region. Certainly, this approach is not an exact deterministic groundwater modelling. But considering the direct connection between surface and groundwater (in the sense of effective recipients), the residence time of groundwater along its flow path between the moment of entry into the upper aquifer and the surface water has to be calculated (Fig. 8.10). The considered hydrogeologic situation and the identification of the source regions and their hydraulic connection to the exfiltration area near the surface waters is demonstrated by the pattern of the calculated residence times which varies from less than 2 years up to more than 500 years. Large areas have typical long residence times resulting from a long path or slow groundwater velocities or both. Shorter groundwater residence times occur in areas located in the immediate vicinity of effective recipients or in regions with higher hydraulic gradients.

Balancing the environment-dependent reaction ratios and matter transport in the groundwater a characterization of the hydrodynamic and stratigraphic conditions in the subterranean catchment area is prerequisite. Environmental conditions, especially redox- and redox transitions zones, are influenced by geological/stratigraphic heterogeneities and hydraulic conditions. Redox processes are mainly controlling the spatial and chronological evolution of reaction processes. Therefore, the qualitative and quantitative description of the matter transformation processes occurs primarily under the consideration of redox processes characterized by the chemical environment in the micro scale as well as in the macro scale. With internationally recognized thermody-

namic programmes like PHREEQC, precipitation-, solution- and ad-/desorption-processes can be calculated in the groundwater. But still, the regionalization of individual point measurements, without loosing information, is a main problem.

Based on exact process studies in selected validation areas (like the redox studies in the Oderbruch region) chemical indicator elements can be used to characterize the environmental conditions with sufficient accuracy. Using the GIS data model, the interpretation of the region by characterizing distinct geohydraulic properties of the different catchment parts in connection with the derived hydrochemical conditions enables a comprehensive spatial hydraulic-chemical characterization on basis of the main chemical characteristics in the identified aquifer complexes. Considering the results of the hydrochemical calculations in the anoxic aquifer in the Oderbruch and at the interface between this aquifer to surface waters, iron measurements in connection with the common hydrochemical parameters can be used to characterize the redox con-

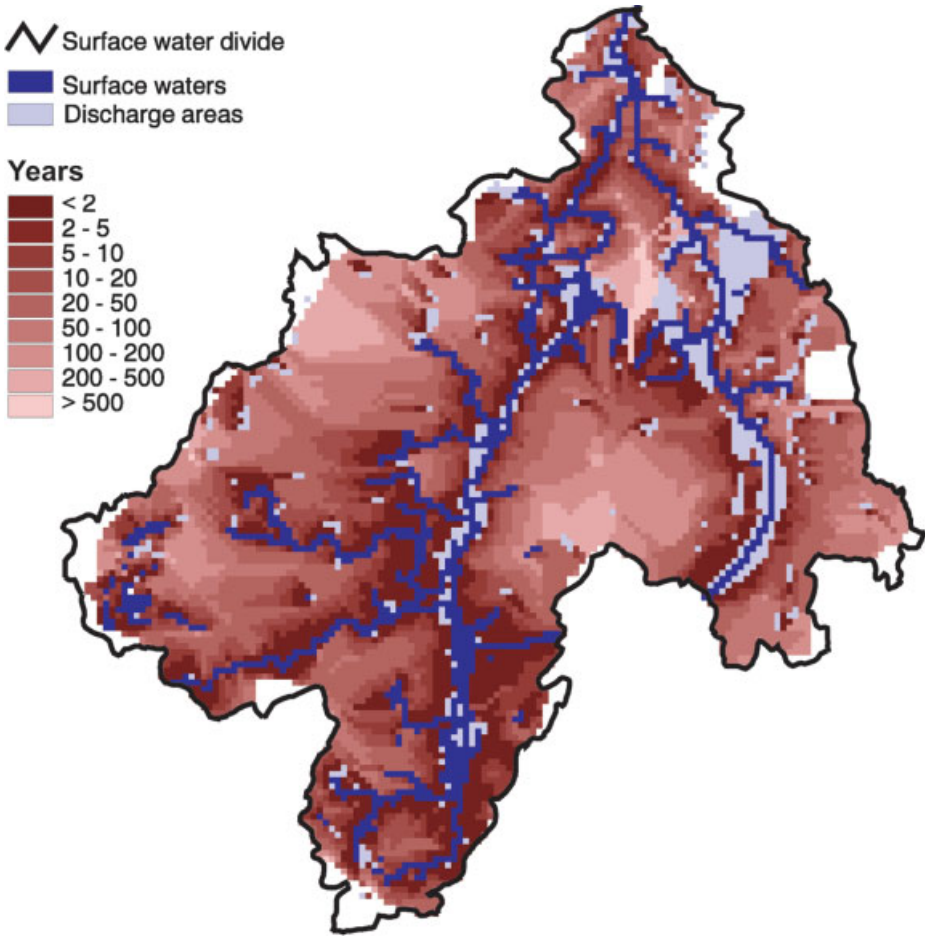


Figure 8.10: Calculated average residence times of groundwater in the Ucker watershed (2400 km$^2$).

ditions and calculate the redox-depending balance and degradation rate of selected substances.

In addition, analysis data and calculation results of individual measurement points can be regionalized by geostatistic approaches (Schafmeister, 1999). Chemical analyses of installed groundwater observation wells as well as data of public institutions, for example Geological Surveys and Environmental Offices, are used.

## 8.4 Discussion

The geohydrologic structure of the pleistocene landscape is very complex with a high variety of the hydraulic and hydrochemical parameter distribution. Therefore various discharge processes result, with complex connections to the hydrological and geochemical system behaviour. Besides, the NE German region is a low precipitation area with significant drying up periods strongly affecting the hydrologic system.

Sufficient knowledge of the hydrogeologic situation is the basis for modelling the regional substance flow. However, regarding the mesoscale, field investigations and direct-measurement methods are too expensive and time-consuming for providing the required geohydrologic data. Therefore a method was developed to derive a comprehensive conceptional data model to calculate the water and substance flow in typical pleistocene aquifer systems. The combination of common deterministic groundwater tools and the conceptional database adapted to different aggregation levels enables modelling at the regional scale using the advantages of the deterministic and conceptional modelling approaches.

The introduced modelling concept allows the solution of different questions regarding the water and substance flow in the landscape. The conceptional approach allows to determine different levels of the data set aggregation. Aggregation, that means no precision lowering of single parameters, but the fitting of parameter records to different model specifications. The base of this approach is the implementation of parameter transfer functions, the determination of parameter sensitivities by process studies at the field scale, and expert knowledge.

Hydrogeologic maps and other thematic information represent the basis of the derived data model. But additional information is needed for complete parameterization. To create a 3D data model, in addition to thematic maps, point informations and measurements are required.

At the regional scale, more and more questions occur regarding the pollution of surface waters by exfiltrating groundwater which is influenced by agricultural contaminants. In the younger pleistocene landscapes most of the water pollution results from diffuse agricultural pollution in combination with intensive water management operations. These operations, for example intensive drainage and groundwater lowering in wetlands and polder areas, derange the source and sink function of the system and should be discussed and evaluated by social and scientific criterions (Quast et al., 2000).

Especially in the Oderbruch region, influenced by intensive agriculture and water management, the calculation of the regional substance balance is substantial to create sustainable management strategies. The model approach in this region clarifies, that knowledge about the major processes is prerequisite for a conceptional processing of the database. Exact identification and quantification of the process parameters are needed to obtain relevant modelling results regarding the regional substance balance.

The results of the process studies show that the hydrochemical processes are characterized by the changing hydraulic situation of the ditches. In the main investigation site *Nieschen*, the deep, anoxic groundwater rises and mixes with shallow, low oxygen content groundwater in different relations regarding normal to high water levels. In connection with this mixing process, iron reduction and oxidation occurs with turnovers between 0.016–0.024 mmol Fe/L. Below the ditch floor, through precipitation, $Fe^{3+}$ is highly enriched as precipitated $Fe(OH)_3$. During the low water level situation oxidation takes place with turnovers between 0.05 and 0.1 mmol/L iron.

Initial local balance calculations show an enrichment of 90 % of the exfiltrated iron below the ditch floor, accumulated in 35 years since the construction of the ditch. The enrichment of manganese below the ditch floor reaches only 15 % of the total exfiltrated amount.

In a final step regional balance calculations are planned. The calculations based on a GIS data model consisting of the geographic distribution of the drainage system and the derived hydraulic and geochemical properties. The regional characterization is carried out by hydrogeologic mapping and a classification of characteristic ditch types by hydraulic and geochemical parameters. The main investigation is focused on the ditches positioned parallel to the dykes because this zone shows the highest hydraulic and hydrochemical gradients. With the described GIS technology and different aggregation steps the mass balances are regionalized and applied for the whole classified ditch system.

In opposite to the model approach in the Oderbruch region, which is based on detailed process studies, the modelling of substance flow in larger catchments ($> 2000$ km$^2$) is carried out by a more intensive aggregation of the database. This modelling approach is not focused on the exact description of the natural heterogeneities of the geologic and stratigraphic situation. To calculate diffuse agricultural pollutant transport, the identification and classification of the flow paths is the main element. That means not an exact calculation of the 1D flow path, possibly calculated by the common groundwater models (MODFLOW, FEFLOW etc.), but the identification of the source regions and their hydraulic connection to the exfiltration area near the surface waters. The created GIS data model enables a hydrologic and hydrogeologic interpretation of the region to characterize the different catchment parts with distinct geohydraulic properties under consideration of the main paths of substance discharge: drainage, groundwater discharge, seepage and interflow. Only for validation a detailed deterministic hydraulic modelling is carried out in selected catchment parts using FEFLOW and/or MODFLOW.

The conceptional data models combined with common deterministic models are useful for practical groundwater flow and matter transport simulations in regions larger than 500 km$^2$. In connection with GIS technology, large amounts of data specifying heterogeneous conditions may be condensed allowing aggregation processes for the necessary resolution and conceptional adaptation to the regional scale.

## 8.5 References


Abbott, M. B.; Bathust, J. C.; Cunge, J. A.; O'Connell, P. E.; Rasmussen, J. (1986): An introduction to the European Hydrological System – Systeme Hydrologique Europeen, SHE' 2: Structure of an physically based distributed modeling system. *Journal of Hydrology* **87**, 61–77.

Abbott, M. B.; Refsgard, Ch. (Eds.) (1996): Distributed Hydrological Modeling. p. m., Water science and technology library, v. 22, pp. 321, Dortrecht/Boston/London.

Appelo, C. A. J.; Postma, D. (1996): Geochemistry, groundwater and pollution, pp. 535, A. A. Balkema, Rotterdam.

Borges, S. (2001): Quantifizierung der Transferfunktionen des Laufgrabens im influenten Grundwassersystem des Oderbruchs bei Neurüdnitz in Brandenburg. Diplomarbeit am Institut f. Geol. Wissenschaften der EMAU Greifswald.

Busch, K.-F.; Luckner, L.; Tiemer, K. (1993): Geohydraulik, Geb. Borntraeger Berlin, pp. 497, Stuttgart.

Canfield, D.E.; Raiswell, R.; Westrich, J. T; Reaves, C. M.;Berner, R. A. (1986): The use of chromium reduction in the analysis of reduced inorganic sulfur in sediments and shales. *Chemical Geology* **54**, 149–155.

Cornell, R. M.; Schwertmann, U. (1996): The Iron Oxides, pp. 573, VCH Verlagsgesellschaft, Weinheim.

Davis, J. C. (1986): Statistics and data analysis in geology.– 2. Edition, p. 646; John Wiley & Sons, New York.

Diersch, H.-J. (1993): GIS-based groundwater flow and transport modeling – The simulation system FEFLOW. In: Praxis der Umwelt-Informatik, Band 4 (Rechnergestützte Ermittlung, Bewertung und Bearbeitung von Altlasten) (Ed.: Ossing, F.), Metropolis-Verlag, Marburg, pp. 187–208.

Hsieh, Y. P.; Yang, C. H. (1989): Diffusion methods for the determination of reduced inorganic sulfur species in sediments. *Limnology Oceanography* **34**, 1126–1130.

Hutchinson, M. F. (1989): A new procedure for gridding elevation and stream line data with automatic removal of spurious pits. *Journal of Hydrology* **106**, 211–232.

Hydrogeologisches Kartenwerk der GDR, Hyka 50 (1987), Halle.

Lovley, D. R. (1991): Dissimilatory Fe(III) and Mn(IV) Reduction (1991). *Microbiological Reviews* **55**(2), 259–287.

Matsunaga, T.; Karametaxas, G.; Von Gunten, H. R.; Lichtner, P. C. (1993): Redox chemistry of iron and manganese minerals in river recharged aquifers: A model interpretation of a column experiment. *Geochimica et Cosmochimica Acta* **57**, 1691–1704.

Parkhurst, D. L. (1995): User´s Guide To PHREEQC – A computer program for speciation, reaction-path, advective-transport and inverse geochemical calculations: U.S. Geological Survey: Water-Resources Investigations Report 95–4227, pp. 143, Lakewood, Colorado.

Plummer, N.; Busby, J. F.; Lee, R. W.; Hanshaw, B. B. (1990): Geochemical Modeling of the Madison Aquifer in Parts of Montana, Wyoming and South Dakota. *Water Resources Research* **26**(9), 1981–2014.

Postma, D.; Appelo, C. A. J. (2000): Reduction of Mn-oxides by ferrous iron in flow system: Column experiment and reactive transport modeling. *Geochimica et Cosmochimica Acta* **64**(7), 1237–1247.

Quast, J.; Merz, Ch.; Steidl, J. (2000): Überlagerung von Grundwasserdynamik und Stoffumwandlungsprozessen in Grundwasserleitern von Flußauen mit eingedeichten Poldern. In: Friese, Witter, Miehlich, Rode (Eds.): Stoffhaushalt von Auenökosystemen, Springer-Verlag, 149–158.

Schafmeister, M. T. (1999): Geostatistik für die hydrogeologische Praxis, pp. 172, Springer Verlag.

Steidl, J.; Dannowski, R. (1999): GIS-base Analysis of the subsurface flow of dissolved Nitrogen into Ground and Surface Water. In: Diffuse entries in rivers of the Oder Basin. Ed.: Deutscher Verband für Wasserwirtschaft und Kulturbau (DVWK) e. V., Bonn. DVWK-Materialien 7/1999, XVI + pp.133.

Steidl, J.; Dannowski, R.; Schindler, U.;Müller, L. (1997): Parametrisierung hydrologischer Modelle jungpleistozäner Einzugsgebiete am Beispiel von MIKE-SHE.– Symposium Modellierung in der Hydrologie, Tagungsband, 371–372; Dresden.

Wendland, F.; Kunkel R. (1997): WEKU, a GIS-Supported stochastic model of groundwater residence times in upper aquifers for the supraregional groundwater management. *Environmental Geology* **30**, 1–9, Springer Verlag.

Wurbs, A.; Kersebaum, K. C.; Merz, Ch. (1999): Quantification of leached pollutants into the groundwater caused by agricultural land use – scenarios as a method for – quantitative risk assessment of groundwater pollution. In: Integrated Watershed Management in the Global Ecosystem, CRC, Boca Raton, Florida, 239–250.

# 9 The "Virtual Aquifers" – Concept as a Tool for Evaluation of Exploration, Remediation and Monitoring Strategies

Dirk Schäfer*, Andreas Dahmke, Olaf Kolditz and Georg Teutsch

## Abstract

Today virtual realities are used more and more frequently to simulate complex processes in systems which are hard to parameterise. Well-known examples from the industry are the simulation of car crash tests or the simulation of traffic for town planning. Here a concept is presented for the use of virtual realities to investigate exploration, monitoring and remediation strategies for contaminated aquifer systems.

Because of the heterogeneous spatial distribution of physical and chemical parameters such as hydraulic conductivity, Fe(II)/Fe(III)-mineral content models of aquifer systems are mostly limited by an insufficient amount of input data. The idea of virtual aquifers is to engineer a data set describing a virtual aquifer system in the computer as realistically as possible in order to simulate different monitoring and remediation strategies. The quality and limitations of such strategies can be evaluated without measurement of concentrations in the field, which is costly and not very helpful for this task. The capabilities of virtual aquifers to identify and solve problems in evaluation of natural attenuation processes will be presented in three examples.

## 9.1 Introduction

Transport, microbial and chemical processes relevant in the natural attenuation of contaminants in aquifers are complex and take place on different scales of magnitude from below pore scale up to macro scale. Exploration, identification and quantification of these processes are difficult in natural heterogeneous aquifer systems and often numerical models are used to interpret measured concentrations and to predict the future behaviour of a contaminant plume. Many model approaches therefore currently exist to describe reactive transport processes in contaminated aquifers (overviews: Steefel and

* Christian-Albrechts-Universität zu Kiel, Institut für Geowissenschaften, Angewandte Geologie, Olshausenstr. 40/60, 24098 Kiel; e-Mail: ds@gpi.uni-kiel.de



*Geochemical Processes: Conceptual Models for Reactive Transport in Soil and Groundwater. Research Report.* Deutsche Forschungsgemeinschaft (DFG).
 ISBN: 978-3-527-27764-3

MacQuarrie, 1996; Steefel and van Cappellen, 1998). Though these models are quite advanced in simulating processes, important input parameters such as the spatial distribution of hydraulic conductivity and of chemical parameters are unknown and the models are therefore poorly parameterised on the scale relevant for remediation measures.

One way of gathering more information on such heterogeneously distributed parameters is through collection of many data points for example by installation of a large number of multi-level sampling wells, such as has been done in Borden (e.g. Woodbury and Sudicky, 1991) or Cape Cod. But even this extensive sampling method cannot measure heterogeneous structures on a scale smaller than the distance of the wells or larger than the test site. For practical purposes this approach is far too expensive.

Another approach is the outcrop analogue model that has been developed for crude oil extraction (Flint and Bryant, 1993) and transferred to aquifers (Koltermann and Gorelick, 1996; Siegenthaler and Hugenberger, 1993; Webb and Anderson, 1996). In the outcrop analogue project the unsaturated zone of a specific sedimentological system was investigated and the spatial distribution for instance of hydraulic conductivity was measured at an outcrop. The determined structures could be transferred to the saturated zone since the geological genesis of saturated and unsaturated soil was similar. Based on these sedimentological, hydrological and geochemical information reactive transport processes could be calculated by numerical models for this specific aquifer system (Bersezio et al., 1999; Weissmann et al., 1999). The geological system of "braided river" aquifers was investigated at different sites in Southern Germany, the geological system of "meandering river" aquifers will be studied in the future.

Here, the "virtual aquifers" approach is to be used to investigate exploration, remediation and monitoring strategies. A synthetic heterogeneous aquifer is constructed based on statistical properties determined as described above only in the virtual reality of a computer. New test sites can be generated at low costs by modifying the data e.g. by Monte Carlo simulations or other stochastic methods. Though this generated data set does not describe a real natural aquifer, it is as near to reality as possible. In contrast to real aquifers the virtual aquifer has the advantage that its hydraulic and geochemical properties are exactly known at every point. Numerical models can be used without additional assumptions to simulate reactive transport processes of contaminants in this virtual aquifer resulting in concentration distributions which are very similar to real aquifer systems. With the help of virtual aquifers different strategies can be tested without much effort to explore and remediate the virtual contaminated aquifer. Since the distribution of concentrations in our virtual aquifer is exactly known it can be compared to the monitoring results, which is not possible in real aquifer systems.

In addition, virtual aquifers are a helpful tool for visualisation of remediation techniques and thus can be used to teach and convince problem owners, administrators, students and the public.

Three preliminary studies will be used to illustrate the use of virtual aquifers to identify problems in real aquifer systems. It will also be shown that there is a need for additional scientific research resulting in an outline of a "Virtual Aquifers"-project expected to commence in the year 2003.

## 9.2 Examples for the Use of the Virtual Aquifer Concept

### 9.2.1 Effect of Screening and Pumping Rate on Measured Concentrations in a Heterogeneous Aquifer

The concentrations measured in the plume downstream of a contaminated site are an important parameter for evaluation of the site. The concentrations of the contaminants are traditionally used as indicators for commencement of remediation or protection measures. Together with the concentrations of electron acceptors they are also indicators for degradation processes in the subsurface. However, a virtual heterogeneous aquifer will be used to investigate the changes of measured concentrations due to variation of screen emplacement in an observation well and due to different pumping rates.

A vertical slice of an aquifer with a heterogeneously distributed hydraulic conductivity is simulated in a two-dimensional model (Fig. 9.1). The hydraulic conductivity of the aquifer is assumed to follow a log normal distribution with an average hydraulic conductivity of $10^{-3.6}$ = 2.5 E–4 m/s, a standard deviation of log 0.8 and a correlation coefficient of 0.15 and 0.50 in thickness and length respectively. These statistical parameters are only more or less realistic assumptions since this example is not based on a real aquifer system.

Flow occurs from the left to the right side due to a gradient of 2.5 ‰, simulated by two constant head boundaries. The effective porosity of 20 % is assumed to be homogeneously distributed. The dispersivity for transport calculations is small, 0.5 m in longitudinal direction and 0.005 m in the vertical direction, since heterogeneities of hydraulic conductivity are already considered.

An idealised DNAPL in residual saturation contaminates the aquifer in the lower part near the inflow, simulated by a simple rectangular constant concentration boundary condition. In a homogeneous aquifer having the average hydraulic conductivity of the heterogeneous aquifer, first traces of the dissolved contaminant ($> 0.10\ c/c_0$) would arrive at an aquifer length of 45 m, hence, a virtual sampling well is placed at X = 42 m. The transport simulation in the heterogeneous aquifer (Fig. 9.1) shows that the concentrations have been transported about twice as far as in the homogeneous case due to preferential pathways. For investigation which concentrations are possibly measured three different sampling wells are assumed with a screen positioned:

a) within the contaminant plume,
b) downgradient of the contaminant source, but slightly above the plume,
c) over the entire thickness of the aquifer.

Figure 9.2 shows the concentrations measured in these different virtual sampling wells over time for three pumping rates respectively. The samples in the well screened within the plume (assumption a) show high concentrations immediately nearly independently of the pumping rate. The well is screened in a high permeable area of the aquifer

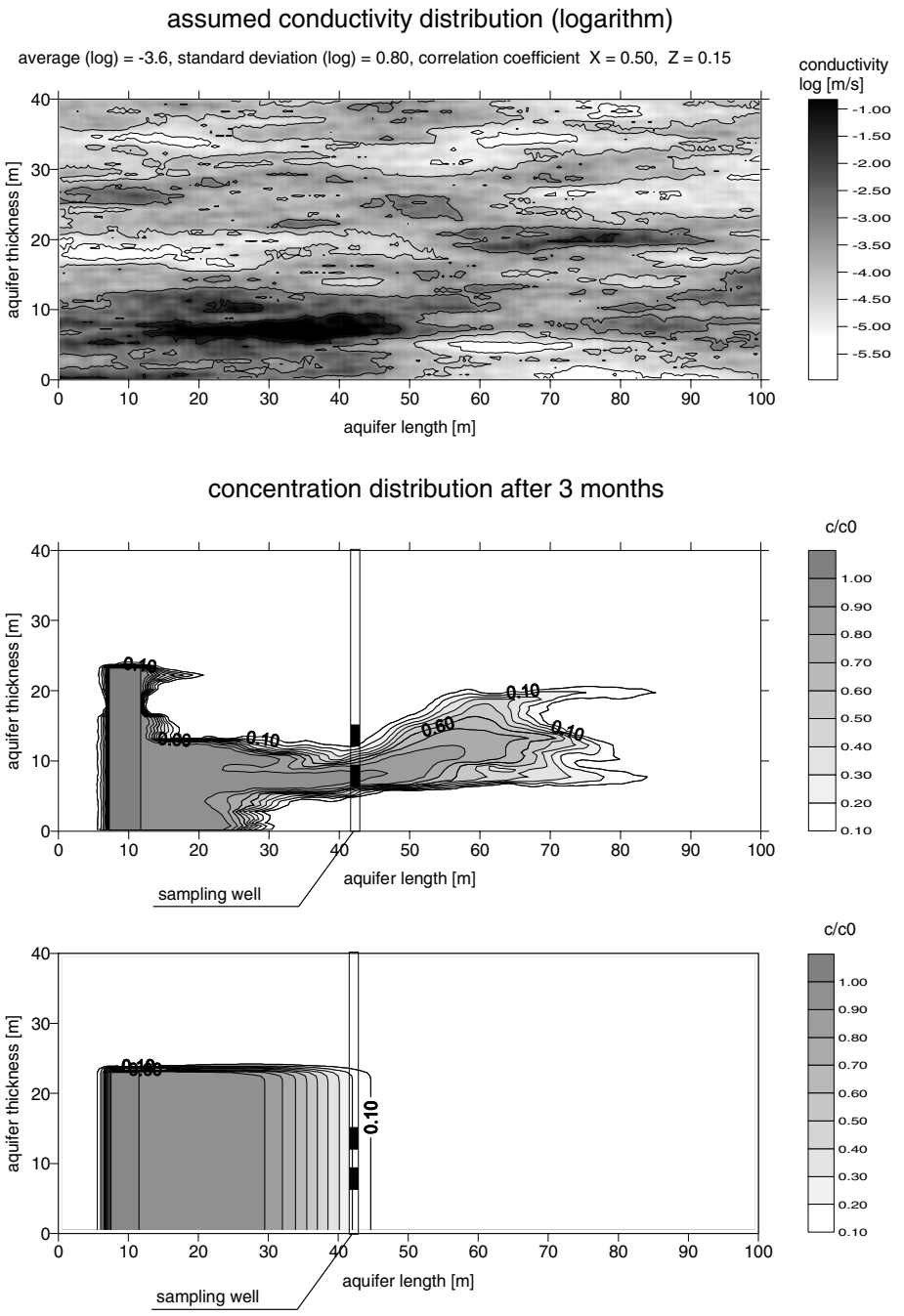


Figure 9.1: Generated hydraulic conductivity distribution of the virtual aquifer and simulated concentration after 3 months for a heterogeneous aquifer and a homogeneous aquifer for comparison.

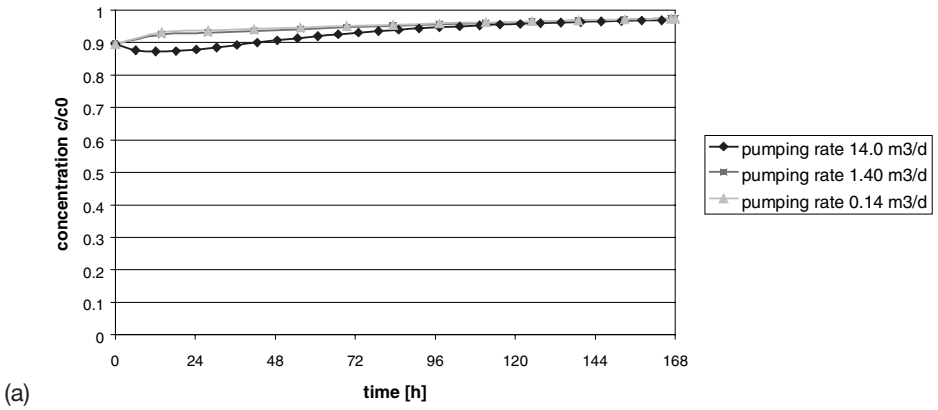


(a)

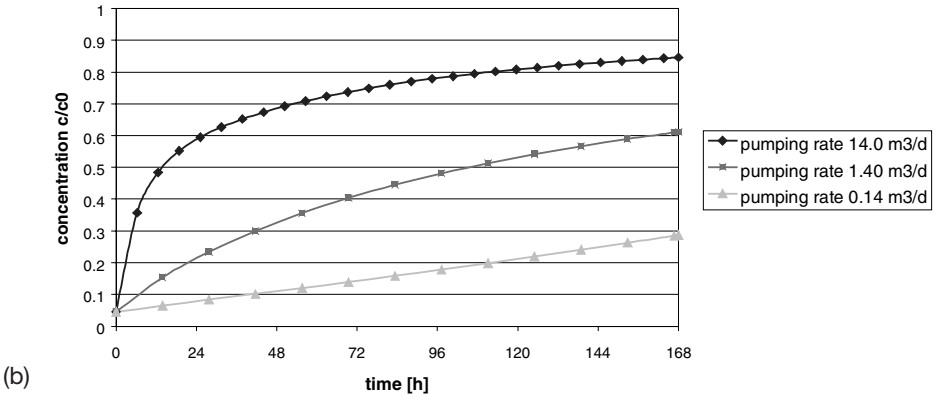


(b)

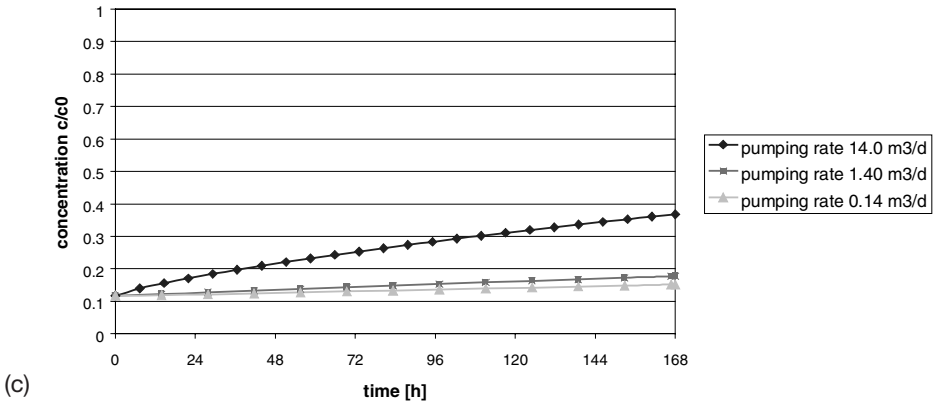


(c)

Figure 9.2: (a) Temporal progression of contaminant concentrations for 3 pumping rates in a sampling well screened directly in the plume; (b) Temporal progression of contaminant concentrations for 3 pumping rates in a sampling well screened above the plume; (c) Temporal progression of contaminant concentrations for 3 pumping rates in a sampling well screened over aquifer thickness.

where most of the contaminant is transported at high concentrations. Pumping in this area shows immediately the high concentrations residing there and more pumped water is pulled in from the contaminant source. Since the conductivity distribution of our generated aquifer is known these observations are understandable but without this knowledge the high concentrations would be surprising.

If the observation well is screened slightly above the plume (assumption b), the measured initial concentrations are low, since the contaminant does not pass this area due to the preferential pathways. Withdrawal of water leads to increasing concentrations in the sampling well with concentrations increasing faster at higher pump rates. Pumping in the well causes a flux of contaminated water from the high permeable area into the sampling well. After withdrawal of more than 2000 $m^3$ nearly all the pumped water is obtained from the well permeable area containing high contaminant concentrations. Obtaining this state at low pumping rates takes longer than at high rates. When samples are taken in a real aquifer normally one single pumping rate is used and samples are analysed after more or less constant conditions (e.g. electrical conductivity) of the pumped water are attained. In a constellation as described above this single measured concentration would not be of any significance and should not be used for e.g. remediation decisions.

In a pumping well screened over the entire thickness of the aquifer (assumption c), water is withdrawn from all parts of the aquifer but more intensively from high permeable areas than e.g. from clay lenses. The initial concentration observed in such a well represents a flux-weighted average over the aquifer thickness. Pumping causes increasing concentrations since more water is withdrawn from more highly permeable and – in this case – highly contaminated areas. In a homogeneous aquifer we would expect the same observation, low concentrations in the beginning and a slight increase of concentrations since higher contaminated water approaches the well. Hence, without understanding the true nature of the heterogeneous aquifer the measurements in a well screened over the complete thickness would erroneously confirm our assumption of a homogeneous aquifer. As visible in Fig. 9.1 this assumption underestimates the longitudinal spread of the plume by a factor of ~2.

The example therefore shows that heterogeneous hydraulic conductivity has significant consequences on concentration measurements in multilevel and full-screened sampling wells: the measured concentrations depend on the position of the screen, the pumping rate and the duration of pumping. Consequently, due care must be exercised in the interpretation and evaluation of measured concentrations obtained in the traditional way.

Although the calculations performed are not beneficial for a specific site in a real aquifer, the results are important for field investigations. The application of a virtual aquifer shows that such general studies can be performed without excessive effort.

### 9.2.2 The Effect of Mixing in an Observation Well on Evaluation of Natural Attenuation Processes in a Heterogeneous Aquifer

The previous example showed that pumping from an observation well screened over the complete thickness of the aquifer results in a mixture of different types of water. This is problematic for the evaluation of natural attenuation processes since the concentrations of various substances such as contaminant, electron acceptors and other chemical parameters have to be considered. The mixing of waters with different redox conditions during the measurement can lead to microbial and chemical reactions which falsify the true conditions within the aquifer.

The previous example was calculated with a common numerical model for flow- and conservative transport. The simulation of natural attenuation processes however, requires three-dimensional transport coupled with complex biochemical and chemical reactions. In the following example the numerical model TBC (**T**ransport, **B**iochemistry and **C**hemistry; Schäfer et al., 1998A) is used to simulate natural attenuation processes in a heterogeneous aquifer.

Figure 9.3 shows a three-dimensional heterogeneous aquifer consisting of four layers, the upper two layers have an average hydraulic conductivity of 1.0E–3 m/s and the lower half of the aquifer 0.5E–3 m/s. Hydraulic conductivity of all layers is assumed to be independently lognormal distributed with a standard deviation of log 0.4 and correlation coefficients of X = 0.2 and Y = 0.2. Again these statistical parameters are only assumptions, since the example is not based on a real site. The effective porosity of 25 % is constant in the whole aquifer. A gradient of 3 ‰ is simulated by two fixed head boundaries causing a flux from the left to right boundary. Dispersivities of $\alpha_L$ = 0.5 m, $\alpha_{T\ horizontal}$ = 0.1 m and $\alpha_{T\ vertical}$ = 0.01 m are chosen for transport simulation.

Near the inflow the aquifer is contaminated over its complete thickness. An immobile NAPL phase is simulated in this area which dissolves into the mobile pore water with a saturation concentration ($C_{sat}$) of 50 mmol/L organic carbon according to the rate law

$$\partial C_{mob} / \partial t = exchc / n_{mob} \cdot (C_{sat} - C_{mob}). \quad (1)$$

$C_{mob}$ denotes the concentration in the mobile phase, exchc is an exchange coefficient controlling the velocity of dissolution, $n_{mob}$ stands for the porosity of the aqueous phase. The dissolved contaminant is transported downgradient via advective and diffusive transport mechanisms (Fig. 9.4). The numerical model TBC uses a node-centred finite volume approach for simulation of transport therefore concentrations are displayed above and below every layer.

Originally the aquifer is aerobic with oxygen concentrations of 0.3 mmol/L. Nitrate with 2.0 mmol/L and sulfate with 1.0 mmol/L serve as additional final electron acceptors for microbial degradation processes. These three mobile oxidants are transported from the inflow boundary left into the simulated aquifer at their initial concentrations. The soil contains an Fe(III) mineral that can be reduced to Fe(II) in order to oxidise organic contaminant.

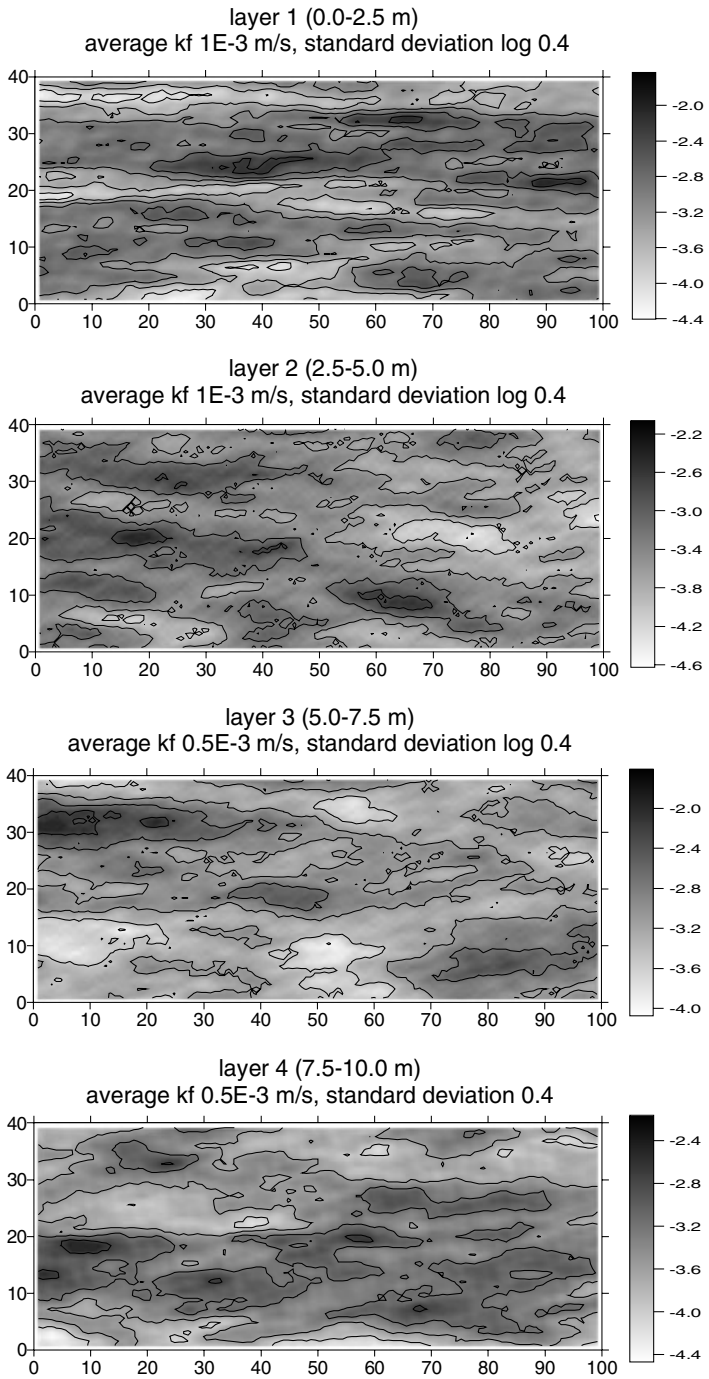


Figure 9.3: Generated hydraulic conductivity distribution of the four layers of the three-dimensional virtual aquifer.

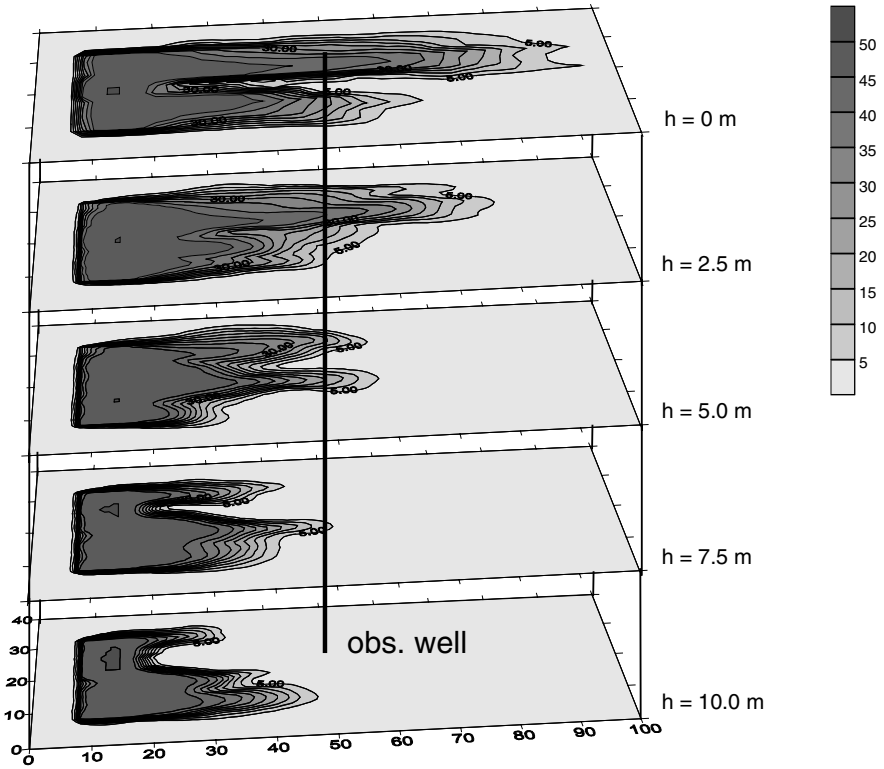


Figure 9.4: Simulated concentrations of contaminant [mmol organic carbon/L] after 500 days, including biodegradation.

For simulation of microbial reactions three different bacteria groups are assumed: aerobic facultative denitrifying, sulfate reducing and Fe(III) reducing. Growth of each bacteria group (X) is simulated by Monod-kinetics (Monod, 1942; Schäfer et al., 1998B):

$$\partial X/\partial t = v_{\max} \cdot X \cdot OC/\left(MK_{OC} + OC\right) \cdot Ox/\left(MK_{Ox} + Ox\right) \qquad (2)$$

Microbial growth is controlled by a maximum growth velocity $v_{max}$ and normally two Monod-terms, the first for organic carbon (OC), the second for the electron acceptor (Ox) consumed. Microorganisms grow exponentially with maximum velocity if both Monod-terms are 1, i.e. organic carbon and electron acceptor are available in high concentrations, larger than their specific Monod-concentration (MK). If the concentration of organic carbon or electron acceptor is low, its Monod-term becomes nearly zero reducing or preventing microbial growth.

Aerobic and facultative denitrifying bacteria can grow by consuming oxygen or nitrate as electron acceptors which is simulated by summing up two Monod-equations (2) for oxygen and nitrate. An inhibition term controls which electron acceptor is preferred by the microorganisms. If oxygen concentrations are high, denitrification is

inhibited. With the help of the same inhibition term sulfate- and Fe(III) reduction is prevented if oxygen is present, since the required bacteria groups are anaerobic.

Decay of bacteria is simulated by a constant decay rate. Total growth of microorganisms is the sum of all growth terms and the decay term.

If bacteria grow, they consume organic carbon and electron acceptors. For calculation of stoichiometric demand of electron acceptors it is assumed that the contaminant consists of toluene.

$$C_6H_5CH_3 + 9\ O_2 + 3\ H_2O \Rightarrow 7\ H_2CO_3$$

$$5\ C_6H_5CH_3 + 36\ NO_3^- + 36\ H^+ \Rightarrow 35\ H_2CO_3 + 3\ H_2O + 18\ N_{2(g)}$$

$$2\ C_6H_5CH_3 + 9\ SO_4^{2-} + 18\ H^+ + 6\ H_2O \Rightarrow 14\ H_2CO_3 + 9\ H_2S$$

$$C_6H_5CH_3 + 36\ Fe(OH)_3 + 72\ H^+ \Rightarrow 7\ H_2CO_3 + 87\ H_2O + 36\ Fe^{2+}$$

The parameters required to describe the kinetic growth of the three groups of microorganisms are taken from a field investigation on microbial in situ remediation.

Microbial reactions also change the chemical composition of the groundwater e.g. due to production of carbonate and sulfide. If the inorganic composition of groundwater is to be used to estimate microbial degradation, chemical reactions have to be considered, too. In this example a simplified geochemistry is simulated, consisting of a calcium-carbonate equilibrium system and precipitation of iron sulfide.

The virtual aquifer shows a typical redox sequence and typical reactions observed in natural aquifers. Figure 9.5 shows the concentrations of a selected set of substances in the upper layer 500 days after contamination of the aquifer. Dissolved contaminant spreads downstream from the NAPL source following two major preferential pathways. Within the plume oxygen and nitrate have been completely consumed by aerobic and denitrifying microorganisms, now degradation occurs only within the diffusive zone at the boundary of the plume where contaminant and oxygen or nitrate are found at the same time. As expected from the redox sequence denitrification occurs slightly deeper inside of the plume. Sulfate reduction can only be observed under anaerobic conditions inside the plume. Like oxygen and nitrate, sulfate is no longer present in the centre of the plume, degradation occurs in the diffusive zone where sulfate and contaminant are available. This is a general problem of mobile electron acceptors, after some time degradation occurs only in diffusive mixing zones at the boundary of the plume. Hence, natural attenuation consuming mobile oxidants is usually limited by slow diffusive processes.

In the example Fe(III) reduction takes place nearly within the whole plume, since iron minerals and contaminant are present and the major part of the plume is anaerobic. With a solid electron acceptor there is no problem of mixing, the minerals remain in place and are in contact with the contaminant as the plume spreads. Hence, the degradation via Fe(III) reduction increases with the volume of the plume, while degradation via mobile electron acceptors occurs only at the surface of the plume. Fe(III) reduction is slow, since it is limited by microbial availability of the minerals. If the minerals are consumed, they cannot be refilled by an external source. In a more heterogeneous aquifer it is possible that reducible Fe(III) is embedded in low permeable lenses. In this case degradation is limited by diffusion of contaminant into the lens.

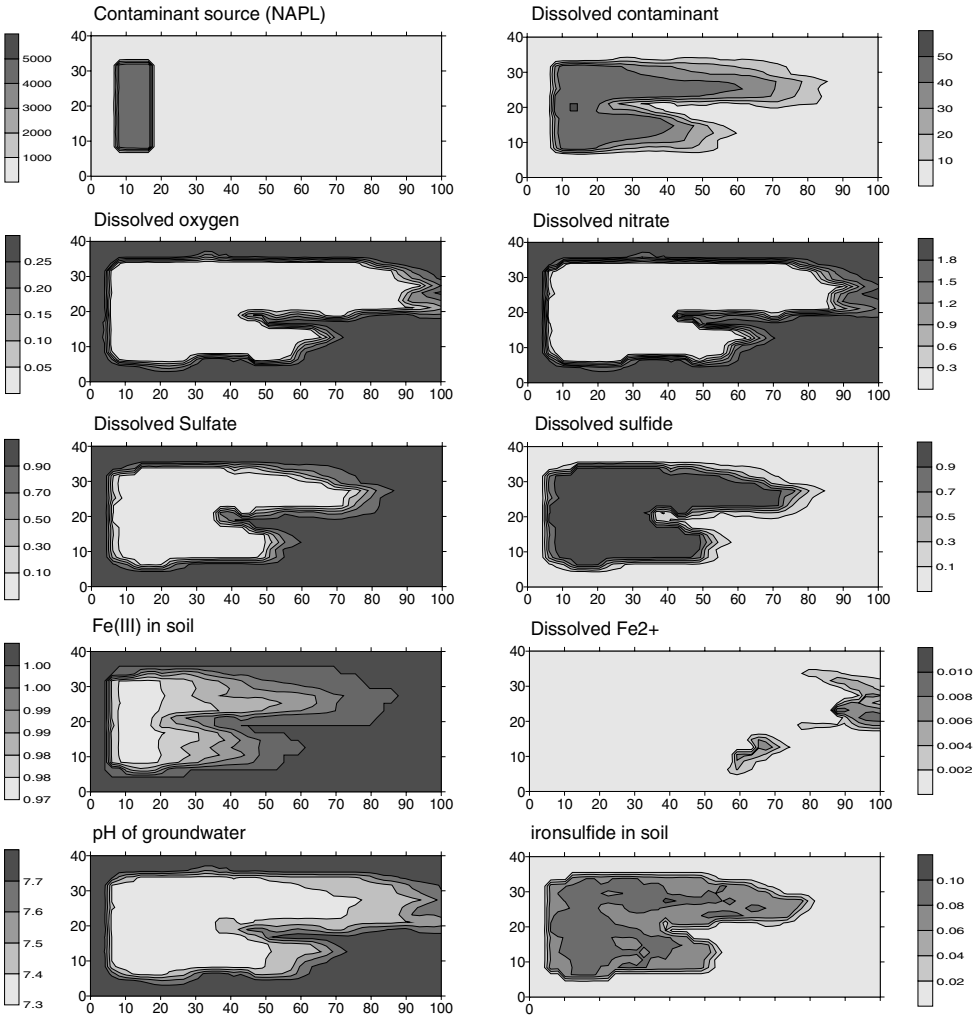


Figure 9.5: Concentrations of a selected set of substances in the upper layer 500 days after contamination of the aquifer.

Normally Fe(III) reduction can be verified and quantified in natural aquifers if the concentration of the degradation product $Fe^{2+}$ increases. Without this signal it is very difficult to distinguish Fe(III) reduction from other microbial degradation reactions or adsorption. In the example $Fe^{2+}$ concentrations within the plume remain at a constant low level, slightly increased concentrations are visible only downstream. Since the groundwater contains sulfate concentrations of 1 mmol/L sulfide is produced by microbial sulfate reduction. High sulfide concentrations cause complete precipitation of $Fe^{2+}$ as iron sulfide (pyrite) with very low concentrations of $Fe^{2+}$ in the groundwater. Increased concentrations of iron sulfide are simulated within the plume. The

locations of iron sulfide precipitation do not correspond to the areas with the lowest Fe(III) content, since iron reducing and sulfate reducing bacteria developed independently over time.

If water is pumped from an observation well screened over the entire thickness of the aquifer the sample shows a mixture of different types of water. Chemical equilibrium reactions take place even if microbial reactions are prevented (e.g. by conservation of the sample). Figure 9.6 shows the concentrations of some selected substances in the upper and the lower layer of the aquifer (for comparison) and measured in the observation well. The water in the upper layer contains high concentrations of the contaminant, while the electron acceptors are completely consumed. The concentrations of total inorganic carbon and sulfides are increased due to degradation reactions and on the other hand despite of Fe(III) reduction $Fe^{2+}$ concentrations are low due to precipitation of pyrite. The water in the lower layer is still uncontaminated and all electron acceptors are still available. Total inorganic carbon, sulfides and $Fe^{2+}$ are present at low concentrations. Thus water pumped from the observation well shows a mixture of all layers with moderate concentrations of the contaminant and the electron acceptors. If the sample is not conserved these are ideal conditions for microbial degradation. Due to mixing of different waters the mixture is undersaturated with respect to calcium carbonate. A slight precipitation of pyrite occurs within the observation well though the $Fe^{2+}$ concentrations are low in all layers. The oxidation of sulfides by oxygen or nitrate are neglected in the model, since they are slow or microbially catalysed.

The concentrations measured in the observation well are therefore difficult to interpret with regard to the evaluation of natural attenuation processes. If the fact that the water is pumped from different layers is neglected, it is difficult to understand why

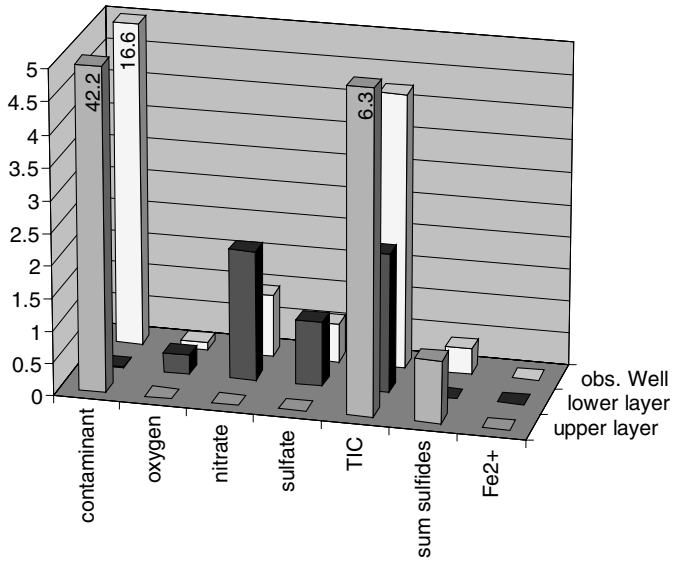


Figure 9.6: Concentrations [mmol/L] “measured” in the upper and the lower layer of the virtual aquifer and in the observation well.

the water contains contaminant, oxygen, nitrate, sulfate and sulfide at the same time. The increased sulfide concentrations indicate a microbial sulfate reduction, but these bacteria are anaerobic and should not grow in the presence of oxygen. Such measurements are sometimes interpreted with "micro-anaerobic" zones within an aerobic aquifer.

For this special aquifer the water sample in the observation well is a simple mixture of different types of water, chemical precipitation reactions play no important role. In aquifers with low sulfide- (respectively sulfate-) concentrations $Fe^{2+}$ does not completely precipitate as FeS and precipitation of Fe(II)- and Fe(III) minerals within the well should change the water significantly. Precipitation of carbonates is also expected if the water is oversaturated with respect to hydrogen carbonate concentration. There are additional reactions (e.g. precipitation of manganese- or heavy metal minerals) which can change the composition of the sampled water, but they are not considered in this yet simplified example.

### 9.2.3 Monitoring of Natural Attenuation in a Heterogeneous Aquifer

For exploration, monitoring and evaluation of (enhanced) natural attenuation processes it is important to understand the possibilities and restrictions of the common monitoring systems such as (multi-level) sampling wells, dosimeters or immission calculations. The influence of heterogeneity on sampled concentrations in a given observation well has already been demonstrated in Section 9.2.2, now we will focus on the problem of installation of a set of sampling wells to measure the concentrations in the subsurface as accurately as possible.

The concentrations in the virtual aquifer calculated in the previous example (Fig. 9.4) will be investigated by different regular arrangements of observation wells. The measured concentrations within the sampling wells are interpolated by SURFER using the Kriging-method with default parameters. The resulting interpolated concentration pattern is compared to the "real" concentrations of the virtual aquifer. This comparison is impossible in natural aquifers since the real concentrations are not known.

Figure 9.7a shows the interpolated concentrations of the contaminant, if a dense grid of multi-level wells is used for exploration. Every well is screened at 5 levels of the aquifer according to the discretisation of the model and samples are taken without intensive pumping to avoid mixing. The interpolated concentrations seem to agree well with the "real" concentrations (Fig. 9.4) but objective criteria for agreement have still to be found. Figure 9.7 also shows the concentrations if sampling wells are used that are screened over the complete thickness of the aquifer. Due to averaging effects the plume is "smeared" and concentration gradients are less sharp. Though the form of the plume is better represented using multi-level wells, completely screened wells are a good tool to explore the presence of a contaminant. Since the mixing ratio within the well is unknown in reality, only qualitative information is obtained. If the contaminant is mixed with too much water the concentrations can fall below the detection limit.

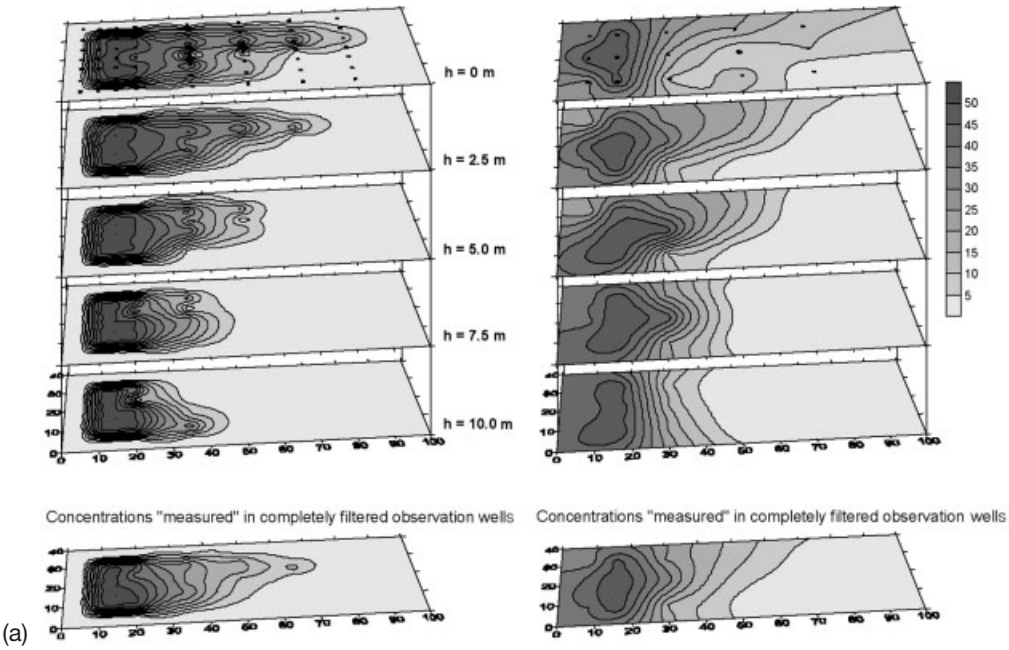


(a) (b)

Figure 9.7: Concentrations of contaminant [mmol organic carbon/L] "measured" in the virtual aquifer with a) 56 b) 15 observation wells. Upper slices show multi-level observation wells, lower slices wells screened over aquifer thickness. Concentrations are interpolated with SURFER (kriging).

56 multi-level observation wells were used to obtain the results described above, much too costly for a common monitoring system. Figure 9.7b shows the results if only 15 observation wells are installed in a regular grid. If additional assumptions such as the assumption of zero concentration at the inflow and at the boundaries are not included, correlation with "reality" is poor.

The example shows that a minimum number of observation wells is required to obtain the original concentration pattern depending on the complexity of the concentration pattern and therefore depending on the heterogeneity of aquifer parameters. For interpolation of concentrations the information where no contaminant is present is as important as the concentration level within the plume. The sharp concentration gradients at the boundary of the plume can only be measured if there are two observation wells, one near the clean groundwater, the other within the plume. Experts need fewer observation wells since they can use their experience to add additional knowledge e.g. on inflow- and boundary-concentrations. Possibly this expert knowledge can be incorporated in a computer programme.

## 9.3 Problems and Requirement for Additional Scientific Research

The examples illustrate the use of virtual aquifers to investigate exploration, monitoring and remediation strategies for contaminated aquifer systems. However, there is a large necessity for further investigation in the following areas:

*a) Construction of a VA-database – description of hydraulic, geochemical and microbial heterogenous structures, related to geological aquifer genesis*
The construction of virtual aquifers as close to reality as possible requires information on the heterogeneity of aquifer parameters. Unfortunately, there are only few studies like the aquifer analogue studies that provide an adequate set of relevant geochemical, hydrogeological and microbiological data. Therefore, a database has to be generated based on the geological genesis of different aquifer types.

The compilation of this database exceeds by far the data obtained by common techniques used to explore contaminated sites. The determination of spatial distribution of parameters on the required small scale is very time consuming, since many samples have to be chemically and statistically analysed. But promising examples like the lithocomponent approach (Bersezio et al., 1999; Kleineidam et al., 1999) demonstrate that such work may be very successful for characterisation of aquifers. In this method an aquifer is characterised by measuring the typical properties (e.g. adsorption coefficients) of the existing lithocomponents (sand, gravel, etc.). Since mixtures of these components compose the investigated aquifer, it is sufficient to determine its petrographic and mineralogical composition on a small scale to describe the adsorption behaviour of the aquifer.

The simulation of natural attenuation processes requires additional parameters for microbial degradation. Such data have been published in the literature but since different approaches exist to simulate biodegradation these parameters are normally not transferable to other models. Public use of numerical models to simulate natural attenuation would require compilation of a data set describing the size and range of microbial degradation constants and their dependencies on other parameters.

As mentioned above such investigations have already been performed for some specific aquifer types from the "outcrop analogue"-project, other investigations are available in the literature (e.g. Borden, Cape Cod). Additionally existing data have to be systematically collected and compiled for different aquifer types. The extent to which data from existing geological investigations can be transferred to the virtual aquifer approach is not known, since they were not performed with this special aspect in mind.

*b) Adaption of statistical methods for structure identification and determination as well as structure mapping in geosystems*
The generation of virtual aquifers requires statistical analysis of aquifer parameters. This has to be done for flow and transport parameters like hydraulic conductivity, porosity and dispersivity as well as for geochemical parameters like the content of dif-

ferent minerals, ion exchange and sorption parameters. It is more than uncertain whether all structures of spatial distribution can be properly described by Gaussian statistics. Other techniques may have to be chosen which can handle rough fronts. Correlation of different soil properties may help to extrapolate parameters.

For interpolation of measured concentrations it would also be very helpful to test new regionalization and interpolation methods. Very often the "Kriging" Method is used, since it seems to produce realistic concentration distributions. With virtual aquifers, where the "real" concentrations are known, the quality of different interpolation methods for a spectrum of parameters can be tested.

Another important problem is the comparison between "measured" spatial concentration distribution with the virtual "reality". This could be done by subjective criteria (e.g. by looking, how similar are measurement and reality?) but objective criteria are preferred. Some solution approaches have already been investigated in computer sciences, e.g. when the shape of a face is compared to a database with faces of known users, and seem to be transferable to problems in hydrogeology

*c) Data handling and internet platform*

The large amount of complex and coupled information, their proper presentation and statistical evaluation will require new approaches in data management. The extraction and visualisation of specific data will be problematic, especially when a lot of different users access the database via internet to add and extract data. The advantage of such a system is, that it is growing and learning from different work groups all over the world.

*d) Consideration of additional processes in the numerical model*

Additional processes have to be considered if biological degradation within the contaminant source has to be simulated. Within the plume the contaminant is dissolved in groundwater, while near the source the contaminant is very often present in the form of a liquid phase (NAPL) or in residual saturation. Models simulating multiphase flow are already available but parameterisation is still difficult especially in a heterogeneous aquifer. In addition, dissolution of the NAPL phase with regard on the size and shape of NAPL droplets, the composition of the NAPL phase and the grassing of microorganisms on the drops have to be considered for simulation of natural attenuation processes. Bacteria release biosurfactants, organic substances increasing the solubility of contaminants (Banat, 1995). The amount of biosurfactants produced and their effect on the solubility of mixed NAPL phases will have to be determined and appropriate functions to describe this process have to be developed and incorporated in a model.

## 9.4 The "Virtual Aquifer" Project

The proposal titled "Virtual Aquifer (VA) – Computer-Based Evaluation of Site Investigation, Remediation and Monitoring Strategies with Regard to the Natural Attenuation (NA) and Enhanced Natural Attenuation (ENA) Potential of Contaminated Soil and Groundwater" has been evaluated by the Bundesministerium für Bildung und Forschung (BMBF) and the project is expected to start in 2003. It is a first step in provision of the required simulation programmes and input data for further investigation. The project will consist of three parts:

1. computer based simulation system,
2. internet information system,
3. application.

In the first part, computer programmes for numerical simulation of (enhanced) natural attenuation processes in aquifer systems (ROCKFLOW – University Tübingen (Kolditz et al., 1998), TBC – University Kiel (Schäfer et al., 1998A)) will be improved and expanded. Simulation will be performed in three dimensions considering typical geological structures and heterogeneities based on outcrop analogue data provided by the University of Tübingen (Teutsch et al., 1999). The numerical models have to simulate transport coupled with microbial degradation processes and geochemical reactions in heterogeneous aquifers. Graphical user interfaces will have to be developed for input and representation of results for simplification of application. The programme packages will be published via internet.

In the second part, input data for the numerical models and a database concerning natural attenuation and enhanced natural attenuation will be established and made available via internet. The database shall include hydrogeological, hydrochemical, biochemical and microbial information, e.g. degradation rates of contaminants or average geochemical composition of typical soils. It will also contain information concerning typical aquifer structures like spatial distribution of hydraulic conductivity and geochemical properties. This information will allow simulation of reactive transport processes in aquifers as realistically as possible. The database will be established within the BMBF-project but it shall be possible for other users to import their own simulation experiences and parameters to create a growing knowledge base.

The third part will be the application of the numerical simulation programmes and the internet database. A first application will be the evaluation of investigative and monitoring strategies in greater detail than the preliminary studies given in this paper. Different aquifers with heterogeneous hydraulic conductivity and geochemical composition will be generated based on parameters obtained from the outcrop analogue database. Using the developed simulation programmes reactive transport processes will be calculated, resulting in concentrations as close to reality as possible. This "virtual reality" will be investigated with various sampling techniques such as wells, dosimeter or pumping tests. The results of the monitoring strategies will be compared to the known "virtual reality" using objective criteria for comparison.

Though the aim of the project is not the set-up of site-specific models, the database will be used to complete data at selected sites using known correlation of parameters. Unknown parameters can be introduced into site-specific models by stochastic approaches. These investigations show the extent to which the approach of virtual aquifers is helpful in evaluating real contaminated sites, e.g. evaluating the suitability of a site for natural attenuation.

Virtual Aquifers will also be a tool for the transfer of know-how to increase acceptance of the natural attenuation concept in administrative circles and by problem owners. Processes during investigation and remediation of a site can be made transparent at relatively little effort and costs, transferring current consolidated knowledge on natural attenuation to all participants.

The planned BMBF-project is however only a first step for the implementation of virtual realities in aquifer systems. In this project it will be impossible to answer all relevant aspects of this new approach, which may open a new door in the understanding and handling of complex groundwater systems und processes.

## 9.5 References

Banat, I. M. (1995): Biosurfactants Production and Possible Uses in Microbial Enhanced Oil Recovery and Oil Pollution Remediation: A Review. *Bioresource Technology* **51**, 1–12.

Bersezio, R.; Bini, A.; Guidici, M. (1999): Effects of sedimentary heterogeneity on groundwater flow in a quarternary proglacial delta environment: joining facies analysis and numerical modelling. *Sedimentary Geology* **129**, 327–344.

Flint, S. S.;Bryant, I. D. (1993): Quantitative clastic reservoir geolgical modelling; problems and perspectives. *The gelogical modelling of hydrocarbon reservoirs and outcrop analogues*, 3–20.

Kleineidam, S.; Rügner, H.; Grathwohl, P. (1999): Influence of petrographic composition / organic matter distribution of fluvial aquifer sediments on the sorption of hydrophobic contaminants. *Sedimentary Geology* **129**(3–4), 311–325.

Kolditz, O.; Habbar, A.; Kaiser, R.; Rother, T.; Thorenz, C. (1998): ROCKFLOW – Theory and Users Manual. Release 3.4. Institut für Strömungsmechanik und Elektronisches Rechnen im Bauwesen, Universität Hannover.

Koltermann, C. E.; Gorelick, S. (1996): Heterogeneity in sedimentary deposits: A rewiew of structure-imitating, process-imitating and descriptive approaches. *Water Resources Research* **32**(9), 2617–2658.

Monod, J. (1942): Recherches sur la croissance des cultures bacteriennes. In: Actualités Scientifiques et Industrielles, Vol. 911 (Ed.: J. Bordet), pp. 70–78, Hermann et Cie.

Schäfer, D.; Schäfer, W.; Kinzelbach, W. (1998A): Simulation of reactive processes related to biodegradation in aquifers: 1. Structure of the three-dimensional reactive transport model. *Journal of Contaminant Hydrology* **31**, 167–186.

Schäfer, D.; Schäfer, W.; Thullner, M. (1998B): TBC – a novel numerical model for simulation of Transport, Biochemistry and Chemistry in aquifers. *Mathematische Geologie* **2**, 79–93.

Siegenthaler, C.; Hugenberger, P. (1993): Pleistocene Rhine gravel: deposits of a braided river system with dominant pool preservation. In: Braided Rivers, Vol. 75 (Ed.: Best, J. Bristow, C.), Geological Society.

Steefel, C. I.; MacQuarrie, K. T. B. (1996): Approaches to modeling reactive transport in porous media. In: Reactive Transport in Porous Media. General Principles and Applications to Geochemical Processes (eds.: Lichtner, P. C.; Steefel, C. I.; Oelkers, E. H.), pp. 34, 83–129.

Steefel, C. I.; van Cappellen, P. (1998): Reactive Transport Modelling of Natural Systems. Special Issue *Journal of Hydrology* **209**.

Teutsch, G.; Rügner, H.; Kohler, W. (1999): Entwicklung von Bewertungskriterien natürlicher Schadstoffabbauprozesse in Grundwasserleitern als Grundlage für Sanierungsentscheidungen bei Altlastenstandorten. Universität Tübingen.

Webb, E. K.; Anderson, M. P. (1996): Simulation of preferential flow in three-dimensional, heterogeneous conductivity fields with realistic internal architecture. *Water Resources Research* **32**(3), 533–545.

Weissmann, G. S.; Carle, S. F.; Fogg, G. E. (1999): Three-dimensional hydrofacies modeling based on soil surveys and transition probability geostatistics. *Water Resources Research* **35**(6), 1761–1770.

Woodbury, A. D.; Sudicky, E. A. (1991): The geostatistical characteristics of the Borden aquifer. *Water Resources Research* **27**(4), 533–546.

# 10 Two-Dimensional Two-Step Modelling of 250 Years of Transport and Reactions in a Virtual Anoxic Aquifer (Oderbruch, Eastern Germany)

Gudrun Massmann* and Horst D. Schulz

## Abstract

The model presented within this paper calculates the iron turnover, i.e. the iron reduction that has taken place in 250 years of river water infiltration into an anoxic aquifer in the northern Oderbruch, Germany. A data set of hydraulic conductivities and iron(III) concentrations measured in the aquifer sediment was used to construct a 2-dimensional virtual aquifer matrix. The two-step model combining advective/dispersive transport with (bio)geochemical reaction is based on the explicite difference method to model the transport component. Only the governing redox reaction, the reduction of iron(III)hydroxide in the sediment by DOC in the groundwater was considered by a first order reaction kinetic. Measured values of DOC in the field served to calibrate the model. The simulation could be validated comparing model results with average Fe(II) concentrations in the groundwater at the field site. Results fit well although various redox reactions observed in the field were disregarded, proving that the Fe(III) reduction truly is the dominating process eliminating DOC from the groundwater. Results show that the iron turnover in 250 years accounts for only 1–3 % compared to the total iron depot available. The model is an attempt towards increasing the dimensionality of coupled transport and reaction models into the second dimension for a well understood system that can therefore be reduced to its major governing processes.

* Institut für Geologie, Geophysik und Geoinformatik, FU Berlin, Malteserstr. 74–100, Haus B, 12249 Berlin; e-Mail: massmann@zedat.fu-berlin.de



*Geochemical Processes: Conceptual Models for Reactive Transport in Soil and Groundwater. Research Report.* Deutsche Forschungsgemeinschaft (DFG).
 ISBN: 978-3-527-27764-3

# 10.1 Introduction

## 10.1.1 Why 2D-Modelling of Transport and Reactions?

One-dimensional models for the simulation of reactive transport of dissolved constituents in groundwater and porewater of sediments have reached quite an advanced state during the last few years. Models such as STEADYSED1 (Van Cappellen and Wang, 1995; Wang and Van Cappellen, 1996) or the model CoTReM (Hensen et al., 1997; Adler et al., 2001) represent tools for the simulation of most meaningful forms of physical transport in both diffusive controlled as well as advective/dispersive determined systems of porewater and groundwater. These models always consider a huge number of geochemical respectively biogeochemical reactions within the aquatic phase, or between aquatic and solid phase. The model CoTReM for instance applies a subroutine, which allows the simulation of any redox-reaction, and in addition – as further subroutine – the geochemical model PHREEQC (Parkhurst, 1995), which allows modelling of any geochemical reaction.

However, users of these types of models will usually reach the limit of feasibility due to two aspects:

In case the modeller wants to include a multitude of (bio)geochemical processes – as in a natural aquatic system – it is indispensable to have first understood these processes quantitatively, in order to describe them afterwards according to the measured parameters. Prerequisites are extensive field measurements and/or laboratory experiments. It is absolutely essential to understand quite a few things about processes in complex aquatic systems and about model theory before running complex models for a coupled transport/reaction-modelling "just like that".

The second restriction results from the time of calculation of these models. It is not at all exceptional, that one-dimensional models with many parameters and for long modelling-times will need hours or even days – despite of fast computers – for one run of the programme. Skilful handling of the model might possibly avoid absurd calculations, and computer networks may speed up the time of calculation, however these models will always be restricted due to their time of calculation.

So why should anyone develop or use a 2-dimensional groundwater model, since this procedure will further increase the number of cells and thus the time of calculation? The answer is relatively simple. Whereas sediment/porewater-systems can normally be modelled properly in the one-dimensional way, aquifer/groundwater-systems mostly show substantial inhomogeneities in two dimensions of the processes and therefore their modelling requires these dimensions. Should the modelling be only one-dimensional, i.e. with an imaginary "tube" in the direction of groundwater flow, it is essential to consider interaction between different "tubes", lying next to each other, in order to avoid severe mistakes.

In case of two-dimensional modelling, other forms of simplification are required, in order to handle the time of calculation. This study proceeds on the assumption that normally well-understandable processes, which are separately measured and separate-

ly calculated in a geochemical model, can be restricted to their total rate of turnover in the aquatic and solid phase. In our case it is the redox reaction between DOC and iron(III)oxide in an anoxic aquifer.

### 10.1.2 Why the Study Site Oderbruch?

With an area of more than 800 km$^2$ the Oderbruch represents Germany's largest river polder area. It is located about 50 km northeast of Berlin (see Fig. 10.1) adjacent to the river Oder at the border to Poland. Formally a swamp-like lowland subject to regular flooding, the Oderbruch has undergone severe changes in the past 250 years. It was Frederic the Great of Prussia who first introduced intensive hydraulic engineering to enable agricultural use of the area. Since the 18$^{th}$ century drainage measures included the redirection of the former river-bed further towards the east, the installation of an extensive drainage-ditch and pumping-station system and the building of a dyke along the entire river.

Today, as a result of the drainage activities, a major part of the region lies below the river water table. The steep hydraulic gradient between the water table of the river Oder and the aquifer results in the permanent lateral infiltration of river water into the shallow upper aquifer which is confined along the river banks. The sands and gravel of

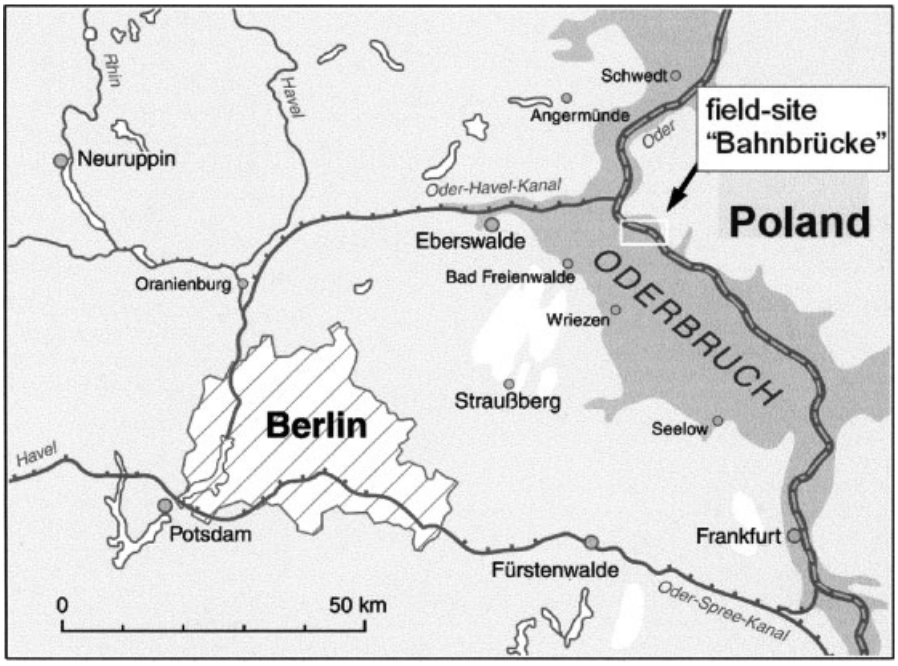


Figure 10.1: Location of the Oderbruch polder and field-site "Bahnbrücke".

this 10 to 30 m deep aquifer, which is the subject of the current study, are of late Pleistocene glacio-fluvial origin. They are margined by a till at the base and an alluvial loam, relict of the regular flooding during the Holocene, at the top.

There are two reasons, why the area is ideal for the study of redox processes in the field. First, the hydraulic situation as it is today, has been artificially initiated 250 years ago. Due to the distinct time marker, a quantification of the redox processes with time is possible. Second, although the hydraulics may be complex due to the drainage measures, the overall trend near the Oder, i.e. infiltration of river water into the aquifer, can be considered consistent within the last 250 years of time.

There are numerous redox-controlled, chemical changes that occur when the oxygenated river water enters into the anoxic environment where the water gets progressively more reduced along its flow-path (see also Chapter 11). Within this study, only the process of reduction of iron(hydr)oxides in the sediments by dissolved organic carbon (DOC) in the river water is taken into consideration. The aim was to quantify the amount of iron that has been dissolved in the past 250 years. We wanted to understand what effect the natural heterogeneity of the aquifer sediment has on the overall turnover rates of iron and DOC. Starting from a redox-front concept, one would expect an iron(hydr)oxide depletion front somewhere close to the Oder. The presence of oxidised and reduced species within the entire aquifer is a seeming disagreement to this concept and will be discussed in Section 10.6. Besides the necessity to make a few simplifications in order to model the iron reduction in two dimensions, the available scarce hydraulic conductivity ($k_f$) data had to be inflated to a 2-dimensional virtual aquifer in this case with 3000 values as described in the following section.

## 10.2 The Study Site: Hydraulic Conductivity and Iron(III) Concentration of the Aquifer

A 1 $km^2$ exemplary field site “Bahnbrücke” in the northern Oderbruch is currently the subject of detailed hydraulic and geochemical investigations. Knowledge of the lithology of the field-site was obtained by 10 sediment cores that where drilled during installation of a dense piezometer network. Groundwater and surface water is collected and analysed regularly (for a detailed description of the field-site see Chapter 11). Sediment samples were sieved and $k_f$-values calculated after Hazen (1893) and Beyer (1964). Fe(III)oxides and Fe(III)hydroxides in the sediment were measured with the dithionite-citrate-hydrogen carbonate method (Mehra & Jackson, 1960) while the total amount of iron was gained by disintegration with nitric acid. DOC was analysed with a DOC-Analyser (Shimadzu) and dissolved Fe(II) by ICP (Jobin Yvon).

Data of 4 sediment cores in 40, 140, 350 and 600 m river distance were used for the construction of the 2-dimensional hydraulic conductivity- and Fe(III)-matrix (core numbers 2/99, 6/99, 10/99 and 12/99, location see Chapter 11). The aquifer thickness within these 4 cores varied between 18 and 20 m. A uniform thickness of 20 m was

assumed to sustain a rectangular flow-field. The cross section was divided into cells of 4 m length and a thickness of 1 m. The result is a matrix of 150 cells in x- and 20 cells in y-direction and a total of 3000 cells for the complete two-dimensional profile.

The $k_f$-values were derived for each cell in an EXCEL®-worksheet after the following scheme: Measured $k_f$-data (8 to 10 sieved samples of each core) was regarded as fixed data points. Within each core, distinct layers, for example layers of peat or very coarse-grained sands, were also given a fixed value according to the geological description. Figure 10.2 shows the lithology of core number 10/99 and gives an exam-

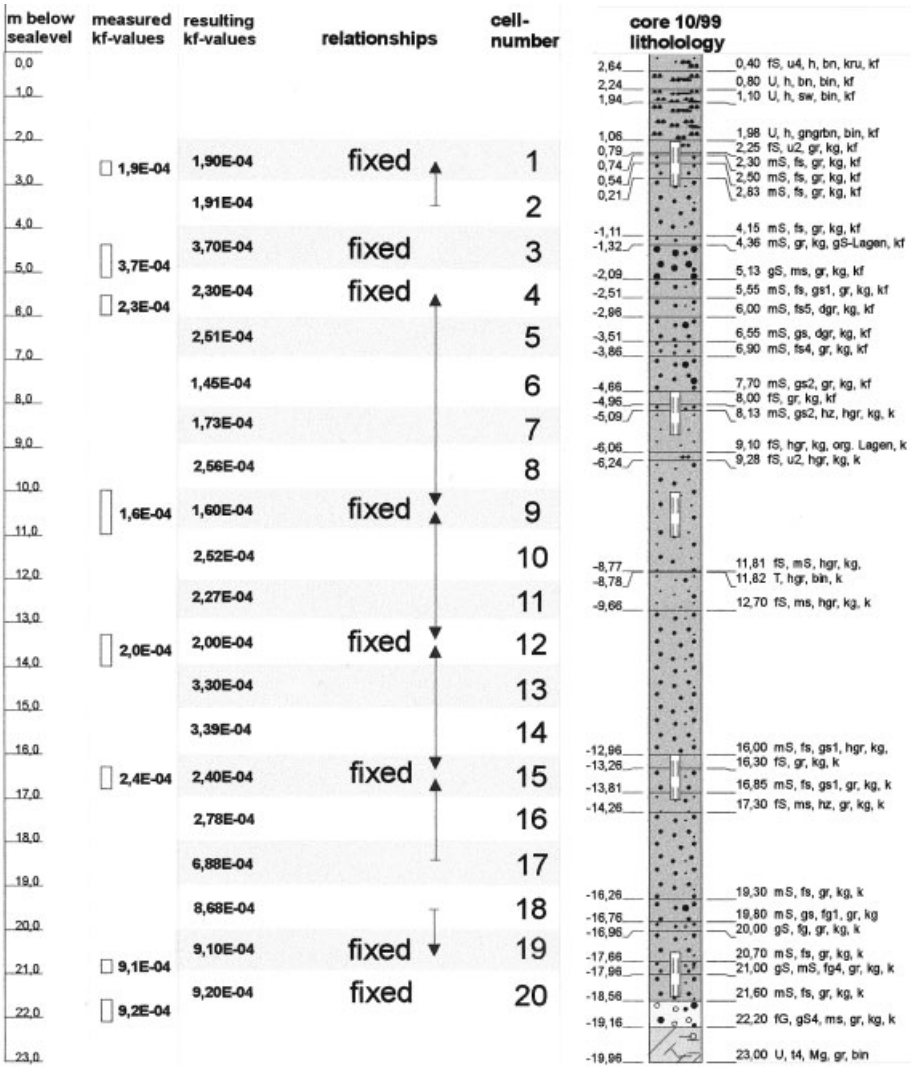


Figure 10.2: Core 10/99 as an example for the relationship between lithology, measured and calculated hydraulic conductivity data. Arrows indicate the relations between cells.

ple of the way cells between measured data-points were filled with hydraulic conductivity data.

The cells 1, 4, 9, 12, 15, 19, 20 contain fixed $k_f$-values according to the sieved samples in approximately the same depth. Cell 3 was given a value for similar coarse-grained sands derived from a different core. In between the cells with fixed data points, some $k_f$-values were calculated relying on the average of both neighbouring cells. A term, the product of a random number (RAND() in EXCEL® notation) minus 0.5 (to gain a random number between –0.5 and +0.5) and one neighbouring cell to keep the term adequately small, was added. An example for this procedure in the case of core 10/99 would be the cells number 5 to 8, resulting in the following formula:

$$k_{f\ cell\ 5\text{-}8} = (k_{f\ cell\ 4} + k_{f\ cell\ 9})/2+(RAND()–0.5) \cdot k_{f\ cell\ 9}$$

In some cases, taking the lithology under consideration, it made more sense to rely on one neighbouring cell only, for example in cell 2:

$$k_{f\ cell2} = k_{f\ cell1} +(RAND()–0.5) \cdot k_{f\ cell1}$$

In horizontal direction, the cells were filled in a similar way. An exemplary section of the excel-matrix can be seen in Fig. 10.3. The first row (x-coordinate) contains the distance to the river.

| 40 | 44 | 48 | 136 | 140 |
|---|---|---|---|---|
| 3.70E-04 | 3.40E-04 | 3.73E-04 | 1.68E-04 | 1.60E-04 |
| 3.60E-04 | 3.72E-04 | 3.28E-04 | 2.67E-04 | 2.70E-04 |
| 2.70E-04 | 2.40E-04 | 2.33E-04 | 1.16E-04 | 1.20E-04 |
| 5.00E-07 | 3.53E-06 | 6.68E-06 | 5.79E-05 | 6.36E-05 |
| 5.53E-05 | 6.12E-05 | 6.03E-05 | 8.09E-05 | 8.34E-05 |
| 9.80E-05 | 1.03E-04 | 9.19E-05 | 6.17E-05 | 6.00E-05 |
| 6.15E-05 | 6.22E-05 | 6.81E-05 | 6.18E-05 | 6.90E-05 |
| 1.09E-04 | 1.08E-04 | 1.07E-04 | 8.88E-05 | 8.51E-05 |
| 7.42E-05 | 8.04E-05 | 7.79E-05 | 1.19E-04 | 1.10E-04 |
| 9.46E-05 | 1.02E-04 | 1.06E-04 | 6.05E-05 | 6.60E-05 |
| 5.63E-05 | 6.03E-05 | 5.70E-05 | 1.08E-04 | 1.16E-04 |
| 8.97E-05 | 9.60E-05 | 9.91E-05 | 7.72E-05 | 8.28E-05 |
| 6.30E-05 | 6.66E-05 | 7.49E-05 | 1.96E-04 | 1.94E-04 |
| 8.51E-05 | 9.58E-05 | 9.60E-05 | 8.87E-05 | 9.36E-05 |
| 3.67E-05 | 4.40E-05 | 4.42E-05 | 1.15E-04 | 1.17E-04 |
| 8.15E-05 | 8.32E-05 | 8.31E-05 | 1.37E-04 | 1.50E-04 |
| 2.30E-04 | 2.53E-04 | 2.68E-04 | 2.38E-04 | 2.21E-04 |
| 8.60E-04 | 9.27E-04 | 8.80E-04 | 4.27E-04 | 4.50E-04 |
| 8.72E-04 | 7.85E-04 | 7.95E-04 | 5.47E-04 | 5.37E-04 |
| 1.22E-03 | 1.09E-03 | 1.15E-03 | 4.03E-04 | 3.60E-04 |

Figure 10.3: Hydraulic conductivity data of cores No. 2/99 and 6/99 in 40 and 140 m river distance with adjacent columns. Within cores, fixed data marked red, fixed given data marked orange and calculated data marked yellow.

The values for the top cell (44,1) in 44 m river distance are, for example, calculated with the following formula (indices according to river distance and aquifer depth):

$$k_{f(44,1)}=((24\cdot k_{f(40,1)}+1\cdot k_{f(140,1)})/25)\cdot 2\cdot \mathrm{RAND}()\cdot 0.1+((24\cdot k_{f(40,1)}+1\cdot k_{f(140,1)})/25)\cdot(0.9)$$

Multiplying $k_{f(40,1)}$ with 24 and $k_{f(140,1)}$ with 1 considers the fact that $k_{f(44,1)}$ is more likely to resemble $k_{f(40,1)}$ than $k_{f(140,1)}$. Multiplying the random number with 0.1 visually produced a distribution that resembles natural aquifers. Using a larger factor results in an aquifer with a $k_f$-distribution that seems unusual and too random for a Pleistocene aquifer of glacio-fluvial origin with a relatively strong horizontal continuity.

The method is clearly arbitrary and can be interpreted as a mixture of geological intuition and stochastic simulation. Another possibility would have been the use of a stochastic simulation method like simulated annealing or even just a simple linear interpolation instead. We chose this method because it combines all information of the measured hydraulic conductivities with our knowledge about the structure of a quarternary aquifer. The final hydraulic conductivity matrix is nevertheless only one possible realisation of the aquifer and it can be seen in Fig. 10.5. The general trend within the field-site "Bahnbrücke" can be seen in Fig. 10.5 as well as in any other realisation. With only a few exceptions the upper parts of the aquifer are highly homogeneous with $k_f$-values ranging between 1.0E–04 to 5,0E–04 m/s. At the aquifer's base, coarser sediments with $k_f$-values around 5.0E–04 to 1.5E–03 m/s exist.

To obtain an iron(III)oxide matrix all available data (Meyn, 1999 and own data) for hydraulic conductivity and total iron in the area was summarised (including data of

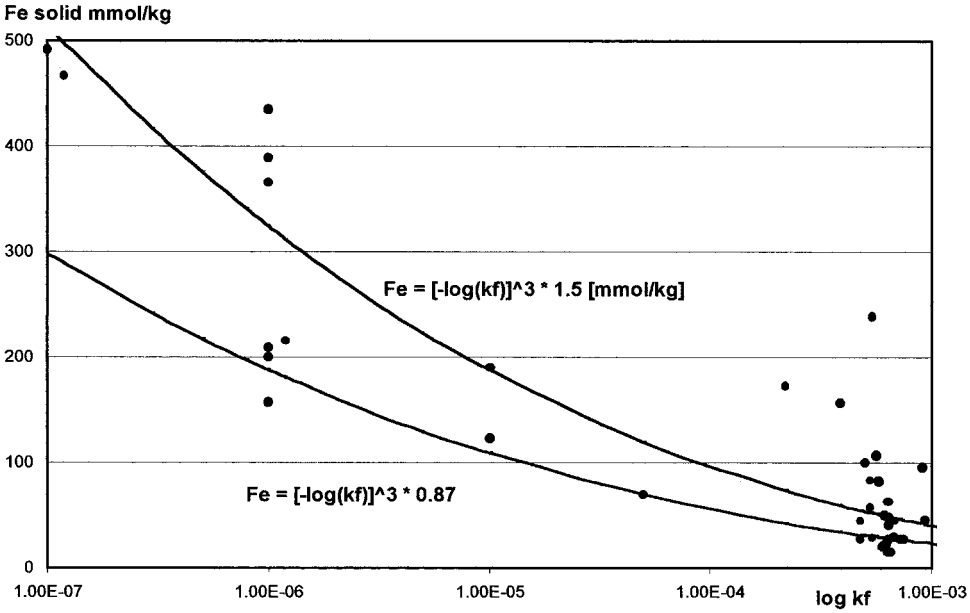


Figure 10.4: Correlation between iron (total) in the sediment and $k_f$-value. Data partly by Meyn (1999).

alluvial loam and till samples). As a first approximation we assumed that 250 years ago all available iron in the aquifer was chemically bound as iron(III)oxide or iron (III)hydroxide. We also assumed that iron(III) that has been reduced in the past 250 years precipitated in the near vicinity of its origin without being transported far. All available data is shown in Fig. 10.4. For samples analysed by Meyn (1999) with a very high iron concentration and likewise a small $k_f$ value the $k_f$ value is only an estimate based on literature values. Since the values Meyn (1999) assumed for fine-grained alluvial loam is much larger (1.0E–06 m/s) than the one we measured in a Darcy-experiment (1.0E–09 m/s) for similar samples, we chose the lower (blue) best fit model shown in Fig. 10.4 out of several possibilities. The purely statistical regression-model does not fit perfectly, indicating that the iron concentration of the sediment is influenced by several parameters other than the $k_f$-value. One possibility is that the relative percentage of finer grains (and likewise the surface area available for iron(hydr)oxide crusts) has an impact. It was nevertheless necessary to select a relationship to produce a tolerable iron matrix and we decided to chose the following:

$$Fe_{total}\ [mmol/kg] = [-\log(k_f)]^3 0.87$$

We used the hydraulic conductivity matrix to calculate an iron(III) distribution that resembles the situation at the beginning of the drainage measures, approximately 250 years ago. The result is illustrated in Fig. 10.5.

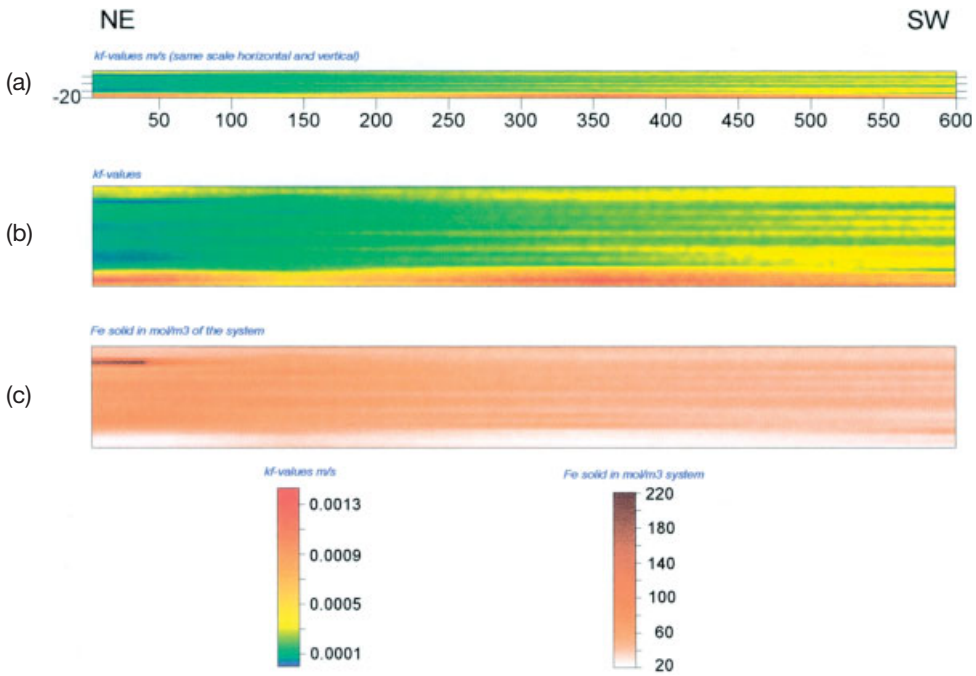


Figure 10.5: *Profile a*: Distribution of $k_f$-values. *Profile b*: The same profile, but with different scale of y-direction. *Profile c*: Distribution of Fe(III) in the aquifer (again with different scale in y-direction).

## 10.3 Principle Structure of the Two-Step Model

Modelling the combination of advective/dispersive transport with (bio)geochemical reactions can be done numerically in a so-called two-step model – apart from some geochemically trivial processes. Transport paths will be discretised in Δx and Δy, the time in Δt. In the course of transport/reaction modelling alternately there will be done one step with physical transport only and one step with geochemical reactions only. This allows modelling of many reactions with as many species as wanted in the aquatic and/or solid phase. Briefly spoken: The majority of processes that have been understood, can be modelled. This procedure has already been applied by Schulz and Reardon (1983).

### 10.3.1 Physical Transport Using the Technique of Explicit Differences

The physical transport technique can either be the explicit, the implicit difference method, or the Crank-Nicolson-Scheme (see Kinzelbach, 1986, for instance). The explicit difference method, used in this study, shows the following equation for a two-dimensional, unidirectional aquifer:

$$C_{x,y,t+\Delta t} = C_{x,y,t} + \Delta t \left[ \begin{array}{l} D_l \left( \dfrac{C_{x+\Delta x,y,t} - 2 \cdot C_{x,y,t} + C_{x-\Delta x,y,t}}{\Delta x^2} \right) \\ -v_a \left( \dfrac{C_{x+\Delta x,y,t} - C_{x-\Delta x,y,t}}{2 \cdot \Delta x} \right) + D_v \left( \dfrac{C_{x,y+\Delta y,t} - 2 \cdot C_{x,y,t} + C_{x,y-\Delta y,t}}{\Delta y^2} \right) \end{array} \right] \quad (1)$$

Here the new concentration in a cell with the coordinates x and y at the time (t+Δt) is calculated from its own concentration at the precedent time t and the concentrations of its four neighbours, also at time t. In this calculation the following constants will be considered: The size of a cell in Δx and Δy direction, the length of a time step Δt, the two dispersion coefficients $D_l$ in direction of flow and $D_v$ vertical, as well as the linear groundwater velocity $v_a$.

The explicit difference method has the disadvantage of a tendency to oscillation, in case the time steps are too large. On the other hand it is relatively simple to handle and can be programmed straight forward, because it requires only a direct assignment per cell according to the equation above. For this study we decided to choose the explicit difference method, since it was possible to avoid oscillations due to rather moderate time steps (Courant criterion).

The cells at the edge of the modelled flow field require special handling. In our example, where we modelled a vertical profile through the aquifer, these are the cells at the front, back, top and bottom of the flow field.

In each time step the cells at the front edge of the field are set to the input concentration of the system. This input for the different cells at the front edge may be either equal or different in concentration for different depths, and it can be constant in each time step or can be variable as function of time. The cells at the top and bottom edge of the aquifer can also be handled easily. These cells are set to the same concentration as their two neighbours within the field, resulting in a gradient of 0.0 and thus eliminating any flux. The cells at the back edge of the field are set in a way, that the concentration gradient between this last cell and the one before is the same as the gradient between the previous two cells. This way it is possible to transport any concentration gradients beyond the end of the field into non-modelled area.

### 10.3.2 Geochemical Reactions

In order to finish computer modelling in an acceptable time (some few hours) we modelled a redox reaction, which is characteristic for this anoxic aquifer, and also is understood well enough in order to be considered as sum-reaction. It is the redox reaction between DOC in groundwater and iron(III)oxide or iron(III)hydroxide in the solid phase of the aquifer. If we assume DOC simplified as $CH_2O$, and the iron(III)oxides and/or iron(III)hydroxides as $Fe(OH)_3$, we will get the following reaction:

$$CH_2O + 4\,Fe(OH)_3 + 8\,H^+ \quad H_2CO_3 + 4\,Fe^{2+} + 10\,H_2O$$

This reaction is assumed to be characteristic for this particular anoxic aquifer and is known to have a rather small reaction rate (Schüring et al., 2000). In each cell and each time step the concentration of DOC in the groundwater will be decreased by a kinetic with a chosen order, at the same time eliminating a stoichiometric equivalent amount of Fe(III) from the iron(III)oxide stocks of the aquifer. If one or the other reaction partner is no longer available, the reaction will come to an end. The state of concentration of each cell can be accessed in the groundwater and in the aquifer at any time.

## 10.4 Calibration of the Model with Measured Values of DOC

The profile described in Section 10.2 was chosen for modelling, since it provided most of hydrogeological and geochemical data and because of its orientation in flow direction. Both top partial graphs (a and b) of Fig. 10.6 present the field of velocities, just as it results from the product of gradient of water table and the hydraulic conductivity $k_f$ in each cell. For the hydraulic gradient we used different values at the coordinates in x-direction, which were interpolated between the measured values of the piezometers.

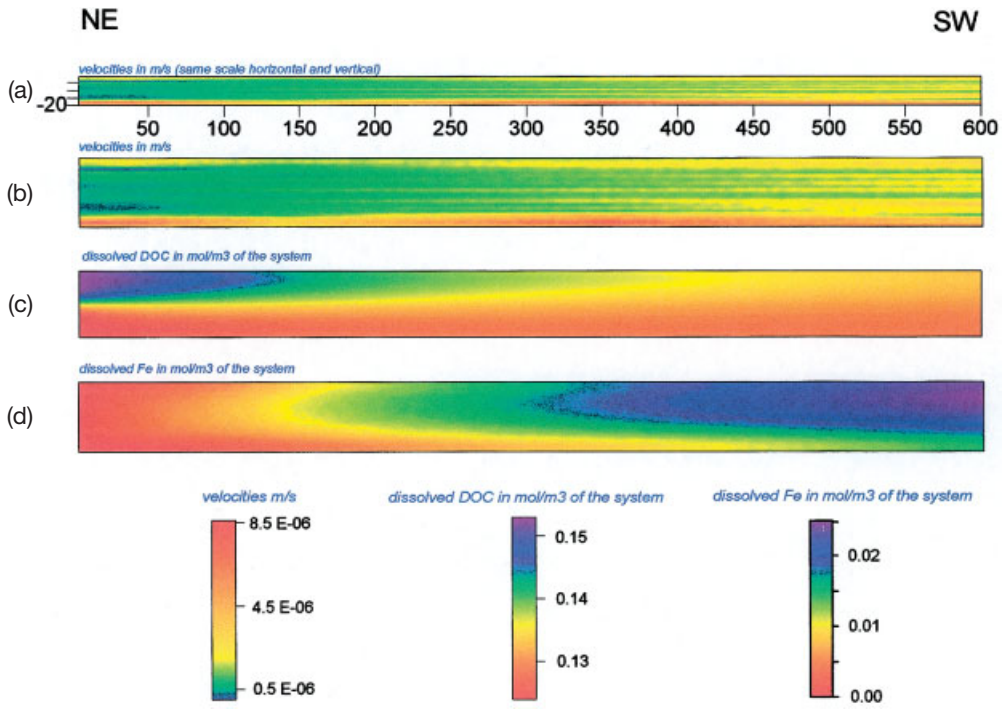


Figure 10.6: *Profile a*: Distribution of velocities (values taken from measured and interpolated gradients of groundwater table and measured and interpolated hydraulic conductivities, $k_f$) with identical scales in x- and y-direction. All values of thickness and length of profile in meter. *Profile b*: The same profile, but with different scale of y-direction. *Profile c*: Modelled distribution of DOC concentrations in groundwater after 250 years (again with different scale in y-direction). *Profile d*: Modelled distribution of $Fe^{2+}$ concentrations in groundwater after 250 years, (i.e. today), again with different scale in y-direction.

The continuous input of DOC into the flow field was simulated by a repeated input within each time step of the measured depth distribution of DOC to the 20 front cells of the field (compare left edge of profile c in Fig. 10.6). Average DOC concentrations of the first shallow and deep piezometer wells were used as input concentrations instead of the DOC concentration of the river. This was done to take account of the high concentration of solid organic carbon in the near surface sediments that were not considered directly in the model. In the top region of the aquifer the values are around 0.15 mol/m$^3$ and in the bottom region the values are around 0.13 mol/m$^3$, each given as concentration per one m$^3$ of total system of aquifer and groundwater. This is based on the assumption that the groundwater with the dissolved DOC will only take up the whole pore space, which we estimated to be 27 %. With this porosity the linear groundwater velocities were also calculated from the darcy velocities mentioned above. It is quite possible that there has been a slight variation of the DOC input over the last 250 years but incorporating this into the model was not possible due to the lack of information on DOC content of soil and river with time.

For the complete flow field the longitudinal dispersion was described with a constant dispersion coefficient of 3.0E–05 $m^2/s$. Under the given velocities, this value can be regarded as realistic for sandy/gravelly aquifers according to Schröter (1984). To decide upon the vertical dispersion was more problematical, since the value of approx. 1:10 – frequently applied – to describe the proportion between vertical dispersion coefficient and longitudinal dispersion coefficient leads to substantial overrating of the vertical dispersion. Theoretically spoken the inhomogeneities of the hydraulic conductivity should already include the main portion of the vertical dispersion, since then only the diffusion – again lower by some orders of magnitude – has to be considered. However discretising with cell sizes in meter range implies loss of some dispersion in this range, thus the value to be expected for the vertical dispersion coefficient lies somewhere between the diffusion and a tenth of the longitudinal dispersion. In our study we chose a value of 3.0E–07 $m^2/s$, which corresponds to a proportion of 1:100 between vertical and longitudinal dispersion.

This quite arbitrary method of two-dimensional transport ignores the components of vertical flow and thus underestimates the transversal dispersion thereby induced. On the other hand we tested a simple non-reacting case with the same hydraulic conditions against an analytical solution and found that the longitudinal dispersion is not influenced by numerical dispersion, whereas the numerical solution overestimates the transversal dispersion by approximately 10 %. The influence of the boundary conditions for top and bottom of the aquifer (no gradient, no flux) is more important in terms of an increased transversal dispersion for these cells. All these effects are negligible compared to the influences of inhomogeneities of hydraulic conductivities onto the modelled transversal dispersion.

The estimated values for the total amount of iron in the solid phase, based on an empirical relation to hydraulic conductivity – as described in Section 10.2, were used as start condition for iron(III)-concentration in the solid phase of the aquifer.

Now all necessary parameters for the groundwater hydraulics in the two-dimensional system are available. The same applies for the start condition of iron(III)-concentration in the solid phase and for the concentration of the continuous input at the beginning of the profile. The start concentrations for DOC in groundwater at the beginning of modelling are more or less unimportant, since due to the constant flow through the system they will sure be “forgotten” after a modelling time of 250 years. We used 0.0 $mol/m^3$ as start concentration in all cells. This leads to slightly less reaction during the first few years. We have chosen 250 years of model time because ever since then, the Oder runs within its present river-bed boundaries and the currently existing hydraulic regime started (see Section 10.1.2).

Since we wanted to model the reaction between DOC and iron(III)oxides in this system, there is only the reaction rate of this reaction left for a calibration of the model. Our example shows a satisfactory fit with the measured values for DOC in the groundwater of the flow field when we use a reaction kinetic of the first order and a rate constant of 3.3E–10 $mol/m^3 \cdot s$ (see Table 10.1). For calibration, we compared measured and modelled (250 years of modelling time) DOC concentrations at 600 m distance to the river with each other. There are two pairs of piezometers in shallow and deep parts of the aquifer in 600 m distance to the river that were used for comparison (9560 T and 9561 F plus 12/99 F and 12/99 T, compare Chapter 11). Measured values indicate that

Table 10.1: Average DOC concentrations of 4 piezometers in 600 m river distance and model values at similar distance, values in mol/m$^3$ of the system and mg/L for comparison; values in mg/L include standard deviations.

| Pietzometer/Modell | DOC [mol/m$^3$ system] | DOC [mg/l] |
|---|---|---|
| *shallow* | | |
| 12/99 F | 0.135 | 6.00 ± 1.15 |
| 9561 F | 0.113 | 5.01 ± 0.86 |
| 1299F+9561 | 0.124 | 5.51 ± 1.13 |
| model | 0.132 – 0.134 | 5.87 – 5.96 |
| *deep* | | |
| 12/99 T | 0.128 | 5.58 ± 1.16 |
| 9560 T | 0.115 | 5.12 ± 0.76 |
| 12/99T+9560 T | 0.122 | 5.40 ± 1.02 |
| model | 0.130 – 0.132 | 5.78 – 5.87 |

the redox reactions today are stationary, we therefore used average DOC concentrations of 9 sampling campaigns which are 5.51 ± 1.13 mg/L for the two shallow piezometers and 5.40 ± 1.02 mg/L for the deeper ones. The model calculated DOC concentrations of approximately 5.87–5.96 mg/L in the upper parts and 5.78–5.87 mg/L in the lower parts of the aquifer. Table 10.1 shows that the different piezometers vary slightly, using only 12/99 F & T would actually produce an even better fit, indicating that local differences of, for example, sediment composition that were not taken into account, are also of importance.

## 10.5 Validation of the Model with Measured Values for Dissolved Iron

For calibrating the model with the reaction rates between DOC and iron(III)oxide in the solid phase of the aquifer we only used the measured distribution of DOC in groundwater. In this case a good fit suggests that the right reaction rates were chosen – assuming that the described reaction reflects the processes in the groundwater. Supposed the reaction rate for each point of the flow field could be chosen freely, then the described model would allow to simulate any DOC concentration distribution, as long as only a decrease of concentration on the flow path is described. In our example Oderbruch we could use exactly the same first order reaction kinetic with the same reaction constant for all 3000 cells. This way we already found a satisfactory description of concentration distribution of DOC in groundwater, valid for the total flow field. However, this is not a real verification or validation of the modelled processes, but it is a good indication that our conceptual model is not principally wrong.

Reaction kinetics between DOC and iron(hydr)oxides are certainly governed by the specific situation of the aquifer. Thus, neither the reaction rates nor their constancy for the entire aquifer may be transferred to other systems.

If we assume that the reaction mentioned in Section 10.3.2 is a fundamental description of the processes controlling the concentration of DOC in groundwater, then this reaction would also control the concentration of iron in groundwater at the same time. An easy way to check this was to run two model calculations, both with identical model parameters. However, one of these calculations was run without considering the reduction of DOC. In this case the distribution of DOC is only controlled by the input from the river Oder and the physical transport with advection and dispersion along the flow through the aquifer. The difference between calculated distribution of concentration with reaction and distribution calculated at same conditions but without reduction of DOC will show the reduced quantity of DOC for each point of the flow field. Now this quantity can be converted stoichiometricly into the equivalent quantity of dissolved iron. Thus one mol of $CO_2$ from oxidised DOC corresponds with four times the amount of used iron(III)oxide and the resulting $Fe^{2+}$ in solution.

The result of this calculation is shown in profile d in Fig. 10.6. It shows the distribution of iron in groundwater in the flow field. Table 10.2 presents model and equivalent field data, again for two deep and two shallow piezometer at 600 m river distance. Table 10.2 shows the good fit between "real" average iron concentration in the groundwater and in the model. With an average of 5.44 ± 1.94 mg/L (field) in comparison to 4.1–5.2 mg/L (model) in the shallow parts and 2.73 ± 0.98 mg/L (field) in comparison to 2.5–3.7 mg/L (model) iron in the deeper parts of the aquifer, values are very similar. Again, the piezometers vary individually. The good fit in this comparison confirms, that in principle the modelled process between dissolved DOC and iron(hydr)oxides in the solid phase was the right one and that the chosen reaction rates were obviously also correct.

Table 10.2: Average $Fe^{2+}$ concentrations of 4 piezometers in 600 m river distance and model values at similar distance, values in mol/m$^3$ of the system and mg/L for comparison; values in mg/L include standard deviations.

| Piezometer / Modell | Fe [mol/m$^3$ system] | Fe [mg/L] |
|---|---|---|
| *shallow* | | |
| 12/99 F | 0.018 | 3.56 ± 0.17 |
| 9561 F | 0.036 | 7.47 ± 0.47 |
| 1299F+9561 | 0.026 | 5.44 ± 1.94 |
| model | 0.020–0.025 | 4.13–5.17 |
| *deep* | | |
| 12/99 T | 0.018 | 3.71 ± 0.10 |
| 9560 T | 0.008 | 1.75 ± 0.07 |
| 12/99T+9560 T | 0.013 | 2.73 ± 0.98 |
| model | 0.012–0.018 | 2.48–3.72 |

## 10.6 Discussion

Figure 10.7 is a picture of the modelled difference in iron concentration in the sediment 250 years ago and now, i.e. the turnover of iron that has been removed from the aquifer in the past 250 years. The iron turnover is very low (about 1–3 %) compared to the total iron depot available in the aquifer (compare Fig. 10.5). The turnover has been highest, were the DOC input concentration was high (i.e. in the upper aquifer parts, close to the river). Less iron has been removed in the deeper parts of the aquifer due to the lower start-concentration in the sediment and the lower DOC input concentration. The iron turnover was much less than we expected, since in many parts of the aquifer, the iron(hydr)oxide fraction makes up only about 50–80 % of the total amount of iron available. This is a strong indication that the reduced iron-minerals (for example sulfides), were probably already present 250 years ago and estimated concentrations in our iron-start-matrix might be too high.

Figure 10.7 also shows that although there are still sufficient amounts of iron(hydr)oxides available near the Oder, the reduction process takes place in the entire aquifer. Thus, the DOC is transported away from the near vicinity of the river, before it has been fully oxidised and removed.

The model introduced within this paper can be seen as one attempt towards developing a virtual aquifer out of only a scarce data-set that resembles natural geological patterns as well as towards increasing the dimensionality of coupled transport and reaction models. This could only be done on behalf of the systems complexity. It is essential to fully understand a system in order to reduce it to the major governing

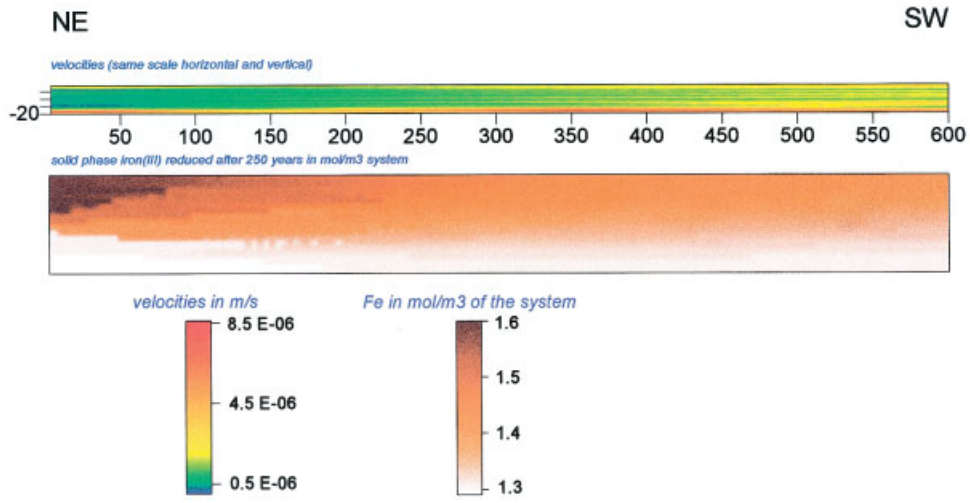


Figure 10.7: Difference in iron(III) concentration in the sediment between the model-start (250 years ago) and today. The distribution of velocities with same scale horizontal and vertical is given for comparison.

processes and variables. There are nevertheless a few problems resulting from the applied simplifications and presumptions.

Firstly only one redox process, the one we thought to be the dominant one consuming the available DOC, has been considered. Other redox processes observed at the field site "Bahnbrücke" are discussed in Chapter 11. We calibrated the DOC oxidation reaction with measured DOC concentrations in the flow field and calculated the iron content of the water with the DOC concentrations. The fact that the calculated iron concentrations strongly resembled the observed iron concentrations in the field supports the presumption, that iron(hydr)oxide reduction really is the dominant DOC consuming process. If another redox process would be of importance, the calculated iron concentrations would have been higher than the observed ones which was not the case. Our presumption is therefore reasonable.

We calculated a flux of dissolved iron at the back edge of the model continuously eliminating iron from the system. For the empirical relationship between $k_f$ and iron in Section 10.1.2, we assumed that the present total amount of iron in the sediment was formally present in the form of iron(hydr)oxide. This assumption is valid because the flux of dissolved iron ($Fe_{diss.}$) is negligible compared to the total amount of iron ($Fe_{total}$) available in the sediment which can be proofed with the help of the following calculations (compare also Fig. 10.7). Over a time period of 250 years we eliminate approximately 493 kg of $Fe_{diss.}$ from the system at the back edge of the model:

$$20\ [m^2] \cdot 0.27 \cdot 0.25\ [m/d] \cdot 1000 \cdot 4\ [mg/L] = 5.4\ g\ Fe_{diss.}/d \text{ or } 493\ kg\ Fe_{diss.}/250\ y$$

while the total amount of iron ($Fe_{total}$) in the sediment is in the order of 33.6 tons:

$$50\ [mol/m^3\ of\ system] \times 56 / 1000 \times 20\ [m^2] \times 600\ [m] = 33600\ kg / slice\ aquifer$$

with: porosity 27 %
darcy velocity at the back edge of the model 0.25 m/d
aquifer thickness 20 m
aquifer width 1 m
aquifer length considered 600 m
iron concentration in groundwater at the back edge of the model ~4 mg/L

Another weak point is the fact that the water balance has not been taken into consideration. Producing a random hydraulic conductivity matrix while using gradients similar to the ones observed in the field has the consequence that thus the water quantity flowing through every aquifer section may vary. With the condition that this quantity of water should be constant throughout the whole flow path, it is easily possible to calculate a distribution of gradients, which would fulfil this condition. In our example, however, this distribution of calculated gradients differed from the measured gradients only in the range of possible uncertainties of measurements and was therefore neglected.

The last problem of the model is the contemplation of horizontal flow only. At the field site "Bahnbrücke", a true 3-dimensional flow field with a generally strong vertical component exists due to the drainage ditches that take up a major portion of the

infiltrating water. We did not consider any vertical flow nor did we consider any water movement out of the profile into the third dimension. Because the main drainage ditch behind the levee is strongly heterogeneous and only efficient in some sections one could say that our model roughly reflects reality in a cross section where the drain is impermeable.

The major challenge for the future will be the step into the third dimension with coupled transport/reaction models. This can only be done in a similar way: Reducing the chemistry of a system down to the essentials to keep calculation time manageable. The construction of a 3-dimensional hydraulic model of the field site is currently in progress. Once it is complete and running, the aim will be to produce a 3-dimensional aquifer to model iron reduction within the whole area and not only within one slice of aquifer. Another aim is the integration of further geochemical processes, for example manganese(hydr)oxide reduction into the model. As a consequence, further validation of interacting processes will be necessary. In addition, it will be important to carefully check the water balance with the help of the hydraulic model once the third dimension is considered.

## 10.7 References


Adler, M.; Hensen, C.; Wenzhöfer, F.; Pfeifer, K.; Schulz, H. D. (2001): Modeling of calcite dissolution by oxic respiration in supralysoclinal deep-sea sediments. *Marine Geology*, **177**, 167–189.

Beyer, W. (1964): Zur Bestimmung der Wasserdurchlässigkeit von Kiesen und Sanden aus der Kornverteilungskurve. *Wasserwirtschaft Wassertechnik* **14**, 165–168.

Hazen, A. (1893): Some physical properties of sand and gravels with special reference to their use in filtration. *Annual Report Mass. State Board of Health* **24**, 541–556.

Hensen, C.; Landenberger, H.; Zabel, M.; Gundersen, J. K.; Glud, R. N.; Schulz, H. D. (1997): Simulation of early diagenetic processes in continental slope sediments off southwest Africa: the computer model CoTAM tested. *Marine Geology* **144**, 191–210.

Holzbecher, E.; Massmann, G.; Horner, C.;Pekdeger, A. (2001): Redox Transport Modelling for the Oderbruch Aquifer (chapter 11).

Kinzelbach, W. (1986): Groundwater Modelling – An Introduction with Sample Programs in BASIC, Elsevier.

Mehra, O. P.; Jackson, M. L. (1960): Iron oxide removal from soils and clays by a dithionite-citrate system buffered with sodium bicarbonate. *Clays Clay Mineral*. **5**, 317–327.

Meyn, U. (1999): Charakterisierung und Bilanzierung von Redoxprozessen an der Uferfiltrationsstrecke Transekte “Bahnbrücke” (Oderbruch), Unveröff. Diplomarbeit, Fachbereich Geowissenschaften, Univ. Bremen.

Parkhurst, D. L. (1995): User’s guide to PHREEQC: a computer model for speciation, reaction-path, advective-transport, and inverse geochemical calculations, US Geol. Surv., Water-Resources Investigations Report, 95–4227.

Schröter, J. (1984): Mikro- und Makrodispersivität poröser Grundwasserleiter. *Meyniana* **36**, 1–34.

Schulz, H. D.; Reardon, E. J. (1983): A combined mixing cell/analytical model to describe two-dimensional reactive solute transport for unidirectional groundwater flow. *Water Resour. Res* **19**, 493–502.

Schüring, J.; Schlieker, M.; Hencke, J. (2000): Redox Fronts in Aquifer Systems and Parameters Controlling their Dimensions. In: Schüring, J.; Schulz, H. D.; Fischer, W. R.; Böttcher, J.; Duijnisveld, W. H. M. (Eds.): Redox – Fundamentals, Processes and Applications, 1st Edition, Springer.

Van Cappellen, P.; Wang, Y. (1995): STEADYSED1: A Steady-State Reaction-Transport Model for C, N, S, O, Fe and Mn in Surface Sediments, Version 1.0 User´s Manual, Georgia Inst. Technol.

Wang, Y.; Van Cappellen, P. (1996): A multicomponent reactive transport model of early diagenesis: Application to redox cycling in coastal marine sediments. *Geochim. Cosmochim. Acta* **60**, 2993–3014.

# 11 Redox-Transport Modelling for the Oderbruch Aquifer

Ekkehard Holzbecher*, Christoph Horner, Gudrun Massmann, Asaf Pekdeger and Christoph Merz

## Abstract

The Oderbruch is a region aside of the Oder river on the border between Germany and Poland. As the region lies mainly below the river's water level, there is a permanent infiltration of surface water into the hydraulically connected aquifer. A field study was started in order to understand, and quantify redox processes in the groundwater. The measurement campaign is accompanied by modelling. Transport and geochemical processes are modelled by a coupled approach. The DOC biodegradation reactions using different electron acceptors (primary reactions) were modelled by a Monod kinetic approach. The model accounts for several redox components in the solid and fluid phases. Relevant non-redox reactions, such as sorption, precipitation, and dissolution are also taken into account. In a former study Holzbecher et al. (2001) reported about a steady manganese peak with 0.12 mmol $L^{-1}$ in approximately 150 m distance from the river and proposed a model concept for manganese chemistry. Concerning Fe and Mn the release by the primary reactions is compensated by precipitation/dissolution reactions of solid Mn and Fe carbonates (rhodochrosite and siderite), which are conceived as kinetic reactions. The former simple model approach is extended to consider iron and carbon chemistry, including calcite dissolution and precipitation and pH. Simulations considering acid-based and carbonate chemistry additionally, show that a verification of the observed spatial Fe and Mn distribution is only possible if the steady state spatial distribution of the main hydrogeochemical parameters (especially the pH values) is correctly simulated.

* Abteilung Ökohydrologie, Institut für Gewässerökologie und Binnenfischerei im Forschungsverbund Berlin e. V. (IGB), Müggelseedamm 310, 12587 Berlin; e-Mail: holzbecher@igb-berlin.de



*Geochemical Processes: Conceptual Models for Reactive Transport in Soil and Groundwater. Research Report.* Deutsche Forschungsgemeinschaft (DFG).
 ISBN: 978-3-527-27764-3

## 11.1 Introduction

In natural aquatic systems, redox processes often have a significant impact on solute chemistry. The concentration of redox components reflects and influences the geochemical environment and thus the behaviour of chemical components in the system. The migration of other dissolved constituents, such as metals, organic compounds and other pollutants, is substantially affected by redox components and their reactions. An understanding of redox is thus indispensable in studies on the chemical environment in surface and groundwater.

Redox processes are of particular importance at the interface between surface water and porous medium, i.e. when surface water enters the connected pore space at the bottom of rivers and lakes. The changed environment, characterised by the contact with the solid phase, initiates several types of biogeochemical processes, in particular redox reactions. It is nearby that redox components are in the focus of sedimentological studies, some of which will be mentioned in the following. Although redox processes may be similarly important for groundwater chemistry, less attention has been given to redox processes in aquifers, which are recharged from rivers or lakes.

In sediments, redox fronts can be observed on the scale of centimetres, whereas the distance of redox fronts in aquifers might be much longer. It can be expected that all soluble components are transported by groundwater flow and thus reaction fronts are widened and can be found at greater distance from the point of infiltration. Although groundwater velocities are small, advective transport in aquifers generally is important. A description of different dimensions of redox fronts in aquifers has been given by Schüring et al. (2000). Numerical modelling can approach the complex interaction of various fluid and solid phase species, which lead to the spreading of redox fronts.

Recently, several studies have been published demonstrating the use of computer models to understand the interaction of chemistry, biochemistry, and the transport of redox species (Boudreau, 1986; van Cappellen and Wang, 1996; Soetaert et al., 1996; Park and Jaffé, 1996; van den Berg et al., 2000). These papers have in common that they focus on the concentration of the species and less on the energetic phenomena accompanying redox chemistry. Biochemistry is modelled as a kinetic reaction. While the above-mentioned studies deal with sediments of surface water bodies, in one exceptional work Hunter et al. (1998) utilise the novel approach for groundwater research. Keating and Bahr (1998) use a quasi-kinetic concept as well. The expert system approach presented by Chapelle et al. (1995) takes up the argument as follows: “this methodology is based on measurable water chemistry parameters … it provides a better description of predominant redox processes in groundwater systems than more traditional Eh-based methods”. In this paper another model is presented, which follows the indicated line.

Within this book, two different approaches of geochemical models are presented. This paper is an attempt to model the transport and reaction of all major redox components observed. At current stage, it is possible to model the interaction of a larger number of participating redox-processes in one space dimension only. In Massmann and

Schulz (Chapter 10), the dimensionality has been increased on behalf of the system's geochemical complexity. A virtual aquifer was produced and the oxidation of DOC by iron (hydr)oxides was simulated in a two-dimensional transport and reaction model. Both model attempts focus on different aspects and have different priorities but are based within the same region, using the same data set and should be regarded in context.

## 11.2 Site and Measurement Description

The Oderbruch is situated in eastern Germany, at the border to Poland about 50 km northeast of Berlin (for a map of the location see Chapter 10, Fig. 10.1). It covers an area of more than 800 km$^2$ and represents Germanys largest enclosed river polder. It is bordered by the Geest high-plains in the west and the river Oder in the east. The region has been intensively drained during the past 250 years (compare Chapter 10). As a result of the drainage measures, the river embankment is situated below the groundwater table within the polder, resulting in permanent lateral infiltration of river water into the aquifer. A levee prevents the low-lying, predominantly agriculturally used region from being flooded.

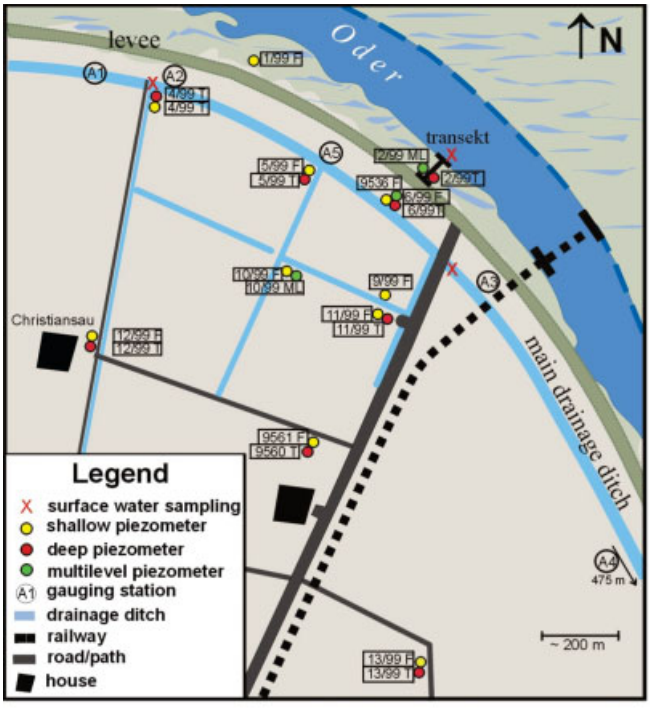


Figure 11.1: Schematic map of the piezometer field "Bahnbrücke".

Several redox-controlled, chemical changes occur when oxic river water enters into the anoxic aquifer. Along its flow-path, the water becomes progressively more reduced, making the region ideal for groundwater redox studies. A 1 $km^2$ exemplary field-site "Bahnbrücke", located adjacent to the river Oder in the northern Oderbruch, was chosen for detailed hydraulic and hydro chemical investigation.

In 1999, 10 sediment cores were drilled at the field site, reaching to the base of the aquifer body. The instrumentation consists of 24 conventional piezometers at varying depths and three multilevel wells located in a distance of 3 to 620 m from the river (Fig. 11.1). The area has been intensively surveyed and monitored over $1^1/_2$ years for relevant parameters. A 3D transient hydraulic model serves as a base for investigating groundwater flow paths for different river levels.

Nine surface- and groundwater sampling campaigns were undertaken over a period of $1^1/_2$ years. Measurements of $E_H$, pH, $O_2$, temperature and conductivity were carried out in the field using a flow cell. Samples were filtered through 0.45 µm membrane filters immediately after sample retrieval to minimise Fe and Mn precipitation. Sample aliquots were acidified with nitric acid for cation analysis. Alkalinity was measured soon after the samples were returned to the laboratory. The complete suite of analysis was generally performed one day after sampling. Water samples were analysed for Ca, Mg, K, Na, Cl, $NO_3$, Br, $SO_4$, and $NO_2$ by ion chromatography (DIONEX DX 500). Mn and Fe were determined by ICP (JOBINYVON). $NH_4$, $PO_4$, S and $SiO_2$ were analysed by photometry (UVICON 931 KONTRON, DR 2000 HACH), and DOC was determined by a DOC analyser (SHIMADZU).

### 11.2.1 Hydrogeology

At the field-site Bahnbrücke, the 20–22 m deep aquifer consists of glacial sands and gravel of late Pleistocene age. It is bordered by a till at the base and an alluvial loam, relict of regular Holocene flooding, at the top. The upper parts of the aquifer are mainly fine to medium sands with hydraulic conductivities ranging from 5.5 $10^{-5}$ to 4.0 $10^{-4}$ m $s^{-1}$, becoming coarser with depth (hydraulic conductivities of 2.9–8.9 $10^{-4}$ m $s^{-1}$). For a possible statistical realisation of the aquifer see Chapter 10. Due to the strong river current, the riverbed sediments are generally coarse and highly permeable, the hydraulic contact between river and groundwater is therefore unrestrained (hydraulic conductivities from 9 $10^{-4}$ to 1.5 $10^{-3}$ m $s^{-1}$). Mean flow velocities vary from 0.5–1.5 m $day^{-1}$ near the river and decline to 0.2–0.3 m $day^{-1}$ further inland.

Most of the groundwater discharge occurs from a main drainage ditch, which runs parallel to the levee at 150 m distance from the river. The resulting infiltration is complex and has a strong vertical component (see Fig. 11.2).

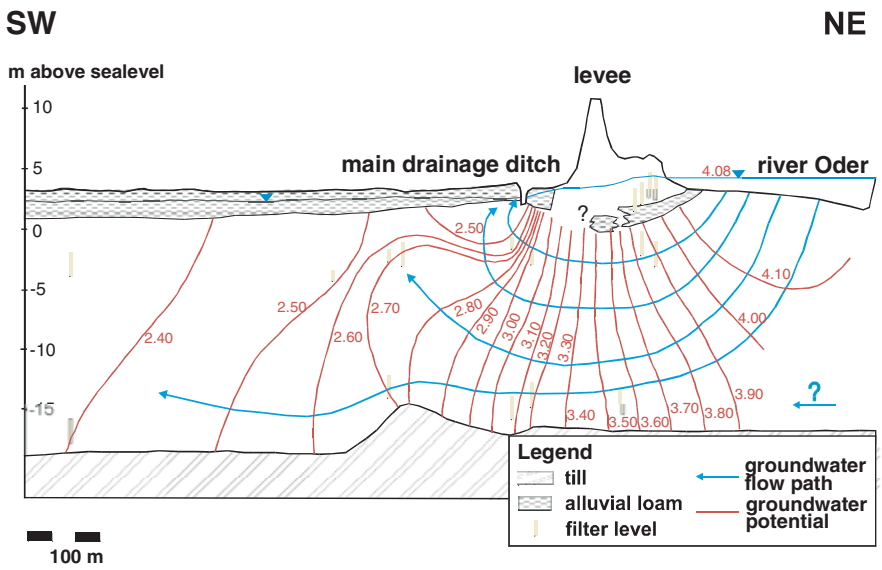


Figure 11.2: Vertical schematic cross-section through the aquifer at the field-site; filter-levels shown, water-level data measured on the 28.09.1999; schematic flow-paths included.

## 11.2.2 Water Chemistry

During bank-filtration of oxic river water a sequence of redox reactions occurs with increasing travel and reaction time of the infiltrating water. The $Fe^{2+}$ and particularly $Mn^{2+}$ content of the water can best describe the redox state of the system. Due to the complex flow behaviour and the natural heterogeneity of the sediments, the distribution of water constituents varies strongly. As an example, Fig. 11.3 shows the $Fe^{2+}$ concentration in January 2000 along the transect shown by Fig. 11.2.

It can clearly be seen that generally, the highest $Fe^{2+}$ concentrations were measured in the upper parts of the aquifer near the river. This is due to the higher abundance of reactive organic matter in the sediment that is made up of post-glacial alluvial material. This can also be seen from the DOC concentrations in the groundwater that are considerably higher in these wells (see also Schüring et al., 2000). Because of the complex situation, we will only refer to the deeper groundwater paths (13 to 20 m below sea level in the following. They are also most representative for processes within the Oderbruch aquifer, since they reach further behind the levee.

The redox sequence starts with the reduction of $O_2$ and $NO_3^-$ present in the river water. $O_2$ and $NO_3^-$ are probably consumed within the first few m or even dm along the groundwater flow path since they are not observed in any of the observation wells (see also Massmann et al., 2001).

As a result of Mn (hydr) oxide reduction, the $Mn^{2+}$ concentration of the water continuously increases from the river to a distance of 150 m, where it reaches a maxi-

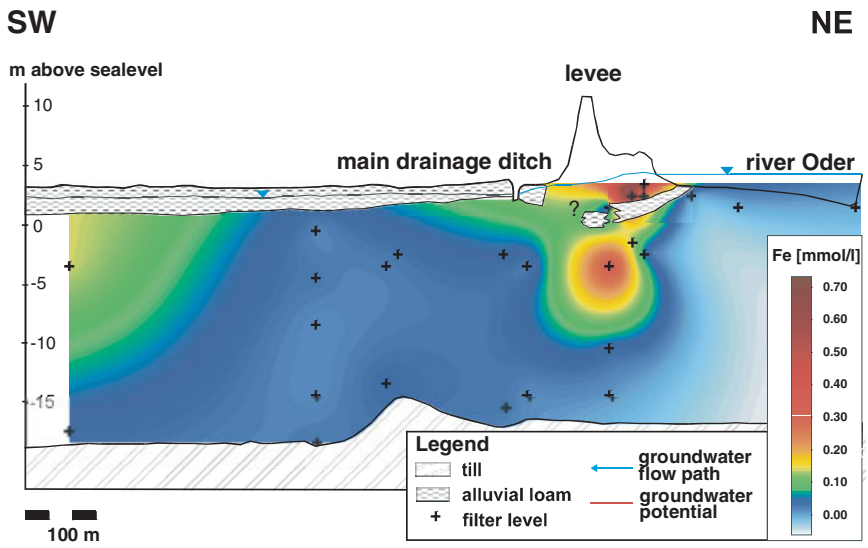


Figure 11.3: Spatial distribution of the $Fe^{2+}$ concentration along the transsect shown by Fig. 11.2.

mum of 5–6 mg $L^{-1}$ $Mn^{2+}$. The $Mn^{2+}$ concentration then decreases to less than 1 mg $L^{-1}$ at 620 m from the river.

While the reduction of Mn (hydr) oxides is certainly the source for $Mn^{2+}$ in solution, groundwater $Mn^{2+}$ concentration is controlled by the saturation of Mn carbonate ($MnCO_3$, rhodochrosite). Rhodochrosite is the most abundant reduced $Mn^{2+}$ mineral in nature (Berner, 1980). It commonly precipitates in aquatic systems according to the reaction

$$Mn^{2+} + HCO_3^- \Leftrightarrow MnCO_3 + H^+$$

and consequently removes $Mn^{2+}$ from the groundwater. It seems that the precipitation of rhodochrosite is encouraged when the dissolution of Mn and Fe (hydr) oxides produces a more alkaline and thus $CO_3^{2-}$ richer solution. The similar decrease in $Mn^{2+}$ concentration, alkalinity, and pH after 150 m lateral river distance, which is 300–350 m travel distance on a lower flow path (Fig. 11.2), suggests that rhodochrosite is precipitating. Similar observations were reported by Matsunaga et al. (1993).

Whereas groundwater $Mn^{2+}$ concentration increases to 150 m from the river and then decreases to 620 m, the $Fe^{2+}$ concentration increases along the transect reaching a maximum of 2–5 mg $L^{-1}$ at 620 m. The redox conditions do not reach the post-oxic, ferrous precipitates, and $SO_4^{2-}$ is not reduced, i.e. $S^{2-}$ was not detected. The $SO_4^{2-}$ content of the groundwater is about 100 mg $L^{-1}$, which is similar to the river water concentration.

The groundwater composition was relatively constant during the one-year collection period. The modelling approach, therefore, is focused on finding (quasi) steady-state solutions of the differential equations. Further details, concerning the filed site and measurements are given by Massmann et al. (2001).

## 11.3 Modelling Concept

In order to verify the geochemical changes along the Bahnbrücke transect, a reactive transport model was conceptualised and implemented. This model describes a one-dimensional reactive transport along a streamline leaving the Oder riverbed into the deeper parts of the adjacent aquifer. The reactive transport model considers primary, and secondary redox reactions as well as precipitation/dissolution reaction. The principal reaction pathways as outlined by van Cappellen and Wang (1996) are given below.

The primary redox reactions release dissolved species, as $Fe^{2+}$, $Mn^{2+}$, $H_2S$, and in extreme cases $CH_4$ into the pore water. These dissolved ionic species are redistributed by secondary redox reactions or precipitation/dissolution reactions, which depend on other geochemical parameters as alkalinity and pH conditions. Both primary and secondary redox reactions are considered as irreversible reactions (van Cappellen and Wang, 1995).

As primary redox reactions six reaction steps are significant (cf. van Cappellen and Wang, 1995):

(1A) $$(CH_2O)_x(NH_3)_y(H_3PO_4)_z + (x+2y)O_2 + (y+2z)HCO_3^- \xrightarrow{R_1/x} (x+y+2z)CO_2 + yNO_3^- + zHPO_4^{2-} + (x+2y+2z)H_2O$$

(2A) $$(CH_2O)_x(NH_3)_y(H_3PO_4)_z + \frac{(4x+3y)}{5}NO_3^- \xrightarrow{R_2/x} \frac{(2x+4y)}{5}N_2^- + \frac{(x-3y+10z)}{5}CO_2 + \frac{(4x+3y-10z)}{5}HCO_3^- + zHPO_4^{2-} + \frac{(3x+6y+10z)}{5}H_2O$$

(3A) $$(CH_2O)_x(NH_3)_y(H_3PO_4)_z + 2\cdot MnO_{2(s)} + (3x+y-2z)CO_2 + (x+2y-2z)H_2O \xrightarrow{R_3/x} 2\cdot MN^{2+} + (x+y+2z)HCO_3^- + yNH_4^+ + zHPO_4^{2-}$$

(4A) $$(CH_2O)_x(NH_3)_y(H_3PO_4)_z + 4\cdot Fe(OH)_{3(s)} + (7x+y-2z)CO_2 \xrightarrow{R_4/x} 4\cdot Fe^{2+} + (8x+y-2z)HCO_3^- + yNH_4^+ + zHPO_4^{2-} + (3x-y+2z)H_2O$$

(5A) $$(CH_2O)_x(NH_3)_y(H_3PO_4)_z + \frac{x}{2}SO_4^{2-} + (y-2z)CO_2 + (3x-y+2z)H_2O \xrightarrow{R_5/x} \frac{x}{2}H_2S + (x+y-2z)HCO_3^- + yNH_4^+ + zHPO_4^{2-}$$

(6A) $$(CH_2O)_x(NH_3)_y(H_3PO_4)_z + (y-2z)H_2O \frac{(x-2y+4z)}{2} \xrightarrow{R_6/x} \frac{x}{2}CH_4 + CO_2 + yNH_4^+ + zHPO_4^{2-} + (y-2z)HCO_3^-$$

The focus in this study is on manganese and iron, i.e. on Reactions (3A) and (4A). Oxygen and nitrate are not present in groundwater observation wells (see Section 11.2) and are already consumed in the very vicinity of the river. Sulphate and methane show no variations on the entire field site, and are thus not of interest for the study of redox fronts.

The species released by the primary reactions can enter secondary redox reactions (van Cappellen and Wang, 1996) resulting in a back oxidation of released species. As an example the $Fe^{2+}/MnO_{2(s)}$ redox coupling is given:

(1B) $2Fe^{2+} + MnO_{2(s)} + 2HCO_3^- + 2H_2O \xrightarrow{R_{11}} 2Fe(OH)_{3(s)} + Mn^{2+} + 2CO_2$

Additionally depending on acid-based conditions. Non-redox precipitation/dissolution reactions are significant which causes further redistribution of released Fe and Mn:

(1C) $Mn^{2+} + 2HCO_3^- \xleftarrow{R_{12}R_{-12}} MnCO_{3(s)} + CO_2 + H_2O$

(2C) $Fe^{2+} + 2HCO_3^- \xleftarrow{R_{13}R_{-13}} FeCO_{3(s)} + CO_2 + H_2O$

Distributions of redox species as observed along the Bahnbrücke transect result from a coupling of primary and secondary redox reactions involving precipitation/dissolution reactions over a long time generating a quasi-steady spatial distribution over the transect.

### 11.3.1 Reaction Model

The overall DOC degradation is a sum of different enzymatic reactions involving different bacterium populations specialized to consume different electron acceptors. Only few models consider these biochemical reactions in detail (cf. Schäfer et al., 1998). For simplicity we follow the common simplified concept, in which an overall DOC decay constant including all enzymatic reactions is formulated. For the overall degradation of DOC first order kinetics are assumed.

Considering the consumption of electron acceptors by DOC degradation two alternative formulations can be found (see Boudreau, 1997):

- The *Blackman kinetics* which make the reaction rate discontinuously independent of electron acceptor concentration if a minimal limiting concentration is reached.
- The *Monod kinetics*, which produce a continuous transition from linear dependence of reaction rate to independence by means of the half saturation concentration.

Both formulations of the reaction dependence on electron acceptor concentration are shown in Fig. 11.4. Both have two parameters. The Blackman kinetics have a sharp switch between zero and first order at a limit concentration, while the Monod concept

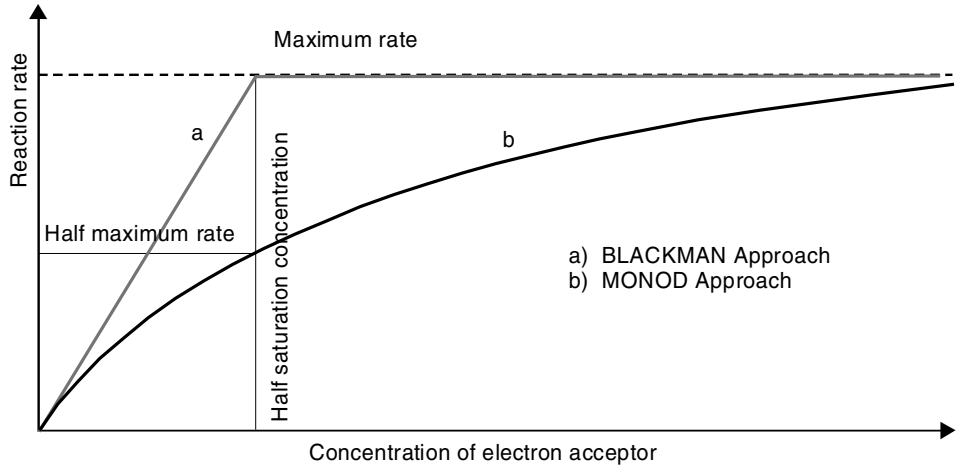


Figure 11.4: Dependence of DOC decay rate on electron acceptor concentration: Blackman and Monod kinetics.

connects both regimes by a smooth (differentiable!) transition. When the behaviour of both for $C \to 0$ and for $C \to \infty$ is identical, the rate of the Monod kinetics at the limit concentration is half of that of the Blackman kinetics – for that reason one may adopt the name *half-saturation concentration*.

The programmes STEADYSED1 (van Cappellen and Wang, 1995) and BIOTRNX (Hunter et al., 1998) use a Blackman kinetics approach for the electron acceptors.

For this modelling the Monod kinetic approach was chosen. In this work the primary redox reaction sequence (1A)–(5A) was set up introducing appropriate threshold values (half saturation concentrations) as reaction limiting factors. The contribution of a given electron acceptor $i$ to the overall DOC degradation is given by

$$\frac{\partial C_i}{\partial t} = -k_{r,i} \underbrace{\frac{C_i}{C_i + C_{\lim,i}}}_{=:f_i} \qquad \text{for } i=1,..6 \tag{1}$$

For concentrations $C_i \gg C_{\lim,i}$ (the half saturation concentration of the electron acceptor $i$) the reaction kinetic is approximately of first order with decay constant $k_{r,i}$. At concentrations $C_i < C_{\lim,i}$, the reaction rate becomes constant, i.e. independent of the concentration (zero-order kinetics).

The Gibbs free energy of each reaction step determines the preferential order of the different redox reaction pathways. Starting from oxic conditions, the subsequent consumption of the electron acceptors favours the reaction with the next lower amount of Gibbs free energy. In this way, the overall decay rate of DOC, $R_C$, is formulated using $f_i$, as defined in Eq. (1), as contributions of all reaction steps to the overall reaction and the overall rate constant $\lambda$. During the redox degradation of DOC, all contributions $f_i$ sum up to 1.

$$R_c = -\lambda \frac{\partial C_{org}}{\partial t} \sum_{i=1}^{6} f_i \tag{2}$$

The availability of dissolved Fe and Mn, and also of matrix bounded $MnO_{2(s)}$ and $Fe(OH)_{3(s)}$ as electron acceptors is additionally controlled by secondary redox reactions (as Reaction (1B)) und and Precipitation (non redox) reactions (e.g. Reactions (1C) and (2C)). Redox coupling of dissolved Fe with matrix bounded $MnO_{2(s)}$ consumes additionally $MnO_{2(s)}$ so that the half saturation concentration of $MnO_{2(s)}$ will be reached faster than without considering redox Fe–Mn coupling in the redox process.

Acid-based equilibria in the aquifer, such as pH buffering and speciation of TIC (total inorganic carbon), affect additionally the mobility of Fe and Mn with respect to saturation of rhodochrosite and siderite (Reaction (1C) and (2C)). Similar to the model STEADYSED1 (van Cappellen and Wang, 1995) TIC is considered as an excess component as indicated by the hydrogeochemical analyses. The contribution of TIC as reaction product from DOC degradation may be of minor importance. The infiltration water of the Oder shows only supersaturation of calcite (but not of rhodochrosite and siderite) whereas the aquifer apart from the Oder is generally supersaturated with respect to rhodochrosite and siderite.

Carbonate chemistry was incorporated into the model in order to verify realistic geochemical conditions. First, the carbonate chemistry is characterized by the dissociation of carbonic acid yielding $HCO_3^-$ and $CO_3^{2-}$. The two dissociation constants $K_{1c}$ and $K_{2c}$ are defined as follows

$$K_{1c} = \frac{\left[HCO_3^-\right]\left[H^+\right]}{\left[H_2CO_3\right]} \tag{3}$$

(First dissociation step yielding hydrogen carbonate, $HCO_3^-$), and

$$K_{2c} = \frac{\left[CO_3^{2-}\right]\left[H^+\right]}{\left[HCO_3^-\right]} \tag{4}$$

(Second dissociation step yielding carbonate, $CO_3^{2-}$).

The total inorganic carbon (TIC) is the sum of all three species $H_2CO_3$, $HCO_3^-$ and $CO_3^{2-}$. The contribution of these species depends on the hydrogen ion concentration:

$$\left[TIC\right] = \left[H_2CO_3\right] \cdot \alpha_1^{-1} \tag{5a}$$

$$\left[TIC\right] = \left[HCO_3^-\right] \cdot \alpha_2^{-1} \tag{5b}$$

$$\left[TIC\right] = \left[CO_3^2\right] \cdot \alpha_3^{-1}. \tag{5c}$$

The distribution coefficients of $H_2CO_3$ ($\alpha_1$), $HCO_3^-$ ($\alpha_2$) and $CO_3^{2-}$ ($\alpha_3$) are defined as follows

$$\alpha_1\left(\left[H^+\right]\right)=\left(1+\frac{K_{1c}}{\left[H^+\right]}+\frac{K_{1c}K_{2c}}{\left[H^+\right]^2}\right)^{-1}$$
$$\alpha_2\left(\left[H^+\right]\right)=\left(\frac{\left[H^+\right]}{K_{1c}}+1+\frac{K_{2c}}{\left[H^+\right]}\right)^{-1} \quad (6)$$
$$\alpha_3\left(\left[H^+\right]\right)=\left(\frac{\left[H^+\right]^2}{K_{1c}K_{2c}}+\frac{\left[H^+\right]}{K_{2c}}+1\right)^{-1}$$

A similar formulation was used by Holzbecher and Nützmann (2000). Due to the values of the dissociation constants ($K_{1c} = 10^{-6.30}$ and $K_{2c} = 10^{-10.30}$ at 25°C, cf. Sigg and Stumm, 1989) at nearly neutral or weak alkaline pH conditions (as recorded for most groundwater environments) hydrogen carbonate predominates as TIC species.

A further constraint of pH buffering and of the availability of TIC, Ca, Fe and Mn is caused by the solubility equilibrium with rock forming solid carbonates, as calcite, rhodochrosite, and siderite. The solubility products $L_{Calcite}$, $L_{Rhodochrosite}$, and $L_{Siderite}$ can be formulated in terms of TIC and hydrogen ion concentration as

$$L_{CaCO3}=\left[Ca^{2+}\right]\cdot\left[CO_3^{2-}\right]=\left[Ca^{2+}\right]\cdot[TIC]\cdot\alpha_3\left(\left[H^+\right]\right) \quad (7a)$$

$$L_{MnCO3}=\left[Mn^{2+}\right]\cdot\left[CO_3^{2-}\right]=\left[Mn^{2+}\right]\cdot[TIC]\cdot\alpha_3\left(\left[H^+\right]\right) \quad (7b)$$

$$L_{FeCO3}=\left[Fe^{2+}\right]\cdot\left[CO_3^{2-}\right]=\left[Fe^{2+}\right]\cdot[TIC]\cdot\alpha_3\left(\left[H^+\right]\right) \quad (7c)$$

Ca as a major constituent of groundwater composition (compared with Fe and Mn) provides in most cases a predominant acid-based buffering by the Calcite solubility equilibrium especially if Calcite is abundant in the solid matrix. For TIC in deeper portions of the aquifer a closed system can be assumed with minor additional contributions resulting from DOC biodegradation.

The pH value results from the actual charge balance

$$\begin{aligned}&\left[H^+\right]+2\cdot\left[Ca^{2+}\right]+2\left[Mg^{2+}\right]+\left[K^+\right]+\left[Na^+\right]+\left[NH_4^+\right]+2\cdot\left[Fe^{2+}\right]\\&+2\cdot\left[Mn^{2+}\right]-\left[Cl^-\right]-2\cdot\left[SO_4^{2-}\right]-\left[HCO_3^-\right]-2\cdot\left[CO_3^{2-}\right]-\left[OH^-\right]=0\end{aligned} \quad (8)$$

pH-dependent species parameters such as $HCO_3^-$, $CO_3^{2-}$ and $NH_4^+$ have to be currently adapted to the pH value by internal iterations.

The precipitation/dissolution of Ca and Mn carbonates is realised by a kinetic approach similar to van Cappellen and Wang (1995) and Hunter et al (1998). This model approach is described for calcite precipitation/dissolution. For rhodochrosite

the same approach is applied. The precipitation/dissolution of calcite is formulated as follows

$$Ca^{2+} + CO_3^{2-} \xleftrightarrow{k_1, k_{-1}} CaCO_{3(s)}$$

The kinetic is expressed in the differential equation h

$$\frac{\partial [CaCO_3]}{\partial t} = k_1 (\Omega - 1) - k_{-1} (1 - \Omega) \tag{9}$$

With $\Omega = \frac{C_{Ca} \cdot C_{CO_3}}{L_{CaCO_3}}$, the *saturation index* of $CACO_3$.

Depending on the calculated saturation index $\Omega$ ($\Omega < 1$ subsaturation, $\Omega = 1$ saturation or $\Omega > 1$ supersaturation with respect to $CaCO_3$) the Ca concentration and total carbonic species (which implicitly depends on the pH value) enter the ionic charge balance.

### 11.3.2 Reactive Transport Simulation

The model has a reactive module, which solves reaction kinetics and equilibrium reactions, and a transport module, which incorporates the advection-dispersion equation. The transport/reaction equation is formulated for each redox acceptor in the fluid phase as follows

$$\frac{\partial}{\partial t} C_i = \frac{\partial}{\partial x} \left( D \frac{\partial}{\partial x} C_i \right) - v \frac{\partial}{\partial x} C_i - f_i \cdot \lambda \cdot C_{org} + q_i \tag{10}$$

The transport equation is formulated differently when for reaction *i* the redox product is in the fluid phase

$$\frac{\partial}{\partial t} C_i = \frac{\partial}{\partial x} \left( D \frac{\partial}{\partial x} C_i \right) - v \frac{\partial}{\partial x} C_i + F \cdot f_i \cdot \lambda \cdot C_{org} + q_i \tag{11}$$

Here $F$ is the liquid-solid conversion factor $F = \frac{1 - \Phi}{\Phi} \rho_s$ with porosity and bulk matrix density $\rho_s$. $f_i$ denotes the contribution of an electron acceptor to the overall DOC degradation (see above). $q_i$ represents additional source- and sink-terms. For sources there is a positive sign, for sinks a negative. Non-zero q-terms appear, when reactions are taken into account (see Section 11.4). The contributions of all primary reactions (Reactions (1A)–(6A)) sum up to 1:

$$\sum_{i=1}^{6} f_i = 1 \tag{12}$$

For DOC as aqueous component, the transport/reaction equation is

$$\frac{\partial}{\partial t} C_{org} = \frac{\partial}{\partial x}\left( D \frac{\partial}{\partial x} C_{org} \right) - v \frac{\partial}{\partial x} C_{org} - \lambda \cdot C_{org} \tag{13}$$

Alternatively, a steady state DOC spatial distribution representing the steady state solution of the transport reaction equation for DOC can be formulated:

$$C_{DOC} = C_{DOC,0} \exp(-\lambda_x x) \tag{14}$$

for $x$, the distance from the DOC inflow and $\lambda_x$ the depletion constant. The latter approach is used by the STEADYSED1 code of van Cappellen and Wang (1995).

## 11.4 Model Implementation

The reaction/transport model was implemented using the software system MODELMAKER TM 1. The model software MODELMAKER is a compartment modelling system and has tools for a simple interactive formulation of differential equations without applying explicit programming in FORTRAN or C. By a graphic user interface an input of model compartments (arrays, variables, parameters), equations and interrelations is possible. Non-linear algebraic equations (such as acid-based conditions, local chemical equilibrium, saturation indices, speciation) are incorporated via special tools (events which can be programmed in a macro language similar to PASCAL) and linked to the components or compartments, which depend on acid-based solution chemistry. The output of results is available as spreadsheets or graphs.

With MODELMAKER the electron acceptors ($O_2$, $NO_3^-$, $MnO_{2(s)}$, $Fe(OH)_{3(s)}$ and $SO_4^{2-}$), DOC and secondary precipitation products as well as the dissolved components Fe and Mn were defined as compartments and assembled with special modules for acid-based chemistry to a 1D reactive transport model along a flow path.

The reaction system implemented in the model included the primary DOC decay reactions with $O_2$, $NO_3^-$, $MnO_{2(s)}$, $Fe(OH)_{3(s)}$ and $SO_4^{2-}$ as electron acceptors (Reactions (1A)–(5A)). The redox couple $Fe^{2+}/MnO_{2(s)}$ (Reaction (1B)) was implemented as a secondary redox reaction. Precipitation/dissolution reactions were considered in two steps in order to verify the observed distribution of Mn and Fe.

In a first step, a generic approach for the precipitation/dissolution reactions without acid-based chemistry and inorganic carbon speciation is used. By a further step, these geochemical factors are included in order to obtain a more complete representation of the hydrogeochemistry in the aquifer.

In the following the model as one realisation of variables and parameters including links and couplings in the sense of MODELMAKER, is applied to various different situations. The set of input values is different for the following generic cases, which serve as test cases in the process of model development.

## 11.4.1 Model Application

### 11.4.1.1 Generic Precipitation/Dissolution

First a simple precipitation/dissolution reaction without carbon speciation and acid-based chemistry is considered (cf. Boudreau, 1997) using an approach similar to non-linear adsorption/desorption (Langmuir isotherm). As shown above, the component $A_{(aq)}$ released by DOC biodegradation consuming a given electron acceptor can be buffered or precipitated by a precipitation/dissolution reaction

$$A_{(aq)} \Leftrightarrow B_{(s)}$$

This reaction results as a sum in a kinetic forward (precipitation) and kinetic backward reaction (dissolution) with different reaction rate constants. The equilibrium state is described by the equilibrium constant $K_{(eq)}$ which is the ratio of the backward ($k_{backward}$) to the forward reaction rate ($k_{forward}$). In terms of the concentrations, the equilibrium state is characterized by the equilibrium concentrations of $A_{(aq)}$ and $B_{(s)}$ according to the mass action law.

$$K_{(eq)} = \frac{k_{backward}}{k_{forward}} = \frac{\left[B_{(s)}\right]}{\left[A_{aq}\right]} \tag{15}$$

The saturation state of pore solution is described by the saturation index Ω. This index indicates which process dominates. Ω Is defined by

$$\Omega = \frac{K_{(eq)} \cdot \left[A_{aq}\right]}{\left[B_s\right]} \tag{16}$$

$\Omega < 1$ describes subsaturation, $\Omega \geq 1$ denotes saturation or supersaturation of the solution with respect to the solid B.

The reaction rate is noted as

$$q = -k_{backward} \cdot \left[B_{(s)}\right](\Omega - 1) \tag{17}$$

and incorporated into the system of DOC biodegradation reactions.

At the beginning of the consumption of the electron acceptor by the biodegradation of DOC the dissolved component $A_{(aq)}$ can be expected in low concentration far away from equilibrium (subsaturation condition). By a continuous release of dissolved $A_{(aq)}$ during DOC biodegradation equilibrium and supersaturation of the solid $B_{(s)}$ can

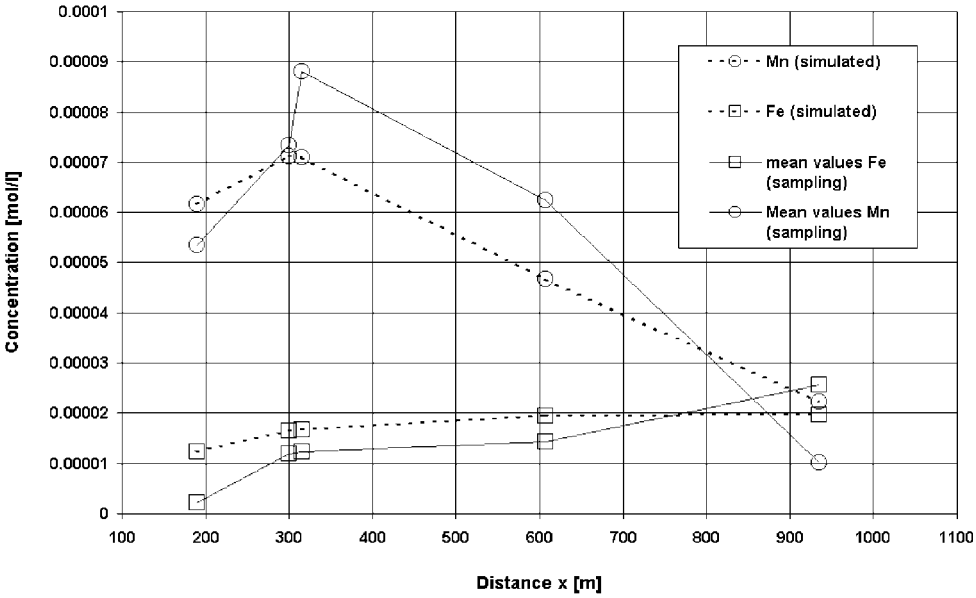


Figure 11.5: Calculated and sampled Fe and Mn distribution along a flowpath in the Bahnbrücke transect (model: generic precipitation).

be reached resulting in removing $A_{(aq)}$ from the solution by precipitation of $B_{(s)}$. At a final steady state, the solution system will tend to equilibrium.

As shown by Fig. 11.5, supersaturation of the pore water depending on available solute concentration results not in a continuous rise in solution content but in a peak-like distribution if a stationary exponential depleting DOC distribution is assigned.

Critical, sensitive factors governing shape and extension of solute distribution are the rate constant (and its relation to the pore velocity and to the overall biodegradation rate constant $\lambda$) and the generic equilibrium constant $K_{(eq)}$ constraining saturation conditions. The lower the precipitation rate constant $k_{backward}$ the greater the distance of the maximum solute concentration from inflow will be. For a given equilibrium constant $K_{(eq)}$ the amount of maximal solute concentration will depend mainly on the biodegradation rate constant $\lambda$.

### 11.4.1.2 Precipitation/Dissolution, Carbonate and Acid-Based Chemistry

As indicated above a model of DOC biodegradation including acid-based chemistry and solid carbonate precipitation/dissolution is a more realistic approach to verify the hydrogeochemical situation along the transect.

Solid carbonate precipitation/dissolution are included as kinetic processes to the overall DOC biodegradation reactive model depending on the actual saturation. Further TIC (total inorganic Carbon) and the Calcite solubility equilibrium (dissolved Calcium and solid Calcite) are considered as main pH buffering factors. The actual

hydrogen ion concentration is evaluated using the charge balance, which is implemented as non-linear algebraic equation within an event (see description of MODELMAKER) and uses TIC, Ca, Fe and Mn as input parameters from the previous time step. Using the calculated hydrogen ion concentration Carbon speciation ($H_2CO_3$, $HCO_3^-$, $CO_3^{2-}$) and saturation indices ($\Omega_{CaCO3}$, $\Omega_{MnCO3}$ and $\Omega_{FeCO3}$) are evaluated. To maintain realistic pH conditions, major components as $SO_4^{2-}$, $Cl^-$, Na, Ca, K, Mg and $NH_4^+$ with concentrations available from sampling must considered. They only enter the charge balance. The saturation indices govern precipitation and/or dissolution of solid carbonates and correct the available TIC for the next time step.

As primary reactions focussing the solid carbonates rhodochrosite and siderite only the biodegradation reactions with $MnO_{2(s)}$ and $Fe(OH)_{3(s)}$ were considered.

As outlined above for the generic precipitation and dissolution also for precipitation/dissolution reactions including acid-based chemistry the kinetic solid carbonate precipitation/dissolution rate constant is a critical and sensitive factor influencing the Fe and Mn distribution along a given flow path. Depending from actual pH conditions at stationary conditions saturation of the solid carbonates with saturation indices $\Omega$ can be expected.

## 11.4.2 Parameterisation

### 11.4.2.1 Generic Precipitation/Dissolution

The model column has an extension of 1000 m and was set up by a compartment of 400 blocks with a block length of 2.5 m. The model parameters used in the numerical experiments are given in Tables 11.1–11.4. Especially the kinetic reaction constants and the half saturation concentrations of the electron acceptors used in Monod kinetics had to be calibrated. A first guess for these values was taken from literature (van Cappellen and Wang, 1996; Hunter et al., 1998). These authors report for $O_2$ and $NO_3^-$ half saturation concentrations $c_{lim}$ magnitude orders of $10^{-6}$ to $10^{-5}$ [mol $L^{-1}$]. For $MnO_{2(s)}$ and $Fe(OH)_{3(s)}$ half saturation concentration with a magnitude of $10^{-5}$ to $10^{-4}$ [mol $dm^{-3}$] are reported by these authors. For the DOC decay rate constant a large range, from $10^{-7}$ to $10^{1}$ [$yr^{-1}$], is recorded in the literature depending on nature and reactivity of DOC species.

For secondary redox reaction comparatively large rate constants (magnitude order $10^4$ to $10^{10}$ (L $mol^{-1}$ $yr^{-1}$) are reported. This confirms that these reactions are fast compared to primary redox reactions and can be assumed to be in local equilibrium. Non-redox precipitation/dissolution reaction result from literature data as slow kinetic reactions with rate constants ranging from $10^{-5}$ to $10^{-11}$ [l $mol^{-1}$ $yr^{-1}$].

Using the simple approach of the precipitation/dissolution mechanism for rhodochrosite without inorganic carbon speciation the sampled variation of Fe and Mn along the Bahnbrücke transect could be verified. For the steady Fe and Mn profile is shown in Fig. 11.5. Note that the distances in Fig. 11.2 (geological transect) represent pathway distances along a flow path starting at the river bottom reflecting three-dimensional flow close to the river, and not linear distances to the Oder.

Crucial parameters influencing Fe/Mn distribution are

- the overall decay constant of DOC,
- the half saturation concentration of the electron acceptors $O_2$, $NO_3^-$, $MnO_{2(s)}$, $Fe(OH)_{3(s)}$ and $SO_4^{2-}$,
- the precipitation/dissolution rate constant of rhodochrosite,
- the DOC distribution coefficient $\lambda_x$ generating the idealized steady distribution of reactive DOC.

Another aspect of modelling is the assumption concerning DOC availability. Using DOC as a diluted component subjected to reactive transport only a continuous decrease of Mn with increasing distance form the inflow, but not a Mn peak as observed during sampling along the transect was realised. Assuming the steady state distribution of DOC along the modelled flow path a peak like Mn distribution resulted.

First a simulation based on steady spatial distribution of DOC is presented. The corresponding model parameters are given in Tables 11.1–11.3. Especially the half saturation constants and the kinetic constants were calibrated starting from the values cited above. For simplicity, the reactive transport calculations are based on a uniform velocity field with average velocities deduced from long term groundwater flow field near the transect Bahnbrücke. If 3D flow modelling is completed, the reactive transport modelling will be repeated based on realistic non-uniform flow patterns and flow paths.

Table 11.1: Parameters of model run concerning generic rhodochrosite precipitation: transport parameter.

| Parameter | Value |
|---|---|
| Block length [m] | 2.5 |
| Pore velocity [m $d^{-1}$] | 0.1 |
| Porosity [–] | 0.25 |
| Solid bulk density [g $cm^{-3}$] | 2.65 |
| DOC distribution coefficient $\lambda_x$ | 0.04 |

Table 11.2: Parameters of model run concerning generic rhodochrosite precipitation: concentrations.

| Component | Initial | Boundary |
|---|---|---|
| $[O_2]$ (mol $L^{-1}$) | $2.0\times10^{-6}$ | $5.0\times10^{-6}$ |
| $[NO_3^-]$ (mol $L^{-1}$) | $2.0\times10^{-6}$ | $5.0\times10^{-6}$ |
| $[MnO_{2(s)}]$ (mol $dm^{-3}$) | 0.2 | – |
| $[Fe(OH)_3]$ (mol $dm^{-3}$) | 0.02 | – |
| $[SO_4^{2-}]$ (mol $L^{-1}$) | 0 | 0.0 |
| $[Fe^{2+}]$ (mol $L^{-1}$) | 0 | 0.0 |
| $[Mn^{2+}]$ (mol $L^{-1}$) | 0 | 0.0 |
| [DOC] (mol $dm^{-3}$) | – | 0.001 |

Table 11.3: Parameters of model run concerning generic rhodochrosite precipitation: kinetic parameters and half saturation concentrations.

| Parameter | Value |
|---|---|
| Overall decay constant of DOC $\lambda$ ($d^{-1}$) | 0.00003 |
| $[O_2]_{lim}$ (mol $L^{-1}$) | $1.0\times10^{-6}$ |
| $[NO_3^-]_{lim}$ (mol $L^{-1}$) | $1.0\times10^{-6}$ |
| $[MnO_{2(s)}]_{lim}$ (mol $dm^{-3}$) | $1.0\times10^{-3}$ |
| $[Fe(OH)_3]_{lim}$ (mol $dm^{-3}$) | $1.0\times10^{-7}$ |
| $[SO_4^{2-}]_{lim}$ (mol $L^{-1}$) | $1.0\times10^{-6}$ |
| "Solubility" K (mol $L^{-1}$) | $2.0\times10^{-6}$ |
| Precipitation/dissolution rate constant $\alpha$ ($d^{-1}$) | $5.5\times10^{-10}$ |

The model runs were carried out for a simulation time of 250 years with a time step length of 10 days.

### 11.4.2.2 Precipitation/Dissolution, Carbonate and Acid-Based Chemistry

Inorganic carbon (TIC) speciation and pH are interdependent and implicitly calculated using the ionic charge balance which include all major ionic species available from hydrogeochemical sampling. The ionic charge balance is defined as follows

$$\begin{aligned}&\left[H^+\right]+2\cdot\left[Ca^{2+}\right]+2\cdot\left[Mg^{2+}\right]+\left[Na^+\right]+\left[K^+\right]+\left[NH_4^+\right]+2\cdot\left[Fe^{2+}\right]\\&+2\cdot\left[Mn^{2+}\right]=\left[OH^-\right]+\left[HCO_3^-\right]+2\cdot\left[CO_3^{2-}\right]+\left[Cl^-\right]+2\cdot\left[SO_4^{2-}\right]\end{aligned} \tag{18}$$

By this way pH can be actualised during simulation. The TIC speciation arises from

$$TIC=\left[HCO_3^-\right]\cdot\left(1+\left(K_{d2}/\left[H^+\right]\right)+\left(H^+/K_{d1}\right)\right) \tag{19a}$$

$$TIC=\left[CO_3^{2-}\right]\cdot\left(1+\left[H^+\right]^2/\left(K_{d2}\cdot K_{d1}\right)+\left[H^+\right]K_{d2}\right) \tag{19b}$$

with $K_{d1}$ and $K_{d2}$ as the first and second dissociation constants of carbonic acid using the actual hydrogen ion concentration. By this way both hydrogen ion concentration and TIC speciation can be calculated. The TIC was modelled as DOC degradation reaction product but also as a main hydrogeochemical constituent with a specified initial concentration of 1 mmol $L^{-1}$. According to the Reactions (1A)–(4A) 1 mmol DOC reacts with 4 mmol matrix bound $Fe(OH)_{3(s)}$ (or with 2 mmol matrix bound $MnO_{2(s)}$) releasing 4 mmol dissolved Fe (or 2 mmol dissolved Mn) and 1 mmol TIC per mmol released Fe and Mn. During DOC degradation first an increase of pH can be expected due to the proportional higher release of Fe and Mn compared with the release of additional TIC. By further reaction progress pH buffering by calcite, rhodochrosite and siderite can be expected depending on the relation of the DOC degradation rate to the solid carbonate precipitation/dissolution rates. As indicated above solid carbonate pre-

cipitation/dissolution is also assumed as a kinetic process depending on the saturation of the pore water with the solid carbonates.

The actual acid-based conditions are assumed in local chemical equilibrium. The reactions included and their equilibrium constants (Sigg and Stumm, 1989; Langmuir, 1997; Appelo and Postma, 1999) are given in Table 11.4.

A first preliminary reactive transport simulation including acid-based chemistry is set up using a 1D model consisting of 10 elements with an element length of 100 m. Other parameters are selected as noted in Table 11.1.

The reaction model included DOC biodegradation with matrix bound $MnO_{2(s)}$ and $Fe(OH)_{3(s)}$ which was assumed in a concentration of 0.05 [mol $dm^{-3}$ matrix]. Matrix bound Calcite was assumed with a concentration of 0.01 [mol $dm^{-3}$ matrix]. For Ca an inflow concentration of 0.0009 [mol $L^{-1}$] , and an initial concentration of 0,001 [mol $L^{-1}$] were specified. TIC was specified by an inflow concentration of 0.001 [mol $L^{-1}$] and an initial concentration over whole the model area of 0.0015 [mol $L^{-1}$]. DOC was modelled as a dissolved component with an inflow concentration of 0.001 [mol $L^{-1}$] and an initial concentration of 0.0005 [mol $L^{-1}$].

Table 11.4: Reactions and equilibrium constants used in modelling including acid-based chemistry.

| Reaction | Log K (25 °C) |
|---|---|
| $H_2O \leftrightarrow H^+ + OH^-$ | – 14.00 |
| $H_2CO_{3(aq)} \leftrightarrow H^+ + HCO_3^-$ | – 6.35 |
| $HCO_3^- \leftrightarrow H^+ + CO_3^{2-}$ | – 10.33 |
| $NH_4^+ \leftrightarrow NH_{3(aq)} + H^+$ | – 9.30 |
| $CaCO_{3(Calcite)} \leftrightarrow Ca^{2+} + CO_3^{2-}$ | – 8.47 |
| $MnCO_{3\ (Rhodochrosite,\ disordered)} \leftrightarrow Mn^{2+} + CO_3^{2-}$ | – 10.39 |
| $FeCO_{3(Siderite,\ disordered)} \leftrightarrow Mn^{2+} + CO_3^{2}$ | – 10.45 |

Table 11.5: Kinetic parameters for modelling with acid-based chemistry.

| Parameter | Value |
|---|---|
| Overall DOC decay constant [$d^{-1}$] | 0.00005 |
| Half saturation concentration of $MnO_{2(s)}$ [mol $dm^{-3}$] | $1e^{-6}$ |
| Half saturation concentration of $Fe(OH)_{3(s)}$ [mol $dm^{-3}$] | $1e^{-6}$ |
| Rate constant for calcite precipitation [$d^{-1}$] | $1.0e^{-5}$ |
| Rate constant for calcite dissolution [mol $dm^{-3}$ $d^{-1}$] | $1.0e^{-3}$ |
| Rate constant for rhodochrosite and siderite precipitation [$d^{-1}$] | $1.0e^{-8}$ |
| Rate constant for rhodochrosite and siderite dissolution [mol $dm^{-3}$ $d^{-1}$] | $1.0e^{-6}$ |

Other ionic species as sodium, potassium, magnesium, ammonium, chloride and sulphate were introduced as variables at constant concentrations as indicated by the groundwater analyses. These are regarded as inert species only used to guarantee a nearly correct charge balance for the ph value calculation.

The kinetic parameters for DOC biodegradation and solid carbonate precipitation/dissolution are given in Table 11.5. For calcite precipitation and dissolution rate constant were assigned for both solid carbonates. The simulation time was 100 years with a time step length of 10 d.

## 11.5 Results from Measurements and Modelling

Figure 11.5 compares simulated and sampled Fe and Mn distributions when the model is only slightly extended from the state, presented by Holzbecher et al. (2001), i.e. in which Fe is included as additional redox process of minor priority. Both measured Fe and Mn concentrations are well reproduced by the model. Thus observed Fe and Mn concentrations in the Oderbruch can be simulated when the redox model is supplemented only by a kinetic precipitation/dissolution approach.

For an adequate description of the geochemical environment, acid-based relations and calcite saturation are considered in a further extended model, as described in section 11.3. Stationary conditions for acid-based chemistry were reached after 6000 days and resulted in realistic pH values ranging from 7.5 to 7.6, slightly decreasing with distance from the inflow (see Fig. 11.6). The calculated pore water chemistry shows saturation of calcite and a slight supersaturation of rhodochrosite. Dissolved Mn concentrations range about 0.03 [mmol $L^{-1}$] along the entire flow path, which is the order of magnitude of observed Mn concentration. As the hydrogeochemical composition along the path becomes nearly uniform towards the end of the simulation, converges in a quasi-steady-state, also uniform spatial pH and Mn distribution result.

In order to reproduce a peak of a redox component concentration, as observed for Mn, alterations of acid-based chemistry have to be considered. For an adequate simulation of the observed Mn concentration a correct representation of the spatial pH distribution is decisive. A spatial (stationary) variation of pH values of 0.1 to 0.3 pH units along the model grid (from field measurements pH values ranging from 7.6 to 7.9 are available) generate steeper gradients in the calculated Mn contents. Such pH values can be generated using variable contents of matrix-bound calcite and slightly varying Ca and TIC concentrations. The observed and simulated pH values reflect mainly a buffering of the pore solution by calcite as the most abundant solid carbonate.

A further model variation worked with adjusted pH. In detail: pH is calculated according to Eq. (8) using ion concentrations, which partially stem from model simulation and are partially fixed. For example $NH_4^+$ concentrations changing along the

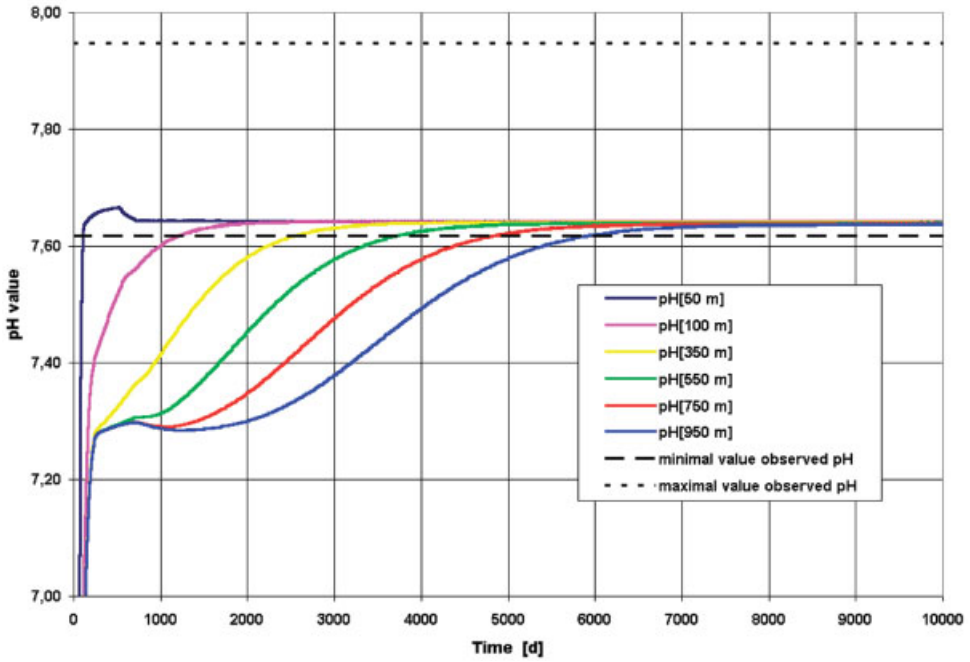


Figure 11.6: Simulated and observed pH concentration distribution at observation points along the Bahnbrücke transect (extended model, unadjusted pH).

flow path were used according to measured data. These influence local pH. As all dissolution/precipitation reactions depend on pH, the entire geochemistry is affected.

Figure 11.7 depicts Mn concentrations at selected observation points along the first part of the flow path. Because of computer storage problems the model had to be simplified in a manner deviating from the Bahnbrücke transect. Nevertheless the occurrence of a steady Mn peak is demonstrated, as after the initialisation phase concentrations at 35 m distance are highest. It can be expected that with some additional adjustments of all parameters to fit with the Bahnbrücke flow path, the observed Mn peak can again be reproduced with the extended model.

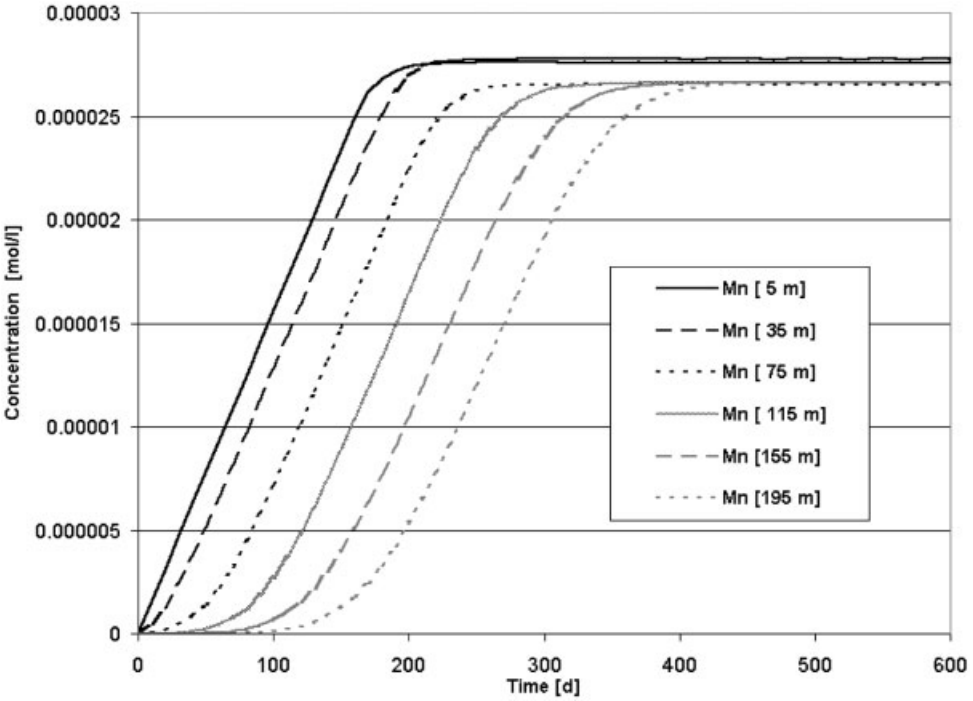


Figure 11.7: Simulated Mn for the first part of the flowpath, concentrations at observation points (extended model, adjusted pH).

## 11.6 Conclusions

Redox fronts exist in aquifers and can be compared to the occurrence of redox fronts in marine and limnic sediments. However the spatial scale is quite different in groundwater compared with lake or river sediments. While sedimentologists usually report fronts in the scale of cm, in groundwater these move much further and are more extended. In the Oderbruch aquifer a steady peak of Mn could be observed in a travel distance of 360 m from the river. Fe increases along the entire cross-section. A front for Fe could exist even beyond the final position in about 1000 m linear distance away from the river.

Transport and redox reactions can be modelled simultaneously in a numerical simulation. In order to abtain realistic results it is necessary to include geochemical expertise. In order to model the geochemistry in the aquifer a reactive transport model was set up. Starting from a preliminary state, in which only redox and precipitation were considered, finally inorganic carbon and acid based chemistry were included.

From a theoretical point of view this means that kinetic as well as equilibrium reactions had to be implemented in addition to the genuine transport processes as advection and dispersion.

The chosen approach, using a dynamic system simulator (MODELMAKER), turned out to be appropriate as it allows a simultaneous simulation of the kinetic processes and transport. Another advantage is that it is quite easy to extend or reduce the complexity of the model by introducing or ommitting further chemical components or reactions. Thus it is easy to alter the chosen model concept, concerning components and their reactions, during the process of modelling following geochemical expertise from new additional measurements or other findings.

The chosen model approach is not only valuable because it demonstrates that conceptual approaches concerning biogeochemistry can be successful adopted from the field of sedimentology to hydrology with their typically different spatial scales (this was shown by some other researchers in the meantime (Hunter et al., 1998). It points out the perspective that a flexible software design which allows an easy handling of components and their reactions can be very helpful to understand the geochemistry in aquifers and sediments, not only concerning redox reactions.

There still remain some open questions which could be mentioned partially only in this paper. One is to deal with the number of unknown parameters. The number of parameters in geochemical and biogeochemical models is often very high, so that even modern parameter estimation tools, like PEST, have problems to handle the problem. There are problems with the execution time of these models and with their convergence towards an optimal solution in the parameter space!

Nevertheless the combination of a reactive model with an optimization software is easier to obtain with the model approach presented above, than with standard geochemical software, like PHREEQE. By purpose the number of chemical components was kept as small as possible with respect to the regarded processes. By purpose the details of biochemistry, i.e. bacterial speciation (cf. Schäfer et al., 1998), were not included. Moreover a high number of relevant (or irrelevant) parameters is surely an obstacle to understand complex (and easy) systems.

## 11.7 References

Appelo, C. A. J.; Postma, D. (1999): Geochemistry, Groundwater and Pollution, Balkema, Rotterdam.

Berner, R. A. (1980): Early Diagenesis, Princeton Univ. Press, Princeton.

Boudreau, B. P. (1986): Mathematics of tracer mixing in sediments I: spatially dependent diffusive mixing, *Am. J. Sci*. **286**, 161–198.

Boudreau, B. P. (1997): Diagenetic Models and their Implementation. Springer Publ., Berlin.

Chapelle, F.; McMahon, P.; Dubrovsky, N.; Fujii, R.; Oaksford, E.; Vroblesky, D. (1995): Deducing the distribution of terminal electron-accepting processes in hydrologically diverse groundwater systems. *Water Res. Res*. **31**(2), 359–371.

Holzbecher, E.; Maßmann, G.; Horner, C.; Pekdeger, A. (2001): Redox-processes in the Oderbruch Aquifer. In: Impact of Human Activity on Groundwater Dynamics (Eds. Gehrels, H. et. al.). IAHS-Publ. No. 269, 229–238.

Holzbecher, E.; Nützmann, G. (2000): Influence of subsurface watershed on eutrophication – Lake Stechlin case study. *Environmental Engineering* **16**, 31–38.

Hunter, K. S.; Wang, Y.; van Cappellen, P. (1998): Kinetic modelling of microbially driven redox chemistry of subsurface environments: coupling transport, microbial metabolism and geochemistry. *J. of Hydrol*. **209**, 53–80.

Keating, E. H.; Bahr, J. (1998): Reactive transport modelling of redox geochemistry: approaches to chemical disequilibrium and reaction rate estimation at a site in northern Wisconsin, *Water Res. Res*. **34**(12), 3573–3584.

Langmuir, D. (1997): Aqueous Environmental Geochemistry, Prentice Hall, Upper Saddle River, N. J., U.S.A.

Massmann, G.; Pekdeger, A.; Merz, C.; Schafmeister, M.-Th. (2001): Redox chemistry of a river-recharged aquifer in the Oderbruch region in eastern Germany. In: Cidu, R. (Ed.): Water-Rock-Interaction, Proceedings, Vol. 1, Balkema, Lisse, 561–564.

Matsunaga, T.; Karametaxas, G.; von Gunten, H. R.; Kichner, P.C. (1993): Redox chemistry of iron and manganese minerals in river-recharged aquifers: A model interpretation of a column experiment, *Geochim. Cosmochim. Acta* **57**, 1691–1704.

Park, S. S.; Jaffé, P. R. (1996): Development of a sediment redox potential for the assessment of post depositional metal mobility. *Ecol. Modelling* **91**, 169–181.

Schäfer, D.; Schäfer, W.; Kinzelbach, W. (1998): Simulation of reactive processes related to biodegradation in aquifers. 1. Structure of the three-dimensional reactive transport model. *J. of Contaminant Hydrology* **31**, 167–186.

Schüring, J.; Schlieker, M.; Hencke, J.(2000): Redox Fronts. In: Aquifer Systems and Parameters Controlling their Dimensions (Eds.: Schüring, J.; Schulz, H. D.; Fischer, W. R.; Böttcher, J.; Duijnisveld, W. H. M.), Springer Publ., Berlin.

Sigg, L.; Stumm, W. (1989): Aquatische Chemie – Eine Einführung in die Chemie wässriger Lösungen und in die Chemie natürlicher Gewässer, B. G. Teubner, Stuttgart.

Soetaert, K.; Herman, P. M. J.; Middelburg, J. J. (1996): A model of early diagenesis processes from the shelf to abyssal depths. *Geochim. Cosmochim. Acta* **60**(6), 1019–1040.

van Capellen, P.; Wang, Y. (1995): STEADYSED1, A Steady-State Reaction-Transport Model for C, N, S, O, Fe and Mn in Surface Sediments – Version 1.0: User's Manual, School of Earth and Atmospheric Science, Georgia Inst. of Techn., Atlanta, Georgia.

van Cappellen, P.; Wang, Y. (1996): Cycling of iron and manganese in surface sediments: a general theory for the coupled transport and reaction of carbon, oxygen, nitrogen, sulphur, iron, and manganese. *Am. J. Sci*. **296**, 197–243.

van den Berg, G.; Loch, J., van der Heijdt, L.; Zwolsman, J. (2000): Redox processes in recent sediments of the river Meuse. *Biogeochemistry* **48**, 217–235.

# 12 Oxoanion Transport in Aquifers Containing Iron Hydroxide – Modelling of Column Experiments with PHREEQC2

Max Kofod*, Verena Haury, Nandimandalam Janardhana Raju and Margot Isenbeck-Schröter

## Abstract

The adsorption onto iron hydroxides is an important solubility limiting process of oxoanions in aquifers. PHREEQC2 is equipped to model this adsorption using the surface complexation concept but a consistent data set of surface complexation constants is only available for amorphous hydrous ferric oxides. We examined whether this data set can also be used to model the movement of the oxoanions arsenate, chromate and phosphate in quartz sand columns containing an commercially available iron hydroxide with a much lower specific surface area. It is shown that PHREEQC2 model runs using site density typical for amorphous hydrous ferric oxides overestimated the retention of the three tested oxoanions by a factor of 2.1 to 4.7 and model runs using the site density of goethite underestimated the retention by a factor of 2.2 to 4.6. But the results for the three oxoanions are quite consistent. It indicates that the complexation constants derived for amorphous hydrous ferric oxides may also be suitable for other iron hydroxide materials when the surface site density has been adjusted. After adjusting the surface site density some deviations between measured and modelled oxoanion concentrations remain, which can be attributed partly to inaccurate pH modelling. This inaccurate pH modelling is less important for the prediction of the gross oxoanion retardation but has a significant effect on the exact shape of the breakthrough curves. Model runs with a pH fixed to the mean measured values gave for all three studied oxoanions better results than model runs with a pH calculated by PHREEQC2.

* Institut für Umwelt-Geochemie, Universität Heidelberg, Im Neuenheimer Feld 236, 69120 Heidelberg; e-Mail: maxkofod@web.de



*Geochemical Processes: Conceptual Models for Reactive Transport in Soil and Groundwater. Research Report.* Deutsche Forschungsgemeinschaft (DFG).
 ISBN: 978-3-527-27764-3

## 12.1 Introduction

PHREEQC is a computer programme for hydrogeochemical calculations such as speciation of water constituents, mineral-water saturation indices, batch reactions, 1D–transport (Parkhurst and Appelo, 1999). The recent version of the programme (PHREEQC2 Ver. 2.3) is able to model sorption processes using the surface complexation concept (Dzombak and Morel, 1990). At present PHREEQC2 is distributed with a set of surface complexation constants that are derived from amorphous, freshly precipitated iron hydroxide. The data for the surface complexation reactions in the database of PHREEQC2 are taken from Dzombak and Morel (1990).

At the Institut für Umwelt-Geochemie in Heidelberg various column experiments were conducted with the aim of studying the transport of oxoanions in aquifers containing iron hydroxide. This chapter examines whether PHREEQC2 is suitable for modelling the data obtained from these column experiments. This work presents results concerning column experiments using artificial groundwater and a mixture of quartz sand and iron hydroxide.

The iron hydroxide material that was used in the column experiments differs significantly from amorphous hydroxides. The most obvious difference between the iron hydroxide used and the freshly precipitated amorphous substance is the considerably lower specific area. One important question concerning the modelling of these column experiments is whether the surface complexation constants derived for amorphous, freshly precipitated iron hydroxides by Dzombak and Morel are also suitable for other iron hydroxide materials. If this is the case, then it would be sufficient to adjust the available surface sites to achieve an adequate model of the oxoanion transport through aquifers containing iron hydroxides.

## 12.2 Experimental Set-Up and Analytical Methods

Three column experiments were performed to investigate the transport of the oxoanions arsenate, chromate and phosphate in an aquifer containing iron hydroxides. Table 12.1 lists the relevant data of the column experiments. All materials that were used in the experiments are commercially available and are of high purity. The sand and the used iron hydroxide material were washed with hypochloric acid prior to the filling of the columns. The used iron hydroxide material is the so called “Eisenoxihydrat” supplied by Riedel de Haen (in this text termed Riedel de Haen Hfo material). The x-ray spectroscopic analysis of a sample of this powdery Riedel de Haen Hfo material showed a significant amount of goethite (Haase, 1995). The point of zero net charge was measured with a particle charge detector (PCD 03, Mütek) between pH 7.3 to pH 8.2 with an average value of pH ≈ 8. Titration data of Hadeler (1999) confirmed this value (sample of same package). The specific surface area ($N_2$-BET) of the Riedel de

Table 12.1: Column characteristics.

| Column | A ($AsO_4$) | B ($CrO_4$) | C ($PO_4$) |
|---|---|---|---|
| Length (m) | 0.448 | 0.447 | 0.446 |
| Total volume ($cm^3$) | 712.15 | 710.56 | 708.97 |
| *Solids:* | | | |
| Pebbles (g/column) | 49.44 | 49.09 | 48.53 |
| Sand (g/column) | 1207.52 | 1208.74 | 1209.39 |
| RdH material (Hfo) (g/column) | 0.60 | 0.60 | 0.61 |
| Pore volume ($cm^3$/column) | 237.60 | 235.68 | 234.06 |
| Flow rate (m/d) | 0.62 | 0.62 | 0.58 |
| Flow rate (V/Vo×d) | 1.39 | 1.39 | 1.31 |
| Min.–Max. (V/Vo×d) | 1.28–1.47 | 1.28–1.48 | 1.21–1.41 |
| Dispersivity (m) | < 0.0005 | < 0.0005 | < 0.0005 |
| Oxoanion | 0.070 | 0.055 | 0.060 |
| of adsorption step (mmol/L) | $Na_2HAsO_4 \times 7H_2O$ | $Na_2CrO_4$ | $Na_2HPO_4 \times 2H_2O$ |
| Start of desorption step V/Vo | 24 | 24.8 | 23.5 |

Haen Hfo material was determined as 65 $m^2/g$ (Kofod et al., 1997), which is quite low compared with the specific surface area of amorphous iron hydroxides. These results showed that the Riedel de Haen Hfo material used in the column experiments more closely resembles goethite than freshly precipitated iron hydroxide.

The column experiment was conducted in three steps (conditioning step → adsorption step → desorption step). First the columns were conditioned by the inflow of artificial water without any arsenate, phosphate or chromate (conditioning). The artificial groundwater pumped through the columns was characterized by a pH of 5.9 and an electrical conductivity of 255 µS/cm. The ion content was (calculated from the recipe of the stock solution): $Na^+$ 0.979 mmol/L, $K^+$ 0.051 mmol/L, $Ca^{2+}$ 0.261 mmol/L, $Mg^{2+}$ 0.200 mmol/L, $Cl^-$ 0.629 mmol/L, $SO_4^{2-}$ 0.461mmol/L, $NO_3^-$ 0.401 mmol/L. The development of the outflow solution during the first conditioning step is not considered here. During the second step (adsorption) the artificial water was spiked with an oxoanion (see Table 12.1). This step was continued until the breakthrough of the oxoanion in the outflow had occurred. After that artificial water without any phosphate, arsenate or chromate was pumped through the columns again (desorption step). Because of slightly different pumping rates during the experiment, the desorption steps of the three column experiments did not begin simultaneously (see Table 12.1). The analytical methods used are listed in Table 12.2.

Table 12.2: Analytical methods.

| Parameter | Method |
|---|---|
| P conc. | Standard calibration, ICP-AES, parallel samples with Merck Nova 30 plus Spectroquant reagents |
| As conc. | Standard calibration, graphite tube furnace–AAS |
| Cr conc. | Standard calibration, Flame–AAS |
| pH | pH-Electrode |

## 12.3 Modelling of the Oxoanion Breakthrough

Parkhurst and Appelo (1999, examples 11 and 14) describe how to model transport and surface complexation with PHREEQC2. Detailed information on the surface complexation concept is given in Dzombak and Morel (1990). This chapter only gives specific information on how the oxoanion breakthrough was modelled.

### 12.3.1 Data Used

PHREEQC2 is distributed with different databases. The database *Minteq.dat* was chosen for the modelling of the column experiments. Constants of the protonation reactions for all oxoanions are included in this database. It also contains constants of various soluble phosphate and chromate species (complexes with all major cations and anions). The formation of soluble arsenate complexes is not considered because this seems not to be necessary (compare Cullen and Reimer, 1989).

To model the sorption of oxoanions onto the solid surface with PHREEQC2, it is necessary to define the reactive surface by a set of surface complexation constants and parameters describing the availability of surface sites.

The artificial water used in the column experiments contained various ions which are intended to react with the surface of iron hydroxides. To obtain a realistic model, PHREEQC2 has to be used with a database which not only considers surface complexation constants for the sorption of the studied oxoanions but for all reactive ions of the artificial water. It is assumed that only chloride and nitrate do not react with the iron hydroxide surface (Dzombak and Morel, 1990).

The constants for the surface complexation of calcium, sulphate, phosphate and arsenate are included in the file *minteq.dat*. This data was not sufficient for the modelling of the column experiments performed and had to be augmented. Surface complexation constants for magnesia and chromate for amorphous iron hydroxide were taken from Dzombak and Morel (1990) (see Table 12.3). Van Geen (1994) showed that also carbon dioxide has to be considered for the modelling of adsorption. Carbon dioxide is not mentioned in Dzombak and Morel (1990). The database used contains complexation constants derived from data of Van Geen et al. (1994) and were reoptimized by Dr. C. A. J. Appelo (Amsterdam) for use with PHREEQC2 and amorphous iron hydroxide. This data was transferred from the database file *PHREEQC.dat* to *Minteq.dat*.

Silicate can potentially also affect the surface charge of iron hydroxide (Goldberg, 1985). Silicate is not a primary constituent of the artificial water but it may be dissolved from the quartz sand. The concentration of silicate in equilibrium with $SiO_2$ (amorphous) calculated by PHREEQC2 is about 1 mmol/L $H_4SiO_4$ in case of the artificial water at pH 6. Experimentally determined surface complexation constants for the adsorption of silicate on iron hydroxide were not available. Instead estimates made by linear free-energy relationships from Dzombak and Morel (1990) were implemented in

Table 12.3: Surface complexation constants added to the database file "minteq.dat" (PHREEQC2 data base notation).

| Reaction | Surface complexation constant |
|---|---|
| Hfo_wOH + Mg+2 = Hfo_wOMg+ + H+ | log_k –4.6 |
| Hfo_wOH + H+ + H2SiO4-2 = Hfo_sH2SiO4- + H2O | log_k 15.9 |
| Hfo_wOH + H2SiO4-2 = Hfo_wOHH2SiO4-2 | log_k 8.3 |
| Hfo_wOH + CrO4-2 + H+ = Hfo_wCrO4- + H2O | log_k 10.82 |
| Hfo_wOH + CrO4-2 = Hfo_wOHCrO4-2 | log_k 3.9 |
| Hfo_wOH + CO3-2 + H+ = Hfo_wCO3- + H2O | log_k 12.58 |
| Hfo_wOH + CO3-2 + 2H+ = Hfo_wHCO3 + H2O | log_k 20.62 |

the database for this work (note: the test model runs considering saturation and 10-fold saturation of the solution with respect to $SiO_2$ (amorphous) showed that under the circumstances of the column experiments adsorption of silicate does not have any effect on the oxoanion sorption).

### 12.3.2 Parameters Describing the Available Surface

According to Dzombak and Morel (1990) only one type of surface site is necessary to model the anion adsorption onto the surface of amorphous iron hydroxide. The input parameters specifying the availability of these sites are *total amount of sites* (moles/L), *specific area* ($m^2$/g) and *mass* (g/L).

The site density for anion adsorption onto the amorphous iron hydroxide surface ranges mainly between 0.1 and 0.3 mol sites/mol $Fe_{(solid)}$ (see data collection of Dzombak and Morel, 1990). Dzombak and Morel used 0.2 mol sites/mol $Fe_{(solid)}$ as an approximate value and assumed a specific area of 600 $m^2$/g when deriving the complexation constants from the collected experimental batch test data.

The site density of amorphous iron hydroxide is probably not suitable for modelling the column experiment performed because the Riedel de Haen Hfo material used more closely corresponds to goethite in view of the low specific area (65 $m^2$/g). Ali and Dzombak (1996) derived a site density of 0.016 mol/mol $Fe_{(solid)}$ from titration data for goethite which is much lower. Both, the value for goethite and the value for amorphous iron hydroxide were considered for predicting the oxoanion breakthrough with PHREEQC2. The parameter "total amount of sites" was calculated by using these two values. The calculation considered the amount of iron and the proportion between pore water and solid mass in the columns. Using the site density of amorphous iron hydroxide gave 0.0054 mol sites/L pore water for the total number of sites and using the site density of goethite resulted in 0.00043 mol sites/L pore water. The mass and specific area of the Riedel de Haen Hfo material in the columns was determined by measurement (2.56 g iron hydroxide/L pore water, 65 $m^2$/g BET surface area).

### 12.3.3 pH Buffering

Because surface complexation is very sensitive to changes in pH, it was important to consider all the relevant pH-buffering reactions. Therefore in addition to the surface reactions the dissolution of the sand and the dissolution of the iron hydroxide were also considered in the model (solid phase equilibrium concerning $SiO_2$ (a) and ferrihydrite). The model runs were at first performed in respect of the inflow and outflow of the columns as in equilibrium with atmospheric $CO_2$ (term for these model runs in the figures is "Aw + $CO_2$"). At the very beginning of the column experiment a deviation occurred between the measured and modelled pH of the inflow water of the column experiment. The deviation between measured and modelled pH values of the inflow solutions was 5.8 to 5.7 for the artificial water, 6.8 to 6.5 for the artificial water plus 0.06 mmol/L phosphate, 6.7 to 6.6 for the artificial water plus 0.07 mmol/L arsenate and 6.6 to 6.5 for the artificial water plus 0.055 mmol/L chromate. This deviation may be explained by the absence of an equilibrium with the atmosphere. Because it is not known if $CO_2$ equilibrium is attained, additional model runs were performed without any $CO_2$ (model runs termed in Figures as "Aw no $CO_2$") and with equilibrium to atmospheric $CO_2$ but with a pH value fixed to the mean value measured in the outflow water (termed "Aw fix pH").

### 12.3.4 Cell Number and Diffuse Layer Options

The exact shape of the breakthrough curves (BTC) calculated with PHREEQC2 depends on the discretization of the model column (cell number) but as the cell number increases, differences between the calculated BTCs decrease. The model results shown are achieved by using 10 cells/column. This cell number is a compromise between result precision and calculation time.

The modelling of the surface complexation with PHREEQC2 can be performed with three different options concerning the electrical double layer (EDL). The results shown are achieved with the default option, which considers the electrostatic term of the mass action expression of the surface complexation but does not calculate the composition of the diffuse layer explicitly. The more correct modelling option with explicit calculation of the diffuse layer composition (-diffuse_layer) slowed down the calculation drastically but did not give deviating results in the case of the column experiments during some test runs. The third option disables the electrostatic term of the mass law expressions for the surface complexation and was therefore not adequate in this case.

(a)

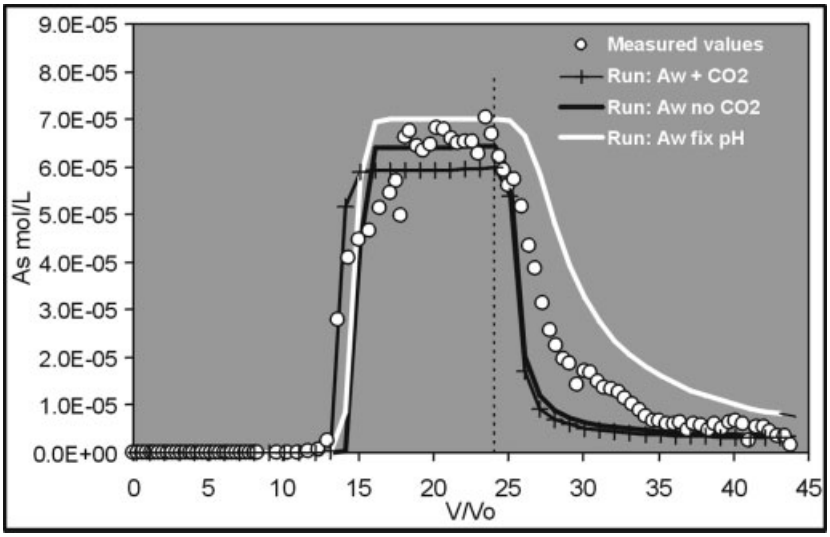


(b)

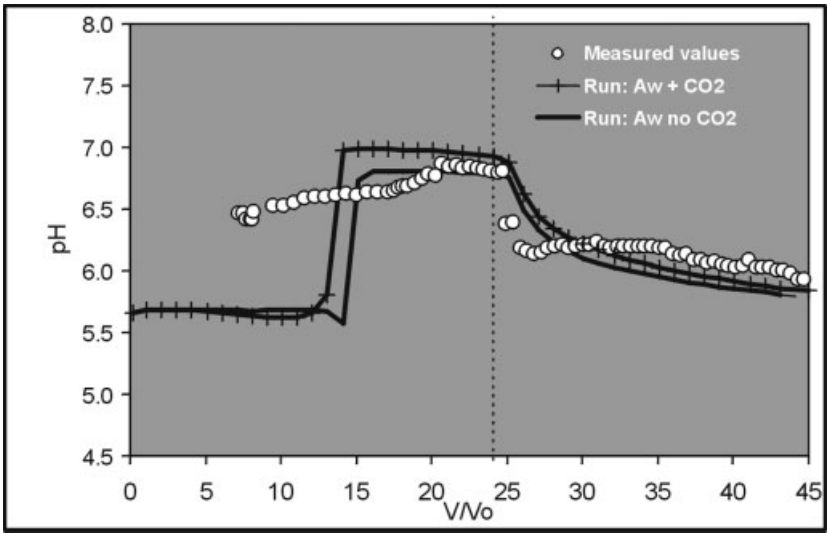


Figure 12.1: (a) Arsenate breakthrough (measured values and model runs with fitted number of surface sites). (b) pH of arsenate breakthrough experiment (measured values and model runs with fitted number of surface sites).

(a)

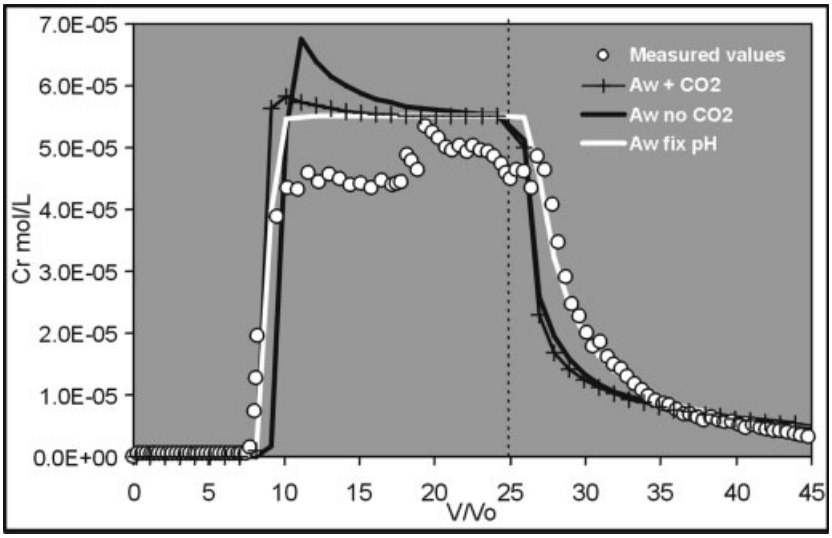


(b)

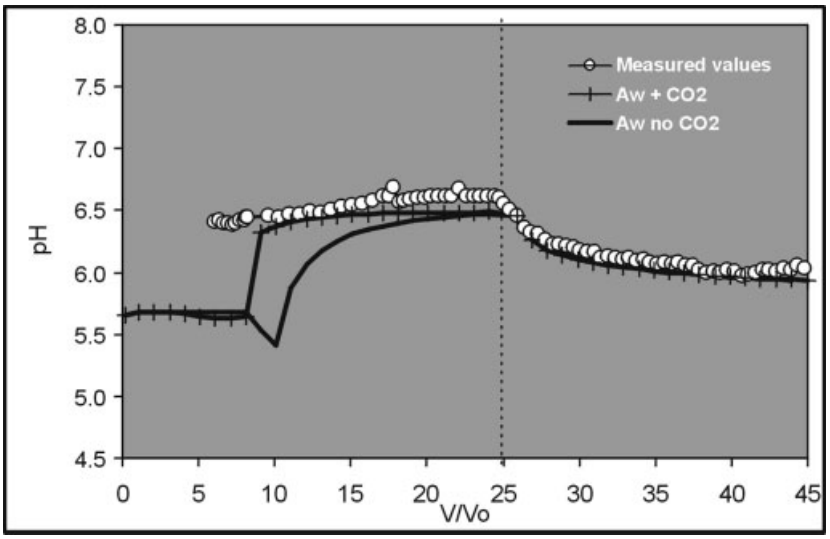


Figure 12.2: (a) Chromate breakthrough (measured values and model runs with fitted number of surface sites). (b) pH of chromate breakthrough experiment (measured values and model runs with fitted number of surface sites).

(a)

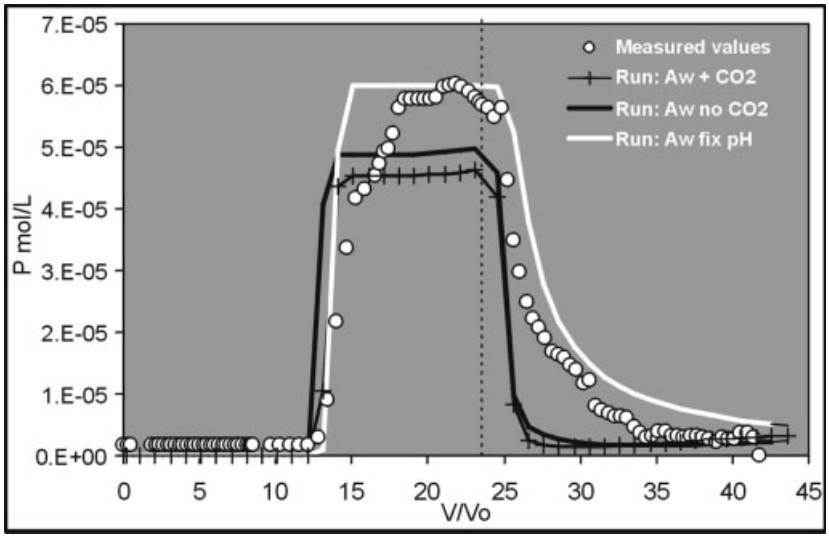


(b)

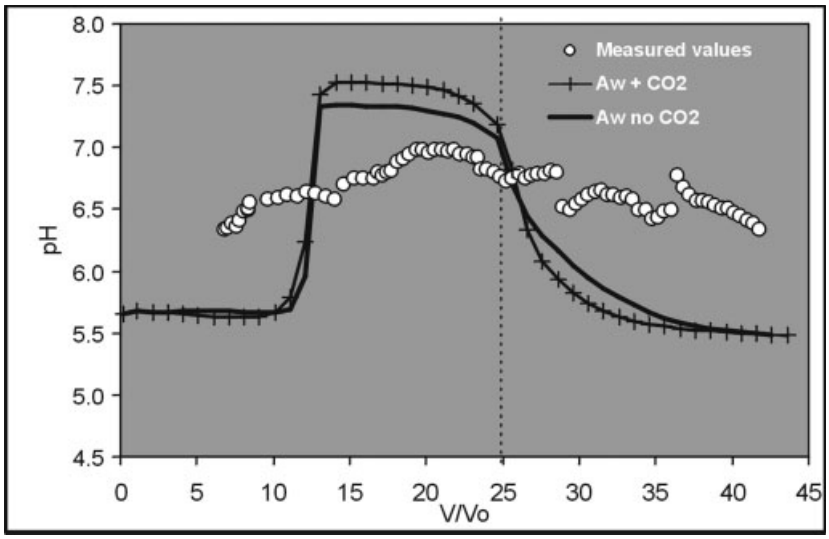


Figure 12.3: (a) Phosphate breakthrough (measured values and model runs with fitted number of surface sites). (b) pH of phosphate breakthrough experiment (measured values and model runs with fitted number of surface sites).

## 12.4 Results

### 12.4.1 Model Runs Using the Site Density of Amorphous Iron Hydroxide and Goethite

Using the values of the amorphous iron hydroxide for the number of surface sites (0.0054 mol/L) the breakthrough (BT) of phosphate, arsenate and chromate was calculated by PHREEQC2 to occur at V/Vo = 38 (arsenate), V/Vo = 30 (chromate) and V/Vo = 61 (phosphate) in the case of the model runs with fixed pH (see Table 12.4). The prediction of the oxoanion movement with a pH calculated by PHREEQC2 gave for arsenate and phosphate a significant earlier breakthrough (Table 12.4). Using the value of the site density of goethite the modelled oxoanion breakthrough occurred at V/Vo ≈ 3 (arsenate), V/Vo ≈ 3 (chromate) and V/Vo ≈ 6 (phosphate). The experimental BT occurred a factor of 2 to 3.5 later than modelled using the site density typical for goethite, and it occurred a factor of 0.2 to 0.3 (chromate, phosphate) and 0.4 to 0.5 (arsenate) earlier than modelled using the site density of amorphous material (Table 12.4).

Table 12.4: Prediction of the oxoanion breakthrough (BT) with PHREEQC2 and experimental results.

| | $AsO_4$-breakthrough | | $CrO_4$-breakthrough | | $PO_4$-breakthrough | |
|---|---|---|---|---|---|---|
| | Fix pH (6.4) | Equil. pH | Fix pH (6.4) | Equil. pH | Fix pH (6.4) | Equil. pH |
| Model run: | Aw fix ph | Aw +$CO_2$ | Aw fix ph | Aw +$CO_2$ | Aw fix ph | Aw +$CO_2$ |
| Prediction of BT Assumption 1 number of surface sites 0.0054 mol/L (Hfo amorphous) | 38 | 29 | 30 | 30 | 61 | 48 |
| Assumption 2 number of surface sites 0.000432 (goethite) | ≈ 3 | ≈ 3 | ≈ 3 | ≈ 3 | ≈ 6 | ≈ 5 |
| Observed BT in this column experiment | 14 | 14 | 8 | 8 | 13 | 13 |
| Best fit value for specific site density (mol/mol $Fe_{(solid)}$ ) | 0.074 | 0.094 | 0.054 | 0.054 | 0.044 | 0.054 |

### 12.4.2 Fitting the Site Densities

The similar deviation between predicted and experimental BTC for all three oxoanions indicated that the complexation constants may be suitable for the Riedel de Haen Hfo material used but the site density has to be fitted (as expected). Adjustment of this value to the observed breakthrough gave the modelled BTCs in Figs. 12.1 to 12.3. The fitted values for the specific site density of the Riedel de Haen Hfo material are 0.074 mol/mol $Fe_{(solid)}$ (arsenate), 0.054 mol/mol $Fe_{(solid)}$ (chromate) and 0.044 mol/mol $Fe_{(solid)}$ (phosphate) when a fixed pH was assumed in the model. The fitted values for the model runs with a pH calculated by PHREEQC2 are in the case of arsenate and phosphate higher (Table 12.4). The calculated site densities were a factor of ≈ 3 (chromate, phosphate) to 5 (arsenate) larger than the surface density of goethite and a factor of ≈ 0.25 (chromate, phosphate) and ≈ 0.4 (arsenate) lower than the value used by Dzombak and Morel (1990) for amorphous iron hydroxide. The results obtained were plausible because the Riedel de Haen Hfo material used is neither a pure goethite nor a pure amorphous iron hydroxide. Dzombak and Morel assumed that all anions are adsorbed at the same surface site. Therefore the site density should be also the same for the three oxoanions. The results for chromate and phosphate were indeed similar but the fitting of the site density for the arsenate shows a approximately 40 % to 70 % higher site density depending on the kind of model run.

### 12.4.3 pH Modelling

A characteristic of surface complexation modelling is that the pH development depends on the modelling. In the model the pH was influenced by various processes such as dissociation reactions, solid and gas phase equilibria, oxoanion surface complexation (see Section 12.2.2). A further process influencing the pH might be the desorption of anions sorbed onto the iron hydroxide surface at the beginning of the adsorption step. The surface was calculated to be in equilibrium with the artificial water. One modelling result is that the surface is only minimally occupied by carbonate > sulphate > silicate ($\Sigma < 10$ % of surface sites). The complexation of carbonate, sulphate and silicate is very weak compared with the studied oxoanions (note: the modelling of this experiment already simulates the competing surface complexation). These anions were quantitatively displaced by the oxoanions introduced and cannot obstruct arsenate, chromate or phosphate from reaching the iron hydroxide surface. Important is that after desorption these anions can principally have an indirect effect on the adsorption of the oxoanions introduced by influencing the pH. Taking all these reactions into consideration turns prediction of the pH into an ambitious task. On the other hand, precise prediction of the BT of the oxoanions can only be achieved when the pH development is correctly described by the model.

The measured pH increased steadily during the adsorption step and decreased with the start of the desorption step. The decrease was sharp in the case of the desorption of arsenate and chromate. In the case of phosphate, the decrease occurred with fluctuations.

Figures 12.1b, 12.2b and 12.3b show that the modelled pH development for all three column experiments matches the measured pH inaccurately. Only the modelled pH decrease during the desorption of arsenate and chromate matches the measured values quite well. The modelled pH development during the adsorption step showed marked deviations with jumps in the moment of oxoanion breakthrough. The height of the pH is predicted correctly for the arsenate and the chromate column. The most pronounced deviations between measured and modelled pH values occurred during the modelling of the phosphate transport through the column. The modelled pH is substantially higher when the breakthrough occurred and drops one pH unit lower than measured during the desorption step. The pH curve of the model runs with a $CO_2$ equilibrium did not differ in a larger extent from the curves produced by the model runs without $CO_2$. Only the two modelled pH curves for the chromate column differ during the adsorption step.

In principle, all of the processes that are able to influence the pH may be responsible for the erroneous pH modelling and it would be necessary to examine whether the modelling of these processes in PHREEQC2 needs to be adjusted (reaction formulations, reaction constants). Looking at the pH curves of the adsorption step can lead to the assumption that a pH buffering reaction is missing in the database. But there is no hint as to which reaction this could be. Often the deviation between measured breakthrough curves and curves produced by models using isotherms for describing the adsorption processes assume kinetic effects (Isenbeck-Schröter, 1995). In the case of the three column experiments it would primarily be necessary to integrate a pH change depressing kinetic effect in the model (a more detailed discussion of this problem will follow elsewhere).

Because of the inaccurate pH modelling for the adsorption step it is not astonishing that the shape of the breakthrough curves did not match the measured breakthrough curves (Figs. 12.1a to 12.3a). The breakthrough curves calculated with a fixed pH match the measured data best. The strongest deviations between the modelled and the measured oxoanion concentration occurred when the modelled pH showed the greatest deviation from the measured pH. This is the case for all three column experiments at the moment of the oxoanion breakthrough and also for the phosphate column experiment during the desorption step. The measured chromate breakthrough curve does not reach the input concentration during the adsorption step. The chromate adsorption is still going on at a lesser extent. Instead, the modelled chromate concentration is in the moment of breakthrough higher than the input concentration. This is accompanied by pH values modelled too low and in the case of the model run without $CO_2$ equilibrium by a short pH decrease. Both, the decrease of the chromate concentration and the pH change with the beginning of the desorption step is predicted relatively well. The modelled arsenate breakthrough curves do not reach the input concentration. This effect can also be seen in the measured arsenate breakthrough curve but is weaker. The pH curve and the arsenate breakthrough curve of the model run with $CO_2$ equilibrium differ stronger to the measured values than the

curves of the model run without $CO_2$ equilibrium. Shortly after the beginning of the desorption step the modelled pH is too high and the decrease of the arsenate concentration is too steep. In the case of phosphate the deviation between measured and modelled values is in principal the same but stronger. The model runs predict too high pH values during the adsorption step and a too low phosphate concentration after breakthrough and both, the decrease of the pH and the phosphate concentration after the beginning of the desorption step is too steep.

## 12.5 Summary and Conclusions

Column experiments were conducted to simulate the transport of oxoanion aquifers containing iron hydroxides. The Riedel de Haen Hfo material used in these column experiments exhibits a low specific surface area and contains a significant proportion of goethite. PHREEQC2 is equipped to model surface complexation of oxoanions onto iron hydroxides but a consistent data set of surface complexation constants is only available for amorphous hydrous ferric oxides. Tests were conducted to determine whether it is possible to use PHREEQC2 with this data set to model the oxoanion transport in the columns. If the data set of surface complexation constants is also suitable for the Riedel de Haen Hfo material than it should be sufficient to adjust the site density of the iron hydroxide surface in the model.

At first the data of the column experiments were compared with model predictions achieved by using the site density of amorphous iron hydroxide (0.2 mol sites/mol $Fe_{(solid)}$) and by using the site density of goethite (0.016 mol sites/mol $Fe_{(solid)}$). The PHREEQC2 model runs with a site density typical for amorphous iron hydroxide overestimated the retention of the three tested oxoanions by a factor of 2.1 to 4.7 and the model runs with the site density of goethite underestimated the retention by a factor of 2.2 to 4.6. The relative deviation between the observed breakthrough of the oxoanions and the model predictions is quite similar for all three oxoanions. Best approximations of the model predictions were achieved with site densities (mol sites/mol $Fe_{(solid)}$) of 0.054 (chromate), 0.044 (phosphate) and 0.074 (arsenate).

This result appears quite consistent. It indicates that the complexation constants derived for amorphous iron hydroxide may also be suitable for the Riedel de Haen Hfo material used and that only the surface site density has to be adjusted. Nevertheless the difference between the best-fit value for the number of sites differs between phosphate (minimum) and arsenate (maximum) is about 70 %. An entirely consistent result would require the same result of the fitting for all three oxoanions.

One characteristic of the surface complexation modelling with PHREEQC2 is that the pH of the column outflow is also predicted while considering several reactions. As a result it must be stated that this modelling of the pH seems to be a problem. In all three column experiments a steady increase in pH was measured during the adsorption step and a steady decrease during the desorption step. The general effect of proton con-

sumption during the adsorption step and the proton release during the desorption step is predicted by the model runs but the model runs were not able to predict the steady changes in the pH during the adsorption step. Also, the measured pH of all three column experiments was at the beginning of the adsorption step one grade higher than in the model runs. This inaccurate pH modelling is less important for the prediction of the gross oxoanion retardation but has a significant effect on the shape of the breakthrough curves. Model runs with a pH fixed to the measured mean value gave in all three cases (phosphate, chromate, arsenate) better results for the shape of the BTCs than model runs with a pH calculated by PHREEQC2.

## 12.6 References

Ali, M. A.; Dzombak, D. A. (1996): Interactions of copper, organic acids and sulphate in goethite suspensions. *Geochimica et Cosmochimica Acta* **60**(24).

Cullen, W. R.; Reimer, K. J. (1989): Arsenic Speciation in the Environment. *Chem. Rev.* **89**, 713–764.

Dzombak, D. A.; Morel, F. M. M. (1990): Surface complexation modelling: hydrous ferric oxide, John Wiley and Sons, Inc.

Goldberg, S. (1985): Chemical Modelling of Anion Competition on Goethite Using the Constant Capacitance Model. *Soil. Sci. Soc. Am. J.* **49**.

Haase, I. (1995): Bewertung des Schadstoffpotentials von Wasserwerksschlämmen (Evaluation of the contaminant inventory of water works sludges), Dissertation TU Hamburg-Harburg.

Hadeler, A. (1999): Sorptionsreaktionen im Grundwasser: Unterschiedliche Aspekte bei der Modellierung des Transportverhaltens von Zink, Berichte, Fachbereich Geowissenschaften, Universität Bremen, Nr. 145, Bremen.

Isenbeck-Schröter, M. (1995): Transportverhalten von Schwermetallkationen und Oxoanionen: Laborversuche in Säulen und ihre Modellierung. Berichte, Fachbereich Geowissenschaften, Universität Bremen, Nr. 67, p. 182, Bremen.

Isenbeck-Schröter, M.; Döring, U.; Möller, A.; Schröter, J.; Mattheß, G. (1993): Experimental approach and simulation of retention processes limiting orthophosphate mobility. *J. Contam. Hydrol.* **14**, 143–161.

Kofod, M.; Hadeler, A; Isenbeck-Schröter, M. (1997): Surface Charge of Hydrous Ferric Oxides in Sediments and Aquifer Solids. Seventh Annual V. M. Goldschmidt Conference, 2nd–6th June 1997, LPI Contribution No. 921, Tucson, Arizona, p. 114–115.

Parkhurst, D. L.; Appelo, C. A. J. (1999): User's guide to PHREEQC (Version 2): a computer programme for speciation, batch-reaction, one-dimensional transport, and inverse geochemical calculations, U.S. Geological Survey Water-Resources Investigations Report 99–4259, p. 312.

Van Geen, A.; Robertson, A. P.; Leckie, J. O. (1994): Complexation of carbonate species at the goethite surface. Implications for adsorption of metal ions in natural waters. *Geochim. Cosmochim. Acta* **58**, 2073–2086.

# 13 Problems of Upscaling the Time in $Fe^0$ Reactive Barriers

Markus Ebert*, Andreas Dahmke, Ralf Köber and Dirk Schäfer

## Abstract

By the example of column experiments for the prediction of long term reactivity of zero valent granular iron problems related to upscaling the time are discussed in this chapter. These types of laboratory studies are actually used to predict the geochemical behaviour of reactive barriers for in situ groundwater remediation over time periods of up to ten years, whereas the duration of the experiments is normally a few months. Microbial mediated processes with lag time, an effect of flow velocity on observed degradation rates and the extent and effect of passivation reactions may cause diffculties in long term prediction. Microbial catalysed nitrate or sulphate reduction were often observed at field applications of $Fe^0$ permeable barriers. In column studies the lag time processes are not noticeable in short observation times, which is obviously a problem for long time prognosis. Because the mechanisms of microbial colonisation in permeable iron barriers are still unknown, a geochemical model can not take those effects into account. Various relations between flow velocity and degradation rates can be observed in column studies probably due to physicochemical characteristics of the type of granular iron used. Once again, these differences can not be integrated in a model concept, until the mechanisms are well known and described successfully. A simplified model is capable of simulating the passivating effects of mineral precipitation on the reduction of chlorinated hydrocarbons typically observed in column experiments. Assuming a decrease in reactive iron surface due to an increase in mineral precipitation the model PHREEQC generates concentration profiles of hydrocarbon degradation in columns in general similar to experimental results. The model results show differences of degradation velocity along the flow path as well as a shift in reaction fronts. This points to the capability of modern transport-reaction models to simulate the relevant processes in zero valent iron reactors but the majority of process interactions in the highly reactive milieu of iron reactors is still unknown. Therefore, process identification and quantitative verification is more important for the upscaling problem described than model development.

* Institut für Geowissenschaften, Universität Kiel, Olshausenstr. 40/60, 24098 Kiel; e-Mail: me@gpi.uni-kiel.de



*Geochemical Processes: Conceptual Models for Reactive Transport in Soil and Groundwater. Research Report.* Deutsche Forschungsgemeinschaft (DFG).
 ISBN: 978-3-527-27764-3

## 13.1 Introduction

The term 'upscaling' is often used in transfer situations when results of an investigation are transferred to a larger dimension in space. From this point of view upscaling signifies that findings from a micro or median scale laboratory experiment are transferred to macro, technical or field scale conditions. It is then the heterogeneities and their importance which must be considered between the different systems. In some cases, however, a laboratory experiment reproduces the reality in its actual dimensions and with the correct heterogeneity and then it is the time that has to be upscaled and not the spatial dimension. Therefore, temporal upscaling can be understood as the prediction of the development of a system over longer times than the observation period in the laboratory experiment. This may be based on column experiments using either true or forced flow velocity as well as investigations of accelerated transport in the unsaturated zone using enlarged leachate rates, either in the lab or in the field. Also field investigations rarely cover long observation periods, so that the findings usually document only one actual condition, and possible temporal variations are not considered. Groundwater sampling systems capable of cumulative sampling over longer periods are an exception, e.g. the ceramic dosimeter for the estimation of halogenated volatile organic carbon (VOC) loads in an aquifer (Martin et al., 2000).

The problems of temporal upscaling might be clarified by the example of column experiments for the prediction of long term reactivity of zero valent granular iron, used in permeable reactive barriers mainly for the passive remediation of halogenated VOC contaminated ground water (RTDF web site). Since the time of patenting of this ground water remediation technique (Gillham, 1993), several investigations have been carried out either in the laboratory or at field sites aimed at understanding the degradation process of halogenated hydrocarbons at iron surfaces as well as the factors which are responsible for the (long term) reactivity in iron reactors. This is documented by more than one hundred publications during the last years. Nevertheless, the long term performance of in situ iron reactors is still unpredictable, based only on theoretical calculations. In an extensive compilation and evaluation of the past results Gavaskar et al. (1997) suggest laboratory studies before a reactive barrier is installed in a contaminated aquifer. According to Gavaskar et al. (1997) column experiments should be carried out using the original contaminated ground water from the potential site for the estimation of degradation velocities as well as for the prediction of long term reactivity. These column experiments must invariably be carried out with higher flow velocities than under site conditions because the normal observation time in the laboratory is only around 4 months while prediction is required for usually more than 5 and often up to 10 years.

In most cases VOC degradation in iron reactors has been described by a pseudo first order rate law with respect to dissolved VOC concentration normalized to the BET iron surface. Other kinetic expressions are used to consider reactive site saturation and increased iron surface passivation (e.g. Wüst et al., 1999; Farrel et al., 2000) or more complex reaction pathways (Arnold and Roberts, 2000). The objective of this study is to evaluate three principal processes related to problems of temporal upscaling, i.e. lag time processes, the effect of flow velocity on degradation rates and the extent and effect of passivation reactions.

## 13.2 Microbially Mediated Processes

Microbially catalyzed processes often have a lag time before a significant effect can be observed (Ehrlich, 1996) obviously a problem in temporal upscaling of short time experiments. Figure 13.1 shows the temporal development of sulfate and ammonium concentrations measured in wells upstream and within the pilot scale $Fe^0$ reactive barrier at the Rheine site (NRW, Germany). A site description and monitoring results are reported elsewhere (Ebert et al., 1999A, B). A most probably microbially mediated sulfate reduction with subsequent sulfide precipitation accounts for the decrease in sulfate concentration within the reactive barrier over a period of several months. Sim-

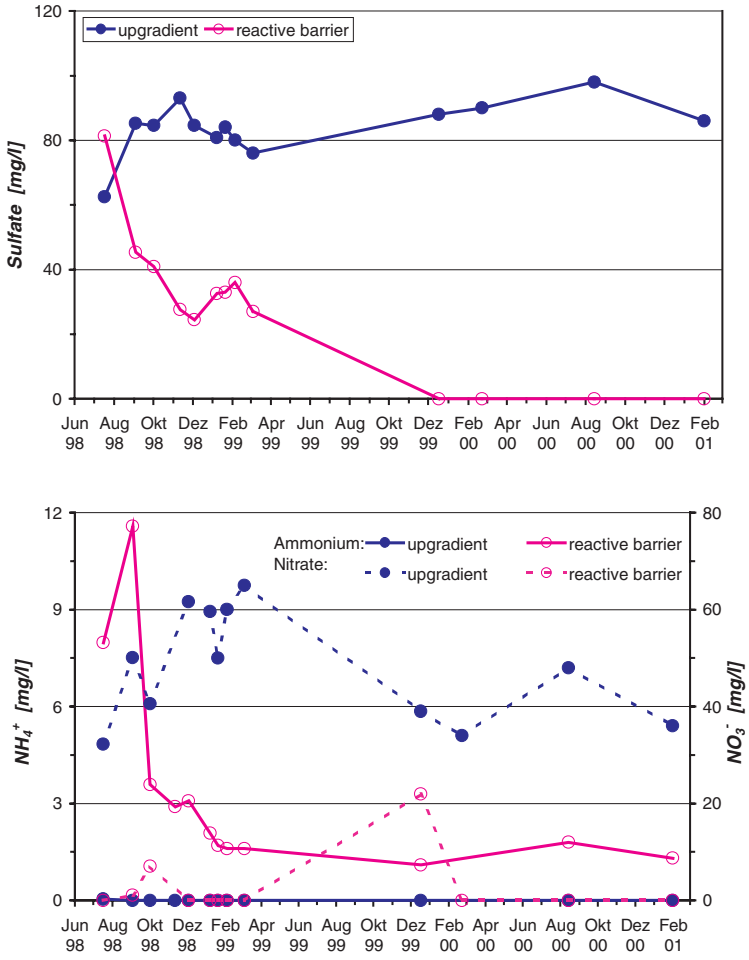


Figure 13.1: Temporal development of sulfate and ammonium concentration upgradient and within the reactive barrier at the Rheine site (NRW, Germany).

ilar results have been observed at other field sites where iron was implemented. In column experiments, on the other hand, noticeable sulfate reduction could only be detected after longer times even if the system was inoculated intensively (Gu et al., 1999).

Metallic iron can reduce nitrate abiotically, unlike sulfate, producing ammonium stoichiometricaly (Schlicker et al., 2000; Till et al., 1998; Devlin et al., 2000). Microbially mediated nitrate reduction usually produces $N_2$ and $N_2O$ and not ammonium (Ehrlich, 1996).The decreasing ammonium concentration within the reactive barrier, as opposed to nitrate which was detected upstream but not within the wall, points to microbial nitrate reduction with time. In column experiments using contaminated ground water it could be shown that a runtime of around 4 months is too short for the observation of the influence of sulfate and nitrate reduction. Yet these processes should be taken into account for long term prediction because sulfate reduction affects the pH and a sulfide precipitation may change the porosity as well as the reactive iron surfaces. Furthermore, the abiotic nitrate reduction is a competition reaction with respect to the chlorinated hydrocarbon (CHC) degradation whereas the biotic nitrate reduction does not affect the iron surfaces. Because the mechanisms of microbial colonization in permeable iron barriers are still unknown, a model cannot take those effects into account and it might be necessary to use a longer run time in laboratory experiments to predict the impact of microbially mediated processes.

## 13.3 Degradation Rates and Flow Velocity

Some studies have shown a dependence between the degradation velocity of halogenated hydrocarbons and the flow velocity in iron reactors (e.g. Matheson and Tratnyek, 1994; Scherer and Tratnyek, 1995; Thomas et al., 1995). Conversely, other studies (e.g. Gillham and O'Hannesin, 1994; Liang et al., 1995) have shown that degradation is nearly unaffected even if the flow velocity varies between 0.4 m/d and 2.4 m/d. In our own investigations different effects were observed by changing flow rates consistent with the former. Figure 13.2 shows concentration profiles of tetrachloroethene (PCE) from two column experiments using the same contaminated ground water and differing only in the type of granular zero-valent iron. The flow-through was reduced by a factor of 3 after around 40 exchanged pore volumes (PV), which is consistent with a threefold lowering of the pore velocity from around 36 cm/day to 12 cm/day. The reduced flow did not result in a significant alteration of the degradation behaviour in the experiment using sponge iron (ISPAT, Hamburg, Germany) (Fig. 13.2a), while the experiment with granular iron (Gotthart Maier AG, Rheinfelden, Germany) shows a significantly slower degradation of PCE at reduced flow rates (Fig. 13.2b). The PCE half life time remains around 10 h in the first case and increases from around 4 h to 7 h in the second experiment.

Dependence of degradation rates on flow velocity indicates rate limitation by transport processes, e.g. reported by Sivavec and Horney (1995) or Burris et al. (1995) for the degradation of trichloroethene (TCE) by zerovalent iron in batch reactors. Even if there has been no real explanation for the different degradation behaviour at the two column experiments, it must be dependent on the characteristics of the granular iron, because of the similar experimental conditions. The diverse granulate shape or the distribution of reactive surface as well as mineral precipitations usually present in iron

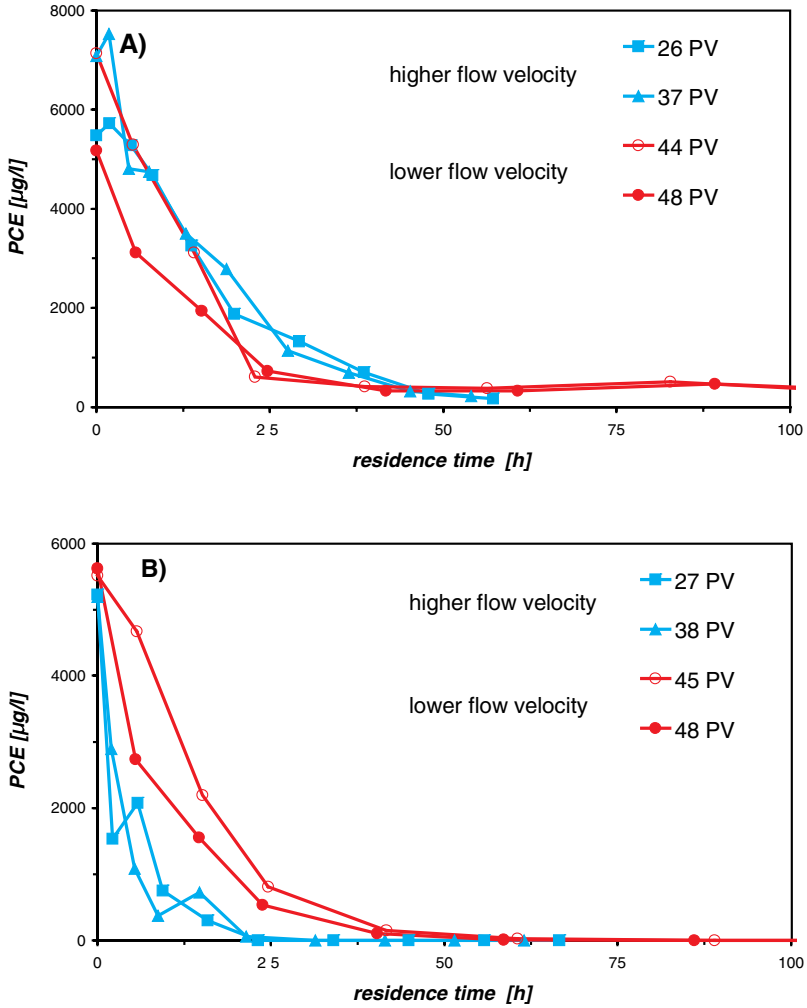


Figure 13.2: Concentration profiles of PCE in two-column experiments with different iron granulates but with the same groundwater. A lowering of the pore velocity by a factor of three after around 40 PV results in no noticeable alteration of the degradation behaviour (A, sponge iron) and in a significant lowering of the rate of PCE degradation (B, "Gotthart Maier" granular iron).

reactors and changing the surface properties may be responsible. While the BET surface of the two granulates is in the same order of magnitude (~0.5–0.6 $m^2/g$), the inflated sponge iron has a high inner porosity and therefore high inner surface in contrast to the "Gotthart Maier" granular iron. Nevertheless, these differences specific to the physicochemical characteristics of the iron can not be integrated in a model concept, until the mechanisms are well known and described successfully. And furthermore, in temporal upscaling an experiment should be carried out at different flow velocities each time, until the behaviour characteristic of an iron granulate is verified.

## 13.4 Mineral Reactions, Passivation and Degradation Rates

Passivation of iron granulates in permeable barriers used for in situ groundwater remediation may result in a shorter life time and in contaminant breakthrough earlier than expected. Therefore, mineral reactions or generally the effect of other groundwater constituents on the long term reactivity of iron is of major interest for the application of this technology in environmental clean up. For interpretation of column experiments it is also important to estimate the effect of flow velocity on the extent of passivation due to mineral reactions.

In simplified iron reactor systems in the laboratory, e.g. deion. water and moderate TCE concentration (< 20 mg/L), the degradation behaviour stays constant over longer time periods (> 1 year). The concentration profiles in column experiments then show nearly steady state conditions. The addition of other common ground water constituents to the influent solution may result in lower degradation rates or in higher turnover rates, respectively (Dahmke et al., 2000; Gavaskar et al., 1997).

A group of reactions (mineral precipitation like carbonates or (hydr)oxides, reduction of common oxidants or aerobic and anaerobic corrosion described elsewhere e.g. Gavaskar et al., 1998; Dahmke et al., 2000; Mackenzie et al., 1999; Farrell et al., 2000; Phillips et al., 2000) might be responsible for passivation of iron surfaces. The strong change in the geochemical milieu between the aquifer and the iron filled reactive barrier drives these reactions. In column experiments using a more complex real ground water a migration of reaction fronts can be observed in the concentration profiles of inorganic ground water components such as alkalinity, calcium or silicon (Fig. 13.3). The decrease in calcium concentration indicates calcite precipitation probably in a mixed crystal formation with siderite. The shift in concentration profiles in the flow direction points to a migration of the reaction zones, which is similar for other inorganic concentration profiles. Under these non steady state conditions the concentration profiles of the contaminant of interest usually also show a non-stationary front which migrates in the direction of flow over time (Figs. 13.4 and 13.5).

The concentration profiles often indicate a slower degradation at the beginning and a forced decrease of contaminant concentration at the end, which might be a result of a superposition of sorption at non reactive sites and degradation. The different degradation rates along the flow path may result in concentration profiles divided into two parts as

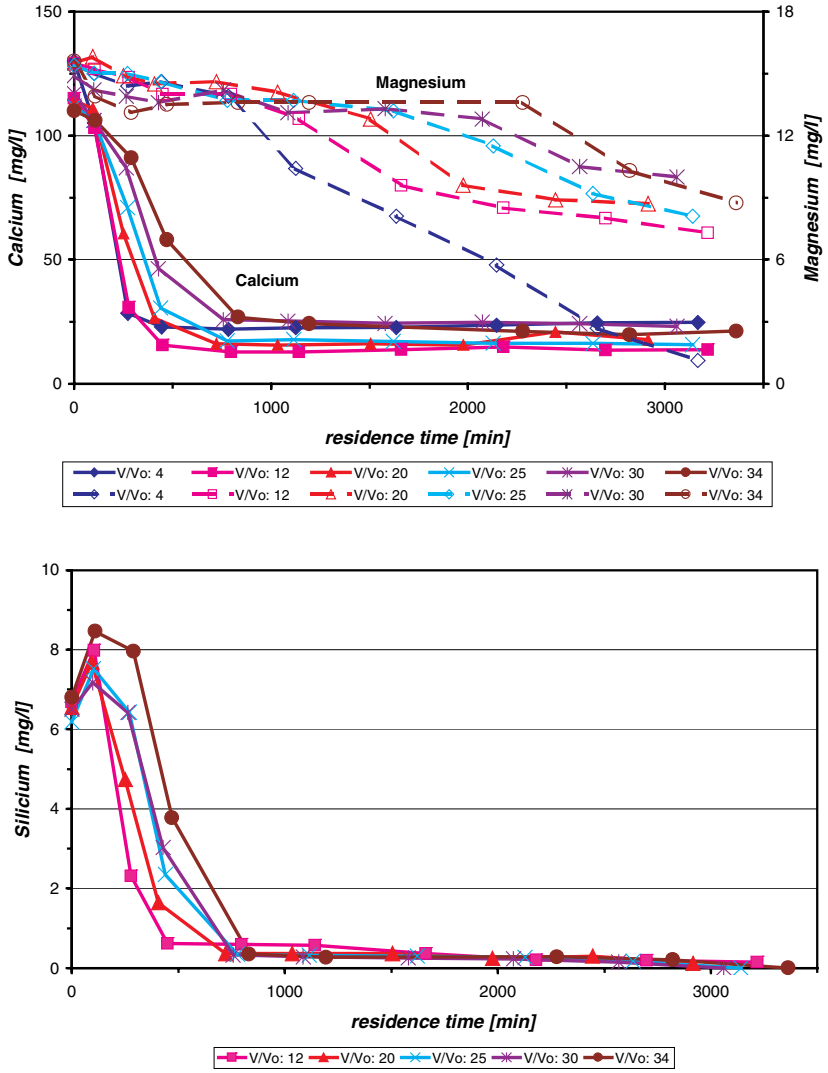


Figure 13.3: Typical concentration profiles of calcium, magnesium and silicon along the flow path of an iron filled column experiment.

shown in Fig. 13.4 or in continuously decreasing reaction rates as shown in Fig. 13.5. Furthermore, the reaction rates decrease continuously over experiment run time. However, in either case the overall degradation cannot be described by one pseudo first order rate law as indicated by a non linear curve shape in a half-logarithmic plot. More generally there is a positive correlation between experiment run time and the decrease of degradation rates as well as of the migration of the concentration fronts. The passivation of iron surfaces may increase to such an extent that the reduction of CHCs is inhibited absolutely. For example at an on-site iron reactor at the Backnang site (Germany) (Köber et al., 2002)

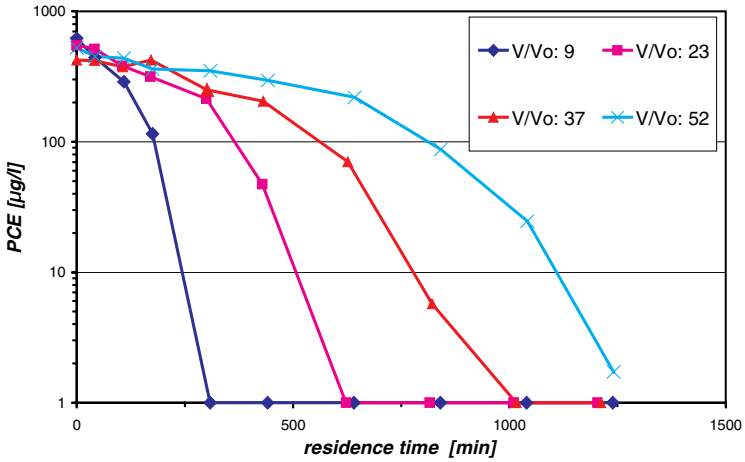


Figure 13.4: Typical development of PCE concentration profiles in a column experiment with contaminated ground water and strong inhibition.

strong inhibition of *cis*-1,2-Dichloroethene (*cis*-1,2-DCE) degradation was observed over short times (Fig. 13.5a). The same was observed for PCE degradation (Fig. 13.5b).

Even if the mechanisms or the extent of passivation of iron by mineral reactions are still unknown in detail the inorganic reactions most probably effect the degradation behaviour of CHC. A simplified model is capable of simulating the effects of these reactions on CHC reduction at different flow velocities on the assumption that mineral precipitation as well as continuous anaerobic corrosion decrease the reactive iron surface. PHREEQC (Parkhurst and Apello, 1999) can be used for qualitative simulation after modification of the data set integrating ethene and chlorinated ethene species as well as some iron minerals. Figure 13.6 shows the results of two simulations at five times different pore velocities and the model assumptions in Table 13.1.

Table 13.1: Model assumptions.

| | |
|---|---|
| Input solution | – c(PCE) = 0.15 mmol/L<br>– NaCl = 1 mmol/L<br>– Calcite saturation at $p(CO_2) = 10^{-1.5}$ atm |
| *In each cell (40):* | |
| Iron consumption | – First order kinetics with respect to $[H^+]$ as well as active iron<br>– Stoichiometric with PCE reduction |
| PCE reduction | – Stoichiometric reduction with ethylene as final product<br>– First order kinetics with respect to c(PCE) as well as active iron |
| Calcite, Siderite, Magnetite | – Equilibrium precipitation and dissolution (if present)<br>– Precipitation causes passivation of iron |
| Active iron | (Total unconsumed iron) – (Passivated iron) |

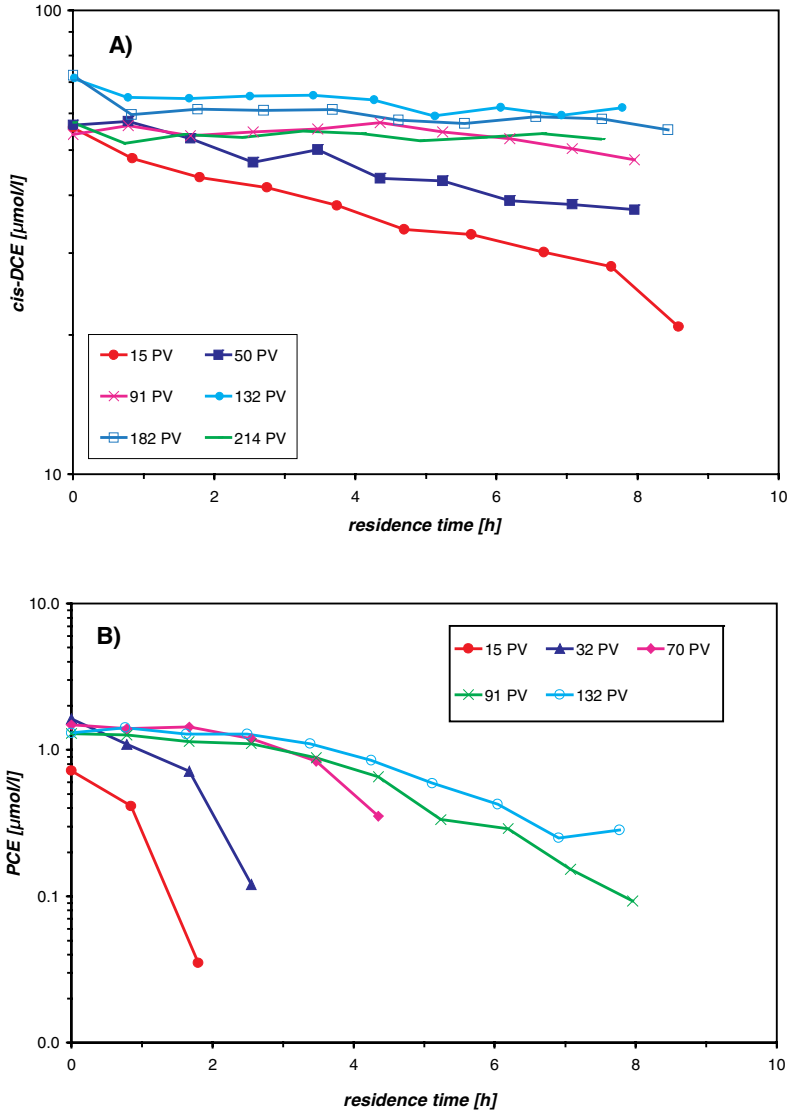


Figure 13.5: Inhibition of (A) *cis*-1,2-DCE and (B) PCE degradation in the $Fe^0$ on-site reactor "Backnang".

The content of iron was used in place of an iron surface in the simplified model and linear relationships were presumed between mineral precipitation and passivation of iron. Only a small iron content was used in each cell to achieve results in acceptable simulation times. The model results in PCE concentration profiles which are typically observed in column experiments (Fig. 13.6), even if the assumptions cannot be verified as the real mechanisms of passivation. Nevertheless, the simulation shows a migration

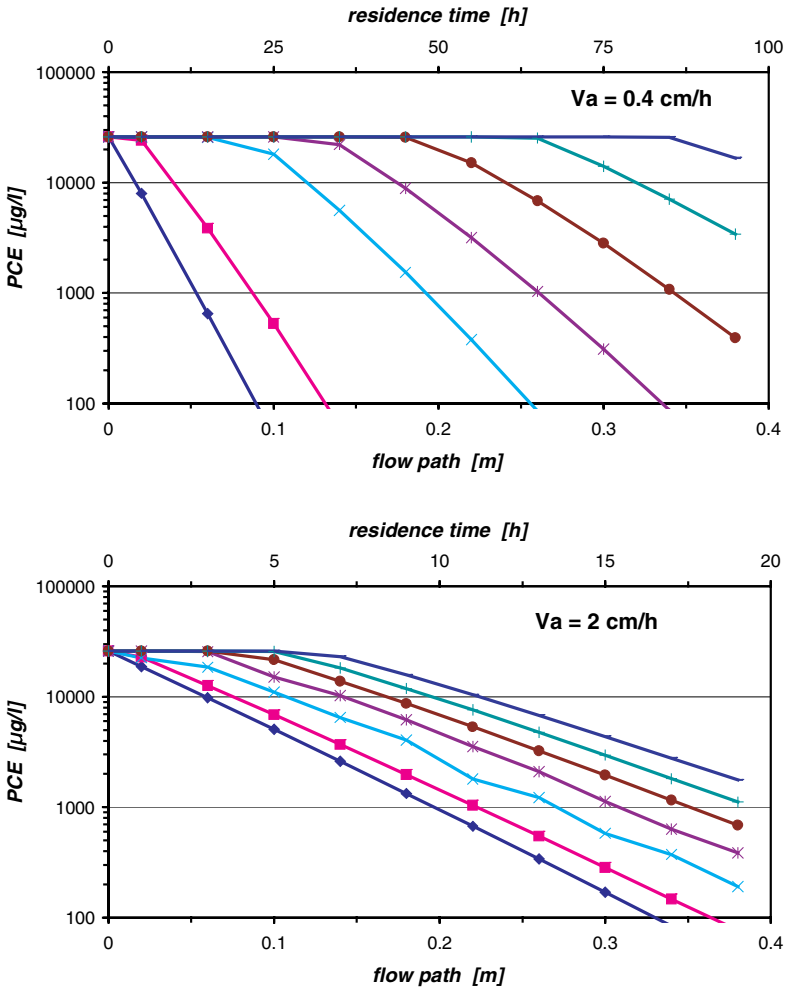


Figure 13.6: Simulated PCE concentration profiles at different pore velocities (1 and 5) in an iron reactor in progressive time steps. Same symbols indicate equal relative run times (exchanged pore volumes).

of concentration fronts as well as non-linear profiles in the half logarithmic plot which is clearly visible at lower transport velocity (Fig. 13.6, Va = 0.4 cm/h).

The simplified model suggests different relative migration speeds of reaction fronts as well as dissimilar total PCE reduction capacities at different flow rates. The continuous anaerobic iron corrosion and the ongoing mineral precipitation in the rear part of the reaction path causes the difference even if the turnover rates are small. In the case of reduced flow velocity the PCE concentration front reaches the rear part of the reactor at a later point in absolute time so that here is less reactive iron available. Therefore the degradation velocity decreases and the total reduction capacity for PCE becomes smaller (Fig. 13.7).

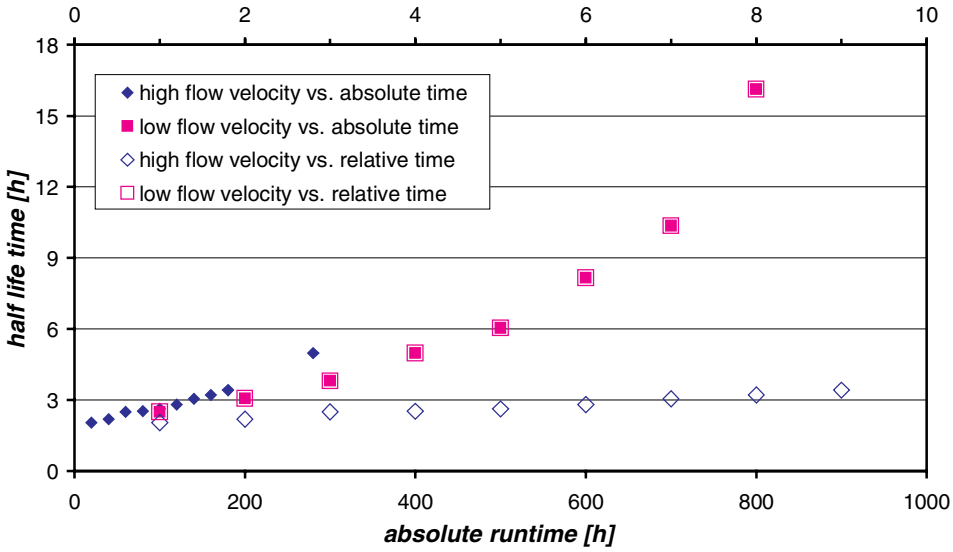


Figure 13.7: Development of PCE half life times during runtime as a result of modelling different flow velocities.

These findings point to an enlarged flow accelerating the time in a column experiment for the prediction of long term performance, may result in an underestimation of the migration rate of CHC degradation fronts but also point to the capability of actual models to simulate the effect of passivation processes. Therefore, further investigations of long term prediction should be directed more to process identification and quantitative verification than model development.

## 13.5 Conclusions

Column experiments with accelerated flow are actually the best way to predict long term performance of $Fe^0$ reactive barriers for in situ groundwater remediation. The evaluation in this study of three effects due to forced pore velocity in column experiments shows that the time lapse comprised a few problems which result in uncertainties of the long term prediction. This points to the necessity of further investigations of the mechanism aiming to understand processes and rate limitations which influence the degradation of chlorinated VOCs and also that only slight pore velocity forcing should be used in column experiments. An experiment run time of only a few months is too short to observe the effect of microbially mediated reactions so it may be necessary to spend longer time in the laboratory or to determine the colonisation rates of

microbes in reactive barriers with the aim of verification of model terms. Overall, the actual transport-reaction models are capable of simulating absolutely the relevant processes in zero valent iron reactors (e.g. mineral precipitation/dissolution, VOC degradation and sorption, passivation) but the majority of process interactions in the highly reactive milieu of iron reactors is still unknown. Therefore process identification and quantitative verification is more important for the upscaling problem described than model development.

## 13.6 References


Arnold, W. A.; Roberts, A. L. (2000): Pathways and Kinetics of Chlorinated Ethylene and Chlorinated Acetylene Reaction with Fe(0) Particles. *Environ. Sci. Technol.* **34(9)**, 1794–1805.

Burris, D. R.; Campbell, T. J.; Manoranjan, V. S. (1995): Sorption of Trichloroethene and Tetrachloroethene in a batch reactive metallic iron-water system. *Environ. Sci. Technol.* **29**, 2850–2855.

Dahmke, A.; Ebert, M.; Köber, R.; Schäfer, D.; Schlicker, O.; Wüst, W. (2000): Konstruktion und Optimierung von passiven geochemischen Barrieren zur In-situ-Sicherung und Sanierung CKW-kontaminierter Aquifere, 02-WT9546/2, BMBF.

Devlin, J. F.; Esdy; R.; Butler, B. J. (2000): The Effects of Electron Donor and Granular Iron on Nitrate Transformation Rates in Sediments from a Municipal Water Supply Aquifer. *J. Cont. Hydr.* **46**, 81–97.

Ebert, M.; Möller, W.; Wegner, M. (1999A): F+E-Vorhaben Reaktive Wand in Rheine. *Altlasten Spektrum* **2**, 109–112.

Ebert, M.; Möller, W.; Wegner, M. (1999B): Abiotischer Abbau von chlorierten Kohlenwasserstoffen in Eisengranulaten. Abschlussbericht über das F+E Fördervorhaben AZ 07837 von der Deutschen Bundesstiftung Umwelt.

Ehrlich, H. L. (1996): Geomicrobiology, 3rd ed., M. Dekker, New York.

Farrell, J.; Kason, M.; Melitas, N.; Li, T. (2000): Investigation of the Long-Term Performance of Zero-Valent Iron for Reductive Dechlorination of Trichloroethylene. *Environ. Sci. Technol.* **34**(3), 514–521.

Gavaskar, A.; Gupta, N.; Sass, B.; Fox, T.; Janosy, R.; Cantrell, K.; Olfenbuttel, R. (1997): Design Guidance for Application of Permeable Barriers to Remediate Dissolved Chlorinated Solvents, Battelle, Columbus, OH.

Gavaskar, A.; Sass, B.; Gupta, N.; Hicks, J.; Yoon, S.; Fox, T.; Sminchak, J. (1998): Performance Evaluation of a Pilot-Scale Permeable Reactive Barrier at Former Naval Air Station Moffett Field, Mountain View, California. Battelle, pp. 172.

Gillham, R. W. (1993): US Patent No. 5.266.213.

Gillham, R. W.; O'Hannesin, S. F. (1994): Enhanced Degradation of Halogenated Aliphatics by Zero-Valent Iron. *Ground Water* **32**(6), 958–967.

Gu, B.; Phelps, T. J.; Liang, L.; Dickey, M. J.; Roh, Y.; Kinsall, B. L.; Palumbo, A. V.; Jacobs, G. K. (1999): Biochemical Dynamics in Zero-Valent Iron Columns: Implications for Permeable Reactive Barriers. *Environ. Sci. Technol.* **33**(13), 2170–2177.

Köber, R.; Ebert, M.; Schlicker, O.; Dahmke, A. (2002): Degradation of Chlorinated Ethenes by Fe(0) – Inhibition Processes and Mineral Precipitation. *Environ. Geology* **41**(6), 452–644.

Liang, L.; Goodlaxson, J. D.; Korte, N. E.; Clausen, J. L.; Davenport, D. T. (1995): ORLN/MMES Research into Remedial Applications of Zero-Valence Metals: Laboratory Analysis of Reductive Dechlorination of Trichlorethylene. *209th American Chemical Society National Meeting*, 728–731.

Mackenzie, P. D.; Horney, D. P.; Sivavec, T. M. (1999): Mineral Precipitation and Porosity Losses in Granular Iron Columns. *J. Hazardous Materials* **68**, 1–17.

Martin, H.; Piepenbrink, M.; Grathwohl, P. (2000): Ceramic Dosimeters for Time-Integrated Contaminant Monitoring. IFPAC–2000 (International Conference & Exibition), ONSITE (Eighth International Conference on Site Analysis), Las Vegas, USA.

Matheson, L. J.; Tratnyek, P. G. (1994): Reductive dehalogentaion of chlorinated methanes by iron metal. *Environ. Sci. Technol.* **28**, 2045–2053.

Parkhurst, D. L.; Apello, C. A. J. (1999): User's Guide to PHREEQC (Version 2) – A Computer Program for Speciation, Batch-Reaction, One-Dimensional Transport, and Inverse Geochemical Calculations. Water-Resources Investigations Report 99–4259, Colorado, Denver.

Phillips, D. H.; Gu, B.; Watson, D. B.; Roh, Y.; Liang, L.; Lee, S. Y. (2000): Performance Evaluation of a Zerovalent Iron Reactive Barrier: Mineralogical Characteristics. *Environ. Sci. Technol.* **34**(19), 4169–4176.

RTDF web site: Web presentation of the Remediation Technologies Development Forum: http://www.rtdf.org

Scherer, M. M.; Tratnyek, P. G. (1995): Dechlorination of carbon tetrachloride by iron metal: Effect of reactant concentration. 209th American Chemical Society National Meeting. Division of Environmental Chemistry Preprints of Papers, Anaheim, California, pp. 805–806.

Schlicker, O.; Ebert, M.; Fruth, M.; Weidner, M.; Wüst, W.; Dahmke, A. (2000): Degradation of TCE with Iron: The Role of Competing Chromate and Nitrate Reduction. *Ground Water* **38**(3), 403–409.

Sivavec, T. M.; Horney, D. P. (1995): Reductive Dechlorination of Chlorinated Ethenes by Iron Metal. 209th American Chemical Society National Meeting, Anaheim, California, pp. 695–698.

Thomas, A. O.; Drury, D. M.; Norris, G.; O'Hannesin, S. F.; Vogan, J. L. (1995): Considertions. In: Contaminated Soil 95 (Eds.: van den Brink, W. J.; Bosman, R.; Arendt, F.), Kluwer Academic Publisher, The Netherlands, 1083–1091.

Till, B. A.; Weathers, L. J.; Alvarez, P. J. (1998): Fe(0)-Supported Autotrophic Denitrification. *Environ. Sci. Technol.* **32**(5), 634–639.

Wüst, W.; Köber, R.; Schlicker, O.; Dahmke, A. (1999): Combined Zero- and First-Order Kinetic Model of the Degradation of TCE and cis-DCE with Commercial Iron. *Environ. Sci. Technol.* **33**(23), 4304–4309.

# 14 Comparing Two Approaches for Modelling Natural Attenuation of Organic Compounds in Heterogeneous Porous Media

Anita Peter*, Rudolf Liedl, Thomas Ptak and Georg Teutsch

## Abstract

Two model approaches are compared by simulating reactive transport of acenaphthene in a heterogeneous porous medium. In a Monte Carlo approach a Lagrangian one-dimensional streamtube model is used to assess the transport behaviour at field scale for distances of up to 800 m. Aquifer properties are taken from results of field experiments characterising a test site in a shallow quaternary sand and gravel aquifer. The results of the streamtube model are compared to model results of a two-dimensional Eulerian model. Both models account for kinetic sorption, described as diffusive transport in intra-particle pores.

As the Lagrangian approach neglects the heterogeneity of sorption and diffusion parameters, the aim of the present study is to assess the influence of these heterogeneities on model predictions.

It was found, that by applying the streamtube model the mean mass fluxes of all realisations, i.e. the mean transport behaviour of acenaphthene, was simulated very well for transport distances larger than 100 m. For shorter transport distances it is important to consider spatial variability of physico-chemical parameters.

* Institut und Museum für Geologie und Paläontologie, Universität Tübingen, Sigwartstr. 10, 72076 Tübingen; e-Mail: anita.peter@uni-tuebingen.de



*Geochemical Processes: Conceptual Models for Reactive Transport in Soil and Groundwater. Research Report.* Deutsche Forschungsgemeinschaft (DFG).
 ISBN: 978-3-527-27764-3

## 14.1 Introduction

Natural attenuation is controlled by numerous processes, which include sorption, intra-particle diffusion as well as biological and chemical degradation. In order to be able to quantify respectively predict the fate and transport of contaminants, appropriate models that are able to deal with the complexity and interactions of the involved processes need to be developed. Due to insufficient information on the spatial distribution of transport parameters in the subsurface, stochastic methods are a preferred alternative to deterministic approaches. In the present paper a one-dimensional Lagrangian streamtube model is used to describe the reactive transport of acenaphthene as a sample organic compound at field scale. As the streamtube model does not consider the heterogeneity of hydrogeochemical parameters but only hydraulic heterogeneity, model results from the streamtube model are compared in a Monte Carlo approach to results of a two-dimensional Eulerian model.

## 14.2 Model Approaches

### 14.2.1 The Lagrangian Model

Based on the Lagrangian idea of discretising a heterogeneous model domain along flow paths by travel time of inert tracers (Dagan and Cvetkovic, 1996), Finkel et al. (1999) developed the one-dimensional streamtube model SMART (**S**treamtube **M**odel for **A**dvective and **R**eactive **T**ransport). In this Lagrangian approach hydraulic heterogeneity is considered by the probability density function of travel times (pdf), which serves as input for the reactive transport modelling. Kinetic sorption is described as retarded diffusion of dissolved contaminants into intra-particle pores (e.g. Ball and Roberts, 1991; Grathwohl, 1998). As diffusion into the intra-particle pores and sorption in the pores depend on material characteristics, the aquifer material is characterised by different lithological components and grain size classes. SMART allows for a non-uniform composition of lithological components and grain sizes, which has to be the same in all model cells. As a result of the spatial discretisation by travel time, the spatial variability of the lithological composition and the associated hydrogeochemical parameters cannot be taken into account.

### 14.2.2 The Eulerian Model

As Eulerian model the finite difference code MT3D is used (Zheng, 1990), which was extended by a module for kinetic sorption, called IPD (**I**ntra**P**article **D**iffusion module) (Jäger and Liedl, 2000). Like in the streamtube model, kinetic sorption is accounted for by the time-dependent diffusion process of dissolved contaminants into intra-particle pores. In contrast to the SMART model, the Eulerian model MT3D-IPD additionally allows for a spatial variation of the hydrogeochemical parameters. Hydraulic and hydrogeochemical heterogeneity is described by a spatial distribution of different facies types consisting of different lithological components and different grain sizes. Therefore, MT3D-IPD simulations in principle may yield more detailed modelling results than SMART. This advantage, however, is accompanied with a tremendously high computational effort for simulating the transport in a two- or three-dimensional model domain.

## 14.3 Reactive Transport Modelling of the 'Testfeld Süd' Site

The transport modelling was performed using field data obtained at the test site 'Testfeld Süd' (Herfort, 2000), located in an alluvial aquifer in Southwest Germany. From borehole and sieve analysis data, three different facies types were distinguished (Table 14.1): A highly conductive facies 'gravel', consisting mainly of limestone, summarised by the effective component *G_eff;* a well conductive facies 'gravel with matrix' and a 'sand' facies with a relatively low permeability. Geostatistical analysis of the spatial distribution of the facies types provided the input for the generation of equi-probable aquifer realisations using the sequential indicator simulation algorithm from Deutsch and Journel (1992). Correlation lengths were determined in the range of 30–60 m.

Table 14.1: Composition of facies types, derived from borehole and sieve analysis data obtained at the field site 'Testfeld Süd' (Herfort, 2000).

| | Facies 'Gravel' (G) | Facies 'Gravel with Matrix' (Gm) | Facies 'Sand' (S) |
|---|---|---|---|
| Overall frequency (–) | 0.337 | 0.59 | 0.073 |
| Share of lithological component *G_eff* (–) | 1.0 | 0.0 | 0.0 |
| Share of lithological component *Limestone* (–) | 0.0 | 0.673 | 0.147 |
| Share of lithological component *Quartz* (–) | 0.0 | 0.327 | 0.853 |

*G_eff* = effective lithological component of the facies type G, consisting of limestone, sandstone and quartz (Herfort, 2000).

Table 14.2: Physical and chemical parameters of the lithological components used in the simulations. Isotherm parameters are valid for acenaphthene.

| Lithology | Share (–) | $n_{ip}$ (–) | $\tau$ (–) | $\rho$ (g · cm$^{-3}$) | $K_{fr}$ (L·kg$^{-1}$) | $1/n_{fr}$ (–) |
|---|---|---|---|---|---|---|
| G_eff[1] | 0.337 | 0.013 | 61.8 | 2.72 | 5.75 | 0.83 |
| Limestone[2] | 0.408 | 0.012 | 59.0 | 2.73 | 3.29 | 0.83 |
| Quartz[3] | 0.255 | 0.0005 | 9.0 | 2.65 | 0.07 | 1 |

Data origin: [1]Herfort, 2000; [2]Rügner et al., 1997; [3]Grathwohl and Kleineidam, 1995.
$n_{ip}$ = intra-particle porosity.
$\tau$ = tortuosity.
$\rho$ = density.
$K_{fr}$ = Freundlich coefficient, determined for concentrations in mg·L$^{-1}$.
$1/n_{fr}$ = Freundlich exponent.

Eight aquifer realisations with 50 m width and 800 m length were used for the simulation of

- the groundwater flow,
- the reactive transport using SMART based on pdf's of arrival time from the flow model, and
- the reactive transport using MT3D-IPD.

Table 14.2 denotes the physico-chemical properties of the lithological components, which have been measured in various laboratory experiments (Rügner et al., 1997; Grathwohl and Kleineidam, 1995). In the simulations with MT3D-IPD the spatial distribution of the facies types was represented together with their lithological components, whereas in SMART only one effective facies type was considered. This effective or bulk facies itself represents a heterogeneous composition of the lithologies according to the overall frequency of the three facies types.

## 14.4 Results and Discussion

Analysing a single realisation, the difference between simulation results of MT3D-IPD and SMART are expected to be high, especially at small transport distances, i.e. less than the correlation length of physico-chemical properties. In Fig. 14.1 relative mass fluxes of acenaphthene, which represent the integral product of groundwater discharge and concentration across a control plane perpendicular to the flow, are shown at different transport distances.

For transport distances of 50 m and 100 m, the SMART model leads to higher retardations of acenaphthene than the MT3D-IPD model. This is due to the spatial distribution of the different facies types, which is considered in MT3D-IPD but not in

SMART. Figure 14.2 shows the cumulative proportions of facies types with travel distance for this realisation. In comparison to the mean facies proportion, which is taken into account in SMART (horizontal lines in Fig. 14.2), the spatially varying proportion of the highly sorptive facies type 'G' (light grey in Fig. 14.2) is smaller than the mean share at distances up to 200 m. This causes the lower retardation in MT3D-IPD compared to SMART in the first 200 m.

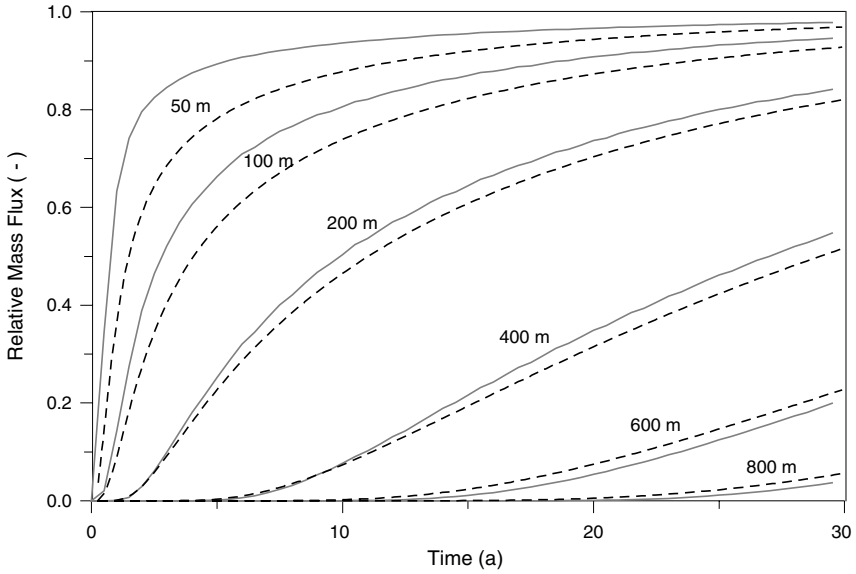


Figure 14.1: Comparison of model results for a single realisation: Solid lines represent the relative mass fluxes at different transport distances simulated with MT3D-IPD, dashed lines show the corresponding SMART results.

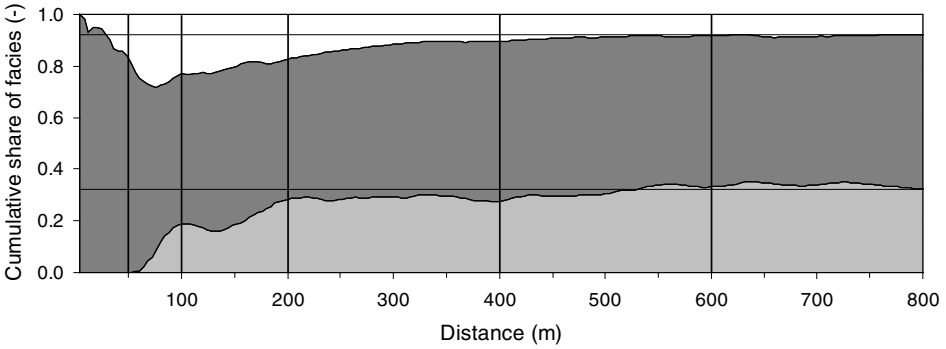


Figure 14.2: Cumulative proportions of facies types with travel distance for a single realisation. The horizontal lines mark the constant share of facies types in SMART, while the vertical lines denote the distances at which the relative mass fluxes are shown in Fig.14.1. (white = facies 'S'; dark grey = facies 'Gm'; light grey = facies 'G').

With increasing transport distance and consequently decreasing deviations between the facies proportions of both model approaches, the differences in the simulated mass fluxes decrease. Because of a presently very high computation time needed for MT3D-IPD, only 30 years of transport were calculated.

Model results for the entire simulated ensemble of eight realisations show some different characteristics. Figure 14.3 depicts the mean mass flux, determined by simulating the reactive transport for each realisation and subsequently averaging over all realisations. This was performed for both model approaches. Two major observations can be made:

(1) The differences between the mean breakthrough curves resulting from both approaches decrease with increasing travel distance. This is valid for distances of up to 400 m. From then on the differences seem to increase again. There are two possible explanations:

(a) Due to the high computational effort, complete breakthrough curves were not simulated. It could be presumed, that with increasing time the breakthrough curves might become more similar, accordingly to the 400 m breakthrough curve at 30 years.

(b) The upstream finite difference solver, used in MT3D-IPD, produces numerical dispersion, whereas the streamtube model is free of numerical dispersion. In a heterogeneous field numerical dispersion leads to an earlier first arrival (not visible in

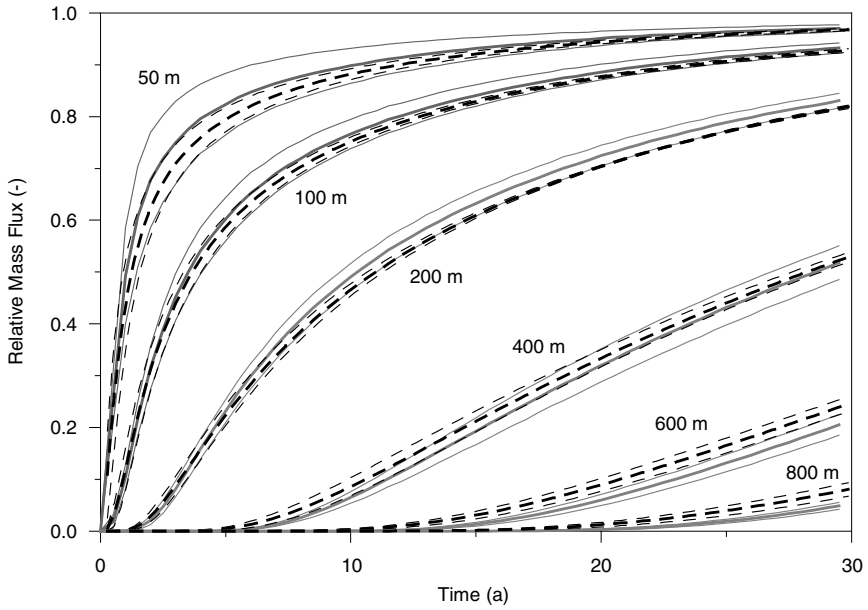


Figure 14.3: Comparison of model results for all realisations: solid lines represent the relative mass fluxes at different distances simulated with MT3D-IPD, dashed lines show the corresponding SMART results. Bold lines denote the mean of all realisations, thin lines denote mean +/– one standard deviation of relative mass flux.

the resolution of Fig. 14.3) and to an increased artificial retardation for later arrival times. The effect was demonstrated for conservative transport by comparing breakthrough curves from particle tracking and finite difference schemes (not shown here), indicating that numerical dispersion in our case has a significant influence for distances larger than 400 m. Due to even higher computation times, it was not feasible to simulate transport in MT3D-IPD with the 'dispersion-free' method of characteristics.

(2) The maximum variance of the realisation ensemble shows a decreasing tendency with increasing travel distances for both model approaches. This is expected, as with increasing travel distance the contaminant plume has experienced the mean aquifer composition in each realisation. As in MT3D-IPD also the hydrogeochemical heterogeneity is considered, the variances of the realisation ensemble are higher than the variances of the SMART results.

These findings show that the one-dimensional streamtube model SMART is able to appropriately represent the mean transport behaviour for travel distances larger than 100 m, which corresponds to approximately two to four correlation lengths at the investigated site. Single realisations cannot be simulated satisfactorily using the streamtube approach.

For larger travel distances or longer travel times SMART is thus an alternative modelling tool for predictions of the mean plume development. The advantages are that the SMART modelling approach is not affected by numerical dispersion, consumes far less CPU time and, due to its integral approach, also requires less detailed site investigations.

## 14.5 References

Ball, W. P.; Roberts, P. V. (1991): Long-term sorption of halogenated organic chemicals by aquifer material. 2. Intraparticle diffusion. *Environmental Sciences and Technology* **25**, 1237–1249.

Dagan, G.; Cvetkovic, V. (1996): Reactive transport and immiscible flow in geological media. I. General theory. *Proceedings of the Royal Society of London* **A452**, 285–301.

Deutsch, C. V.; Journel, A. G. (1992): GSLIB – Geostatistical Software Library and User's Guide, Oxford University Press.

Finkel, M.; Liedl, R.; Teutsch, G. (1999): Modelling surfactant-enhanced remediation of polycyclic aromatic hydrocarbons. *Environment Modelling & Software* **14**, 203–211.

Grathwohl, P. (1998): Diffusion in Natural Porous Media: Contaminant Transport, Sorption, Desorption and Dissolution Kinetics, Kluwer Academic Publishers.

Grathwohl, P.; Kleineidam, S. (1995): Impact of heterogeneous aquifer materials on sorption capacities and sorption dynamics of organic contaminants. *Groundwater Quality: Remediation and Protection*, 79–86.

Herfort, M. (2000): Reactive Transport of Organic Compounds within a Heterogeneous Porous Aquifer. Tübinger Geowissenschaftliche Arbeiten, TGA C54, Universität Tübingen.

Jäger, R.; Liedl, R. (2000): Prognose der Sorptionskinetik organischer Schadstoffe in heterogenem Aquifermaterial. *Grundwasser* **2**, 57–66.

Rügner, H.; Kleineidam, S.; Grathwohl, P. (1997): Sorptionsverhalten organischer Schadstoffe in heterogenem Aquifermaterial am Beispiel des Phenanthrens. *Grundwasser* **3**, 133–138.

Zheng, C. (1990): MT3D – A modular three-dimensional transport model for simulation of advection, dispersion and chemical reaction of contaminants in groundwater systems, Program documentation, S. S. Papadopulos & Associates, Inc.

# 15 A Steady-State Approach to Model Redox Potentials in Groundwaters Contaminated with Chlorinated Ethenes

Stefan Peiffer* and Christine Laskov

## Abstract

The dechlorination of the solvents tetra- and trichloroethene to dichloroethene, vinylchloride and ethene under anaerobic conditions is to a large extent controlled by the redox conditions, which are a function of the prevailing microbial metabolisms (sulfate, nitrate, iron reduction and methanogenesis). In this presentation, the hypothesis is examined that degradation rates of chlorinated ethenes are predictable, if the redox potential or at least the redox environment is known. Therefore, field studies, where in-situ degradation rates of chlorinated ethenes were evaluated with respect to the question as to whether a relationship exists between these variables. The redox conditions were parameterized using $H_2$-partial pressure, measured EH-values, and the soft parameter "redox environment". No relation could be identified between $E_H$-values or $H_2$-partial pressure and the degradation rate. Meaningful results where obtained only for the imprecise parameter redox environment. We therefore present a concept, according to which the concentration ratio of ethene compounds of different chlorination degree (for example c(trichlorethene):c(dichloroethene) ) can be used as a direct measure for the redox potential at which degradation occurs. This concept is based on the assumption that the degradation of chlorinated ethenes is limited by the $H_2$ production rate, that is the fermentation rate of organic carbon. Following this concept the degradation of chlorinated ethenes is at steady-state. The few data available from the field studies to calculate redox potentials in such a way suggest indeed proportionality to the degradation rate which suggests this parameter to be a promising tool for the study of natural attenuation processes.

* Lehr- und Forschungsgebiet Hydrogeologie, RWTH Aachen, Lochnerstr. 4–20, 52064 Aachen; peiffer@hydro.rwth-aachen.de



*Geochemical Processes: Conceptual Models for Reactive Transport in Soil and Groundwater. Research Report.* Deutsche Forschungsgemeinschaft (DFG).
 ISBN: 978-3-527-27764-3

## 15.1 Introduction

Chlorinated ethenes are subject to a variety of microbial degradation processes that include reductive dechlorination (Vogel et al., 1987; Maymo-Gatell et al., 1997), aerobic oxidation, anaerobic oxidation (Bradley and Chapelle, 1996), and anaerobic cometabolism (McCarty and Semprini, 1994). Both, laboratory studies (Bradley and Chapelle, 1998), and field studies (Chapelle and Bradley, 2000) show that the efficiency of chlorinated ethene biodegradation depends on ambient redox conditions. Therefore, reliable tools to measure the redox conditions are crucial to understand and even predict chlorinated ethene degradation.

Characterisation of redox conditions is not a straight-forward procedure and no reliable method exists to unambigously predict the fate of a certain compound in a solution with respect to the nature and the concentration of the bulk electron donors and acceptors (Peiffer, 2000). As was emphasized by Chapelle et al. (1996), $H_2$ concentrations in anaerobic systems can be interpreted in the context of electron-acceptor (oxygen, sulfate, nitrate) availability and the presence of reduction products (Fe(II), sulfide, methane) and are therefore useful tools to describe the prevailing anaerobic metabolic activity. Postma and Jakobsen (1996) were able to demonstrate that the segregation of the reduction of the various electron acceptors into different redox zones is understood as a partial equilibrium process. Accordingly, reduction of ferric oxides and of sulfate may proceed simultaneously over a wide range of environmental conditions. Redox conditions could than be predicted according to the concentration of ferrous iron, sulfate and knowledge of the pH. Inherent to these approaches is the concept that not the terminal oxidation step in organic matter degradation but the fermentative step is limiting the overall degradation rate (Postma and Jakobsen,1996).

The intention of this paper is to evaluate as to whether redox parameters derived from the concepts outlined above are predictive with respect to the degradation rate of chlorinated ethenes observed in the field. We used data from 13 field studies where in-situ degradation rates had been determined together with a (partly incomplete) analytical protocol of redox sensitive species. A novel approach will be derived to predict redox conditions based on the assumption that reductive dechlorination of chlorinated ethenes is at steady-state.

## 15.2 Anaerobic Degradation of Chlorinated Ethenes

At anaerobic sites, the solvents tetrachloroethene (PCE) and trichloroethene (TCE) can undergo reductive dechlorination to less-chlorinated ethenes, a process identified as halorespiration (Holliger and Schumacher, 1994). In this process $H_2$ is transferred to the reactant which leads to loss of one chloride ion:

$$Cl_2C = CCl_2 + H_2 \Rightarrow Cl_2C = CClH + H^+ + Cl^- \quad (1)$$

Similar reactions have been shown to reduce DCE to VC and VC to ethene. In general, reductive dechlorination to the ethenes occurs by sequential dechlorination from PCE to TCE to dichloroethene (DCE) to vinyl chloride (VC) and finally to ethene (Wiedemeier et al., 1999).

Dechlorination is more rapid for highly chlorinated compounds than for compounds that are less chlorinated (Vogel and McCarty, 1985). PCE degrades the fastest under all anaerobic environments, while VC will degrade only under sulfate and methanogenic conditions, with a relatively slow reaction rate. Large accumulations of *cis*-dichloroethene (DCE) are often found at contaminated sites undergoing reductive dechlorination, and at some sites there is little or no dechlorination past *cis*-DCE (Wiedemeier et al, 1999). The reasons for *cis*-DCE accumulation may be due to either slower rates of DCE halorespiration or the prevalence of organisms that reduce PCE as far as *cis*-DCE over organisms that can reduce PCE all the way to ethene (Gossett and Zinder, 1996).

The need for sufficient $H_2$ concentrations to reduce chlorinated ethenes has been stressed by several authors (Wiedemeier et al., 1999; Löffler et al., 1999). From these requirements the link between redox conditions and the degradation rate becomes evident. First, the $H_2$ concentration is regarded as a means to characterize the predominating metabolic pathway (Chapelle et al., 1996). Löffler et al. (1999) present threshold values of $H_2$ concentrations to range from 5–95 nmol $L^{-1}$ for methanogenesis, 1–15 nmol $L^{-1}$ for sulfate reduction, 0.1–0.8 nmol $L^{-1}$ for Fe(III) reduction, and < 0.3 nmol $L^{-1}$ for chlororespiration. Second, degradation rates can be expected to be proportional to substrate, that is $H_2$ concentrations.

## 15.3 Evaluation of Literature Data

The requirement for the evaluation was that both, in-situ degradation rates and redox chemical information were available. Initially, we screened 46 references on field studies with respect to these variables. 27 of the references contained redoxchemical information and from only 13 studies also in-situ degradation rates were available. The discussion in this paper is based on the following 13 studies:

1. Buscheck, T.; O'Reilly, K. T. (1999): Intrinsic anaerobic biotransformation of chlorinated solvents at a manufacturing plant. In: Natural Attenuation of Fuels and Chlorinated Solvents in the Subsurface (Eds.: Wiedemeier, T. H.; Rifai, H. S.; Newell, C. J.; Wilson, J. T.), John Wiley, New York, pp. 529–535.

2. Buscheck, T. E.; O'Reilly, K. T. (1997): Intrinsic anaerobic biodegradation of chlorinated solvents at a manufacturing plant. In: In-situ and on-site Bioremediation (Eds.: Alleman, B. C.; Leeson, A.), Volume 3, *Bioremediation* **4**(3), Batelle Press, Columbus, pp. 149–154.

3. Chapelle, F. H. (1996): Identifying redox conditions that favour the natural attenuation of chlorinated ethenes in contaminated ground water systems. In: Proceedings of Symposium on Natural Attenuation of chlorinated Organics in Ground Water, Dallas, Texas, Sept.1996, EPA/540/R–96/509, pp.17–20.

4. Cox, E.; Edwards, E.; Lehmicke, L.; Major, D. (1995): Intrinsic bioremediation of trichlorethylene and trichlorethane in a sequential anaerobic-aerobic aquifer. In: Intrinsic Bioremediation (Eds.: Hinchee, R. E.; Wilson, J. T.; Downey, D. C.), Battelle Press, Columbus, pp. 223–231.

5. Wilson, J. T.; Kampell, D. H.; Weaver, J. W.; Imbrigiotta, B.; Ehlke, T. (1996): A review of intrinsic bioremediation of trichloroethylene in ground water at Picatinny arsenal, New Jersey and St. Jospehs, Michigan. In: Proceedings of Symposium on Natural Attenuation of chlorinated Organics in Ground Water, Dallas,Texas, Sept.1996, EPA/540/R–96/509, 11–14.

6. Fiorenza, S.; Hockman, E. L.;Szojka, S.; Woeller, R. M.; Wigger, J. W. (1994): Natural anaerobic degradation of chlorinated solvents at a Canadian manufacturing plant. In: Bioremediation of chlorinated and polycyclic aromatic hydrocarbon compounds (Eds.: Hinchee, R. E.; Leeson, A.; Semprini, L.; Ong, S. K.), Lewis, Boca Raton, pp. 277–286.

7. Harkness, M. R.; Bracco, A. A. (1998): Natural attenuation of chlorinated aliphatics at the naval air engineering station Lakehurst, NJ. In: Natural Attenuation of chlorinated and recalcitrant compounds (Eds.: Wickramanayake, G. B.; Hinchee, R. E.), Battelle Press, Columbus, 231–236.

8. Lee, M. D.; Mazierski, P.; Buchanan, R. J.; Ellis, D. E.; Sehayek, L. S. (1995): Intrinsic in situ anaerobic biodegradation of chlorinated solvents at an industrial landfill. In:

Intrinsic Bioremediation 3(1) (Eds.: Hinchee, R. E.; Wilson, J. T.; Downey, D. C.), Battelle Press, Columbus, pp. 205–222.

9. Mechaber, R. A.; Su, B. Y.; Cox, E. (1998): Intrinsic bioremediation of chlorinated and non-chlorinated VOCS at a RCRA landfill. In: Natural Attenuation of chlorinated and recalcitrant compounds (Eds.: Wickramanayake, G. B.; Hinchee, R. E.), Battelle Press, Columbus, 275–280.

10. Schilling, K. E.; Sheldon, J. K.; Basel, M. D. (1998): Field evidence for intrinsic bioremediation of trichlorethene in a carbonate aquifer. In: Natural Attenuation of chlorinated and recalcitrant compounds (Eds.: Wickramanayake, G. B.; Hinchee, R. E.), Battelle Press, Columbus, 243–248.

11. Swanson, M. (1999): Natural attenuation of chlorinated solvents: FT-17, Cape Canaveral, Florida. In: Natural Attenuation of Fuels and Chlorinated Solvents in the Subsurface (Eds.: Wiedemeier, T. H.; Rifai, H. S.; Newell, C. J.; Wilson, J. T.), John Wiley, New York, pp.517–528.

12. Swanson, M.; Wiedemeier, T. H.; Mououx, D. E.; Kampbell, D. H.; Hansen, J. E. (1996): Patterns of natural attenuation of chlorinated aliphatic hydrocarbons at Cape Canaveral Air Station, Florida. In: Proceedings of Symposium on Natural Attenuation of chlorinated Organics in Ground Water, Dallas ,Texas, Sept.1996, EPA/540/R–96/509, pp.168.

13. Wiedemeier, T. H.; Wilson, J. T.; Kampbell, D. H. (1996): Natural attenuation of chlorinated aliphatic hydrocarbons at Plattsburgh Air Force Base, New York. In: Proceedings of Symposium on Natural Attenuation of chlorinated Organics in Ground Water, Dallas,Texas, Sept. 1996, EPA/540/R–96/509, pp. 74–82.

References 1–4 are reviewed in Wilson et al. (1996). At some sites more than one measurement was performed so that the total number of data sets is more than 13. Calculation of in-situ first-order degradation rates was performed by various approaches (for example groundwater modelling) so that the data set is not consistent in this respect. In some cases the calculation procedure was not specified. Figure 15.1 gives an overview of the data. It shows that 80 % of all rates determined fall in the range between 0.37 $a^{-1}$ and 10 $a^{-1}$.

The degradation rates were related to measured redox voltages, to hydrogen concentrations and to the parameter "redox environment". This parameter was a subjective, experience-based estimate about the predominating metabolic pathway given either by the authors or by us. Redox potentials corresponding to predominating redox couples could not be calculated because the pH was not specified in several studies.

Measured redox voltages were taken as provided by the authors assuming that corrections of the mV reading for the potential of the reference electrode half cell had been performed.

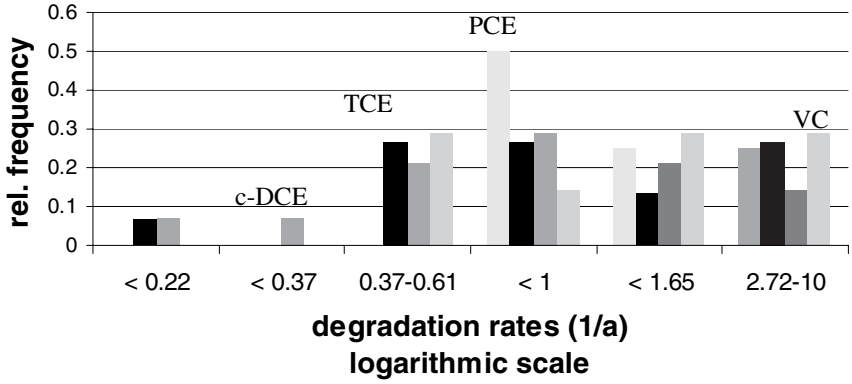


Figure 15.1: Frequency distribution of the rate constants for the degradation of chlorinated ethenes from 13 different field sites.

## 15.4 Application of Redox Chemical Information to Predict Degradation Rates

Figure 15.2 shows the degradation rates of chlorinated ethenes plotted as a function of the measured redox voltages. Only two field rates were available für PCE so that this plot is omitted. It appears that the parameter redox voltage alone does not allow any statement on the relative degradation rate of the chlorinated ethenes, let alone it would be a predictor. Rather, the degradation rates seem to be absolutely independent from the measured redox voltages.

The few data where both, $H_2$ concentrations and degradation rates, are available, reveal a similar pattern (Table 15.1). In Table 15.1, measured $H_2$ concentrations were attributed to metabolic pathways according to the threshold values given by Löffler et al. (1999). Degradation rates of a certain compound can neither be attributed to a single metabolic pathway nor is their any systematic trend visible. It appears, however, that highest rates were measured under sulfate reducing conditions, although the database seems not very reliable given that the rates measured for all four chlorinated ethenes are identical.

Putting the data together by classifying them according to the subjective parameter “redox environment” seems to provide a better insight into the degradation pattern. In Fig. 15.3 median values of the rate constants are plotted as function of this parameter. Median values were chosen, because the mean value is strongly influenced by extreme values. Included in this plot are also field studies where oxic conditions prevailed. The data evaluation suggests that VC degradation is highest under oxic conditions which corroborates the knowledge obtained from other studies (Wiedemeier et al. (1999). The higher chlorinated ethenes with their higher redox potential seem to be

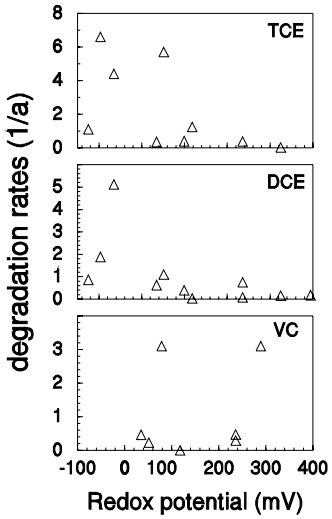


Figure 15.2: Field degradation rates of chlorinated ethenes as a function of calculated redox potentials and measured redox voltage.

Table 15.1: Field degradation rates of chlorinated ethenes and measured hydrogen concentrations. Attribution to metabolic pathways was made according to the threshold values given by Löffler et al. (1999).

| $c(H_2)$ nmol $L^{-1}$ | PCE | TCE | *cis*-DCE | VC | Ref. |
|---|---|---|---|---|---|
| | | Degradation rates ($a^{-1}$) | | | |
| 0.1 (Fe reducing) | 0.69 | 0.39 | 0.39 | | Harkness and Bracco, 1998 |
| 0.1 (Fe reducing) | 0 | 0.02 | 0.15 | | Harkness and Bracco, 1998 |
| 0.1 (Fe reducing) | | | 0.17 | | Harkness and Bracco, 1998 |
| 0.8 (Fe reducing) | | | | | |
| 1.7 (sulfate reducing) | | 0.38 | 0.75 | 0.29 | Wiedemeier et al., 1996 |
| 2.0 (sulfate reducing) | | | | | |
| 4.0 (sulfate reducing) | 3.3 | 3.3 | 3.3 | 3.3 | Chapelle, 1996 |
| 6.7 (sulfate reducing/ methanogenic) | | 1.24 | 0.03 | 0 | Wiedemeier et al., 1996 |

degraded faster under methanogenic conditions. Only few measurements are available for PCE so that they were not included into Fig. 15.3.

One conclusion from Fig. 15.3 is that our idea to use easily measurable parameters to predict in-situ degradation rates is not principally wrong. However, this survey has demonstrated that existing methods applied in the field studies do not provide a quantitative approach to model degradation rates. One of the major reasons that our attempt failed is the lack of reliable data. Most data sets were incomplete with respect to the relevant redox chemical parameters. In some cases not even the pH was specified

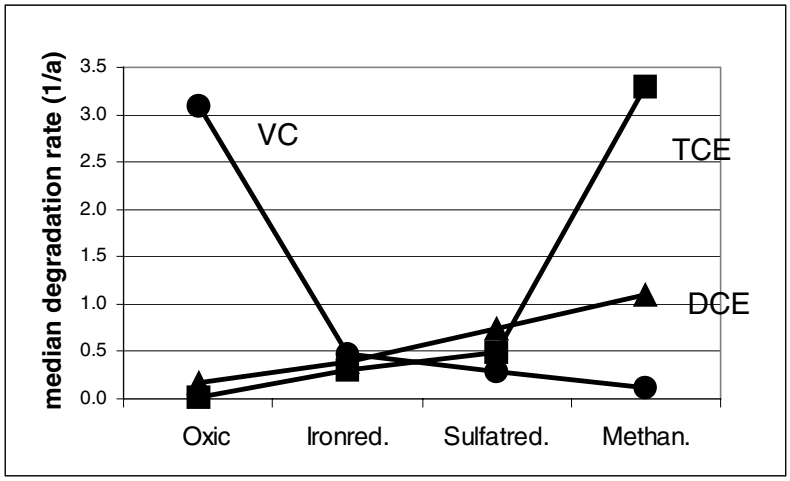


Figure 15.3: Median of degradation rates at different redox environments. The classification of a certain site to a certain redox environment is based on a subjective assessment by the authors of the field study or, if not available, by us.

in the papers (although they were certainly measured) nor was the use of $E_H$. Therefore, a guideline is strongly needed, which lists the parameters necessary to characterize redoxchemical processes and which defines the analytical methods to be used for their determination.

A critical point, of course, is the reliability of degradation rates which we took from the literature. It appears that they were to some degree corrected for dilution and also groundwater transport models were applied to calculate these rates. Yet, this was not always clear and also in this case a standard procedure should be applied to make data comparable.

## 15.5 A Steady-State Approach to Predict Degradation Rates

Inherent to the $H_2$ partial pressure approach to predict metabolic pathways is the concept that $H_2$ producing, i.e. fermentative processes are rate controlling for the terminal electron accepting processes (for a review see Peiffer, 2000). This concept has lead to the partial equilibrium approach (Postma and Jakobsen, 1996) outlined above. Similarly, $H_2$ production rate can be assumed to be controlling also the rate of halorespiration, i.e. the degradation rate of chloroethenes. Applied on the sequential degradation of chlorinated ethenes, this concept implies that steady-state also exists with respect to the reactant (for example TCE) and the corresponding product (for example DCE) of a halorespiratoric reaction according to

$$Cl_2C = CClH + H_2 \Rightarrow HClC = CClH + H^+ + Cl^- \quad (2)$$

The consumption of a reactant at steady-state can be described using chemical kinetics. A reactant is degraded with a rate constant $k_1$ to form product 1, which is subsequently degraded to form product 2 with a rate constant $k_2$.

$$\mathbf{R}\text{eactant} \xrightarrow{k_1} \mathbf{P}\text{roduct 1} \xrightarrow{k_2} \text{Product 2}$$

At steady-state we obtain:

$$\frac{dc(\mathbf{P})}{dt} = k_1 \cdot c(\mathbf{R}) - k_2 \cdot c(\mathbf{P}) = 0 \quad (3)$$

which implies that the concentration ratio between R and P is constant:

$$\frac{c(\mathbf{R})}{c(\mathbf{P})} = \frac{k_2}{k_1} \text{ for example } \frac{\text{c(TCE)}}{\text{c(DCE)}} \quad (4)$$

If the concentration of the reactant is larger than that of the product then the consumption of the product is faster than its formation.

According to this concept concentration ratios allow prediction of the relative degradation rate of the individual reactants. In Fig. 15.4 the ratios from the median concentration values shown in Fig. 15.3 are plotted on a logarithmic scale for the various redox conditions. The ratio PCE/TCE was omitted because no discrimination can be made between TCE as a contaminant source or as a product of the degradation of PCE.

Figure 15.4 suggests that DCE is formed from TCE under all redox conditions at the same rate as it is consumed (the ratio being about 1). In contrast, the ratio DCE/VC is larger than one, which implies that the degradation rate of VC is faster than its formation. This result corresponds to the observation that *cis*-dichloroethene (DCE) frequently accumulates in the pore water. A similar pattern can be observed for ethene which appears, on average, to be faster consumed than produced from VC. The implication of this pattern would be that in the sequence of degradation of chlorinated ethenes the degradation of lower chlorinated ethenes would be ultimatively controlled by the degradation rate of DCE. The observation that the same pattern seems to exist also under oxic conditions may be because the VC in many chlorinated solvent plumes can migrate to oxic zones that can support direct oxidation of VC.

In analogy to the partial equilibrium approach, the assumption of the degradation sequence of chlorinated ethenes to occur at steady-state can be used also to derive equilibrium potentials for their degradation according to

$$E = E^\circ + 1/2 \cdot 0,059 \cdot \log\left(\frac{c(\mathbf{R})}{c(\mathbf{P})} \cdot \frac{c(H_2)}{c(H^+) \cdot c(Cl^-)}\right) \quad (5)$$

and relate it to the rate constants.

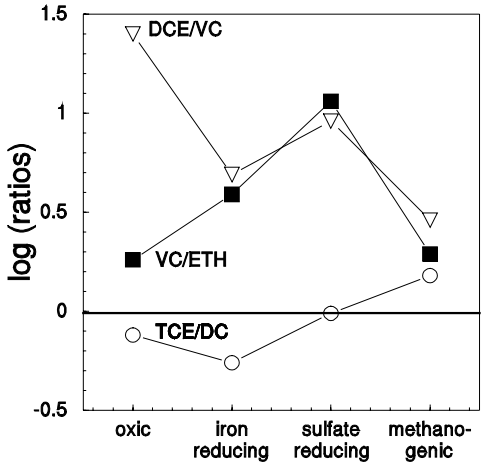


Figure 15.4: Concentration ratio of the median values of reactant/product pairs of the degradation sequence of chlorinated ethenes plotted as a function of the soft parameter 'redox environment'.

E° is the equilibrium potential for the degradation reaction, for example Eqs. (1) and (2), under standard conditions. Unfortunately, sufficient data (that is more than two complete data sets containing rate constant, reactant and product concentration, and $H_2$ concentration) were available only for the redox couple TCE and DCE (Eq. (2)). The standard potential was converted from Gibbs free energy provided by Dolfing (2000) to be 0.72 V. pH values were available only for one of the sites (pH 5.3), the unknown values were set to a value of seven under the assumption that such a value is a best guess for anoxic and reducing conditions. In case of chloride, concentrations were available for two of the studies (between 1 and 2 mmol $L^{-1}$), the unknown value was set to 1 mmol $L^{-1}$.

Figure 15.5 shows that a linear relation seems to exist between the equilibrium potential and the rate constant for DCE degradation. The positive values of E indicate that degradation of TCE to DCE can thermodynamically occur. However, the lower the potential, i.e. the less favourable the reaction is from a thermodynamic point of view, the higher the degradation rate of the product DCE seems to be. This observation implies that conditions that favour degradation of TCE to DCE (high equilibrium potentials) do not favour high DCE degradation rates. As a consequence, acculumulation of DCE occurs which is consistent with the observations in the field (Wiedemeier et al., 1999).

We are aware that the latter discussion remains speculative due to the small database. We believe, however, that similar correlations between rates and thermodynamic parameters, which consider the steady-state approach, will open new opportunities to understand the dynamic behaviour of chlorinated ethenes and also other halogenated compounds that undergo halorespiration.

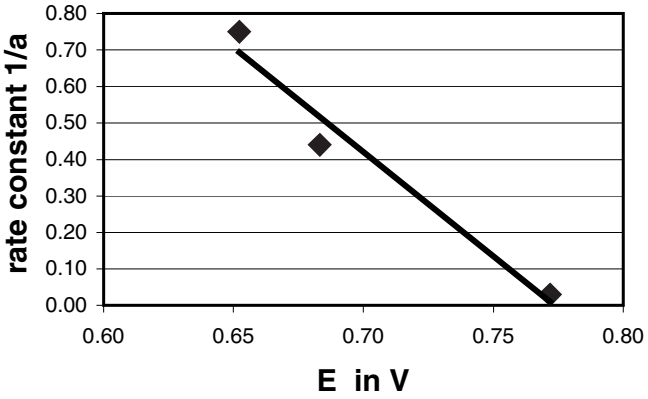


Figure 15.5: Rate constants for the degradation of DCE plotted as a function of the equlibrium potential (Eq. (5)) for the degradation of TCE to DCE (Eq. (2)).

## 15.6 Conclusion

From a hydrogeochemical perspective, there are two major conclusions that can be drawn from this literature review. First, data protocols need to be consistent and complete with respect to redox-sensitive species in order to understand the dynamic behaviour of chlorinated ethenes in the underground and compare it between different sites. Second, the use of the steady-state approach to evaluate field data provided results, which appeared to be more meaningful than those obtained using classical redox chemical parameters. After careful calibration in several field studies, the steady-state approach may allow prediction of in-situ degradation rates and therefore turn out to be a powerful tool for the study of natural attenuation processes.

## Acknowledgements

The complete data set is available upon request from the corresponding authors as an EXCEL file.

# 15.7 References


Bradley, P. M.; Chapelle, F. H. (1996): Microbioal mineralization of vinyl chloride in Fe(III)-reducing aquifer sediments. *Environ. Sci. Technol.* **30**, 2084–2086.

Bradley, P. M.; Chapelle, F. H. (1998): Microbioal mineralization of VC and DCE under different terminal electron accepting conditions. *Anaerobe* **4**, 81–87.

Buscheck, T. E.; O'Reilly, K. T. (1997): Intrinsic aneraobic biodegradation of chlorinated solvents at a manufacturing plant. In: In-situ and on-site Bioremediation (Eds.: Alleman, B. C.; Leeson, A.), Volume 3, Bioremediation 4(3), Batelle Press, Columbus, pp. 149–154.

Buscheck, T.; O'Reilly, K. T. (1999): Intrinsic anaerobic biotransformation of chlorinated solvents at a manufacturing plant. In: Natural Attenuation of Fuels and Chlorinated Solvents in the Subsurface (Eds.: Wiedemeier, T. H.; Rifai, H. S.; Newell, C. J.; Wilson, J. T.), John Wiley, New York, pp. 529–535.

Chapelle, F. H. (1996): Identifying redox conditions that favour the natural attenuation of chlorinated ethens in contaminated ground water systems. In: Proceedings of Symposium on Natural Attenuation of chlorinated Organics in Ground Water, Dallas, Texas, Sept.1996, EPA/540/R–96/509, pp.17–20.

Chapelle, F. H.; Bradley, P. M. (2000): Redox conditions and the efficiency of chlorinated ethene biodegradation – Field studies. In: Chemical-biological interactions in contaminant fate, Preprint of Extended Abstracts (Eds.: Tratnyek, P.; Adriaens, P.; Roden, E. E.). *ACS* **40**, 343–345.

Chapelle, F. H.; Haack, S. K.; Adriaens, P.; Henry, M. A.; Bradley, P. M. (1996): Comparison of Eh and H2 measurements for delineating redox processes in a contaminated aquifer. *Environ. Sci. Technol.* **30**, 3565–3569.

Cox, E.; Edwards, E.; Lehmicke, L.; Major, D. (1995): Intrinsic bioremediation of trichlorethylene and trichlorethane in a sequential anaerobic-aerobic aquifer. In: Intrinsic Bioremediation (Eds.: Hinchee, R. E.; Wilson, J. T.; Downey, D. C.), Battelle Press, Columbus, pp. 223–231.

Dolfing, J. (2000): Hydrogen cycling in dechlorinating ecosystems. In: Chemical-biological interactions in contaminant fate, Preprint of Extended Abstracts (Eds.: Tratnyek, P.; Adriaens, P.; Roden, E. E.). *ACS* **40**, 328–330.

Fiorenza, S.; Hockman, E. L.; Szojka, S.; Woeller, R. M.; Wigger, J. W. (1994): Natural anaerobic degradation of chlorinated solvents at a canadian manufacturing plant. In: Bioremediation of chlorinated and polycyclic aromatic hydrocarbon compounds (Eds.: Hinchee, R. E.; Leeson, A.; Semprini, L.; Ong, S. K.), Lewis, Boca Raton, pp. 277–286.

Gossett, J. M.; Zinder, S. H. (1996): Microbiological aspects relevant to natural attenuation of chlorinated ethenes. In: Proceedings of the Symposium on Natural Attenuation of Chlorinated Organics in Groundwater, Dallas, Texas, Sept. 11–13, EPA/504/R–96/509. U.S. EPA, Washington, DC.

Harkness, M. R.; Bracco, A. A. (1998): Natural attenuation of chlorinated aliphatics at the naval air engineering station Lakehurst, NJ. In: Natural Attenuation of chlorinated and recalcitrant compounds (Eds.: Wickramanayake, G. B.; Hinchee, R. E.), Battelle Press, Columbus, 231–236.

Holliger, C.; Schumacher, W. (1994): Reductive dehalogenation as a respiratory process. *Antonie Leeuwenheok* **66**, 239–246.

Lee, M. D.; Mazierski, P.; Buchanan, R. J.; Ellis, D. E.; Sehayek, L. S. (1995): Intrinsic in situ anaerobic biodegradation of chlorinated solvents at an industrial landfill. In: Intrinsic Bioremediation 3(1) (Eds.: Hinchee, R. E.; Wilson, J. T.; Downey, D. C.), Battelle Press, Columbus, pp. 205–222.

Löffler, F.; Tiedje, J. M.; Sanford, R. A. (1999): Fraction of electrons consumed in electron acceptor reduction and hydrogen thresholds as indicators of halorespiratory physiology. *Appl. Environ. Microbiol.* **65**, 4049–4056.

Maymo-Gatell, X.; Chien, Y. T.; Gosett, J. M.; Zinder, J. H. (1997): Isolation of a bacterium that reductively dechlorinates tetrachloroethene to ethene. *Science* **276**, 1568–1571.

McCarty, P. L.; Semprini, L. (1994): Ground-water treatment for chlorinated solvents. In: Handbook of bioremediation (Eds.: Norris, R. D.; Matthews, J. E.), Lewis Publishers, pp. 87–116.

Mechaber, R. A.;Su, B. Y.; Cox, E. (1998): Intrinsic bioremediation of chlorinated and non-chlorinated VOCS at a RCRA landfill. In: Natural Attenuation of chlorinated and recalcitrant compounds (Eds.: Wickramanayake, G. B.; Hinchee, R. E.), Battelle Press, Columbus, 275–280.

Peiffer, S. (2000): Characterisation of the redox state of aqueous systems – towards a problem-oriented approach. In: Redox – Fundamentals, Processes and Measuring Techniques (Eds.: Schüring, J.; Schulz, H. D.; Fischer, W. R.; Böttcher, J.; Duijnesveld, W. H. M.), Springer Verlag, Berlin.

Postma, D.; Jakobsen, R. (1996): Redox zonations: Equilibrium constraints on the Fe(III)/SO-reduction interface. *Geochim. Cosmochim. Acta* **60**, 3169–3176.

Schilling, K. E.; Sheldon, J. K.; Basel, M. D. (1998): Field evidence for intrinsic bioremediation of trichlorethene in a carbonate aquifer. In: Natural Attenuation of chlorinated and recalcitrant compounds (Eds.: Wickramanayake, G. B.; Hinchee, R. E.), Battelle Press, Columbus, 243–248.

Swanson, M. (1999): Natural attenuation of chlorinated solvents: FT-17, Cape Canaveral, Florida. In: Natural Attenuation of Fuels and Chlorinated Solvents in the Subsurface (Eds.: Wiedemeier, T. H.; Rifai, H. S.; Newell, C. J.; Wilson, J. T.), John Wiley, New York, pp.517–528.

Swanson, M.; Wiedemeier, T. H.; Mououx, D. E.; Kampbell, D. H.; Hansen, J. E. (1996): Patterns of natural attenuation of chlorinated aliphatic hydrocarbons at Cape Canaveral Air Station, Florida. In: Proceedings of Symposium on Natural Attenuation of chlorinated Organics in Ground Water, Dallas, Texas, Sept.1996, EPA/540/R–96/509, pp.168.

Vogel, T. M., Criddle, C. S.; McCarty, P. L. (1987): Transformation of halogenated aliphatic compounds. *Environ. Sci. Technol.* **21**, 722–736.

Vogel, T. M.; McCarty, P. L. (1985): Biotransformation of tetrachloroethylene to trichloroethylene, dichloroethylene, vinyl chloride, and carbon dioxide under methanogenic conditions. *Environ. Microbiol.* **49**, 1080–1083.

Wiedemeier, T.-H.; Rifai, H. S.; Newell, C. J.; Wilson, J. T. (1999): Natural Attenuation of Fuels and Chlorinated Solvents in the Subsurface, John Wiley, New York, pp. 241–297.

Wiedemeier, T. H.; Wilson, J. T.; Kampbell, D. H. (1996): Natural attenuation of chlorinated aliphatic hydrocarbons at Plattsburgh Air Force Base, New York. In: Proceedings of Symposium on Natural Attenuation of chlorinated Organics in Ground Water, Dallas, Texas, Sept. 1996, EPA/540/R–96/509, pp. 74–82

Wilson, J. T.; Kampell, D. H.; Weaver, J. W.; Imbrigiotta, B.; Ehlke, T. (1996): A review of intrinsic bioremediation of trichloroethylene in ground water at Picatinny arsenal, New Jersey and St. Jospehs, Michigan. In: Proceedings of Symposium on Natural Attenuation of chlorinated Organics in Ground Water, Dallas, Texas, Sept. 1996, EPA/540/R–96/509, 11–14.

# 16 Simulation of Two-Column Experiments on Anaerobic Degradation of Toluene and Xylene

Wolfgang Schäfer* and Rainer U. Meckenstock

## Abstract

Simulations with a numerical reactive multispecies transport model were performed for two soil column experiments on anaerobic degradation of toluene and *o*-xylene. The aim of the numerical modelling was to identify relevant interactions of the two degradation processes. Our findings indicated that *o*-xylene degradation was partly inhibited by toluene degradation but it was not possible to decide if *o*-xylene degradation was inhibited directly by toluene or by a special inhibitor produced during toluene degradation. However, the simulations clearly suggested that the two degradation processes were carried out by two different organisms. The parameters of the biochemical model calibrated during a first experiment could be successfully transferred to the simulation of a second experiment with only a slight change in the inhibition constant. Modelling of the second experiment raised the assumption that throughout the course of the experiment the *o*-xylene degradation in the soil column became more and more tolerant towards elevated toluene levels.

In summary, the simulations suggest that two microbial groups should be considered to model reactive transport at the field scale. Perhaps because the two populations did not compete for a common substrate (e.g. sulfate was not limiting) in the soil column they could finally adapt to the conditions in the column and degrade the two substrates completely. However, under field conditions parameters such as the supply of electron acceptors might become limiting and thus promote a sequential degradation of toluene and *o*-xylene because toluene-degrading organisms outcompete *o*-xylene degraders.

* Interdisziplinäres Zentrum für Wissenschaftliches Rechnen, Universität Heidelberg, Im Neuenheimer Feld 368, 69120 Heidelberg; e-Mail: wolfgang.schaefer@urz.uni-heidlberg.de



*Geochemical Processes: Conceptual Models for Reactive Transport in Soil and Groundwater. Research Report.* Deutsche Forschungsgemeinschaft (DFG).
 ISBN: 978-3-527-27764-3

## 16.1 Introduction

Aquifers polluted with aromatic hydrocarbons usually become anoxic and the majority of e.g. BTEX compounds is degraded anaerobically. A number of anaerobic microorganisms using different electron acceptors has been isolated in the past and the respective degradation pathways were studied (Heider et al., 1999). For toluene, it was found in all investigated cases that the primary reaction in the pathway is an addition of fumarate to the methyl group. This reaction turned out to be a general mechanism for anaerobic bacteria to activate aromatic hydrocarbons containing methyl groups. Also for *o*-xylene degradation this type of reaction was demonstrated. However, in contaminated aquifers organisms are facing a complex mixture of hundreds of different compounds which could interfere with the degradation of individual substrates. It is almost impossible to assess such in situ interactions analytically but modelling can be applied to describe complex interactions in situ. We therefore started soil column experiments to investigate anaerobic degradation of mixtures of BTEX compounds and obtain a profound basis to model inhibition processes in the subsurface.

Soil columns with an undefined anaerobic microbial community were supplied with a mixture of the most prominent aromatic contaminants benzene, toluene, ethylbenzene and *o*,*m*,*p*-xylene.

Simulations were performed with a numerical reactive transport model to reproduce the observed concentration behaviour of the aromatic compounds which were subject to biodegradation and to test hypotheses on the controlling degradation mechanisms. Furthermore, it was estimated which of the processes observed at the lab scale might be relevant for reactive transport modelling at field sites.

Two experiments out of a series of laboratory studies were selected for this purpose. The first was conducted in order to study the microbially mediated degradation of benzene, toluene, *m*,*p*,*o*-xylene, and naphthalene with sulfate as terminal electron acceptor (Winter, 1997). No degradation could be observed for benzene, *m*,*p*-xylene and naphthalene and therefore the simulations were carried out for toluene and *o*-xylene only. This experiment will be referred to as Experiment 1. The second experiment described in this paper (Experiment 2) was performed with special emphasis on the interaction of the toluene and *o*-xylene degradation processes.

## 16.2 Set-Up of the Soil Columns

### 16.2.1 Experiment 1

The glass columns used in this study were 38.5 cm long and had a diameter of 4,5 cm. The first 30 cm of the columns were filled with contaminated soil material from the saturated zone of the "Testfeld Süd" site. The remaining 8.5 cm were filled with water only. Five sampling ports P1–P5 were installed along the column with P1–P4 located throughout the soil-filled part of the column and P5 at the water-filled section. The concentrations recorded at P5 were used to represent the outlet concentrations of the column. In addition, the water was sampled before entering the column.

A mineral medium containing a mixture of aromatic hydrocarbons and sulfate was pumped bottom to top through the columns for a period of 79 days. The flow rate as well as the concentrations of solutes were not constant throughout the experiment. The inflow concentrations for toluene varied between 17 µM and 154 µM, those for *o*-xylene between 0 and 58 µM and those for sulfate between 230 µM and 1179 µM. *o*-Xylene was injected throughout the whole period, while toluene injection lasted only up to day 52 of the experiment. The mean flow rate was 450 mL $d^{-1}$.

### 16.2.2 Experiment 2

In this experiment the same type of column was used as in Experiment 1. Experiment 2 was run for 109 days. The mean flow rate was reduced to 290 mL $d^{-1}$ for the initial 22 days and was further reduced to 150 mL $d^{-1}$ for the remaining 87 days. Concentrations were only recorded at the column inlet and outlet. As in Experiment 1 the inflow concentrations for *o*-xylene and toluene varied with time, with maximum concentrations of 374 µM of toluene and 478 µM of *o*-xylene. *o*-Xylene was added more or less constantly throughout the experiment, while four periods of elevated toluene concentrations were applied. Period 1 lasted from the beginning of the experiment until day 11 with a mean toluene concentration of approximately 120 µM, and periods 2 and 3 lasted from day 53 until day 74 and from day 82 until day 101, respectively, with mean toluene input concentrations of approximately 50 µM. Period 4 from day 101 until the end of the experiment (day 109) was characterized by distinctly increased input concentrations for toluene of about 300 µM. Between these periods inflow concentration for toluene were less than 10 µM. The intermittent supply of toluene should promote the observation of the effects of toluene on *o*-xylene degradation.

## 16.3 Set-Up of the Numerical Model

### 16.3.1 Flow and Transport Model

The multi-species reactive transport model TBC (Schäfer et al., 1998) was used for the simulation of both experiments. The model column was discretised into 19 elements, each of 0.02 m length. The temporal discretisation was 0.01 d. The high temporal resolution was necessary to fulfill the stability and accuracy criteria required by the numerical model.

TBC employs a finite-difference approach for both flow and transport modelling.

The boundary conditions for the flow model were a fixed potential boundary at the column inflow and a prescribed flux boundary condition at the outflow side. For the transport modelling a time-variant fixed concentration boundary at the inflow of the column was assumed. The concentrations values at the inflow boundaries were taken from the measurements at the column inlet.

There were no independent measurements for the determination of the effective porosity and the dispersivity of the medium. However, as the residence time of the solutes in the column (approx. 4–5 hours) was much smaller than the time intervals between the concentration measurements (at least 2 days), the solute movement inside the column could not be resolved and hence effective porosity and dispersivity values were of minor importance for the comparison of model results and observations. A value of 15 % was assumed for the effective porosity and 0.01 m for the dispersivity. These are reasonable assumptions for small scale transport in porous media.

### 16.3.2 Degradation Model

Microbial growth is the core of the biochemical reactions in the TBC model. This growth is linked to substrate and electron acceptor concentrations via Monod-terms. The back-coupling between microbial growth and reactive species consumption is performed via turnover coefficients and stoichiometric relationships. The basic equations are exemplified for a single microbial group X, one substrate S and one electron acceptor E:

$$\left(\frac{dX}{dt}\right)_{growth} = \mu_{\max} \frac{S}{K_s + S} \frac{E}{K_E + E} X \quad \text{microbial growth} \tag{1}$$

$$\left(\frac{dX}{dt}\right)_{dec} = -\mu_{dec} X \quad \text{microbial decay} \tag{2}$$

$$\frac{dS}{dt} = -Y\left(\frac{dX}{dt}\right)_{growth} \qquad \text{substrate consumption} \qquad (3)$$

$$\frac{dE}{dt} = F_S \frac{dS}{dt} \qquad \text{consumption of the electron acceptor} \qquad (4)$$

with X = concentration of microorganisms [M $L^{-3}$]
S = concentration of substrate [M $L^{-3}$]
E = concentration of electron acceptor [M $L^{-3}$]
$\mu_{max}$ = maximum growth rate [$T^{-1}$]
$\mu_{dec}$ = constant decay rate [$T^{-1}$]
$K_S$ = Monod-constant [M $L^{-3}$]
Y = turnover coefficient [M $M^{-1}$]
$F_S$ = stoichiometric factor [M $M^{-1}$]

Inhibition is simulated with the help of inhibition terms IF (Kindred and Celia, 1989). An inhibition term is of the following form:

$$IF = \frac{IC}{IC + C_I} \qquad (5)$$

with IC = inhibition constant [M $L^{-3}$]
$C_I$ = concentration of the inhibiting substance [M $L^{-3}$]

The value of IF is low if the concentration of the inhibiting substance $C_I$ is much larger than IC. IF is multiplied to the right hand side of Eq. (1). Therefore low values of IF decrease microbial growth. On the other hand, low values of $C_I$ result in a value of IF close to unity and hence microbial growth is not limited by inhibition. Equation (5) represents a non-competitive inhibition with a gradual transition between concentration ranges with and without inhibition.

The stiff system of non-linear differential equations describing microbial growth and the related species consumption is solved with the DGEAR-method, a special routine for stiff systems of equations (Hindmarsh, 1974). Transport and reaction are coupled by an iterative multistep-procedure. More details on the TBC model can be found in Schäfer et al. (1998).

## 16.4 Model Calibration

For the calibration of the model it was assumed that two different types of microorganisms co-existed in the column: one group that performs exclusively toluene degradation, and a second group which exclusively degrades *o*-xylene. Both groups use sulfate as the only electron acceptor, the hydrocarbons as sole carbon and energy sources (heterotrophic growth) and they completely mineralize the organic carbon to carbon dioxide and water. Thus the growth equations of the two groups comprise the maximum growth rates, Monod-terms for sulfate, toluene and *o*-xylene and an inhibition term for the *o*-xylene degraders.

The two microbial populations interact in a sense that *o*-xylene degradation is partly inhibited by the toluene degraders. In a first attempt an inhibition term (Eq. (5)) was used for the growth equation of the *o*-xylene degraders with toluene as the inhibiting substance.

The maximum growth rates and the turnover coefficients for toluene and *o*-xylene used in the model were obtained from batch experiments with organisms that were isolated from the same soil columns (Meckenstock, 1999; Morasch et al., 2001). The constant decay rate was adjusted so that the microbial growth and decay dynamics derived from the observed reactive species behaviour could be reproduced. The value of the Monod-constant for toluene was adapted to result in the observed residual toluene concentrations. A low value was taken for the Monod-constant for sulfate so that sulfate concentrations will not limit microbial growth. The stoichiometric factor for sulfate consumption was calculated from the underlying redox equations for a total oxidation of the substrates to $CO_2$.

Like for toluene degradation the Monod-constant for *o*-xylene was adapted in a way that the observed residual *o*-xylene concentrations could be reproduced in the model. However, in the case of *o*-xylene the interaction with the inhibition term had to be taken into account as both the Monod-term and the inhibition term affect the calculated growth of the *o*-xylene degraders. Therefore, only the *o*-xylene concentrations observed after day 52, when toluene was omitted from the medium and could no longer inhibit *o*-xylene degradation, were used for the determination of the Monod-constant. It was somewhat surprising that the Monod-constant for *o*-xylene was lower than that for toluene, although the toluene degraders outperformed the *o*-xylene degraders. However, the *o*-xylene decrease at the end of the experiment could not have been reproduced with a larger value of the Monod-constant. The inhibition constant was adjusted on the basis of the *o*-xylene concentrations observed up to day 52.

The parameters used in the calibrated model are displayed in Table 16.1. A comparison between observed and simulated concentrations for toluene, *o*-xylene, and sulfate at the column outlet is shown in Figure 16.1.

A further important model parameter was the initial density of the microorganisms. It turned out during model calibration that it was necessary to provide relatively large initial bacterial densities for the immediate inlet region of the column. Otherwise the rapid degradation of the hydrocarbons inside the column could not have been reproduced. The initial bacterial densitiy was 1 µmol cell carbon per $cm^3$ column mate-

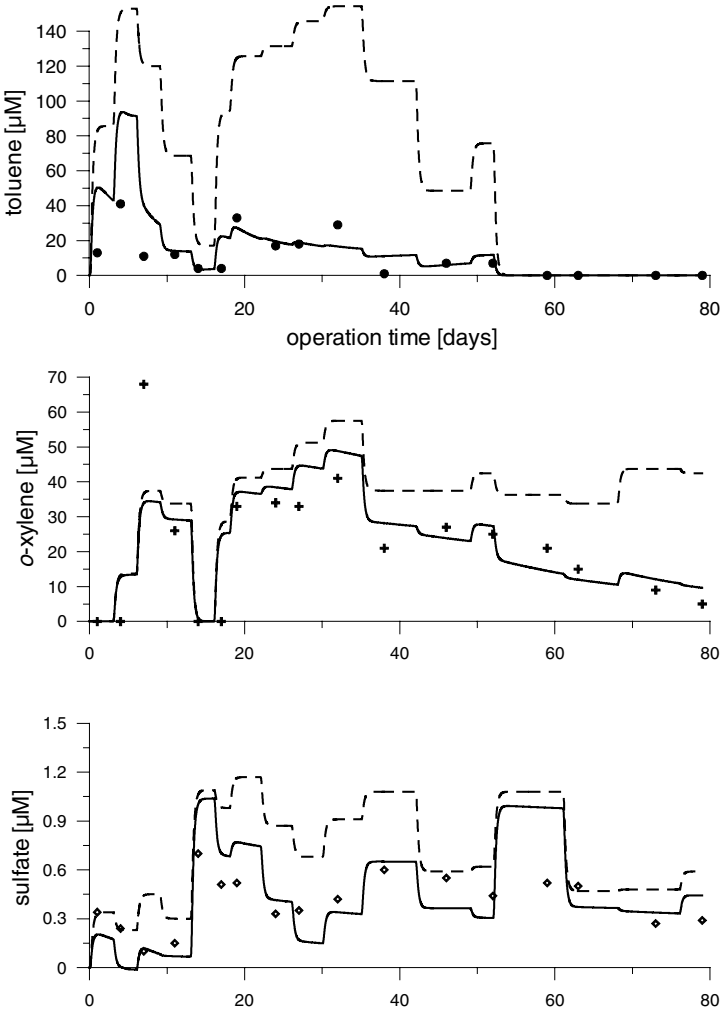


Figure 16.1: Comparison between observed and simulated concentrations for toluene (top), *o*-xylene (middle) and sulfate (bottom) at the column outlet for the simulations with toluene as inhibiting substance. The symbols represent observed values, the solid lines show simulation results with reaction, and the dashed lines show input concentrations.

rial for the first 6 cm of the column and $10^{-3}$ µmol cell carbon per $cm^3$ for the rest of the column. Identical values were used for both microbial groups. Figure 16.2 provides the observed and calculated concentrations for toluene, *o*-xylene, and sulfate along the column for one observation time. Obviously, both toluene and *o*-xylene degradation are already completed at the first observation point.

The assumed high initial bacterial densities at the column inlet seem reasonable if taken into account that the column used in Experiment 1 was operated already for a longer period prior to this experiment so that microbial populations were already established.

Table 16.1: Parameters of the biochemical model used for model calibration.

| Parameter | Meaning | Value<br>Toluene degraders | *o*-xylene degraders |
|---|---|---|---|
| $\mu_{max}$ | Maximum growth rate | 1 d-1 | 0.3 d-1 |
| $\mu_{dec}$ | Decay rate | 0.1 d-1 | 0.03 d-1 |
| $K_{tol}$ | Monod-constant for toluene | 143 µM toluene | – |
| $K_{xyl}$ | Monod-constant for *o*-xylene | – | 63 µM *o*-xylene |
| $K_{sul}$ | Monod-constant for sulfate | 1 µM sulfate | 1 µM sulfate |
| $Y_{tol}$ | Turnover coefficient for toluene | 1 mol toluene/ mol cell carbon | – |
| $Y_{xyl}$ | Turnover coefficient for *o*-xylene | – | 0.9 mol *o*-xylene/ mol cell carbon |
| $F_{sul}$ | Stoichiometric coefficient for sulfate | 3.7 mol sulfate/ mol toluene | 3.5 mol sulfate/ mol *o*-xylene |
| $IC_{tol}$ | Inhibition constant for toluene | – | 23 µM toluene |

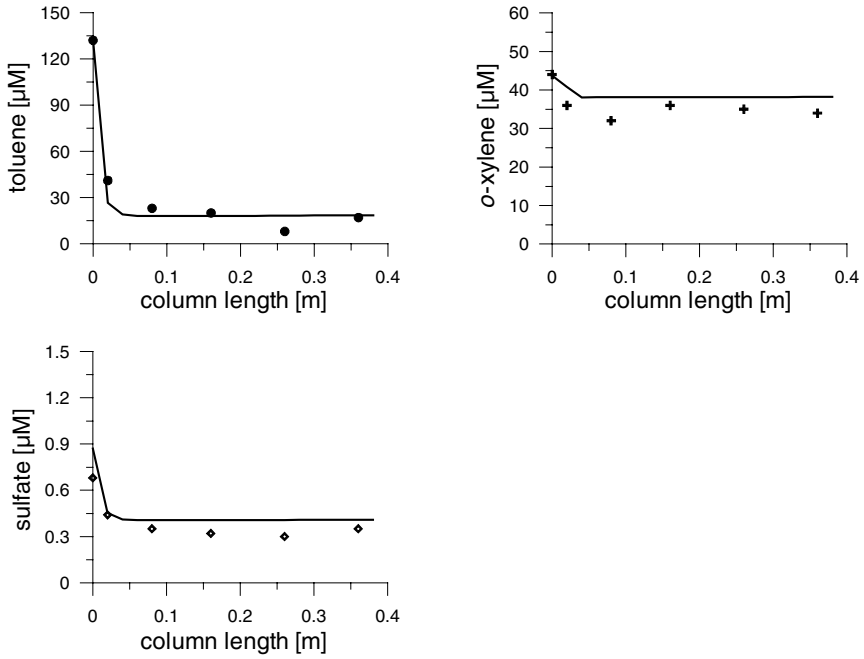


Figure 16.2: Comparison between observed (symbols) and simulated concentrations (solid lines) for toluene (top, left), *o*-xylene (top, right), and sulfate (bottom) along the column for the observations from day 24 of Experiment 1.

## 16.5 Testing of Hypotheses on the Interaction between Toluene and Xylene Degradation

### 16.5.1 Inhibition of Xylene Degradation by a Substance other than Toluene

During model calibration it was assumed that *o*-xylene degradation was limited directly by toluene. Now it was investigated whether the inhibition could have been triggered also by a special inhibitor produced by the toluene degraders. Such an inhibitor could be any excreted metabolite of toluene degradation which could interfere with the very similar *o*-xylene degradation pathway (e.g. benzylsuccinate). The production of this substance in the model is directly proportionate to the gross growth of the toluene-degrading microorganisms. The inhibition itself is again realized with the inhibition term shown before (Eq. (5)). The inhibitor is a hypothetical substance which was not measured during the experiments. Therefore, it cannot be compared to observations and its absolute concentration values are irrelevant. The inhibition effect results from the ratio of the concentration of the inhibitor and the inhibition constant. All other parameters of the biochemical model were adopted from the calibration run (cf. Tab. 16.1). Figure 16.3 shows that the observed *o*-xylene concentrations could have been reproduced with both assumptions concerning the inhibition mechanisms. Hence, it cannot be decided if *o*-xylene degradation is inhibited directly by the presence of toluene or by any special inhibitor produced by the toluene degraders. The inhibition mechanisms with toluene as inhibiting substance was used for further simulations, as the approach with a special inhibitor requires an additional species in the reaction model and therefore is numerically more demanding.

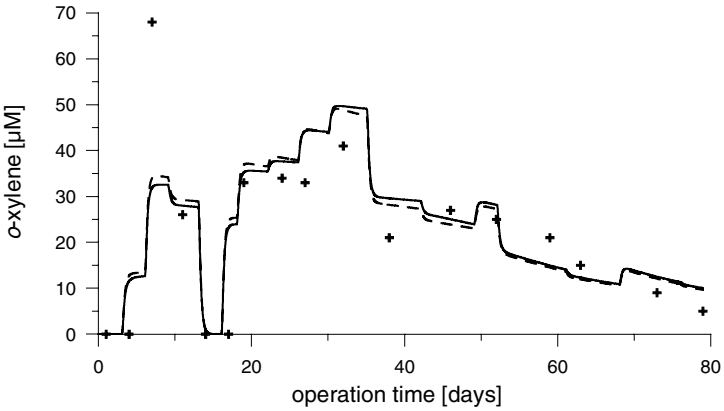


Figure 16.3: Comparison between observed and simulated concentrations for *o*-xylene at the column outlet for the simulations with a special agent as inhibiting substance. The symbols represent observed values, the solid line shows the actual results, and the dashed line shows the simulation results from the model calibration.

### 16.5.2 Competition for Sulfate

In this numerical experiment it was tested whether the preferential degradation of toluene could be the result of a competition of the two microbial groups for their common electron acceptor sulfate. To this end the inhibition term was removed from the model equations and the Monod constant for sulfate of the *o*-xylene degraders was strongly increased from 1 µM to 250 µM. This means that sulfate becomes a limiting substrate for the *o*-xylene degraders. All other parameters remained unchanged (cf. Tab. 16.1). Figure 16.4 illustrates that the reproduction of the observed *o*-xylene concentrations was less successful than in the case with an inhibition mechanism. The high value of 250 µM for the Monod-constant for sulfate was necessary to suppress *o*-xylene degraders during the period when both *o*-xylene and toluene were present in the column (up to day 52). For later times, however, the increased Monod-constant results in a too slow growth of the *o*-xylene degraders and hence in too large simulated *o*-xylene concentrations. Obviously the higher sulfate concentrations available for the *o*-xylene degraders after day 52, when toluene was no longer supplied and hence toluene degraders were no longer active, did not sufficiently compensate the adverse effect of the increased Monod-constant on the *o*-xylene degraders. The simulations suggest that sulfate is not a suitable parameter to control the interaction between toluene and *o*-xylene degraders.

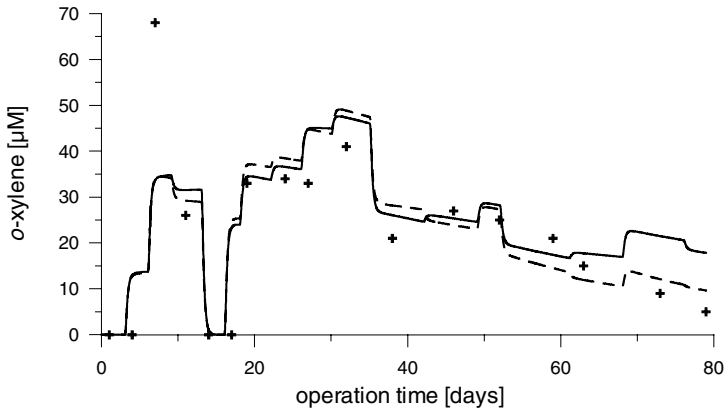


Figure 16.4: Comparison between observed and simulated concentrations for *o*-xylene at the column outlet for the simulations with competition for sulfate. The symbols represent observed values, the solid line shows the actual results, and the dashed line shows the simulation results from the model calibration.

### 16.5.3 Degradation of Toluene and Xylene by a Single Microbial Group

In the last numerical experiment concerning column Experiment 1 the hypothesis was tested that toluene and *o*-xylene degradation could be performed by a single type of organism instead of two groups as it was assumed so far. The population should use toluene preferentially if both toluene and *o*-xylene are present. This mechanisms was realized in the model in a way that the bacteria are able to perform two different metabolic pathways. The *o*-xylene degrading pathway is inhibited by the presence of toluene using the inhibition term from Eq. (5). The inhibition constant was 0.5 µM of toluene. All other parameters of the biochemical model were adopted from the preceding simulations (cf. Tab. 16.1). The simulation results for *o*-xylene are displayed in Fig. 16.5. Up to day 52 both hypotheses on the degradation mechanisms (two different groups or one single group) yield comparable results. However, from day 52 on, when toluene supply was stopped, the results are more convincing when using two different microbial groups in the model. The reason for the differing results is that the *o*-xylene degrading population needs a certain time to develop when the inhibition by toluene is stopped. This leads to a gradual increase in *o*-xylene degrading activity and a corresponding gradual decrease in *o*-xylene concentrations. For the case of one single microbial group the microbial population already developed during toluene degradation. These microorganisms abruptly switch from toluene to *o*-xylene degradation after day 52 and were therefore able to nearly completely degrade *o*-xylene from day 52 on. The observations suggest that the first hypothesis assuming two different microbial populations is more likely. However, at present there are no data available on how fast anaerobic bacteria and especially sulfate reducers can induce the synthesis of enzymes for BTEX degradation. From cultivation studies it is known that some bacteria can need several months before degradation activities can be detected in

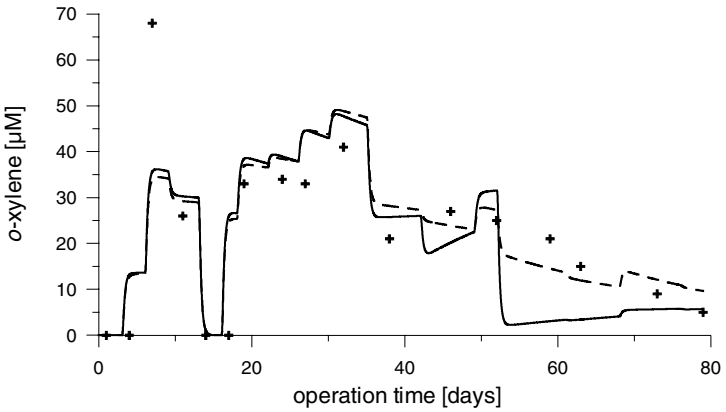


Figure 16.5: Comparison between observed and simulated concentrations for *o*-xylene at the column outlet for the simulations with one single microbial group. The symbols represent observed values, the solid line shows the actual results, and the dashed line shows the simulation results from the model calibration (with two microbial groups).

microcosm studies. Others (e.g. denitrifying strains) can grow more rapidly. Nevertheless, the finding from the modelling studies that two different types of organisms are responsible for the degradation is supported by the fact that two different sulfate-reducing organisms have been isolated from the column which can grow only either on toluene (strain TRM1) or on *o*-xylene (strain OX39) (Meckenstock, 1999; Morasch et al., 2001).

## 16.6 Simulation of Experiment 2

Discretisation and boundary conditions were taken from the simulations of Experiment 1 with the flow rates and influx concentrations being adapted to the new situation. The input concentrations for toluene and *o*-xylene for the 109 days of column operation are displayed in Figure 16.6. The only observations in Experiment 2 besides the input values were the *o*-xylene concentrations at the column outlet.

For the initial model run the biochemical parameters described in Section 16.4 were used, that is two different microbial populations were assumed and *o*-xylene degradation was inhibited by the presence of elevated toluene concentrations (Figure 16.7). Obviously the modelled inhibition of *o*-xylene degradation was too weak from day 40 on. In the simulations, *o*-xylene was nearly completely degraded, while the observations show increased *o*-xylene degradation around day 60 and day 80.

To better adjust simulated *o*-xylene concentrations to the measurements the inhibition constant for toluene was reduced from 23 µM toluene as used in Experiment 1 to 7 µM. Figure 16.8 reveals that the simulation results now correspond much better to the observations. The lower inhibition constant results in a stronger inhibition of the

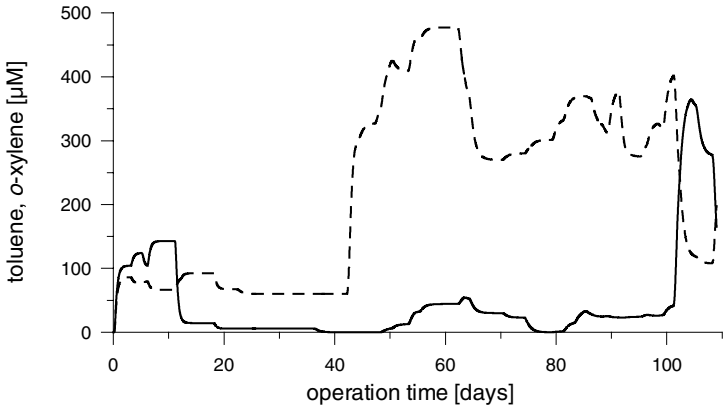


Figure 16.6: Input concentration for toluene (solid line) and *o*-xylene (dashed line) in Experiment 2.

*o*-xylene degraders and therefore to increased simulated *o*-xylene concentrations at the column outlet.

In addition to reducing the inhibition constant, the initial density for the *o*-xylene degrading bacteria at the column inlet had to be reduced from the value of 1 µmol cell carbon per $cm^3$ column material as used in Experiment 1 to 0.4 µmol cell carbon per $cm^3$. Otherwise the higher *o*-xylene concentrations for the initial phase of Experiment 2 could not have been reproduced. Different initial bacterial concentrations are not unrealistic, as different columns (although of the same type) were used for the two experiments.

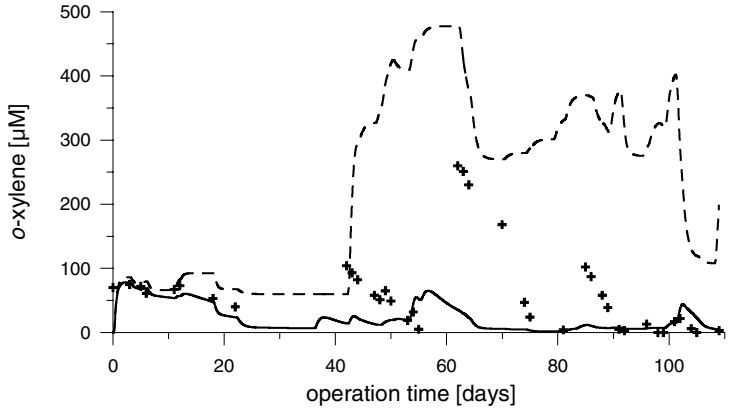


Figure 16.7: Comparison between observed and simulated concentrations for *o*-xylene at the column outlet in Experiment 2 using the biochemical parameters from Experiment 1 (Table 16.1). The symbols represent observed values, the solid line shows the actual results, and the dashed line shows the input concentrations.

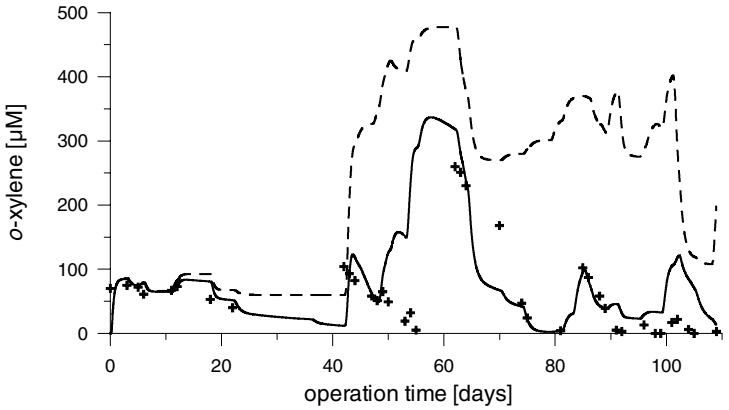


Figure 16.8: Comparison between observed and simulated concentrations for *o*-xylene at the column outlet in Experiment 2 with reduced inhibition constant. The symbols represent observed values, the solid line shows the actual results, and the dashed line shows the input concentrations.

At the end of Experiment 2 the model results show increased *o*-xylene concentrations which are the consequence of the inhibition effect of the high toluene concentrations on *o*-xylene degraders at that time (cf. Fig. 16.6). The observations, however, do not show increased *o*-xylene concentrations for the latest stages of Experiment 2. A better correspondence between simulations and observations would have required an increase of the inhibition constants for later times of the experiment. This hints on some kind of acclimatization effect of the *o*-xylene degraders towards elevated toluene concentrations. However, it has to be considered that during this experiment microbial growth was limited by the substrates toluene and *o*-xylene only. In cases where additional substances become limiting, e.g. if the common electron acceptor sulfate becomes depleted, the toluene degraders might permanently outcompete the *o*-xylene degraders.

## 16.7 Conclusions and Outlook

Numerical simulations with a reactive transport model were performed for two column experiments on the anaerobic degradation of *o*-xylene and toluene. The goal of the simulations was to test hypotheses on the interaction of toluene and *o*-xylene degradation processes.

The simulations and observations did not allow to distinguish whether xylene degradation was directly inhibited by the presence of toluene or whether the inhibition was controlled by a special inhibitor produced during toluene degradation. Toluene itself could be inhibitory as it is structurally and chemically very similar to xylene and could therefore directly inhibit the degrading enzymes. But also metabolites from toluene degradation could inhibit xylene degradation in later stages of the pathway as some metabolites are excreted in rather high concentrations into the medium. The toxicity of such compounds has not been elucidated so far and thus toxic effects of metabolites other than pure inhibition of degradative enzymes cannot be excluded.

The results from another model run suggested that competition for the common electron acceptor of the two hydrocarbons, sulfate, was not controlling the degradation process during the experiments. This was expected, however, because sulfate was added in excess and the medium homogeneously mixed which excludes local limitations due to heterogeneous distribution of substrates and electron acceptor. Nevertheless, limiting supply of electron acceptor may influence the degradation of BTEX in the field to a large extent because inhibition effects as reported here might become dominant under competitive conditions.

Further simulations considered the question whether the two aromatic hydrocarbons are degraded by two different bacterial populations or the degradation is performed by a single organism which is able to use both substrates. Here the comparison of model results with the observations rendered evidence that the first possibility (i.e. two groups) is more likely.

Finally, the model parameters determined during the simulations of the first experiment were used to simulate a second experiment which was conducted under comparable conditions, but with a special emphasis on the inhibition process. With slightly modified parameters, the inhibition model proofed to be suitable for the simulation of the second experiment, too. Observations from the final stage of the second experiment suggest that there is a certain acclimatization of the microbial population in the soil column to elevated toluene concentrations which leads to a nearly simultaneous degradation of both hydrocarbons.

The modelling of the soil column experiments revealed two features that are also of importance for the simulation of the degradation process on the field scale:

- Degradation of toluene and *o*-xylene is probably performed by two different organisms. Therefore, two microbial groups should be considered in field scale modelling of these degradation processes.
- There can be an inhibition of toluene or of one of its metabolites on *o*-xylene degradation which may especially become relevant if the two populations compete for certain limiting nutrients or electron acceptors.

## Acknowledgement

Many thanks to R. Warthmann and C. Winter, University of Konstanz, for performing the soil column experiments and B. Schink for constant support. Financial support was provided by the Deutsche Forschungsgemeinschaft through grants Da 222/2 and Schi 180/7.

## 16.8 References

Heider, J.; Spormann, A. M.; Beller, H. R.; Widdel, F. (1999): Anaerobic bacterial metabolism of hydrocarbons. *FEMS Microbiol. Rev.* **22**, 459–473.

Herfort, M.; Ptak, Th.; Hümmer, O.; Teutsch, G.; Dahmke, A. (1998): Testfeld Süd: Einrichtung der Testfeldinfrastruktur und Erkundung hydraulisch-hydrogeochemischer Parameter des Grundwasserleiters. *Grundwasser* **3**, 159–166.

Hindmarsh, A. C. (1974): GEAR. Ordinary differential equation system solver. UCID–30001, Revision 3, Lawrence Livermore Laboratories, Livermore, Ca.

Kindred, J. S.; Celia, M. A. (1989): Contaminant transport and biodegradation, 2. Conceptual model and test simulations. *Water Resour. Res.* **2**, 1149–1160.

Meckenstock, R. U. (1999): Fermentative toluene degradation in anaerobic defined syntrophic cocultures. *FEMS Microbiol. Lett.* **177**, 67–73.

Morasch, B.; Annweiler, E.; Warthmann, R. J.; Meckenstock, R. U. (2001): The use of a solid adsorber resin for enrichment of bacteria with toxic substrates and to identify metabolites: degradation of naphthalene, *o*-, and *m*-xylene by sulfate-reducing bacteria. *J. Microbiol. Meth.* **44**, 183–191.

Schäfer, D.; Schäfer, W.; Kinzelbach, W. (1998): Simulation of reactive processes related to biodegradation in aquifers 1. Structure of the three-dimensional reactive transport model. *J. Contaminant Hydrol*. **31**, 167–186.

Winter, C. (1997): Anaerober mikrobieller Abbau von BTX-Aromaten und Naphthalin in anoxischen Bodensäulen. Staatsexamensarbeit, Universität Konstanz, pp. 76.